Magnetic Moment Measurements in Unstable Platinum Nuclei

by

Stephen Scott Anderssen

A thesis submitted for the degree of
Doctor of Philosophy
of The Australian National University

May 17, 1995

Preface

The work described here is concerned primarily with the experimental determination of the magnetic moments of the first-excited states in the unstable, neutron-deficient, even-mass platinum nuclei. It was carried out at the Department of Nuclear Physics of the Australian National University. The project was suggested by Dr. A.E. Stuchbery, and inspired by previous work on shape coexistence performed in the Department by the Nuclear Spectroscopy group.

All the experiments were conducted in the Department's 14UD Pelletron Accelerator laboratory with assistance from the academic and technical staff. The modifications to existing major equipment were designed by me and constructed in conjunction with technicians. I prepared the targets with some assistance.

All data analysis was carried out by me using mainly existing computer codes, including a program written by Dr. A.E. Stuchbery to fit perturbed angular correlation data. The interpretation of the results was made by Dr. A.E. Stuchbery and myself. The F-spin mixing calculations I performed were based on the work of Dr. S. Kuyucak and Dr. A.E. Stuchbery.

The material presented in this thesis is being prepared for publication. Parts of the work have been accepted for publication as

- *Measured Static Hyperfine Magnetic Fields Following Implantation of Pt into Fe Interpreted as Evidence for Pre-Equilibrium Effects.*
  S.S. Anderssen and A.E. Stuchbery, Hyperfine Interactions, *in press.*

No part of this thesis has been submitted for a degree at any other university.

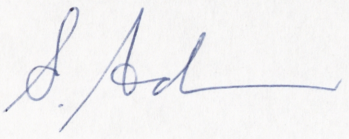

S.S. Anderssen
Canberra, May 17, 1995

Acknowledgements

I would particularly like to acknowledge my principal supervisor Andrew Stuchbery, for his many contributions to this project. I am indebted to him for his invaluable assistance and, also, for his patience with me, an example of which was his proof-reading of the numerous drafts of this thesis.

I am grateful to everyone else that assisted me with the long and difficult experiments needed for this work, especially Aidan Byrne, George Dracoulis, Paul Davidson, Greg Lane, Herb Bolotin, Paddy Regan and Tibor Kibédi. Credit must also go to Gordon Foote (and Paul) and David Wiesser and all the workshop guys for their knowledge and skills. A virtue of all of these people, which I was dependent on many times, is their willingness to help with any problem at anytime.

I have found the Department to be a great place to work, thanks to the friendly atmosphere created by everyone there. I have to admit, however, that I didn't spend all of my time working. For the good times out on the golf-course, on the soccer pitch, in the beer garden and at the various junk-food places, I'd like to *blame* Greg, Roy Lemmon and Paddy.

I must also mention the support of my family and friends and, of course, my wife Sandi.

I feel very privileged to have studied in this laboratory. I would like to thank George Dracoulis and Trevor Ophel for providing me with this opportunity and an Australian National University postgraduate scholarship.

Abstract

An implantation-decay technique has been developed to measure the magnetic moments of short-lived ($\tau < 1$ns), excited states in unstable nuclei. In a series of experiments the gyromagnetic ratios of the 2_1^+ states in ^{184,186,188}Pt were measured relative to that for ^{192}Pt, giving $g(2_1^+,^{184}\mathrm{Pt}) = 0.28 \pm 0.03$, $g(2_1^+,^{186}\mathrm{Pt}) = 0.27 \pm 0.03$ and $g(2_1^+,^{188}\mathrm{Pt}) = 0.29 \pm 0.04$. In separate experiments, the 2_1^+-state g-factor in ^{190}Pt was measured using the transient-field technique to be $g(2_1^+,^{190}\mathrm{Pt}) = 0.285 \pm 0.013$, and the lifetime of the 2_1^+ state in ^{188}Pt was measured as $\tau(2_1^+,^{190}\mathrm{Pt}) = 91 \pm 7$ ps using the Doppler-shift recoil-distance method.

The measured 2_1^+-state g-factors for ^{184,186,188,190,192,194,196,198}Pt are constant within experimental uncertainties, in clear disagreement with the predictions of the proton-neutron interacting boson model (IBM-2) assuming F-spin symmetry, and the 'pairing-plus-quadrupole interaction' calculations of Kumar and Baranger. The g-factor systematics are discussed primarily in terms of the IBM-2, with attention given to: empirical boson g-factor values; effective boson numbers; the g-boson degree of freedom; and F-spin symmetry breaking.

The $g(2_1^+)$ for ^{184,186,188}Pt are consistent with previously proposed shape-coexistence models for these nuclei. In the IBM analysis, the key feature is that the deformed intruder configuration has a larger effective proton boson number than the 'normal', less-deformed configuration. A consistent IBM-2 description of the magnetic dipole properties for ^{190,192,194,196,198}Pt has been found by using appropriate F-spin mixing mechanisms.

Contents

List of Tables

List of Figures

Chapter 1

Introduction

Research into magnetic moments has played an important role in nuclear physics. The Schmidt lines for single-particle states and the collective estimate $g = Z/A$ are two well-known results of early studies. More recently, and continuing to the present day, the magnetic moments of nuclei near closed shells have provided a direct probe of the purity of configurations for individual states. Studies of moment systematics in regions of deformed collective nuclei have given valuable insights into the relative angular momentum carried by protons and neutrons.

The usefulness of moment information is derived, at least partially, from its dependence on the structure of a single nuclear state, as compared with transition data, for example, which depend on the properties of both the initial and final levels of the transition. However, the relative complexity of moment measurements has seen magnetic dipole ($M1$), and also electric quadrupole ($E2$), moments studied less in nuclear spectroscopy than the more familiar level energies and electromagnetic transition rates (or state lifetimes). This is particularly true for short-lived ($\tau < 1$ns) excited states in *unstable* nuclei. For nuclei in the mass region $100 < A < 200$ there have been approximately 200 nuclear magnetic moments (or g-factors) measured and only about 10 of these have been in unstable nuclei. Typical are the even-even platinum ($_{78}$Pt) nuclei, where the g-factors of low-lying nuclear levels have been measured in only the four stable isotopes, ^{192,194,196,198}Pt.

1.1 Overview

This thesis describes the development of an implantation-decay technique for measuring the magnetic moments of short-lived excited states in unstable nuclei, and its implementation for the neutron-deficient Pt isotopes – ^{184,186,188,190}Pt. The results of these experiments have provided a series of measured 2_1^+-state g-factors which covers nearly half of the $N = 82$-to-126 neutron shell, from $N = 106$ to $N = 120$. These data highlight the striking contrast between experimental $g(2_1^+)$ values for the Pt nuclei and the g-factor estimate of the interacting boson model (IBM-2) in the limit of F-spin purity. It will be shown, however, that the magnetic moments can be interpreted in terms of F-spin symmetry breaking and by examining the implications of shape coexistence.

Definitions of the magnetic moment and g-factor, and the simple estimate of $g = Z/A$ for collective nuclei are discussed in the remainder of this introductory chapter. In chapter 2 the interacting boson model (IBM) is reviewed. The principles of magnetic moment measurements and the relevant theoretical background are described in chapter 3. Alternative experimental techniques and their limitations, with a view to making measurements on the neutron-deficient Pt nuclei, are also reviewed. A description of the implantation-decay technique is given in chapter 4 with information on the experimental design, the equipment used and details of the individual experiments. This is followed by a description of the data analysis in chapter 5, and presentation of the results in chapter 6.

A measurement of the 2_1^+ g-factor for ^{190}Pt, using the transient-field technique, is reported in chapter 7. In chapter 8 a recoil-distance measurement of the 2_1^+-state lifetime in ^{188}Pt is described. Chapter 9 contains a brief comparison of the experimental $g(2_1^+)$ values with the results of a variety of theoretical studies, and then a thorough discussion and interpretation of them within the IBM-2. This is split into two sections. The effects of shape coexistence on the 2_1^+ g-factors of the lighter Pt isotopes ($A \leq 188$) is elucidated through band-mixing calculations for these nuclei. For an interpretation of the g-factors in the heavier nuclei ($A \geq 190$) several possible mechanisms are considered. It is shown that F-spin mixing provides the most satisfactory description. A summary of these findings and the conclusions are given in chapter 10 with suggestions for future study. In appendix A a study of the static hyperfine field following ion-implantation is presented.

1.2 Nuclear Magnetic Dipole Moments

A magnetic dipole field is produced by a simple current loop. In classical terms, the circuit carries a current i due to a particle with charge e (and mass m) moving in a circle of radius r at constant velocity v. The resulting magnetic moment, μ, can be written in terms of the angular momentum of the particle, $l = mvr$, as

$$|\mu| = iA = \frac{e}{2\pi r/v}\pi r^2 = \frac{evr}{2} = \frac{e}{2m}|l| \quad . \tag{1.1}$$

In quantum physics, the magnetic moment is defined in terms of the maximum expectation value of l, i.e. $m_l = +l$, and the analog of eq. 1.1 is

$$\mu = \frac{e\hbar}{2m} l \quad . \tag{1.2}$$

For nucleons the nuclear magneton is defined as $\mu_N \equiv e\hbar/2m_p$, with the proton mass, m_p, in place of m. Equation 1.2 may then be written with the gyromagnetic ratio or g-factor for the orbital angular momentum, g_l, as

$$\mu = g_l\, l\, \mu_N \quad , \tag{1.3}$$

where for protons $g_l^{(\pi)} = 1$, and for neutrons, which have no electric charge, $g_l^{(\nu)} = 0$.

The intrinsic spin, s, of an individual nucleon also generates a dipole moment. This may be written in the form of eq. 1.3,

$$\mu = g_s\, s\, \mu_N \quad , \tag{1.4}$$

with the spin g-factors for protons and neutrons; $g_s^{(\pi)} \simeq 5.586$ and $g_s^{(\nu)} \simeq -3.826$. Nuclear magnetism then arises from two sources: the orbital motion of protons, as they each carry one unit of positive charge, and the intrinsic dipole moments of both protons and neutrons.

The magnetic dipole operator is usually expressed in terms of the orbital and intrinsic spin angular momentum of each nucleon, $\vec{l}^{(i)}$ and $\vec{s}^{(i)}$, summed over the A particles of the nucleus, e.g. ref. [Ca90a]

$$T(M1) = \mu_N \sum_{i=1}^{A} (g_l^{(i)}\, \vec{l}^{(i)} + g_s^{(i)}\, \vec{s}^{(i)}) \quad , \tag{1.5}$$

where the orbital and spin g-factors, $g_l^{(i)}$ and $g_s^{(i)}$, are as given above. The expectation value of the $M1$ operator is dependent on M, the projection of the angular momentum I on the quantization axis, and, therefore, the orientation of the nucleus. However, by using the reduced matrix element $\langle I \,||\, T(M1) \,||\, I \rangle$, which is common to all $2I + 1$ substates of a state with spin I, the magnetic dipole moment for the state may be defined independently of nuclear orientation.

Infact, the magnetic moment μ is defined as the expectation value of the z-component of the operator of eq. 1.5 when the nuclear spin is aligned with the quantization axis, i.e. $M = I$, e.g. refs. [St64, Al75]:

$$\begin{aligned} \mu &= \langle I\, M = I \,|\, T(M1) \,|\, I\, M = I \rangle \\ &= \frac{I}{\sqrt{I(I+1)(2I+1)}} \langle I \,||\, T(M1) \,||\, I \rangle \quad . \end{aligned} \tag{1.6}$$

In general, the nuclear dipole moment, which is measured in units of nuclear magnetons μ_N, is related to the nuclear spin by

$$\mu = g\, I\, \mu_N \quad , \tag{1.7}$$

where g is the gyromagnetic ratio or g-factor for the state. It is this gyromagnetic ratio that is measured directly in perturbed-angular-correlation/distribution experiments.

1.2.1 The g-factor estimate for collective even-even nuclei

The simple, classical treatment of an even-even nucleus in the hydrodynamic model, as a rotating charged spheroid consisting of proton and neutron 'fluids', provides an estimate of the g-factor for a collective nuclear state.

It is assumed that all of the nucleons are paired (the spins are said to be 'saturated') so that the total angular momentum is due only to the the orbital motion of the nucleons and the magnetic effects arise solely from the motion of the charged protons. The g-factor is then given by

$$g = \frac{L_p}{L_p + L_n} \quad , \tag{1.8}$$

where $L_{p(n)}$ is the orbital angular momentum of the proton (neutron) fluids. From the initial assumption of a rotating spheroid

$$g = \frac{\mathcal{J}_p}{\mathcal{J}_p + \mathcal{J}_n} \quad , \tag{1.9}$$

where $\mathcal{J}_{p(n)}$ is the moment of inertia of the protons (neutrons), and

$$g = Z/A \quad . \tag{1.10}$$

Although this provides an approximate value for many nuclear g-factors, it generally overestimates experimental results. This may be attributed mainly to the fact that the pairing force for protons is generally stronger than for neutrons, which results in a relatively smaller moment of inertia for protons, and hence $g < Z/A$ [Ni61, Gr66a, Pr68]. Analogous expressions to eqs. 1.8, 1.9 and 1.10 for g-factors in the interacting boson model will be introduced in the next chapter.

Chapter 2

The Interacting Boson Model

2.1 General Features – IBM-1

The interacting boson model (IBM) [Ar87] is an algebraic collective description of nuclear structure. It uses a system of interacting bosons, where each boson is a correlated pair of like nucleons coupled to angular momentum and parity 0^+ or 2^+. The assumption is made, similar to microscopic shell-model theories, that nuclear behaviour is dominated by the finite number of active (or valence) nucleon pairs outside closed shells. The IBM hamiltonian has limiting symmetries that can be identified with different types of collective nuclei. A feature of this approach is that these symmetries can be evaluated through their respective group structures, which provide a simple algebraic formalism. Regardless of its simplicity the IBM has been very successful in describing the low-excitation level energies and $E2$ transition rates in collective nuclei of medium-to-heavy mass.

In the original version of the interacting boson model (IBM-1), which does not distinguish between protons and neutrons, the three limiting symmetries correspond closely to the geometrical descriptions of anharmonic vibrational nuclei, deformed (axially-symmetric) rotational nuclei and γ-unstable nuclei. Transitional nuclei may be treated as intermediate cases between these and the hamiltonian solved numerically. For example, following the observation [Ci78] that aspects of the spectroscopy of ^{196}Pt are very similar to the γ-soft O(6) limit of the IBM-1, the Os-Pt region has been interpreted in terms of a progression from this point towards the SU(3) limit that corresponds to a deformed-rotor.

According to the IBM-1, the low-energy collective properties of an even-even nucleus may be described in terms of six boson-creation and boson-annihilation

operators, $b^\dagger_{l\mu}, \tilde{b}_{l\mu}$, comprising a scalar or s-boson with angular momentum $l = 0$ and a quadrupole $l = 2$ d-boson with magnetic substates $\mu = 0, \pm 1, \pm 2$. The hamiltonian may be written in terms of the thirty-six generators of the special unitary group in six dimensions SU(6), where these operators are the tensor products of the boson operators $G_{ll'} = \{b^\dagger_l * \tilde{b}_{l'}\}$, [Ca90a]

$$H = \sum_l \epsilon_l G_{ll'} + \sum_{l_1 l_1' l_2 l_2'} u_{l_1 l_1' l_2 l_2'} G_{l_1 l_1'} G_{l_2 l_2'} \quad . \tag{2.1}$$

This hamiltonian contains nine parameters; two of them in the one-body terms, which represent the single-boson energies, and seven in the two-body terms describing the boson-boson interactions. This number may be reduced, however, as not all of the terms are independent.

Active bosons are those outside the nearest closed shell, so that pairs of nucleon *holes* are counted in a shell which is more than half full. Boson number is conserved ($N = n_s + n_d$). This means that ϵ is the energy difference between s- and d-bosons and there is a single one-body operator $n_d = (d^\dagger . \tilde{d})$, which is the number of d-bosons. A general hamiltonian may then be written in a multipole form as

$$H = \epsilon n_d + a_0(P^\dagger . P) + a_1(L^\dagger . L) + a_2(Q^\dagger . Q) + a_3(T^\dagger_3 . T_3) + a_4(T^\dagger_4 . T_4) \quad , \tag{2.2}$$

where the two-body terms include operators for pairing, P, orbital angular momentum, L, and quadrupole-quadrupole interactions, Q. For example,

$$L = \sqrt{10}\,[d^\dagger \times \tilde{d}]^{(1)} \quad , \tag{2.3}$$

where the square brackets denote vector coupling, i.e.

$$L = \sum_{\mu_1 \mu_2} \langle 2\mu_1 \mu_2 | 1M \rangle d^\dagger_{\mu_1} \tilde{d}_{\mu_2} \quad .$$

The $M1$ and $E2$ operators are also written in terms of boson operators. The lowest-order $M1$ operator may be written in terms of the angular momentum operator as

$$T(M1) = \beta\,[d^\dagger \times \tilde{d}]^{(1)} = \sqrt{\frac{3}{4\pi}}\, g_B L \quad , \tag{2.4}$$

where g_B is a parameter called the effective boson g-factor. Because the $M1$ operator is proportional to L, the magnetic moments are all equal and $M1$ transitions are forbidden. To obtain g-factor variations and non-zero $M1$ transition rates it is necessary to either include two-body terms in the $M1$ operator or, as is now more commonly done, to extend the model to distinguish between proton and neutron bosons [Ca90a].

2.2 The Proton-neutron Model – IBM-2

It is well established that the strong, attractive quadrupole interaction between protons and neutrons is very important for describing low-energy collective nuclear behaviour. The success of the IBM-1 shows that it does include this. However, to express it explicitly in the IBM and, thereby, make a connection with microscopic theories it is necessary to distinguish between proton- and neutron-bosons and to consider an interaction between them which is different from that between like-bosons. The proton-neutron interacting boson model (IBM-2) is an extension of the IBM-1 which treats the proton and neutron degrees of freedom separately.

The group structure of the IBM-2 is formed by the product SU(6) $\otimes$ SU(6). Although there are limiting symmetries for this model, as in the IBM-1, most realistic cases require numerical solution. The hamiltonian may be written as a sum

$$H = H_\pi + H_\nu + V_{\pi\nu} \quad , \tag{2.5}$$

where H_π and H_ν have the general structure of eq. 2.2 and $V_{\pi\nu}$ is the interaction between proton- and neutron-bosons. With separate conservation of the proton and neutron boson numbers the hamiltonian has thirty parameters. In practical calculations, however, many of these parameters are set to zero. Simple microscopic considerations can suggest the important terms.

A common form for the hamiltonian is [Bi80]

$$H = \epsilon_\pi n_{d,\pi} + \epsilon_\nu n_{d,\nu} + \kappa Q_\pi^{(2)}.Q_\nu^{(2)} + \kappa_\pi Q_\pi^{(2)}.Q_\pi^{(2)} + \kappa_\nu Q_\nu^{(2)}.Q_\nu^{(2)} + V_{\pi\pi} + V_{\nu\nu} + M_{\pi\nu} \quad . \tag{2.6}$$

The $\epsilon_\pi n_{d,\pi} + \epsilon_\nu n_{d,\nu}$ term describes the single-boson energies and accounts for the strong pairing force between like particles. The quadrupole-quadrupole interaction between different particles is expressed by the term $Q_\pi^{(2)}.Q_\nu^{(2)}$ with strength κ, where the quadrupole operator is

$$Q_\rho^{(2)} = [d_\rho^\dagger \times \tilde{s}_\rho + s_\rho^\dagger \times \tilde{d}_\rho]^{(2)} + \chi_\rho [d_\rho^\dagger \times \tilde{d}_\rho]^{(2)} \; (\rho = \pi, \nu) \tag{2.7}$$

and χ_π, χ_ν are parameters. Quadruple-quadrupole interactions between like-bosons, $Q_\rho^{(2)}.Q_\rho^{(2)}$ $(\rho = \pi, \nu)$ with strengths κ_π and κ_ν, may also be included.

To ensure that the low-lying spectrum is dominated by symmetric states in which the protons and neutrons move in phase, as in the IBM-1, non-symmetric states are pushed up in energy by including the Majorana term,

$$M_{\pi\nu} = \xi_2 [d_\pi^\dagger \times s_\nu^\dagger - s_\pi^\dagger \times d_\nu^\dagger]^{(2)}.[\tilde{s}_\nu \times \tilde{d}_\pi - \tilde{s}_\pi \times \tilde{d}_\nu]^{(2)} + \sum_{\lambda=1,3} \xi_\lambda [d_\pi^\dagger \times d_\nu^\dagger]^{(\lambda)}.[\tilde{d}_\pi \times \tilde{d}_\nu]^{(\lambda)} \quad . \tag{2.8}$$

Additional terms describing the residual interactions between like-bosons, $V_{\pi\pi}$ and $V_{\nu\nu}$, may play a substantial role in certain circumstances, for example, near closed shells where the active particles are primarily of one type. These terms are included here for completeness and may be written in the form

$$V_{\rho\rho} = \frac{1}{2} \sum_{\lambda=0,2,4} C_{\lambda\rho} [d_\rho^\dagger \times d_\rho^\dagger]^{(\lambda)}.[\tilde{d}_\rho \times \tilde{d}_\rho]^{(\lambda)} \; (\rho = \pi, \nu) \quad . \tag{2.9}$$

2.2.1 Parameter values

The parameterization of the IBM-2 hamiltonian may vary significantly depending on the nuclear region being studied. For vibrational-like nuclei, at the ends of the shell where the total number of bosons is small, the pairing $\epsilon_\rho n_{d,\rho}$ terms dominate and κ is small. Near the middle of the shell the $Q_\pi^{(2)}.Q_\nu^{(2)}$ term dominates. Rotational characteristics are observed when $\chi_\pi \simeq \chi_\nu$ are both large and negative. The γ-unstable limit is approached for relatively large quadrupole-quadrupole interactions with $\chi_\pi \simeq -\chi_\nu$.

Simple microscopic considerations suggest the general dependence of the interaction parameters on proton and neutron number [Bi80]: ϵ_π and ϵ_ν are roughly constant; κ has a maximum near the middle of the shell and uniformly decreases

on either side; the quadrupole-quadrupole interactions between identical particles are small, $\kappa_\pi \simeq \kappa_\nu \simeq 0$; $\chi_{\pi(\nu)}$ may be approximately constant for changing neutron (proton) number and increases with proton (neutron) number to change sign near the middle of the shell from negative values, where the valence shell is less than half full with particle-bosons, to positive for the upper half of the shell (hole-bosons). For most collective nuclei the structure is dominated by the pairing and quadrupole-quadrupole terms, so that the remaining parameters play a less important role. This is in reasonable agreement with the results of most phenomenological studies based on experimental data for isotopic and isotonic nuclear series.

2.2.2 F-spin

The symmetry in the proton and neutron degrees of freedom, introduced by their differentiation in the IBM-2, is described with the F-spin formalism. Similar to isospin in fermion systems, the F-spin of a boson has the value $F = \frac{1}{2}$ with projections of $F_z = +\frac{1}{2}, -\frac{1}{2}$ for proton- and neutron-bosons, respectively.

In a given nucleus with a fixed number of valence proton and neutron bosons, N_π and N_ν, we define $F_z = \frac{1}{2}(N_\pi - N_\nu)$. Nuclear states are then characterized by different values of the F-spin quantum number, which range from $|F_z|$ to $F_{max} = \frac{1}{2}(N_\pi + N_\nu)$ in unit steps. States which are totally symmetric with respect to protons and neutrons correspond to those of the IBM-1 and have maximal F-spin $F = F_{max}$. Non-symmetric states have lower F-spin symmetry $F < F_{max}$.

F-spin is a good quantum number when the IBM-2 hamiltonian is fully symmetric in the proton-neutron degrees of freedom. This requires, for example, the same energy difference between the s- and d-bosons for protons and neutrons, $\epsilon_\pi = \epsilon_\nu$, and a proton-neutron ($\pi$-$\nu$) boson quadrupole-quadrupole interaction which is equal to that for like-bosons (π-π and ν-ν). The latter is achieved using the strength parameters $\kappa = 2\kappa_\pi = 2\kappa_\nu$ for the interactions and equivalent forms for the quadrupole operators, $Q^{(2)}_\rho$ (which include the parameters χ_ρ), by setting $\chi_\pi = \chi_\nu$. In many cases, however, these three conditions are not all satisfied and there is some degree of proton-neutron asymmetry in the hamiltonian. In most applications it is assumed that $\epsilon_\pi = \epsilon_\nu$, but the structure of the proton and neutron quadrupole operators is different, $\chi_\pi \neq \chi_\nu$, and the quadrupole interaction between like-bosons is commonly assumed to be much weaker than that

between proton- and neutron-bosons, $\kappa \gg \kappa_\pi = \kappa_\nu \simeq 0$. This will break the F-spin symmetry, creating some degree of F-spin mixing for the low-lying states.

The extent of the F-spin breaking is determined not only by the degree of proton-neutron asymmetry in the hamiltonian but also by the strength of the Majorana term. This operator separates states with different F-spin (see sect. 2.2) so that, for a positive Majorana coefficient ξ_2 (see eq. 2.8), maximal F-spin states are at lower excitation energies than levels with $F < F_{max}$. This has the effect of pushing partially symmetric states to higher energies and, therefore, the low-lying states, especially the first-excited 2_1^+ level in an even-even nucleus, are predominantly symmetric with only small admixtures of $F < F_{max}$.

2.2.3 $E2, M1$ operators and g-factors

In the IBM-2 the most general transition operator of angular momentum L has the form

$$T(L) = T_\pi(L) + T_\nu(L)$$

$$T_\rho(L) = \alpha_{2,\rho}\delta_{L2}(d_\rho^\dagger \times \tilde{s}_\rho + s_\rho^\dagger \times \tilde{d}_\rho)^{(2)} + \beta_{L\rho}(d_\rho^\dagger \times \tilde{d}_\rho)^{(L)} + \gamma_{0\rho}\delta_{L0}(s_\rho^\dagger \times \tilde{s}_\rho)^{(0)} \quad , \quad (2.10)$$

where δ_{L2} and δ_{L0} are Kronecker deltas. The electric quadrupole ($E2$) operator, used to calculate quadrupole moments and electric quadrupole transition rates, is given by eq. 2.10 with $L = 2$ and simplifies to

$$T(E2) = e_\pi Q_\pi^{(2)} + e_\nu Q_\nu^{(2)} \quad , \quad (2.11)$$

where $Q_\rho^{(2)}$ are the quadrupole operators of eq. 2.7 and e_π, e_ν are the proton and neutron effective boson charges. These parameters may be determined empirically; e.g. the values $e_\pi = 0.18\,\mathrm{eb}$ and $e_\nu = 0.13\,\mathrm{eb}$ have been determined for the Os and Pt isotopes from fits to $B(E2; 2_1^+ \rightarrow 0_1^+)$ transition rates [Is86]. Although the χ_ρ values in the $E2$ operator are not necessarily the same as those in the hamiltonian (eq. 2.6) they are usually made so, which is known as Consistent Q-Formalism (CQF).

The magnetic dipole properties are calculated using the first-order $M1$ operator which, in its most general form, is given by [Sa84]

$$T(M1) = (\sqrt{\frac{3}{4\pi}})(g_\pi L_\pi + g_\nu L_\nu) \quad . \tag{2.12}$$

The angular momentum operators L_ρ are defined above (eq. 2.3) and the proton- and neutron-boson g-factors, g_π and g_ν given in units of nuclear magnetons μ_N, may be determined empirically using the magnetic moments of low-lying nuclear levels. The simple microscopic expectation of $g_\pi = 1$ and $g_\nu = 0$ for the boson g-factors arises from considering each boson as a pair of nucleons. For collective even-even nuclei the intrinsic spin contribution is very small and the boson g-factors are expected to be dominated by the orbital angular momenta of the constituent fermions, $g_l^{(\pi)} = 1$ and $g_l^{(\nu)} = 0$. This is consistent with microscopic calculations of the boson g-factors [Sa84, Da94b] which have found $g_\pi \simeq 1$ and $g_\nu \simeq 0$.

As low-lying states are largely F-spin symmetric and $e_\pi \simeq e_\nu$, the electric quadrupole properties of these levels depend mainly on the total boson number $N_\pi + N_\nu$ rather than the individual proton- and neutron-boson numbers, and are, therefore, generally similar to those obtained with the IBM-1. This is not the case for magnetic properties, however, where the boson g-factors are very different.

The g-factor of a F-spin symmetric state is given by [Sa81]

$$g = \frac{1}{N_\pi + N_\nu} \left(g_\pi N_\pi + g_\nu N_\nu \right) \quad . \tag{2.13}$$

As this equation is valid for all F-spin symmetric hamiltonians and, in most nuclei, states at low excitation energies are largely F-spin symmetric (see above in sect. 2.2.2), it might provide a reasonable description of the nuclear g-factors of low-lying states across a whole major shell. With the values $g_\pi = 1$ and $g_\nu = 0$ eq. 2.13 simplifies to

$$g \simeq \frac{N_\pi}{N_\pi + N_\nu} \quad . \tag{2.14}$$

For an isotopic series, this predicts the g-factor decreases with increasing neutron number in the lower half of a major shell, reaches a minimum in the middle of the shell and then increases in the upper half. This is in marked contrast to the small linear decrease for the result $g = Z/A$ (sect. 1.2.1), see fig. 2.1. Interestingly, however, if Z and A were considered as effective *valence* nucleon numbers then the results would be equivalent.

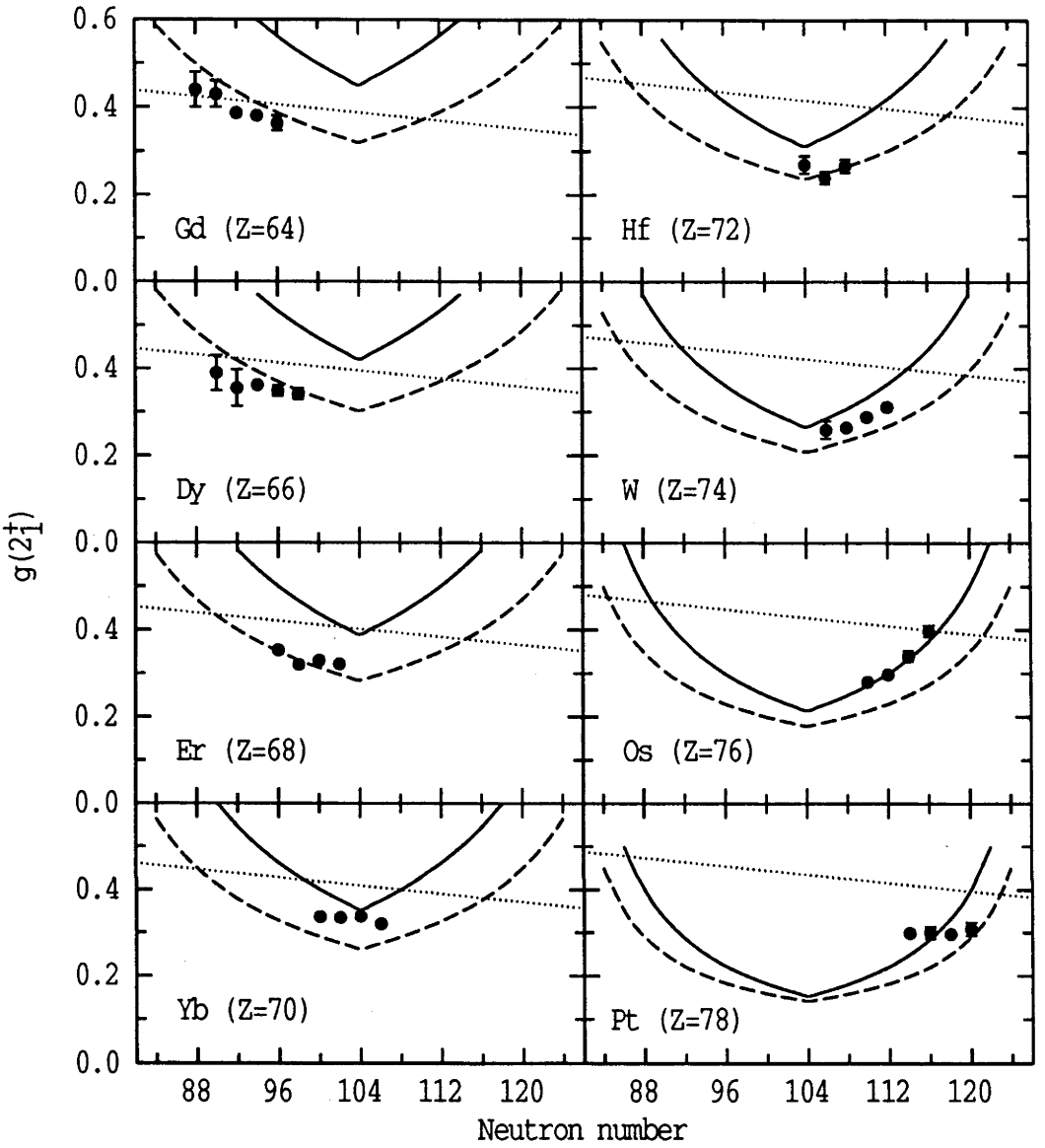

Figure 2.1: Comparison of the experimental $g(2_1^+)$ values for the Gd through Pt isotopes, compiled from refs. [Le78, Ra89, Be87a, Ba90, Al88, St91b, Zi73, Pe68, Al84, St91a, Wa70, St92] and sect. 7.3.2, with $g = Z/A$ (dotted line) and calculations using eq. 2.13 with $g_\pi = 1$, $g_\nu = 0$ (solid) and $g_\pi = 0.65$, $g_\nu = 0.05$ (dashed, see text).

Equation 2.13 has been used extensively for interpreting the g-factors of low-lying levels in even-even medium-to-heavy mass nuclei, e.g. refs. [Sa84, Is86, Wo85, Wo87a, St91a]. In fig. 2.1 the measured 2_1^+-state g-factors of even-even rare-earth and heavy transitional nuclei are compared with two calculations using eq. 2.13: (i) with the microscopic estimates for the boson g-factors; and (ii) with the values $g_\pi = 0.65$ and $g_\nu = 0.05$, which are similar to those obtained in

ref. [Wo85] from an analysis using eq. 2.13 and varying g_π and g_ν. On the whole, the dependence with neutron number for these calculations agrees with the trends observed in the data across the $N = 82$-to-126 shell, showing that eq. 2.13 with $g_\pi \leq 1$ and $g_\nu \simeq 0$ provides a reasonable qualitative description of the $g(2_1^+)$ systematics over this extensive mass region.

Of the nuclei shown the Pt isotopes are an exception – the constancy of the measured values is in marked contrast to the theoretically-implied sharp increase. Clearly, extending the experimental data to the lighter isotopes would help clarify the extent of this discrepancy. It is of relevance here to note that the pairing-plus-quadrupole calculations of Kumar and Baranger [Ku68] also predict the 2_1^+-state g-factors of the lighter Pt isotopes to decrease towards the middle of the neutron shell. (This will be discussed further in sect. 9.1.1, below.)

Chapter 3

Experimental Techniques

3.1 Introduction

3.1.1 The magnetic hyperfine interaction

The magnetic dipole moment μ, or alternatively the g-factor of a nuclear state, may be determined experimentally by measuring the interaction between the nuclear moment and an applied magnetic field.

A magnetic field, B, present at the nuclear site causes the splitting of the eigenstates of the nuclear spin I into its $2I+1$ magnetic substates. The energy spacing between adjacent substates corresponds to the difference in the potential energy for different orientations of the magnetic moment with respect to the magnetic field and is given by

$$\Delta E = \tilde{\mu} . \widetilde{B} = -g \mu_N B \quad . \tag{3.1}$$

In certain cases the nuclear g-factor can be determined by measuring the energy splitting between magnetic substates ΔE, using the Mössbauer effect. The energy resolution of experimental techniques restricts this method to nuclear states with lifetimes $\gtrsim 1$ ns.

Along with energy splitting of the magnetic substates, the application of a magnetic field produces a torque, $\tilde{\tau}$, given by

$$\tilde{\tau} = \tilde{\mu} \times \widetilde{B} \quad , \tag{3.2}$$

which causes the nucleus to precess around the direction of the applied field, see fig. 3.1. As the torque is $d\tilde{I}/dt$, the nuclear precession can be shown to depend

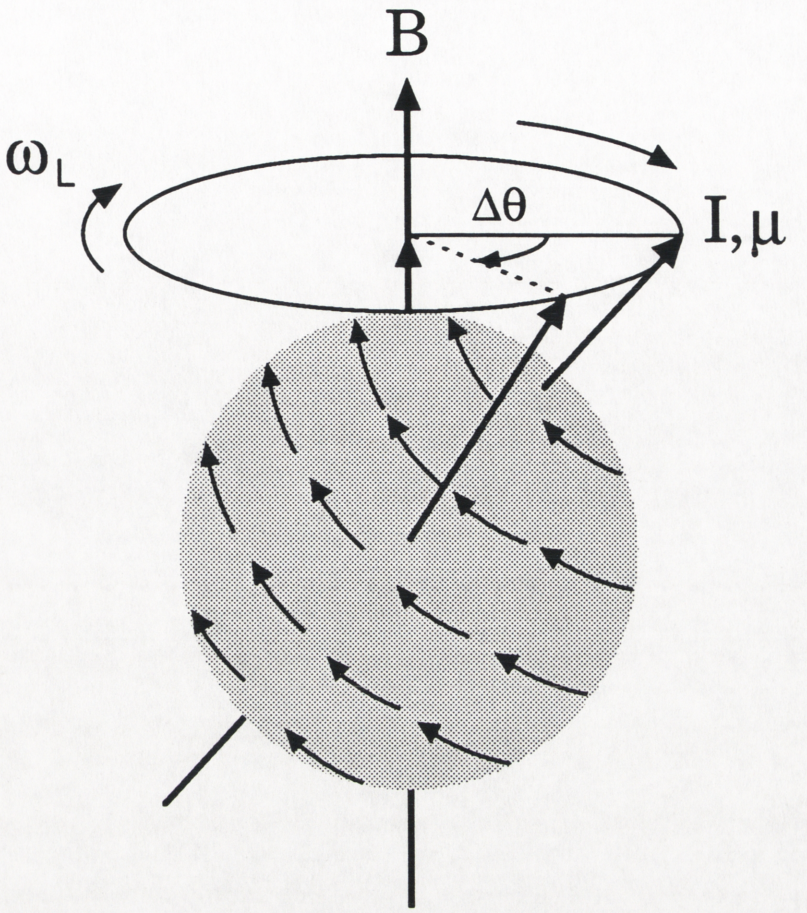

Figure 3.1: Diagram of the nuclear precession around the direction of the applied magnetic field for a short time Δt.

directly on the gyromagnetic ratio (or g-factor), g, rather than the magnetic moment, μ, of the nuclear state. The frequency of the precession, called the Larmor frequency ω_L, is

$$\omega_L = \frac{\mu B}{\hbar I} = g \frac{\mu_N}{\hbar} B \quad . \tag{3.3}$$

With knowledge of the magnetic field strength the g-factor of a level may be inferred from a measured precession frequency.

3.1.2 Measuring magnetic moments

For an excited state, the nuclear precession can be measured as a perturbation of the angular distribution of γ-radiation de-exciting the level. Clearly, this requires some anisotropy in the (unperturbed) radiation pattern depopulating the state of interest. As a randomly oriented collection of nuclei emits radiation isotropically, it is necessary to produce an ensemble of nuclei with a weighted population of the magnetic substates, i.e. with spins that prefer to lie in a particular direction.

Alignment of the nuclear spin can, in general, be achieved in two ways: through the mechanisms involved in the nuclear reaction used to populate the nuclei in the state of interest, causing the γ-radiation de-exciting the level to have an angular *distribution* with respect to the beam direction; or by the observation of coincident (and, hence, correlated) radiation in a well-defined direction, $\vec{k}$, producing an angular *correlation* with respect to $\vec{k}$ for the γ-rays depopulating the level. In the 'out-of-beam' measurements described in this thesis the alignment produced in the nuclear reactions is lost, requiring the use of perturbed-angular-correlation (PAC) methods. The relevant theory of angular correlations is summarized in the following section.

By observing the angular correlation as a function of time it is possible to measure the precession frequency, ω_L, directly. Time-*differential* techniques have accuracies which typically range from 0.1% to 1% and are, therefore, the most appropriate for measuring the magnetic moments of nuclear states with lifetimes $10\,\mathrm{ns} \lesssim \tau \lesssim 10\,\mu\mathrm{s}$ [Re74].

The interaction time between the nuclear moment and the magnetic field is limited to the nuclear lifetime. When the state meanlife is short, $\tau \lesssim 10\,\mathrm{ns}$, direct observation of the precession frequency is not possible and the total angle through which the correlation has precessed, i.e. the precession angle $\omega_L\tau$, must be measured. Time-*integral* methods involve examining the perturbation of the total time-integrated correlation and provide the only available means for measuring the magnetic moments of short-lived ($\tau < 1\,\mathrm{ns}$) excited levels. The low-lying collective nuclear states of interest in the present study have 'short' lifetimes in the range $50\,\mathrm{ps} \lesssim \tau \lesssim 500\,\mathrm{ps}$. Further discussion of techniques and specific details of the methods employed in the present experiments are given in sect. 3.5 and chapter 4.

3.2 Perturbed Angular Correlations

In this section those aspects of perturbed angular correlations relevant to the present work will be reviewed. There are a number of reference works available, e.g. refs. [St64, Fr65, St75], for more comprehensive descriptions.

Consider firstly the general situation where a nuclear state is populated in a nuclear reaction or a radioactive decay, labelled R_1, experiences an extranuclear perturbation and is then depopulated by another radiation, R_2. The expression for the perturbed directional correlation between the two radiations R_1 and R_2, with respective direction vectors $\vec{k_1}$ and $\vec{k_2}$, is given by

$$W(\vec{k_1},\vec{k_2},t) = \sum_{k_1 k_2 N_1 N_2} A_{k_1}(1)\, A_{k_2}(2)\, G_{k_1 k_2}^{N_1 N_2}(t) \frac{1}{\sqrt{(2k_1+1)(2k_2+1)}} \times Y_{k_1}^{N_1}(\theta_1,\phi_1)\, Y_{k_2}^{N_2}(\theta_2,\phi_2) \quad , \tag{3.4}$$

where $G_{k_1 k_2}^{N_1 N_2}(t)$ describes the influence of the perturbation (on the alignment of the nuclear state) and the arguments of the spherical harmonics are the radiation directions in spherical polar coordinates with respect to an arbitrary axis, as in fig. 3.2.

The coefficients $A_{k_1}(1)$ describe the orientation of the state with respect to $\vec{k_1}$ and, therefore, depend on the method employed to populate the nuclear level, while $A_{k_2}(2)$ are determined by the properties of the depopulating radiation, R_2. When the perturbation is removed, $G_{k_1 k_2}^{N_1 N_2} \equiv 1$, the correlation function does not depend on N and eq. 3.4 reduces to the familiar summation of Legendre polynomials $P_k(\cos\theta)$,

$$W(\theta) = \sum_k A_k(1)\, A_k(2)\, P_k(\cos\theta) \quad , \tag{3.5}$$

where $k = k_1 = k_2$ and θ is the angle between the radiation directions.

Now consider the more specific case, shown in fig. 3.3a, with two successive, pure multipole γ-ray transitions in cascade from an initial state (with spin I_i) that is randomly oriented. The orientation and directional distribution parameters, $A_k(1)$ and $A_k(2)$, respectively, can now both be determined in terms of angular momentum algebra alone. They depend on the angular momenta of the nuclear states and the multipolarities of the respective γ-radiations, i.e. the angular momentum transferred in the transitions. For radiations of pure multipolarity,

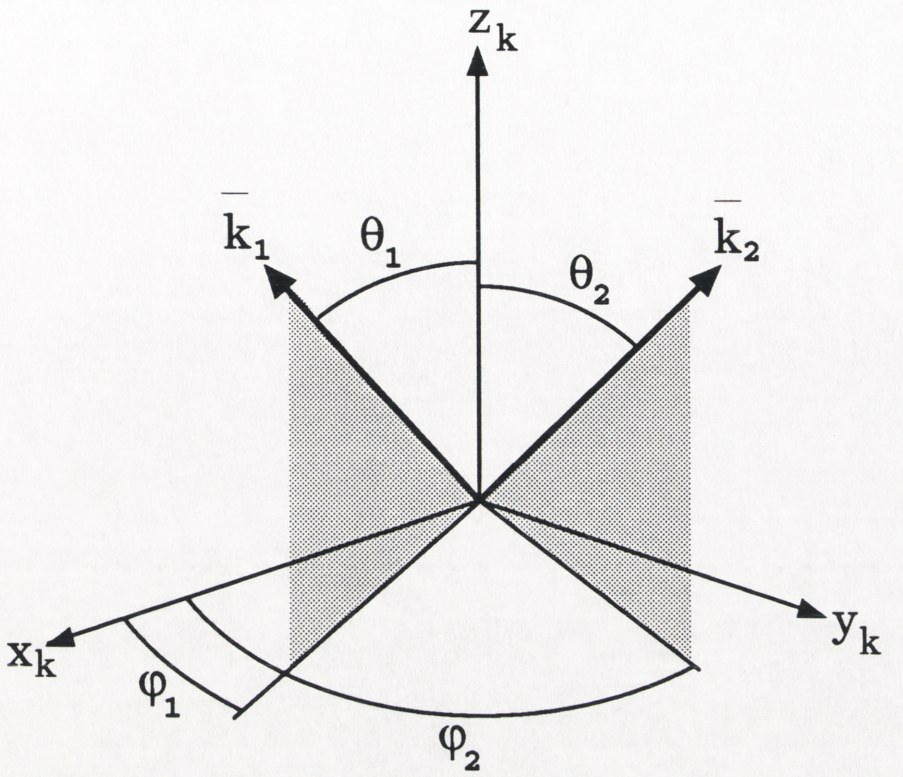

Figure 3.2: Angular coordinates (θ, ϕ) of the radiation observation directions $\vec{k_1}$ and $\vec{k_2}$ with respect to the perturbation coordinate system (x_k, y_k, z_k).

$$A_k(1) = F_k(I_i\, L_1\, I)\,, \quad A_k(2) = F_k(I_f\, L_2\, I) \quad . \tag{3.6}$$

When the first transition has mixed multipolarity (e.g. $E2/M1$) with multipole order $L_1' > L_1$ [Mo76]

$$A_k(1) = \frac{1}{1+\delta^2}\,[F_k(I_i\, L_1 L_1\, I) - 2\delta\, F_k(I_i\, L_1 L_1'\, I) + \delta^2 F_k(I_i\, L_1' L_1'\, I)] \quad , \tag{3.7}$$

where the mixing ratio, δ, is defined as

$$\delta(L'/L) \equiv \frac{\langle\, I||L_1'||I_i\,\rangle}{\langle\, I||L_1||I_i\,\rangle} \quad . \tag{3.8}$$

There is a similar expression for the second γ-ray (with $L_2' > L_2$),

$$A_k(2) = \frac{1}{1+\delta^2}\,[F_k(I_f\, L_2 L_2\, I) + 2\delta\, F_k(I_f\, L_2 L_2'\, I) + \delta^2 F_k(I_f\, L_2' L_2'\, I)] \tag{3.9}$$

with

$$\delta \equiv \frac{\langle I_f || L_2' || I \rangle}{\langle I_f || L_2 || I \rangle} \quad . \tag{3.10}$$

For a transition $I_1 \rightarrow I_2$, the F_k may be written in terms of Racah coefficients as

$$F_k(I_1 L L' I_2) = (-)^{1+I_1+I_2} \sqrt{(2L+1)(2L'+1)(2I_1+1)} \langle L1L'-1|k0\rangle \, W(I_1 I_1 L L'; k I_f) \quad . \tag{3.11}$$

This allows computer evaluation of these factors. Alternatively, they have been tabulated in, for example, refs. [Ya67, Mo76].

Figure 3.4 shows the calculated unperturbed angular correlations for three γ-ray cascades found in even-even nuclei, namely $4^+ \rightarrow 2^+ \rightarrow 0^+$, $2^+ \rightarrow 2^+ \rightarrow 0^+$ and $0^+ \rightarrow 2^+ \rightarrow 0^+$. The distribution for the $0^+ \rightarrow 2^+ \rightarrow 0^+$ cascade has a large anisotropy, as the initial 0^+ state has only one magnetic substate ($M = 0$) which gives rise to maximal alignment of the intermediate state.

When the measured radiations are separated by a cascade of unobserved γ-rays (fig. 3.3b) the alignment formed in the observation of the first radiation may be propagated, possibly with some loss of alignment, to the state depopulated

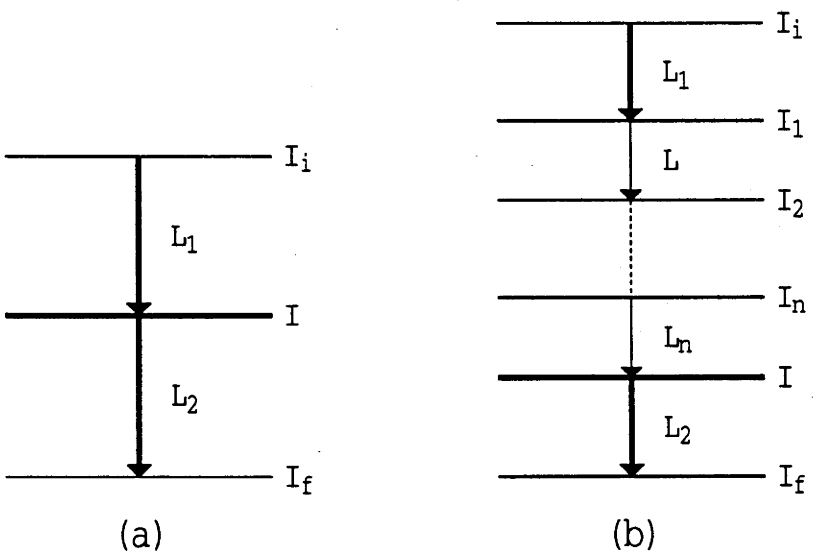

Figure 3.3: Schematic level schemes showing the measured γ-ray transitions (with pure multipolarities L_1 and L_2), the state I in which the precession occurs and the initial, randomly-oriented level I_i. In (a) the two γ-rays are successive, while in (b) they are separated by a cascade of n unobserved transitions.

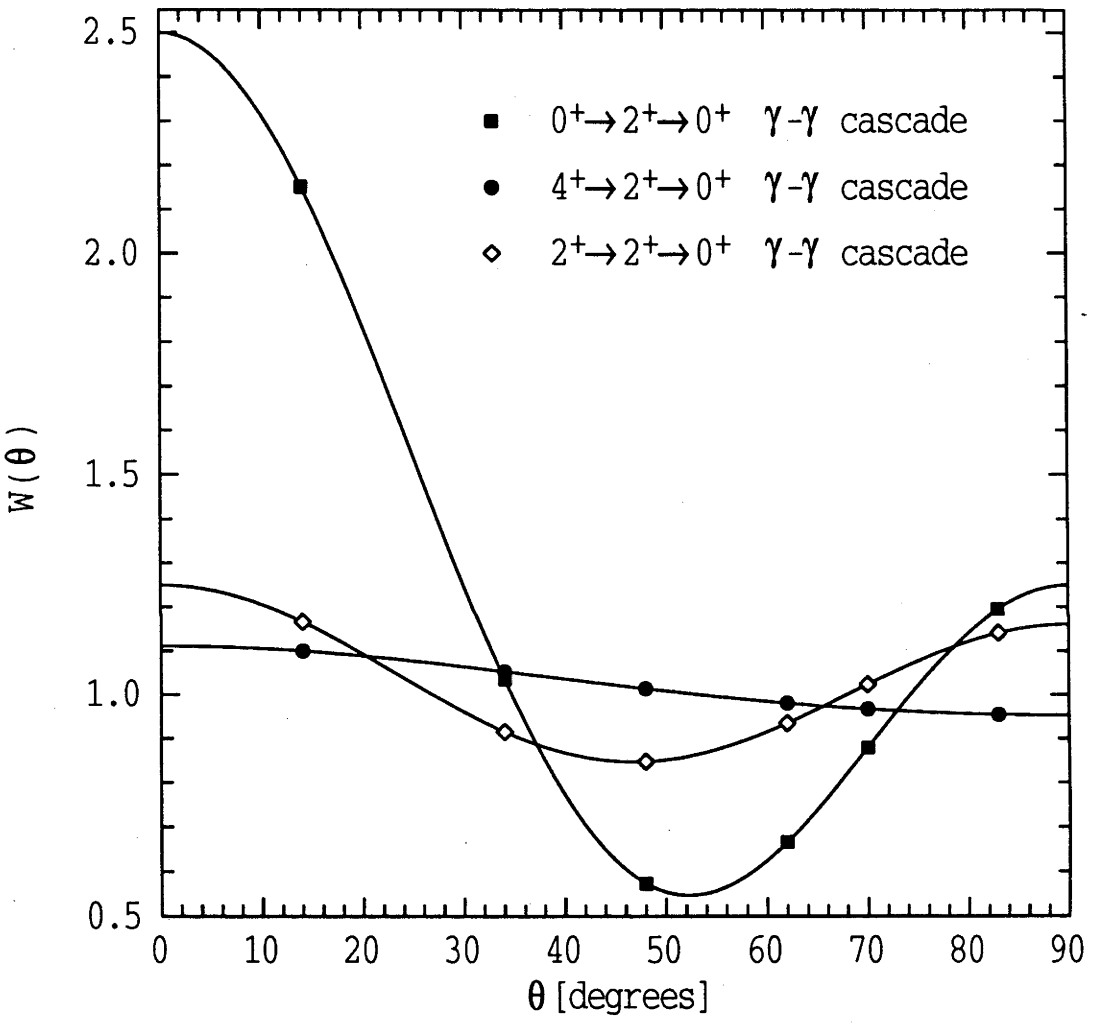

Figure 3.4: Calculated angular correlations for the $0^+ \rightarrow 2^+ \rightarrow 0^+$, $4^+ \rightarrow 2^+ \rightarrow 0^+$ and $2^+ \rightarrow 2^+ \rightarrow 0^+$ γ-ray cascades (where all transitions have pure $E2$ multipolarity). Data points indicate the angles sampled when using the CAESAR array (sect. 4.2.1).

by the second observed radiation. The $A_k(1)$ are then modified by coefficients $U_k(I_1\,L\,I_2)$, which depend on the level spins and transferred angular momentum associated with the unobserved transitions. These may also be expressed in terms of angular momentum algebra as [Mo76]

$$U_k(I_1\,L\,I_2) = (-1)^{1-I_1-I_2}\sqrt{(2I_1+1)(2I_2+1)}\,W(I_1I_1I_2I_2;kL) \tag{3.12}$$

and, for a transition with mixed multipolarity ($L' > L$),

$$U_k(I_1\,LL'\,I_2) = \frac{1}{1+\delta^2}\,[U_k(I_1\,L\,I_2) + \frac{\delta^2}{1+\delta^2}\,U_k(I_1\,L'\,I_2)] \quad . \tag{3.13}$$

Numerical values have been tabulated in refs. [Ya67, Mo76].

The highest value of k in the expansion of eq. 3.5 is determined by the radiation selection rule $k \leq \min(2I, 2L_1, 2L_2)$. Parity conservation limits k to even values for unpolarized γ-radiation. In the case where k is an even integer ≤ 4 an equivalent form of eq. 3.5 is [Re74]

$$W(\theta) = \sum_{k=0,2,4} b_k \cos k\theta \quad , \tag{3.14}$$

with

$$b_0 = 1 + \frac{1}{4}\,a_2 + \frac{9}{64}\,a_4 \;, \quad b_2 = \frac{3}{4}\,a_2 + \frac{5}{16}\,a_4 \;, \quad b_4 = \frac{35}{64}\,a_4$$

and

$$a_k \equiv A_k(1)\,A_k(2) \quad . \tag{3.15}$$

As noted in sect. 3.1.1, the effect of a static magnetic field on an ensemble of aligned nuclei is to cause precession around the field direction. The precession of the nuclei in the aligned 'intermediate' state I leads to a rotation of the angular correlation with the Larmor frequency ω_L (eq. 3.3). In this case the perturbation factor that appears in eq. 3.4 is

$$G^{N_1N_2}_{k_1k_2}(t) = e^{-i\omega_L N t} \quad . \tag{3.16}$$

When the magnetic field is applied perpendicular to the plane in which the γ-rays are observed the perturbed angular correlation (eq. 3.4) becomes

$$W(\theta, t, B) = \sum_k A_k(1)\, A_k(2)\, P_k[\cos(\theta - \omega_L t)] \quad . \tag{3.17}$$

In an integral measurement made over a time much longer than the state meanlife, τ, the measured quantity is the time-integrated function

$$W(\theta, \infty, B) = \sum_k \frac{1}{\tau} \int_0^\infty e^{-\frac{t}{\tau}}\, A_k(1)\, A_k(2)\, P_k[\cos(\theta - \omega_L t)]\, dt \quad . \tag{3.18}$$

Rewriting the unperturbed correlation function as in eq. 3.14 this integral may be evaluated analytically to obtain

$$W(\theta, \tau, B) = \sum_{k=0,2,4} \frac{b_k}{\sqrt{[1 + (k\,\omega_L \tau)^2]}} \cos[k(\theta - \Delta\theta_k)] \quad , \tag{3.19}$$

with

$$\tan k\Delta\theta_k = k\,\omega_L \tau \quad . \tag{3.20}$$

By comparing eqs. 3.14 and 3.19, we find the perturbation of the angular correlation is manifest as a rotation through the angle $\Delta\theta_k$ and an attenuation of $1/\sqrt{[1 + (k\,\omega_L\tau)^2]}$. These factors are dependent on the product $\omega_L\tau$, which in turn depends on the g-factor and meanlife of the state and the magnetic field strength B.

Figures 3.5 and 3.6 show perturbations of the angular correlation for the $0^+ \rightarrow 2^+ \rightarrow 0^+$ γ-γ cascade resulting from different values of $\omega_L\tau(2^+)$. When the sense of the precession is reversed, the rotation of the radiation pattern is also reversed, as displayed in fig. 3.5 for precession angles of $\omega_L\tau(2^+) = \pm 150\,\text{mrad}$. Thus, the *sign* of either the g-factor or the field (if the other is known) may be determined from the sense of the precession.

Figure 3.6 shows the dependence of the perturbed angular correlation on the magnitude of the precession. For small precession angles, $\omega_L\tau \lesssim 100\,\text{mrad}$, the perturbation is essentially a rotation of the radiation pattern with minimal attenuation. For larger precessions, $\omega_L\tau > 200\,\text{mrad}$, the attenuation becomes significant and the features of the correlation are increasingly 'washed out'.

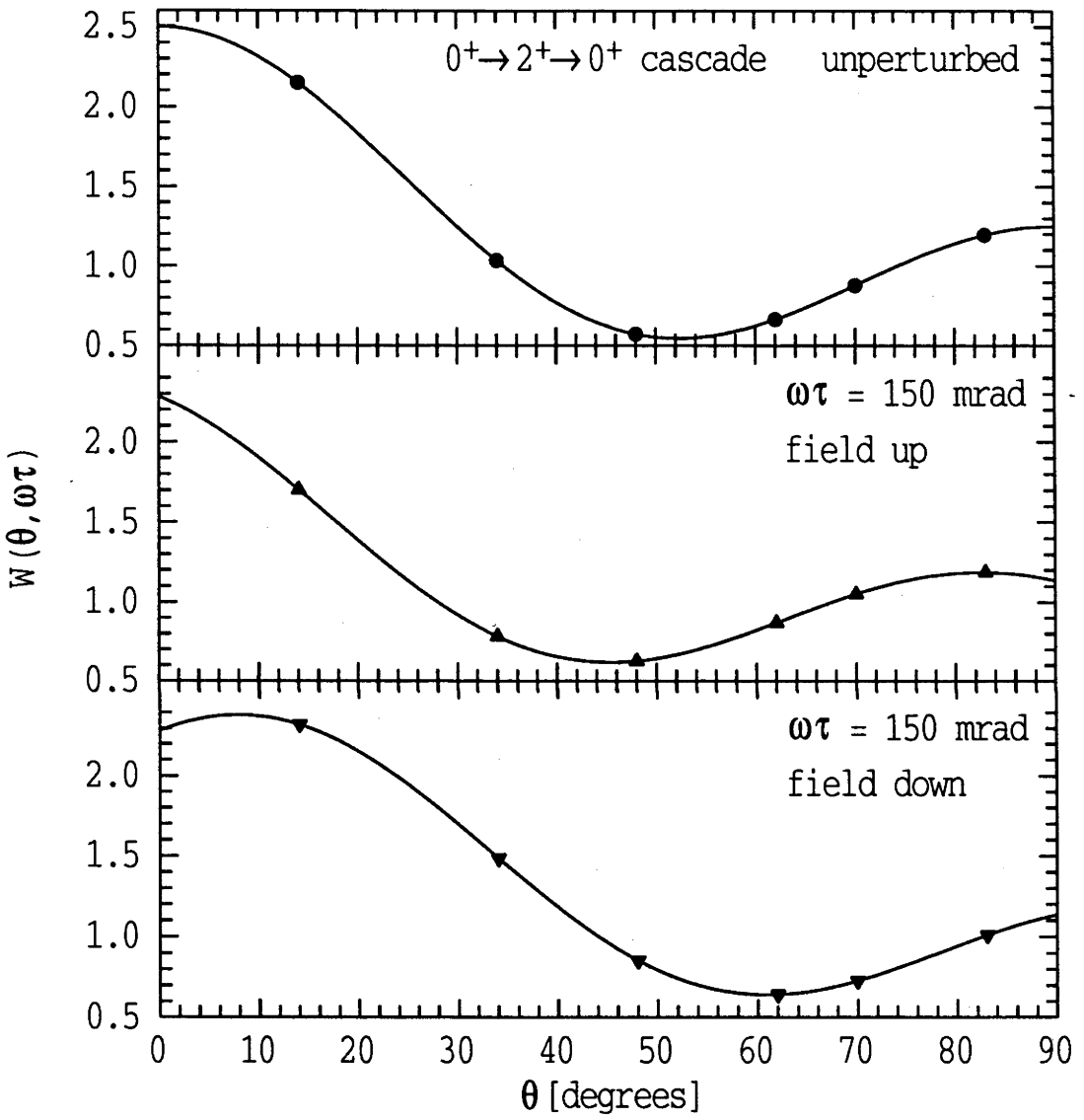

Figure 3.5: Calculated perturbed angular correlations for the $0^+ \rightarrow 2^+ \rightarrow 0^+$ γ-ray cascade and a precession of magnitude $\omega\tau(2^+) = 150$ mrad, with the magnetic field direction and, therefore, the sense of the precession reversed. Data points indicate the angles sampled when using the CAESAR array.

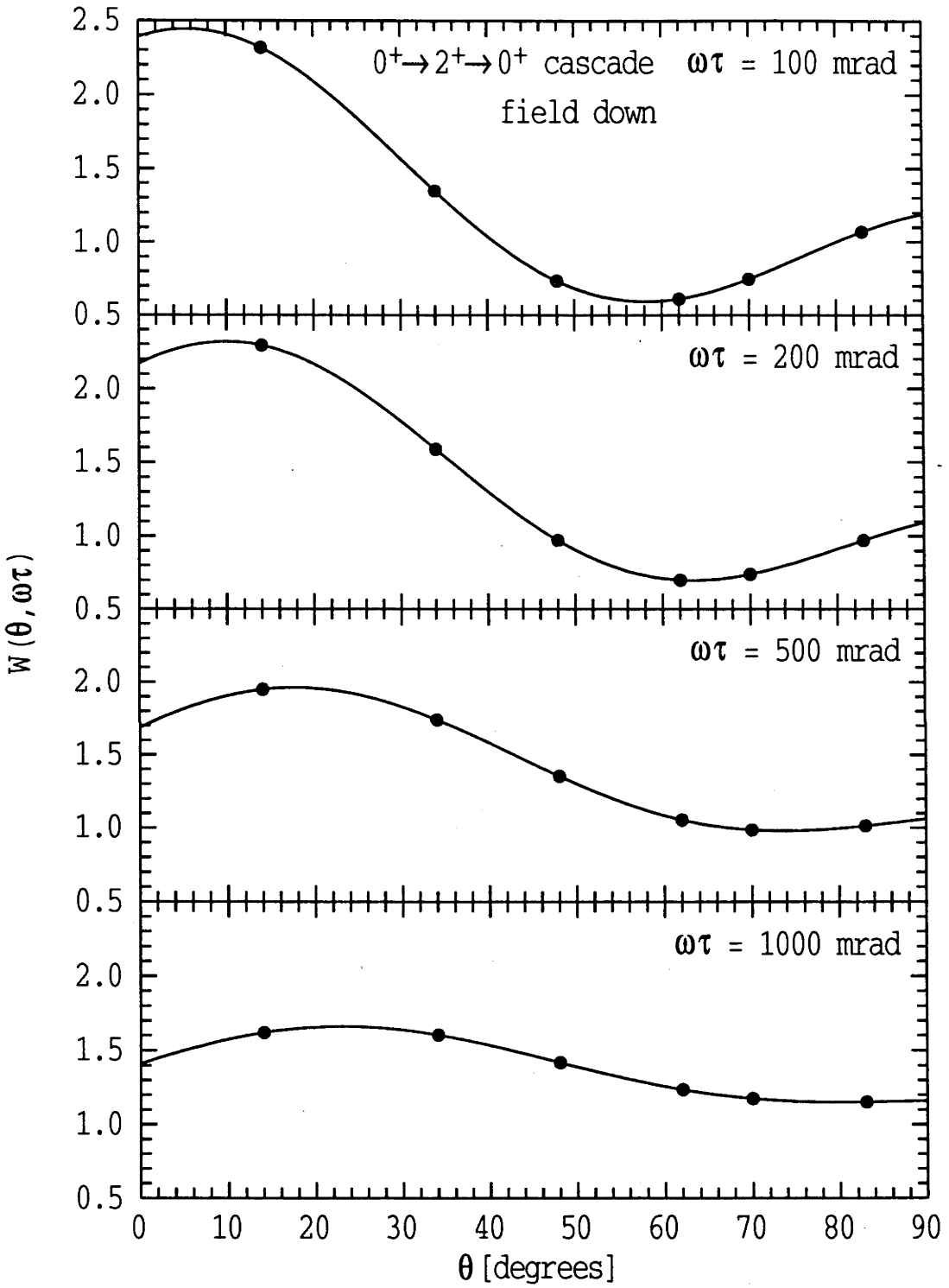

Figure 3.6: Calculated angular correlations for the $0^+ \rightarrow 2^+ \rightarrow 0^+$ cascade perturbed by $\omega\tau(2^+) = 100, 200, 500$ and 1000 mrad.

3.3 Hyperfine Magnetic Fields

The magnetic field strength required to produce an observable precession may be estimated by writing

$$B = \frac{(\omega_L \tau)\hbar}{g\,\mu_N\,\tau} \quad . \tag{3.21}$$

For a nuclear state with $g \simeq 0.3$ and lifetime $\tau \simeq 100\,\mathrm{ps}$, a field of the order of 100 Tesla is needed to produce a precession angle of $\sim 100\,\mathrm{mrad}$. This field strength is an order of magnitude larger than those available macroscopically, as even the largest superconducting magnets only produce fields of around 10 Tesla. Therefore, intense *hyperfine* fields, which are generated by the interaction of an atomic nucleus with its electronic environment, are required. These fields may be broadly categorized as those present at the nuclear site of either highly stripped and excited free atoms or dilute impurities in a ferromagnetic host.

3.3.1 Recoil-into-gas/vacuum fields

Strong hyperfine fields are found for highly-excited ions recoiling in a gas or vacuum, see e.g. refs. [Wa74, Br77b]. An atom moving rapidly through a solid, at a velocity of a few percent of the speed of light, is stripped of many electrons as it leaves the solid. The remaining bound electrons may generate very intense magnetic fields of $\lesssim 10\,\mathrm{kT}$ at the nuclear site. The complex processes producing the field are not well understood and the hyperfine interaction is strongly dependent on both the spin of the electron configuration and the nuclear spin. In view of these complications, techniques employing these fields have rarely been used in recent years.

3.3.2 Ferromagnetic fields

Intense magnetic fields are present at the nuclear sites of dilute impurities in polarized ferromagnetic hosts. They are caused by interactions of the atomic nucleus with the electronic environment found in the ferromagnet. The magnetic field for *stationary* impurities is different to that for ions *moving* within the ferromagnet. However, both internal fields generally behave as strong classically-applied magnetic fields where the polarization of the medium establishes a preferred spin direction for the ionized electron configurations of the ion. The *static* field and the

transient field have been measured extensively for numerous ion-host combinations and used in γ-ray perturbed-angular-correlation/distribution experiments.

3.3.2.1 The transient field

The transient hyperfine field occurs at the nuclei of ions in motion within ferromagnet media. The field strength is approximately proportional to the atomic number of the ion and its velocity v, for $v_0 < v \lesssim 8v_0$ (where the Bohr velocity $v_0 = c/137$). It is typically around 3 kTesla for ions of the Pt region moving at velocities of about $3v_0$ through ferromagnetic iron (Fe) [St94a]. The hyperfine field is always in the same direction as the external magnetic field used to polarize the ferromagnet.

The transient field is caused by the polarization of unpaired inner-shell electrons bound to the moving ion. The mechanisms producing the polarization are not known definitely, but rely on the transfer of polarization from electrons of the conduction band of the ferromagnet perhaps through electron capture or spin-exchange scattering. Although the microscopic origins of the field are not completely understood and are even the topic of some current debate (see ref. [St93] and references therein), reliable empirical parameterizations of the field strength have been determined from extensive experimental data. Two commonly-used, universal parameterizations are usually referred to as the 'Rutgers' [Sh80] and 'Chalk River' [An82, Hä84] parameterizations.

3.3.2.2 The static field

The static hyperfine magnetic field is present at the nuclei of stationary impurities in a polarized ferromagnetic host. It arises primarily from, in order of importance: 'conduction-electron polarization', where the conduction electrons of the ferromagnet cause spin-polarization of electrons bound to the impurty ion, as they scatter off the ion; 'core polarization', in which the electron core of the impurity atom is polarized by a local magnetic moment, possibly from an unpaired outer electron; and when the impurity has a larger metallic radius than the host, 'overlap polarization', which is the direct exchange-polarization of the impurity atom by electrons of neighbouring ferromagnetic atoms. For a more comprehensive description of the complex hyperfine interactions constituting these mechanisms, see e.g. ref. [Sh65].

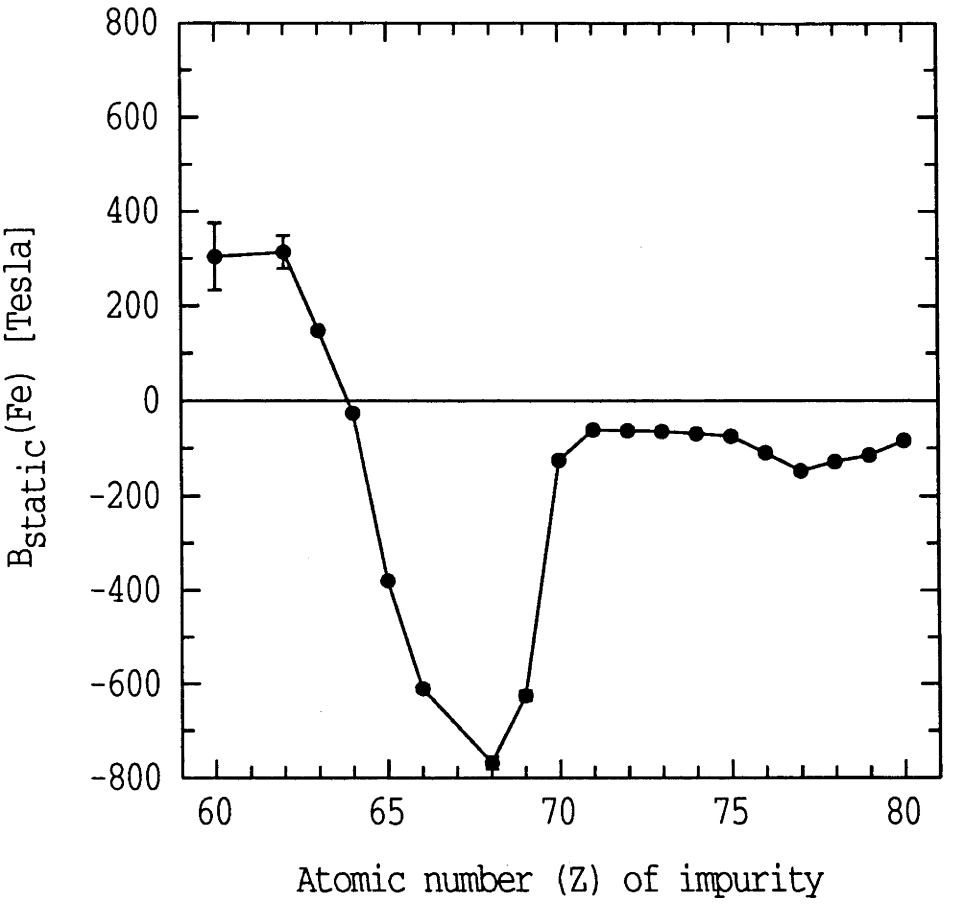

Figure 3.7: The static hyperfine fields for various impurities in ferromagnetic Fe.

A compilation of the static field strengths for a large number of ion-host combinations, measured with a variety of experimental techniques, is given in ref. [Kr83]. The internal fields for impurities with atomic numbers $60 \leq Z \leq 80$ as dilute solutes in Fe are shown in fig. 3.7. Although the fields for rare-earth impurities ($Z \leq 70$) vary dramatically, for atoms with $70 \leq Z \leq 80$ the fields have similar magnitudes $\sim 100\,\mathrm{T}$ and are all negative, i.e. the direction of the static field is opposite that of the external field polarizing the ferromagnet.

3.4 Populating States in Unstable Nuclei

When measuring a nuclear magnetic moment an important consideration is finding a suitable method of populating the state of interest. Coulomb excitation (see fig. 3.8) is the reaction most often used for exciting low-lying, short-lived collective nuclear states in stable nuclei to measure their magnetic moments. While

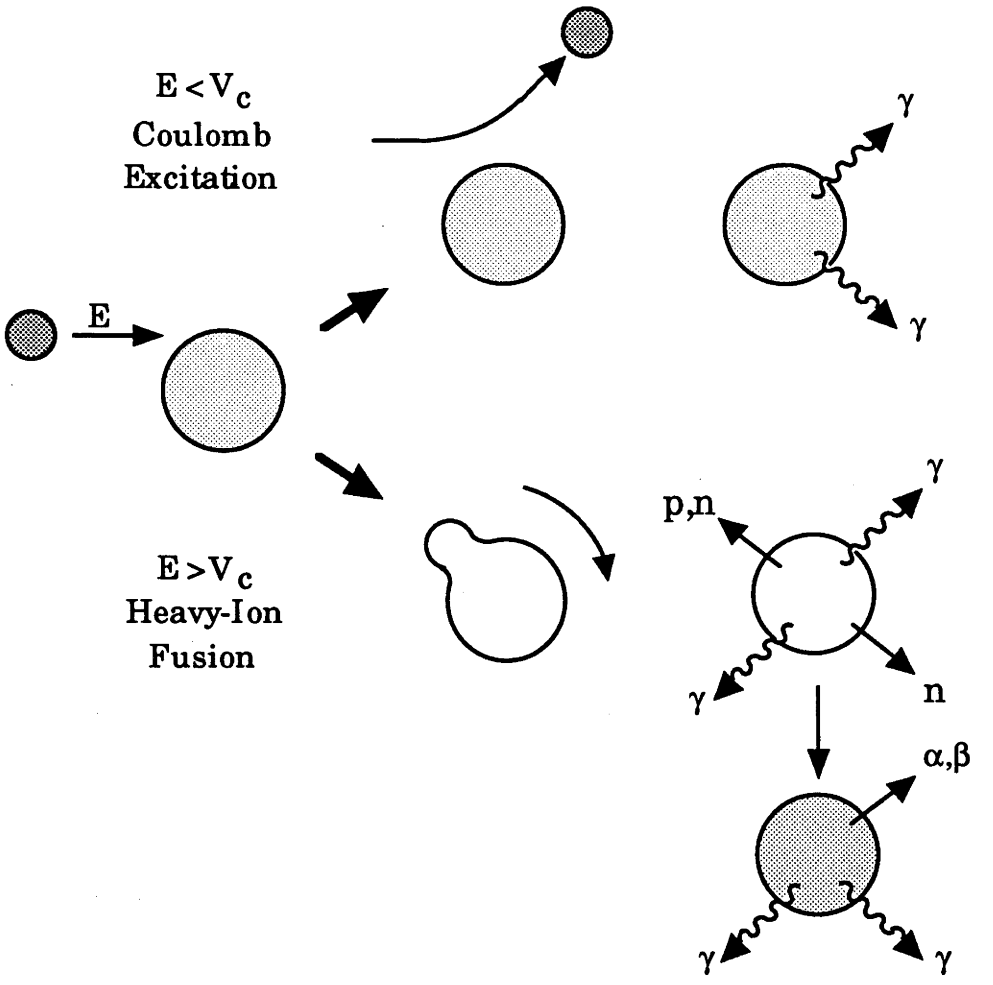

Figure 3.8: An illustration of possible nuclear reactions following heavy-ion bombardment of a stable target. When the projectile energy, E, is less than the Coulomb barrier between the nuclei, V_c, the target nucleus may become excited. It then decays back to its *stable* ground-state by emitting γ-rays. When the Coulomb barrier is overcome fusion takes place. The compound system emits light particles (usually these are predominantly neutrons) forming a hot spinning nucleus, which decays further via γ-radiation. Following this, for an unstable final nucleus, there is (α- or β-) decay into excited levels of a daughter nucleus.

this reaction has a number of advantages, its most severe limitation is that it can be used (at present) only for exciting *stable* target nuclei; as such, it is unsuitable for the present study of the unstable ^{184,186,188}Pt nuclei.

In γ-ray spectroscopy studies neutron-deficient nuclei are commonly formed following heavy-ion induced reactions. As shown in fig. 3.8, a fusion reaction creates a hot compound system which loses energy by particle emission to form the nucleus of interest with high excitation energy and angular momentum, typically

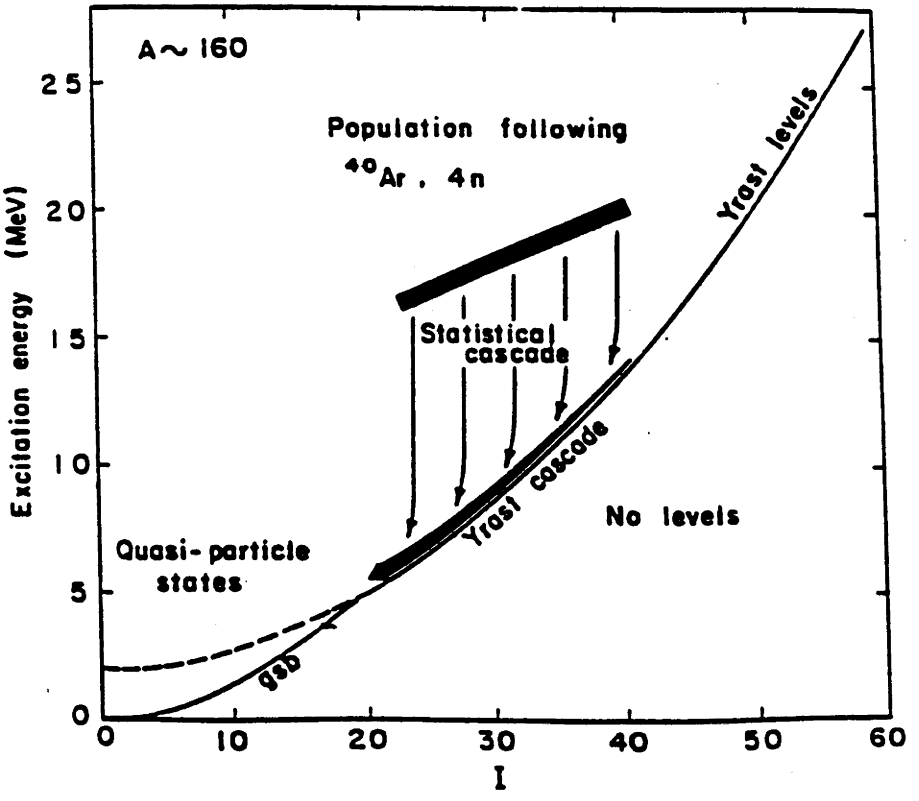

Figure 3.9: Diagram of the decay process in a (Heavy Ion, x n) reaction.

$\sim 15\,\mathrm{MeV}$ and $\gtrsim 30\hbar$ (fig. 3.9). After neutron evaporation the nucleus decays by the emission of γ-rays.

From the highly-excited entry region the nucleus decays in cascades of statistical dipole transitions to states nearer the *yrast* line (those levels with the lowest excitation energy for given angular momentum), as in fig. 3.9. This is followed by γ-ray cascades of primarily stretched-transitions in rotational-band structures, which remove angular momentum. Following this complex feeding path most of the intensity gathers in the yrast states. The time taken to populate the low-lying yrast levels following the reaction is usually of the order of several picoseconds. (For more detailed information on these reaction processes there are a number of references, e.g. ref. [Ne74].)

Low-lying nuclear levels may also be populated via radioactive decay. As the perturbation is most sensitively determined with the $0^+ \rightarrow 2^+ \rightarrow 0^+$ γ-ray cascade in perturbed-angular-correlation measurements (sect. 3.2), maximizing the population of excited 0^+ states would be advantageous. The α-decay of even-even nuclei preferentially populates states with zero spin and, therefore, should be

the favoured decay in the present measurements. Unfortunately, the ^{186,188,190}Pt isotopes are relatively near stability and are not formed by α-decay.

Instead, the dominant decay modes are the weak-interaction processes of positron (β^+) emission and electron capture, ϵ. For the present purposes these are equivalent and are collectively referred to as β^+-decay. The β^+-decay to the even Pt isotopes is from an odd-odd parent nucleus and, therefore, is fragmented. For the Pt nuclei of interest, however, a significant fraction of the decay passes through the first-excited 0^+ state (see fig. 4.8 in the next chapter).

3.5 Survey of Experimental Techniques

In this section, previously-used experimental techniques which employ hyperfine fields to measure g-factors will be surveyed, with an emphasis on studying the unstable Pt nuclei.

3.5.1 RIGV techniques

One limitation of early recoil-into-gas or vacuum (RIGV) experiments was the inability to determine the sign of the g-factor. As these ionic fields (described in sect. 3.3.1) have no preferred spatial orientation, the measured quantity is an attenuation of the γ-radiation pattern proportional to $(\omega_L\tau)^2$ (eq. 3.19). This was overcome with the introduction of the 'tilted-foil' technique [Go77], in which a solid-vacuum interface is positioned at a non-perpendicular angle to the direction of the recoiling ions. This polarizes the electron distribution of the ion and allows measurement of a rotation (which is proportional to $\omega_L\tau$), thereby, permitting sign determination. However, the execution and interpretation of these experiments can be complicated and model-dependent due largely to the complex spin- and velocity-dependence of the interaction. These problems are reduced by the 'multifoil' method [Br81], which more closely mimics rotation about a classically applied field, but the technique is then only suitable for longer-lived states. On the whole, RIGV techniques have fallen into disuse.

If RIGV techniques were employed for measurements on the neutron-deficient Pt isotopes, the fields would be accessed by recoiling excited Pt nuclei from a suitable target foil using the energy produced in a heavy-ion induced nuclear reaction. The neutron-deficient nuclei could be produced readily. However, as

discussed in sect. 3.4, there would be complex feeding patterns for the low-lying states. As these feeding states are populated while the recoiling nuclei experience the hyperfine field, extensive corrections would be necessary. Furthermore, experimental sensitivity would be greatly reduced should there be higher-lying long-lived ($\tau > 100\,\mathrm{ps}$) levels which feed the states of interest, because the recoiling nuclei would then be predominantly in the upper states while experiencing the hyperfine field. As there are such isomers in the Pt isotopes of interest (e.g. see fig. 8.2 below), this technique is unworkable here.

3.5.2 Transient-field techniques

Techniques employing the transient hyperfine field (sect. 3.3.2.1), to measure magnetic moments, use the energy produced in a heavy-ion bombardment to recoil ions *through* a thin ferromagnetic foil and into a non-ferromagnetic backing, where they come to rest. As shown in fig. 3.10, the excited nuclei experience the field while moving in the ferromagnet and then decay in the backing material, which is usually Cu or Pb, without the presence of the static field to cause further precession. A measurement of the g-factor for the 2_1^+ state in ^{190}Pt using the standard transient-field technique following Coulomb excitation is reported in chapter 7.

The time the recoiling ions spend in the ferromagnetic foil is, typically, of the order of 1 ps. When employing (HI, x n) reactions to form the neutron-deficient Pt isotopes, the time taken to populate low-lying levels (see sect. 3.4) is longer than this interaction time. Consequently, the states of interest would never experience the transient field. This may be overcome by including a vacuum gap between the target layers, so that the nuclei decay to the states of interest before entering the ferromagnet. However, this introduces vacuum deorientation effects and, as with the RIGV technique, this method is dependent on complex feeding corrections and is also susceptible to the problem of high-lying isomers, noted in the previous section.

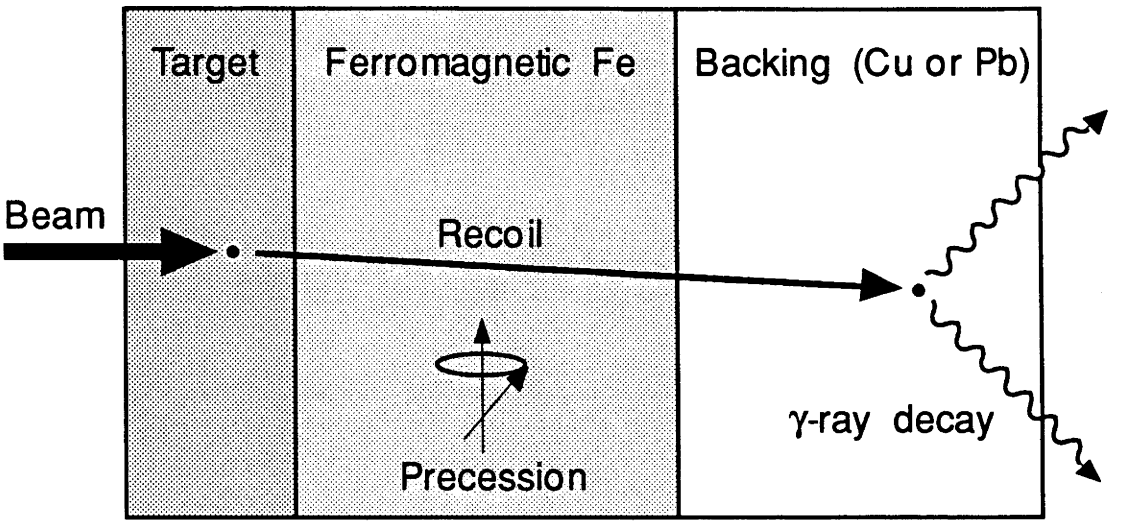

Figure 3.10: Illustration of the processes involved in the thin-foil transient-field technique described in the text. The actual target thickness is ordinarily around 10 μm.

3.5.3 Static-field techniques

3.5.3.1 In-beam

The static hyperfine field may be employed with an implantation method similar to the transient-field technique. As shown in fig. 3.11, the excited nuclei are populated in a heavy-ion induced nuclear reaction and recoil-implanted into a thick ferromagnetic foil to experience the static field, once they come to rest.

As the excited nuclei recoil into the ferromagnet they experience the transient field. For sufficiently large static field precessions the transient field effect can be treated as a small correction, perhaps made with an appropriate transient field parameterization (see sect. 3.3.2.1) extrapolated to zero velocity. There are also feeding corrections introduced by the (HI, x n) reaction mechanism, but again if feeding lifetimes are short these are manageable. However, in the Pt isotopes of interest there are isomers which would be problematic for this technique also.

A more significant problem in many measurements comes from the interaction of the ion beam, necessary to excite and implant the nuclei, with the ferromagnetic foil in the target. The nuclear reactions of the heavy ions with the ferromagnet produce significant contaminant radiation, which tends to overwhelm the γ-rays of interest.

Reported in appendix A is a recent study of the static fields present at stable

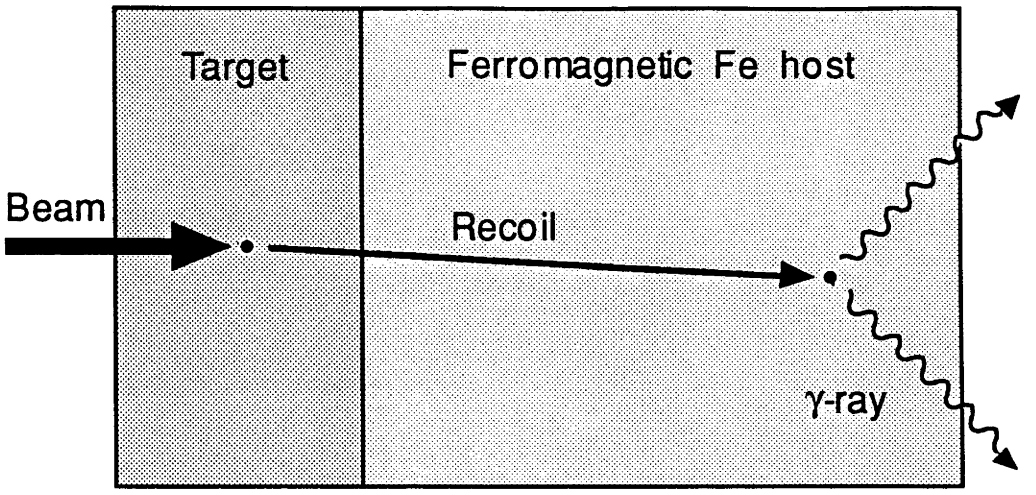

Figure 3.11: Schematic of the in-beam implantation method using the static hyperfine field.

^{192,194,196}Pt nuclei implanted in Fe following Coulomb excitation. This investigation suggests that the observed field strength from in-beam measurements may be reduced by pre-equilibrium effects associated with the ion-implantation process. These may last for around 10 ps and impinge upon the accuracy of the technique for nuclear states with lifetimes $\tau \lesssim 100$ ps. While this would not be significant for most of the isotopes studied here, it is a consideration in the cases of ^{192}Pt and ^{188}Pt.

There are, therefore, several difficulties associated with in-beam measurements of g-factors of short-lived states in the Pt nuclei.

3.5.3.2 Radioactivity, out-of-beam

In 'radioactivity' methods the nuclear states of interest are populated by a suitable radioactive decay. This follows the preparation of a radioactive source, consisting of a dilute alloy of a 'long-lived' radioactive parent nucleus with a ferromagnetic material. The experiments are 'off-line', so that the alignment produced in a nuclear reaction is not available and γ-γ perturbed-angular-correlation techniques are used. As an ion beam is not used here, there is no contaminant radiation from reactions with the ferromagnet. Measurements of the static field strength for Pt in Fe using this technique are summarized and compared with the results of other methods in appendix A.

This method is inappropriate for measurements on the neutron-deficient ^{184,186,188,190}Pt isotopes as the β^+-decay lifetimes of the parent nuclei are short, 1 min. $\lesssim \tau <$ 10 hours (table 4.4), making the preparation of the source difficult, if not impossible.

The next chapter describes the 'implantation-decay' technique used for the present measurements on the unstable Pt nuclei, which combines aspects of the static-field implantation and radioactivity methods and, thereby, overcomes many of the difficulties associated with these techniques.

Chapter 4

The Implantation-Decay Method

4.1 Introduction

The experimental challenge of the present project was to measure the g-factors of short-lived, low-lying excited levels in the neutron-deficient Pt nuclei. The short lifetimes ($\tau < 500\,\mathrm{ps}$) necessitate the use of time-integral perturbed angular distribution (IPAC/D) techniques with large, reliable and reproducible magnetic fields of the order of 100 Tesla. The hyperfine fields present at the nucleus of dilute impurities in a polarized ferromagnetic host are suitable and may be accessed conveniently by ion-implantation into a ferromagnet.

Difficulties arise because the states of interest are in *unstable* nuclei and to populate them requires a heavy-ion induced nuclear reaction. A major problem is that the heavy-ion beam tends to react prolifically with the ferromagnet creating significant contaminant radiation, which makes measurement of the γ-rays of interest very difficult.

The 'implantation-decay' technique, developed for the present experiments, avoids the problems associated with conventional implantation methods through the use of 'out-of-beam' measurements; i.e. the nuclear reaction and ion-implantation are completed prior to the commencement of the γ-ray perturbed-angular-correlation measurement. This is accomplished by using β^+-decay to populate the states of interest following the formation of the radioactive parent nuclei in a suitable heavy-ion fusion reaction.

The parent nuclei are implanted into a polarized ferromagnetic foil where they subsequently decay to the daughter Pt nuclei, which are subject to the static hyperfine magnetic field of Pt in Fe as in a conventional 'radioactivity' PAC

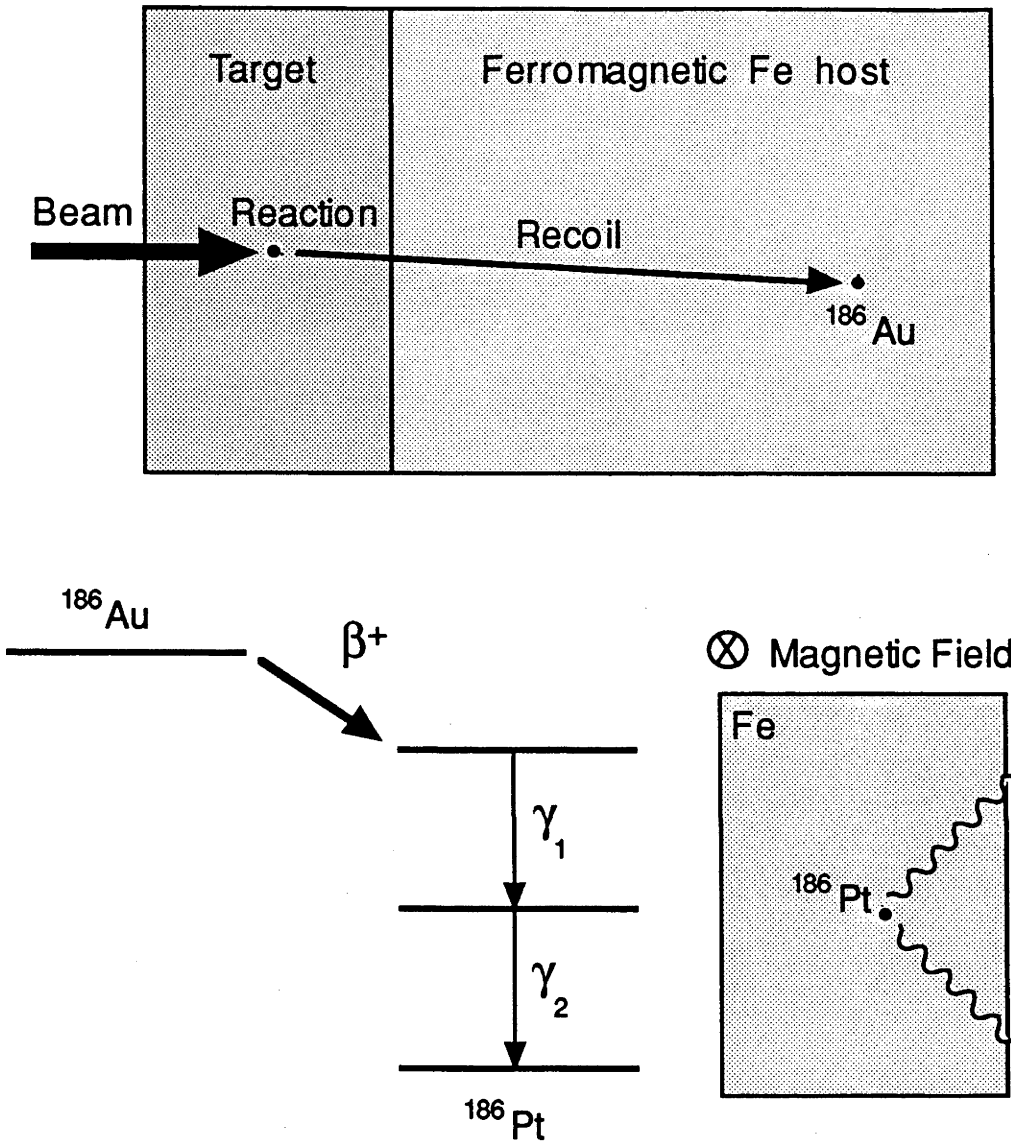

Figure 4.1: Diagram of the processes involved in the implantation-decay technique. Firstly, *parent* nuclei (e.g. ^{186}Au) are formed in a (HI, x n) reaction and recoil-implanted into an Fe foil. They β^+-decay here to become the Pt nucleus of interest (e.g. ^{186}Pt), which then decay further, by emitting γ-rays, while in the presence of the static hyperfine magnetic field.

experiment (sect. 3.5.3.2), see fig. 4.1. The lifetime of the β^+-decay provides the opportunity to stop the beam and measure the γ-rays of interest. After a counting period the irradiation of the ferromagnet-backed target is recommenced to implant more parent nuclei, replacing those which have decayed; the cycles are repeated until sufficient counts are obtained.

The γ-radiation emitted directly from heavy-ion induced fusion reactions and Coulomb excitation of the target materials (including the ferromagnet) dissipates within a nanosecond or so of the ion bombardment. As this is the source of most of the γ-rays produced by the irradiation (because the intensity of the long-lived activity is much less), by measuring 'out-of-beam' the problem, in conventional methods, of overwhelming contaminant radiation is avoided.

Another consequence of the implantation-decay technique, where the nuclei produced in the reaction come to rest and β^+-decay before the emission of γ-rays from the states of interest, is that the alignment produced in the nuclear reaction is lost for the γ-ray measurement. This necessitates the measurement of perturbed γ-γ angular correlations. Although the anisotropy for some γ-ray cascades may be reduced compared with perturbed-angular-distribution (IPAD) techniques, the disadvantages of in-beam measurements are avoided. Specifically, interpretation of the results is simplified by the absence of precession-history and beam-bending effects. Also, the reduced count rate in a γ-γ coincidence measurement is somewhat ameliorated by the exceptionally good signal-to-noise (peak-to-background) ratio obtained when detecting both the populating and de-populating radiations of a state in an out-of-beam measurement.

4.2 Equipment

4.2.1 The CAESAR array

The γ-γ coincidence measurements were made using the Compton-suppressed, high-purity germanium (HPGe) γ-ray detector array, CAESAR [Dr89], in the ANU 14UD Pelletron Accelerator laboratory. This array has seven such detectors, giving twenty-one pairs (listed in table 4.1), and is shown schematically in fig. 4.2.

For the actual angular difference between any two detectors, there is an equivalent angle which is positive and less than 90°, due to the symmetries of the γ-γ angular correlations of interest. From the symmetry of the array, these effective

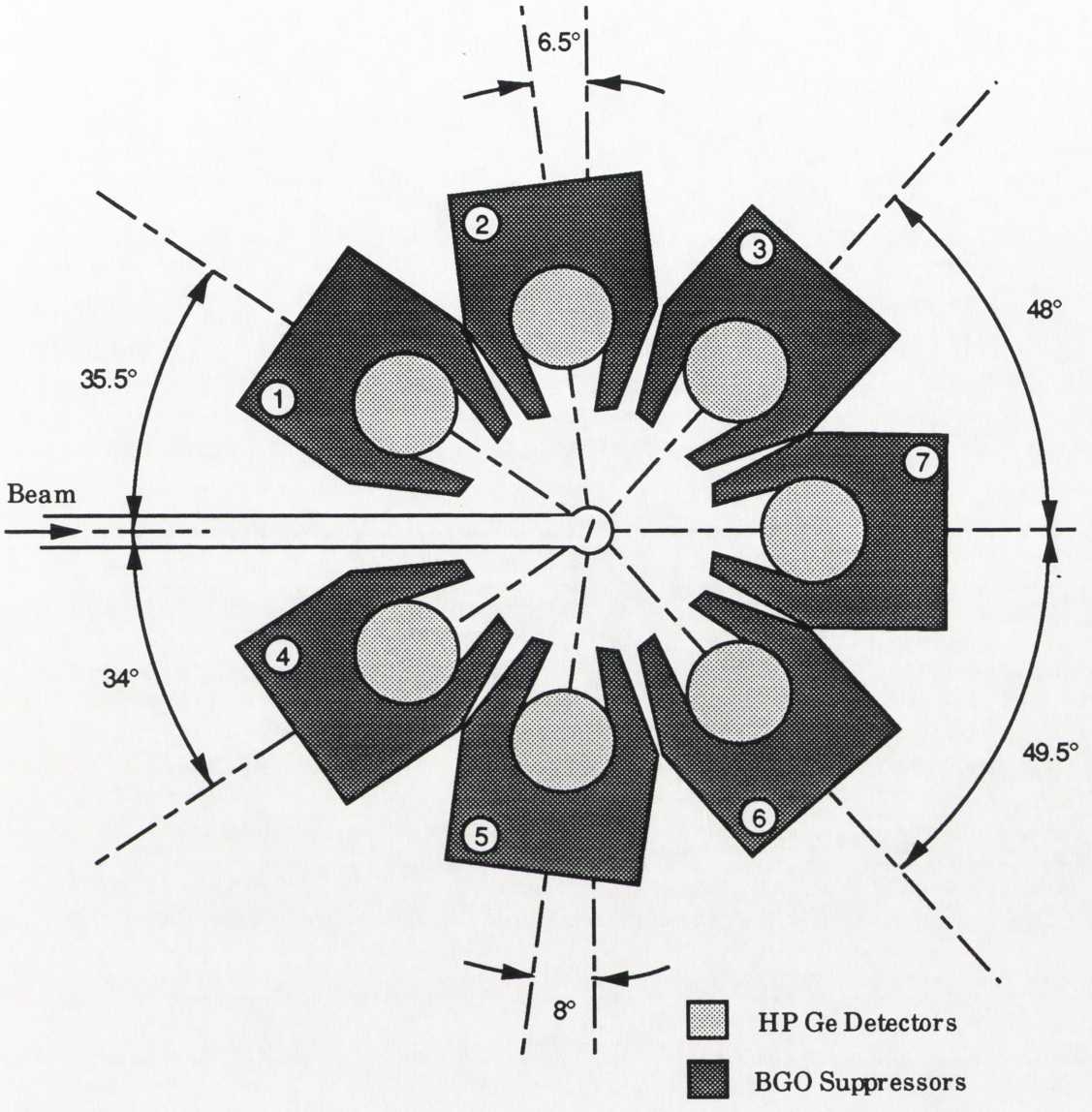

Figure 4.2: Schematic representation of the CAESAR γ-ray detector array.

angular separations for the twenty-one, individual detector pairs may be grouped into seven very similar angles. These are given in table 4.1, where the order of the detectors in each pair is such that the effective angles are all measured in the same direction; on the schematic of fig. 4.2 the clockwise direction is positive.

The main features of the electronics arrangement are shown in fig. 4.3. The coincidence logic can operate in either singles or dual-coincidence mode. Compton suppression was provided by the BGO shields of each detector. If a pulse was received from the corresponding BGO within 250 ns of a HPGe detector firing, the timing signal for that event was inhibited.

Table 4.1: Angular separations for each detector pair in the CAESAR array.

Effective[a] Angle	Detector Combinations[b,c] (Actual Angular Separation [degrees])					No. of pairs
14.0°	**1,6** (166.0)	**2,5** (165.5)	**3,4** (166.0)			3
34.0°	**6,2** (146.0)	**5,3** (146.0)	**4,7** (145.5)			3
35.0°	**7,1** (145.0)					1
48.5°	**1,2** (48.0)	**2,3** (48.5)	**3,7** (48.5)	**5,4** (48.5)	**6,5** (48.5)	
	7,6 (49.0)					6
62.5°	**1,5** (117.5)	**2,4** (117.5)				2
69.5°	**4,1** (69.5)					1
83.0°	**3,1** (96.5)	**7,2** (97.0)	**6,3** (97.5)	**4,6** (96.5)	**5,7** (97.5)	5

[a] Equivalent angular difference $< 90°$.

[b] For detector numbering see fig. 4.2.

[c] Detector ordering for each pair is described in the text.

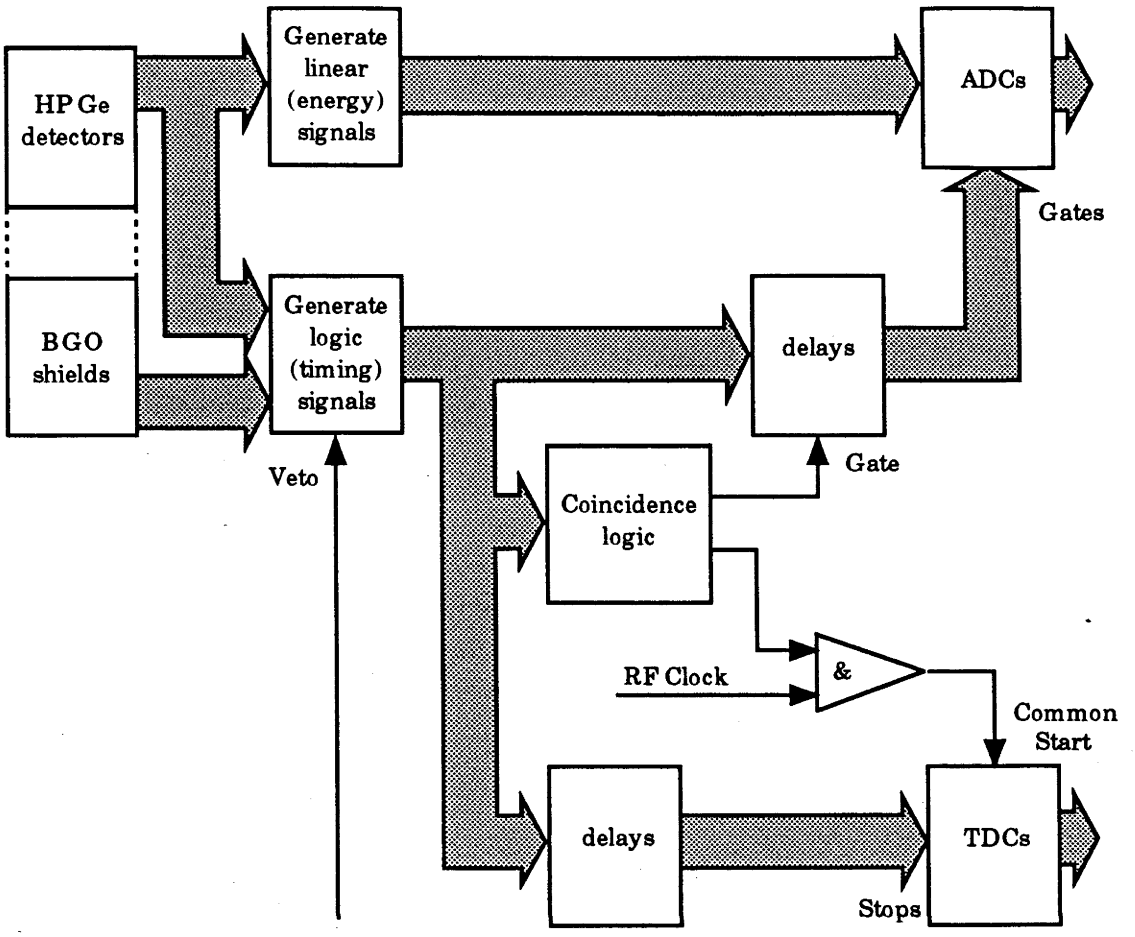

Figure 4.3: Simplified block diagram of the electronics arrangement for the CAESAR array. Wide arrows represent seven equivalent signals. The outputs from the ADC's and TDC's were recorded by computer in event-by-event mode.

To reduce the detection of x-rays, $\sim$ 1 mm thick Fe and Cu absorbers were placed between the target and each detector. For all the detectors the total distance to the target position is approximately 11 cm and the lead (Pb) collimators give detector opening angles of 21°. Corrections to the γ-γ angular correlations to account for the finite size of the γ-ray detectors are described in sect. 5.5.

4.2.2 The 'rabbit'

The parent nuclei were produced remotely from the CAESAR array, on a neighbouring beam line, to reduce the exposure of the HPGe detectors to neutron damage during irradiation. A target transport system or 'rabbit' [By91] (fig. 4.4) was used to move the irradiated target between the array and the beam line.

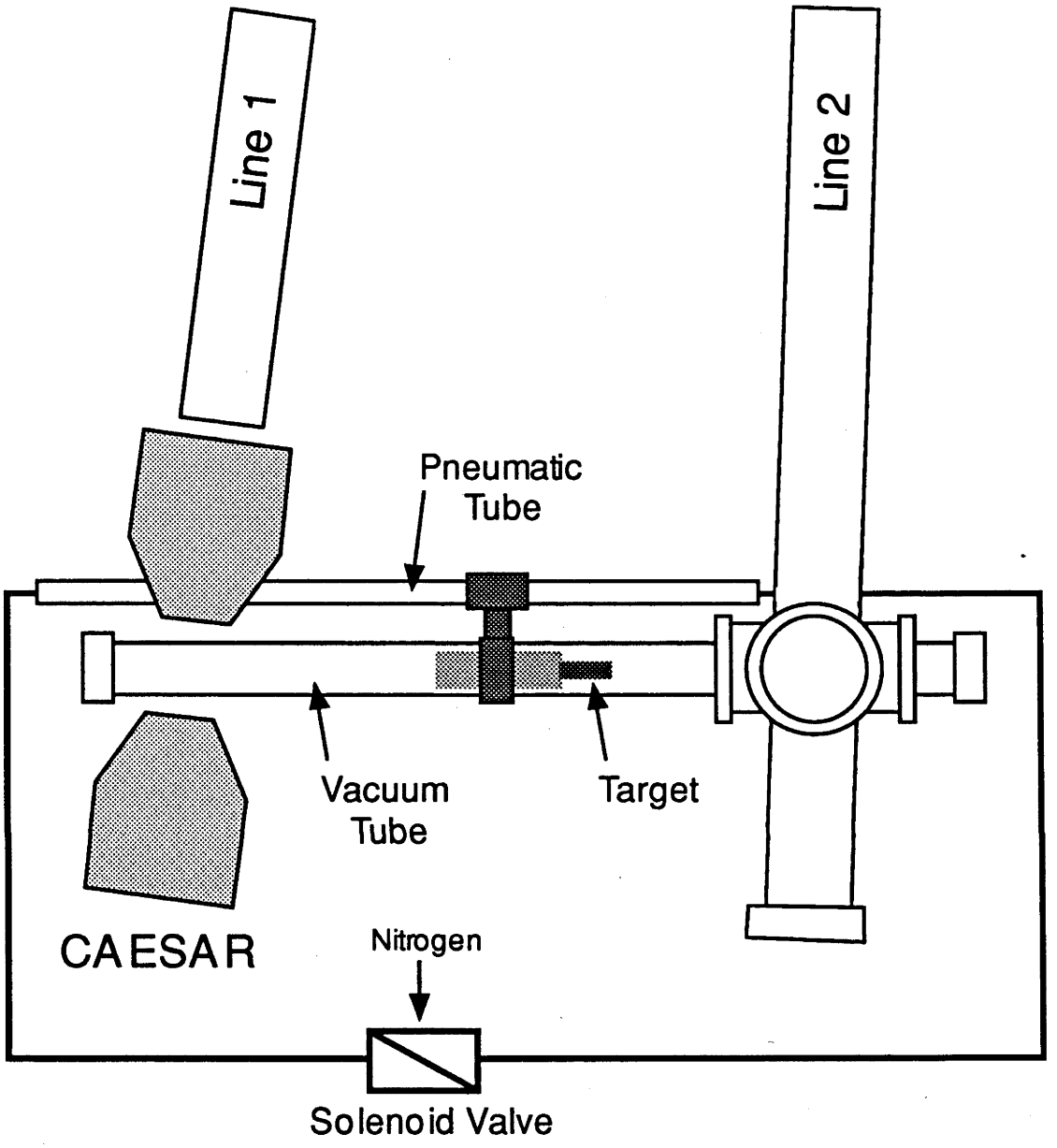

Figure 4.4: Schematic of the 'rabbit' target-transportation system.

Under operating conditions, the rabbit traversed the distance of approximately 3 metres, from the centre of the array to the irradiation site, in around 3 seconds.

The ion beam was injected through the accelerator only when the rabbit target assembly was at the irradiation site; during the counting phase the beam was interrupted by a 'beam chopper' located near the ion source of the 14UD accelerator. Similarly, data were collected only when the target was positioned in the centre of the array. To ensure data collection was stopped during the

irradiation periods, when there was no voltage being applied to the beam chopper (i.e. it was not activated and the beam was on) the control system issued a veto signal which inhibited all timing pulses (fig. 4.3).

The movement of the rabbit was computer controlled and included the automatic switching on and off of both the ion beam and the data aquisition. This permitted the programming of repeated cycles of specified irradiation and measurement times.

4.2.3 Equipment modifications

To optimize the sensitivity of a measurement of the perturbation of an angular distribution, the direction of the magnetic field must be perpendicular to the detection plane [St64]. Achieving this required modifying the existing equipment.

There is an angle of 15° between the plane of the CAESAR array (direction of beam line 1) and the irradiation beam line (beam line 2) [By91]. The resulting angle at which the rabbit assembly enters the array (see fig. 4.5) presented the

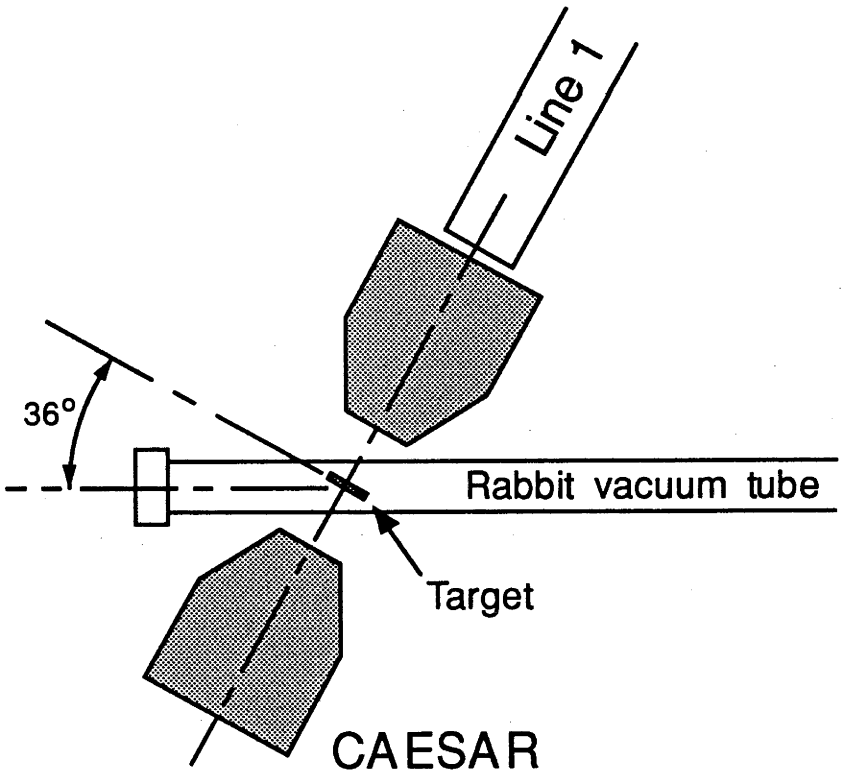

Figure 4.5: Diagram of the positioning of the rabbit system with respect to the CAESAR array.

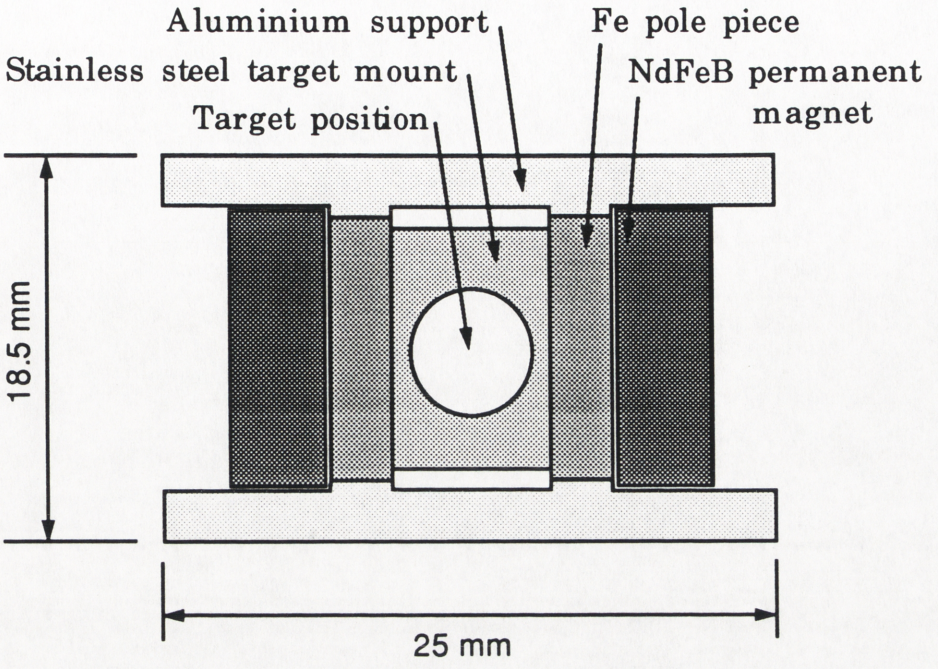

Figure 4.6: Modifications made to the target holder of the rabbit system.

main challenge in designing the target holder, so that the externally-applied polarizing field, provided by a pair of small permanent magnets, was perpendicular to the detection plane of the array.

The target holder modification included the positioning of two small ($12.5 \times 6.0 \times 3.5$ mm), permanent NdFeB magnets, with iron pole tips, at either end of the target (see fig. 4.6) to polarize the ferromagnetic foil. The orientation of this target assembly perpendicular to the plane of the array was achieved by rotating it through an angle of 36° to the centre axis of the rabbit vacuum tube (see fig. 4.5). This introduced further restrictions, such as limiting the target size to keep the assembly within the rabbit target carrier.

An external field of approximately 1100 Gauss was measured at the centre of the target position and is sufficient for saturation of an annealed Fe foil [Ka75]. Reversal of the field direction was achieved by simply swapping the magnets. Although this requires that the vacuum be broken, in principle, it needs to be done only once during a run.

4.3 Aspects of Experimental Design

4.3.1 Choice of ferromagnet

Ferromagnetism is apparent in only a few elements, which are found in two specific regions of the periodic table: the iron-group transitional series consisting of iron ($_{26}$Fe), nickel ($_{27}$Ni) and cobalt ($_{28}$Co); and the rare-earth group of gadolinium ($_{64}$Gd) through to thulium ($_{69}$Th). With the exception of Gd, the rare-earths do not have simple parallel alignments of the ionic moments and are unsuitable for the present measurements.

Some of the properties of Fe, Ni, Co and Gd are given in table 4.2. Cobalt exhibits a phase change at a temperature of around 700 K and for temperatures above this has a face-centered cubic lattice structure, similar to that of Ni. The static hyperfine fields for dilute Pt impurities in Fe and Co hosts have magnitudes of around 100 Tesla, as required for the present measurements (sect. 3.3.2.2). The fields in Ni and Gd are significantly weaker and, except for measurements on

Table 4.2: Selected properties of various ferromagnetic elements[a].

Host	Lattice Structure	Curie Temp. T_c [K]	n_B/atom[b]	B_{st}(Pt)[c] [Tesla]
Fe	bcc	1043	2.22	-125±2[e]
Co[d]	hcp	1388	1.72	-83±2
Ni	fcc	627	0.61	-34±1
Gd	hcp	293	7.10	-38±5[f]

[a] Taken from ref. [Ki71].

[b] Number of polarized electrons per atom.

[c] The static field strength at the site of Pt impurities, at 4 K [Kr83].

[d] The properties given are for temperatures below 660 K (see text).

[e] From ref. [Ko67], see sect. A.5.2.

[f] Field strength at 92 K [St95a].

longer-lived states ($\tau \gtrsim 500\,\mathrm{ps}$), are unsuitable here.

Both Co and Gd have a hexagonal close packed structure. The non-cubic lattice means the possibility of non-negligible electric field gradients cannot be dismissed a priori for these materials. The internal field for Pt in Gd has not been examined as thoroughly as that for the other hosts and, as a consequence, the field strength is not known precisely. Another consideration with serious ramifications for equipment design is that a Gd host, due to its low Curie temperature of 293 K (table 4.2), must be cooled, usually to liquid nitrogen (N_2) temperatures, to exhibit its ferromagnetic properties.

In contrast Fe does not need to be cooled, it has a simple cubic structure, and the PtFe field has been studied extensively with a variety of experimental techniques. Therefore, the preferred ferromagnetic host is Fe. A recent study of the field strength following ion-implantation of Pt into Fe is reported in appendix A.

4.3.2 Optimum irradiation and measurement times

To determine precisely the nuclear precession in a perturbed-angular-correlation measurement it is important to collect data as efficiently as possible. In the present measurements (see table 4.3) the count-rates were maximized by considering a number of factors, including: the selection of nuclear reactions with large cross-sections; increasing the amount of material in the targets, which was limited by the recoil-energy produced in the reaction; increasing the intensity of the incident ion-beams; and the choice of optimum irradiation and measurement times.

In the present measurements the ion beam was turned off during the detection of γ-radiation from the decay of nuclei produced in the target irradiation. Following the counting period, the irradiation was continued to replace the parent nuclei which had decayed in the measurement period. In such experiments it is desirable to achieve an 'equilibrium' condition, shown in fig. 4.7, where the number of nuclei produced in an irradiation period is the same as the number which decay in that cycle: the irradiation period and the following measurement interval. A complete treatment is given in ref. [Ev55] and yields the simple rule-of-thumb that the count-rate is maximized at equilibrium with *equal* irradiation and measurement times. To attain equilibrium quickly, it may be preferable to initially irradiate the target continuously.

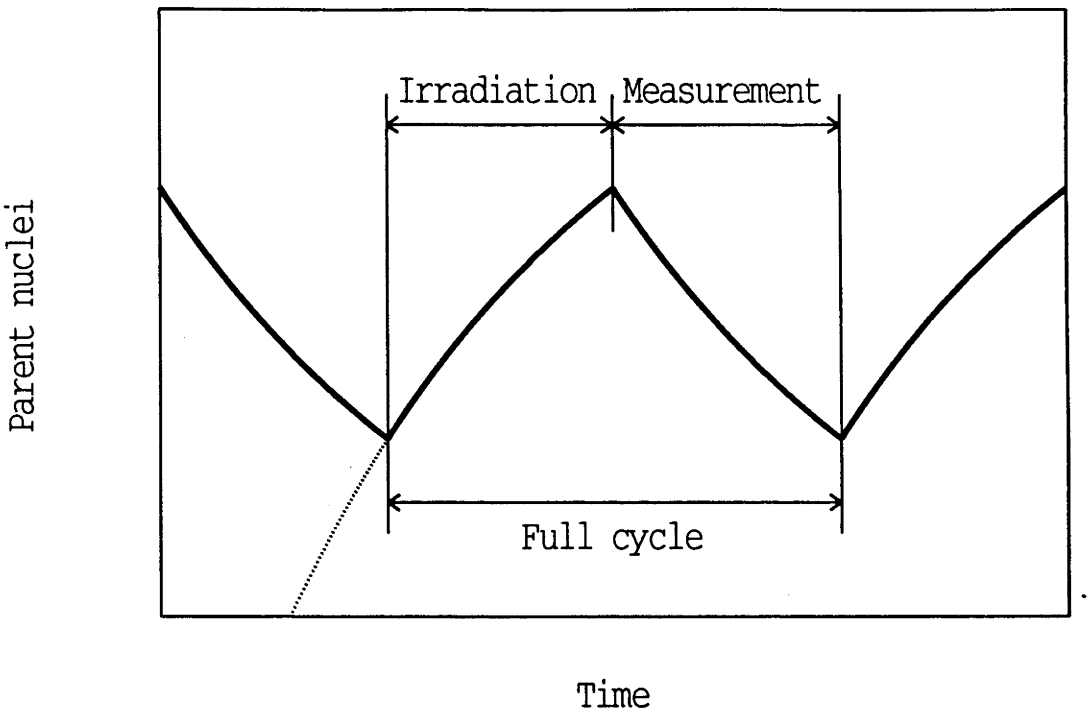

Figure 4.7: The number of parent nuclei present as a function of time, under equilibrium conditions. The irradiation and measurement periods are labelled. The population in the measurement intervals is proportional to the γ-ray rate. The dotted line shows the population during an initial period of continuous irradiation.

The average count-rate increases with shorter cycle times, independent of both the production rate of the nuclear reaction and the lifetime of the radioactive decay. The improvement is minimal (less than 1%), however, for cycle times less than the decay lifetime. Note that these calculations have discounted the rabbit transport time of ~ 3 s (sect. 4.2.2), during which there is neither measurement or irradiation of the target, as it is much shorter than the lifetimes and, therefore, the cycle times used (table 4.4).

4.3.3 Anisotropies and γ-ray intensities

In the present experiments the measured quantity is the perturbation (manifest as a rotation and an attenuation) of an angular correlation between two cascade γ-rays. The sensitivity of such a measurement is improved with greater anisotropy in the observed angular correlation.

For the first-excited 2^+ state the only de-populating radiation is, obviously, the $2_1^+ \rightarrow 0_1^+$ γ-transition. In each Pt nucleus, however, there are a number of

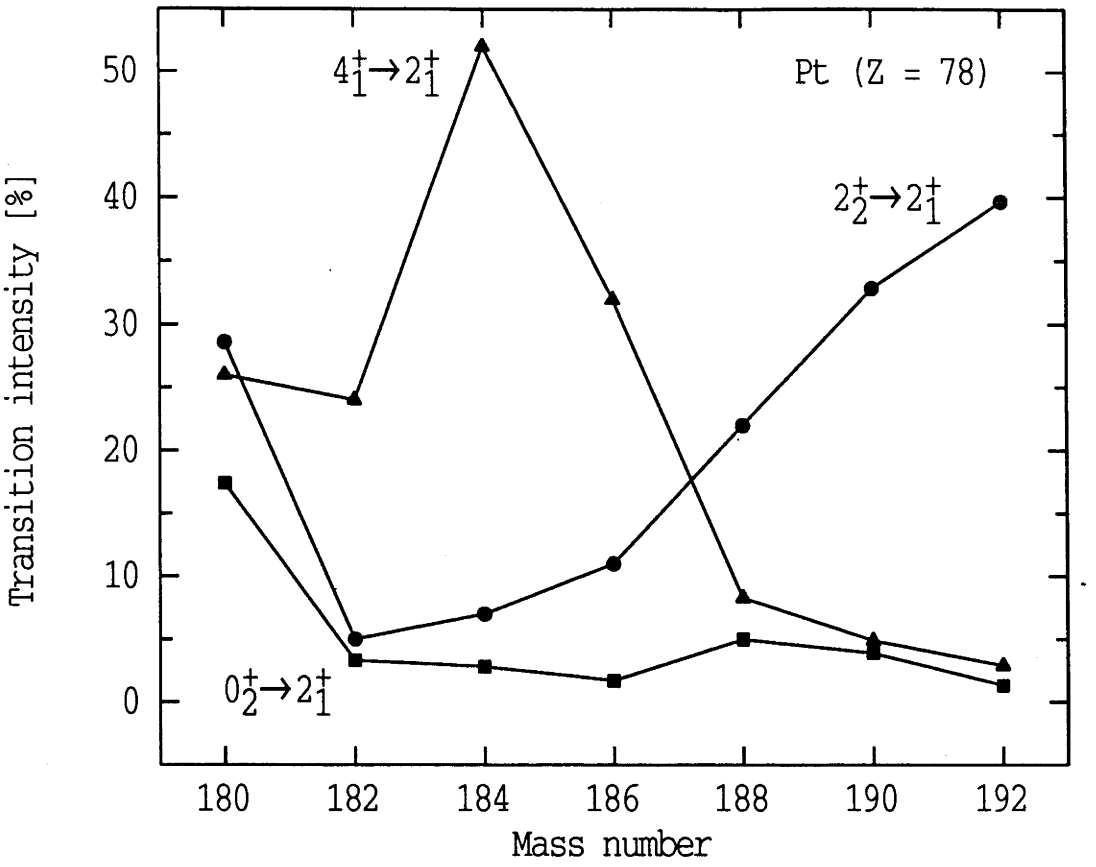

Figure 4.8: Intensities of transitions between low-lying states in the even Pt nuclei relative to the strengths of the $2_1^+ \rightarrow 0_1^+$ transitions.

transitions feeding this state directly. Figure 3.4 shows the *unperturbed* angular correlations for a number of γ-γ cascades found in the Pt nuclei. The anisotropy of the $0_2^+ \rightarrow 2_1^+ \rightarrow 0_1^+$ cascade is clearly the most pronounced.

As discussed in sect. 3.2, the alignment produced by observation of a γ-ray may by transferred by unobserved intermediate transitions. This allows examination of the directional correlation between two non-consecutive cascade γ-rays, although the anisotropy here is usually reduced significantly. A special case is the cascade $I^\pi \rightarrow 0^+ \rightarrow 2^+ \rightarrow 0^+$, where the $0^+ \rightarrow 2^+$ transition is unobserved and the initial state, I^π, may be any spin. As the excited 0^+ state can not be aligned (it has only one magnetic substate), the observed transitions are not correlated and the radiation is emitted isotropically. For an example see sect. 6.4.

The relative population of selected states in the β^+-decay of the parent Au nuclei may be inferred from fig. 4.8. (This is also shown, below, by the intensities of the γ-ray transitions de-populating the states in the simplified $^{184-192}$Pt decay

schemes of figs. 6.2, 6.11 and 6.17.) There is a significantly larger fraction of the decay through the $2_2^+ \rightarrow 2_1^+$ γ-transition (and $2_2^+ \rightarrow 2_1^+ \rightarrow 0_1^+$ γ-γ cascade) in ^{188}Pt and the $4_1^+ \rightarrow 2_1^+ (\rightarrow 0_1^+)$ in ^{184,186}Pt (and also the $6_1^+ \rightarrow 4_1^+ (\rightarrow 2_1^+ \rightarrow 0_1^+)$ in ^{184}Pt) than the respective $0_2^+ \rightarrow 2_1^+ \rightarrow 0_1^+$ cascades. This improves the precision of measurements made with these cascades. Consequently, the precession angles, $\omega_L\tau(2_1^+)$, determined with these cascades in the present experiments have similar precisions to those obtained using the more anisotropic, but less intense, $0_2^+ \rightarrow 2_1^+ \rightarrow 0_1^+$ correlations.

4.3.4 Nuclei at field-free sites

In transporting the entire target assembly, rather than only the irradiated ferromagnetic foil, a potential problem is the possibility of detecting γ-rays emitted from the recoils which have come to rest not in the ferromagnetic foil, but in the front layer of the target. The nuclei of these ions are not subject to the hyperfine field in Fe and, therefore, the emitted radiation pattern is *not* perturbed. The result is a superposition of the *un*perturbed angular correlation on the perturbed distribution of interest, which reduces the experimental sensitivity to the precession and complicates analysis.

The number of ions which came to rest in the target layer was minimized by the use of thin target layers, at the expense of count-rate, and by maximizing recoil-energy, through the selection of heavy ion beams and beam energies as high as practical. The fraction of ions stopping in the foil was calculated with the kinematics for each experiment using the Monte-Carlo code TRIM [Zi85a]. In the ^{192}Pt measurement, which used an ^{16}O beam at 100 MeV, approximately 3% of the recoils did not escape from the front layer of the target. In the other measurements, where the recoil energy was larger (the beams used are listed in table 4.3), this fraction was $\lesssim 2\%$. In each experiment this relatively small effect was taken into account (sect. 5.4).

A general problem with ion-implantation is that the final resting sites of the ions are not well controlled. This results in a number of the implanted ions having positions in (i) non-substitutional sites of the host lattice and (ii) regions with residual structural damage caused by the implantation process. For a ferromagnetic host, the possibility that some implanted nuclei will experience magnetic field strengths reduced from the full internal field cannot be excluded. This too

results in the measurement of a superposition of radiation patterns with different perturbations.

An examination of the fields experienced when ions of the Pt region are implanted in ferromagnetic Fe using standard methods is reported in appendix A. With a simple two-site model, where the impurity nuclei are assumed to experience either the full field strength or no magnetic field, the data suggest that $\gtrsim 90\%$ of the implanted nuclei are subject to the hyperfine field. This is consistent with the results of a study by Béraud *et al.* [Bé68], which imply $95 \pm 12\%$ of the implanted ions are on full-field sites, and channelling experiments [Al71] that found $\sim 85\%$ of implanted Au atoms reside on substitutional sites in Fe.

Both the implantation-decay technique and the conventional implantation method, which employs the static field following Coulomb excitation, use ion bombardment to recoil ions of the Pt region into a thick Fe foil. As the implantation kinematics for the measurements made with these techniques (given in sects. 4.4 and A.4) are similar, one expects the final sites of the implanted nuclei to also be similar and the values given in the previous paragraph to be valid for the present implantation-decay measurements. Also, the resting site of an implanted ion depends primarily on the elastic 'nuclear' collisions of the recoiling ion with lattice atoms near the *end* of the ion's range and, therefore, does not depend on the initial recoil energy of the ion, which is the quantity that may vary somewhat between experiments made with the different methods.

Another feature of the implantation-decay experiments is that the parent nuclei β^+-decay to the states of interest in Pt following their implantation in the ferromagnet. A consideration is then whether the Pt nuclei in interstitial lattice sites were deposited there directly (as parent nuclei in the ion-implantation) or if they were moved to these sites by the recoil energy from a β^+-decay, following implantation in a substitutional site. Recently, Hinfurter *et al.* [Hi92] have obtained the first evidence for β-decay induced site changes. From an NMR-ON experiment on ^{90m}Zr<u>Fe</u> they were able to show that about 15 to 20% of the ^{90m}Zr nuclei experienced a slightly ($\sim 10\%$) reduced hyperfine field due to changes in site following β-decay.

In the implantation-decay measurement on ^{192}Pt, the Q-value for the first decay from ^{192}Tl to ^{192}Hg is such that the recoil energy of the ^{192}Hg nucleus is similar to that of the ^{90m}Zr nucleus in the work of Hinfurter *et al.* [Hi92]. Therefore, the possibility of changes in the nuclear site during the chain of β^+-

decay from ^{192}Tl to ^{192}Pt cannot be excluded. The results of Hinfurter *et al.* imply a reduction of the net hyperfine field due to β-induced recoils of only 2 or 3%. This is similar to the effect expected from the stopping of a fraction of recoils in the non-ferromagnetic layer of the target, and is less than the reduction expected due to imperfections in the implantation process (up to $\sim$ 15%, see above).

The corrections made for these effects in the analyses are described in sect. 5.3, and the field calibration for the measurements is discussed in sect. 6.1.1.

4.4 Experimental Details

The present work includes five separate implantation-decay experiments on the ^{184,186,188,190,192}Pt nuclei. The measurement made on the stable, naturally-occurring nuclide ^{192}Pt provided a check of the experimental technique and a calibration of the effective hyperfine magnetic field strength. The experimen-

Table 4.3: Particulars of the implantation-decay experiments.

Nuclide	Reaction	Beam Energy [MeV]	Reaction X-section[a] [mb]	Target Thickness [μg/cm^2]	Running Time[b] [hrs]
^{192}Pt	^{181}Ta (^{16}O , 5n) ^{192}Tl	100	450	393	140
^{190}Pt	^{170}Er (^{25}Mg , 5n) ^{190}Hg	128	250	780	35
^{188}Pt	^{169}Tm (^{24}Mg , 5n) ^{188}Tl	128	170	685	135
^{186}Pt	^{173}Yb (^{19}F , 6n) ^{186}Au	112	450	400	100
^{184}Pt	^{165}Ho (^{24}Mg , 5n) ^{184}Au	128	250	800	170

[a] Calculated estimate, see text.

[b] Approximate total running time, including beam on and off periods.

Table 4.4: Details of the decays used in the implantation-decay experiments.

Mass No.	Decay	Total[a] $T_{1/2}$	Cycle[b] Time
192	^{192}Tl (10m) → ^{192}Hg (5h) → ^{192}Au (5h) → ^{192}Pt	~ 10h	120m
190	^{190}Hg (20m) → ^{190}Au (43m) → ^{190}Pt[c]	63m	60m
188	^{188}Tl (71s) → ^{188}Hg (3m) → ^{188}Au (9m) → ^{188}Pt (10d)	~ 13m	20m
186	^{186}Au (11m) → ^{186}Pt (2h)	11m	20m
184	^{184}Au (53s) → ^{184}Pt (17m)	53s	200s

[a] Total half-life for the decay.

[b] The cycle time is twice the length of the equal irradiation and measurement periods.

[c] ^{190}Pt has a half-life of 6×10^{11} years.

tal details, including the reactions used and the subsequent radioactive decays of interest, are summarized in tables 4.3 and 4.4. Statistical model estimates of production yields from the reactions were made with the program ZPACE [Ga74].

In addition to the information provided in the tables: in each experiment the beam intensity was ~ 20 pna, except for the ^{190}Pt measurement where only about 5 pna of $^{25}Mg^{8+}$ was obtained. The direction of the polarizing field was reversed at least once during each experiment and approximately equal number of coincident events were collected in each direction. For the lighter isotopes, in particular ^{184,186}Pt, the subsequent β^+-decay of the Pt nuclei produces an increasing background radiation. This was minimized by replacing the Fe foil periodically. The Fe foils used had thicknesses of ~ 3 μm to ensure no recoils left the target. All foil and layer thicknesses (table 4.3) were determined by weight and area measurements made during each target preparation.

All Fe foils were annealed in vacuum prior to use, in order to enlarge the magnetic domains of the ferromagnet, relieve pressures and strains apparent in the foils, and clean the surfaces of the foils. This involved heating the foils in a small Tantalum oven to ~ 800°C for around 20-30 minutes in a vacuum of

$< 10^{-5}$ Torr.

The γ-radiation was recorded in event-by-event mode with the γ-γ coincidence requirement. In each experiment, γ-ray singles spectra were collected separately to allow the relative detector efficiency calibration described in sect. 5.3.1. The detectors were gain matched, and the maximum γ-ray energy recorded was 2 MeV.

Chapter 5

Data Analysis

5.1 Data Sorting

In table 4.1 the twenty-one detector pairs of the array are listed in seven groups, where the combinations in each group have the same effective angular separations. For each γ-γ coincidence measurement, the event-by-event data were sorted into fourteen, separate, 4096×4096 channel, two-dimensional matrices. Each of these γ-γ coincidence matrices included events collected at one of the seven effective detector angles and in only one field direction. The perturbed angular correlations for each γ-ray cascade, measured at seven angles and with the applied field in both directions, are given by the intensities of the appropriate coincident peaks in these matrices.

Figure 5.1 shows a typical total time-difference (TDC) spectrum for a detector pair of the array. The central peak corresponds to 'real' coincidences and the background to random events. The two side peaks are due mainly to x-rays. The number of random coincidences was small for the low count rates of the out-of-beam measurements. To extract only real events the γ-rays must be gated on the peak region with a subtraction of the random background level. This was not done universally, once it had been demonstrated that inclusion of the few random events did not affect the extracted precessions angles.

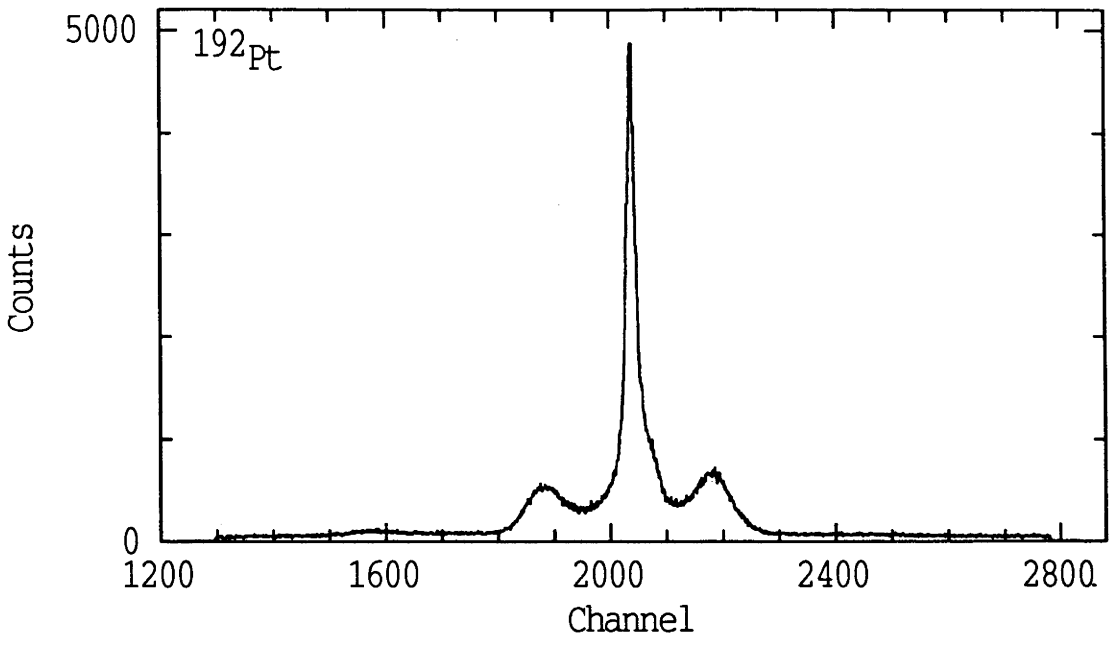

Figure 5.1: A TDC spectrum of coincident events collected in γ-ray detectors 1 and 5 during the ^{192}Pt measurement. Only events separated by less than 432 ns were recorded, i.e. the spectrum width is 864 ns. The prompt peak is around 70 ns wide and the shoulders (centred at approximately $\pm$100 ns) are delayed events which include x-rays and low-energy (< 100 keV) γ-rays, as these are subject to the 'time-walk' effect.

5.2 Measuring Peak Areas

Each axis of a matrix corresponds to one detector of each pair that have the given effective angular difference (where the detectors listed first in each pair, from table 4.1, are on the same axis). Coincidence spectra were generated by setting an energy window on one axis and projecting a spectrum on the other from the selected 'slice' of the matrix. Background subtraction of the spectrum for a particular peak was made by slicing on the background adjacent to the peak. For each matrix, the total projections on each axis were examined for the selection of peak and background regions.

The intensity of a coincidence peak in a matrix was taken from the appropriate peak area in the coincidence spectrum. Due to the high signal-to-noise ratios and low level of contaminant radiation in these out-of-beam coincident measurements (sect. 4.1), this was usually done by simply summing the counts in the peak with an appropriate allowance for the background under the peak. This involved subtracting a background level for the peak region, determined in a

linear interpolation of the average levels for background regions defined on both sides of the selected peak. To avoid introducing systematic variations, the same peak and background regions were used for a given transition with data collected in opposite field directions. In the few cases where peaks were not completely resolved from one another, the areas were determined by fitting the overlapping peaks to a gaussian shape with a small tail on the low-energy side and a linear background.

5.3 The Experimental Angular Correlations

From the coincident peak areas, four 'independent' measures of the perturbed angular correlation for each γ-γ cascade were constructed. These are from the opposite directions of the *internal* magnetic field (labelled 'up' and 'down' and denoted by $\pm B$, respectively) and the two gating senses, where the detectors in which the two coincident γ-rays were observed are reversed (as displayed in fig. 5.2). This is denoted by the sign of the detector separation angle, $\pm\theta$, and achieved by gating on the same transition, in turn, on the x- and y-axes of the γ-γ matrix.

When referring to fig. 5.2 and the diagram of the CAESAR array (fig. 4.2) the field 'up' direction is *into* the page, as the angular separations (of table 4.1) are measured in a clockwise direction. Note that the hyperfine field for Pt in Fe is in the opposite direction to the external magnetic field of 1.1 kG used to polarize the ferromagnetic foil.

As the orientation of the magnetic field is perpendicular to the detection plane (sect. 4.2.3), the perturbation of an angular correlation has the opposite sense when either the field direction or gating order is reversed. Then the statistically independent measures of the perturbed-angular-correlation function (eq. 3.19) for a γ-ray cascade are given by

$$W(\theta, \pm B) = \sum_{k=0,2,4} \frac{b_k}{\sqrt{1+(\omega_L \tau)^2}} \cos k(\theta \mp \Delta\theta) \tag{5.1}$$

and

$$W(\pm\theta, B) = \sum_{k=0,2,4} \frac{b_k}{\sqrt{1+(\omega_L \tau)^2}} \cos k(\theta \mp \Delta\theta) \quad , \tag{5.2}$$

with the relationships

$$W(-\theta,-B) = W(+\theta,+B) \quad \text{and} \quad W(-\theta,+B) = W(+\theta,-B) \ . \qquad (5.3)$$

An example of four γ-ray spectra corresponding to the four measures of an angular correlation is supplied in fig. 5.3. This shows the data collected in the ^{186}Pt experiment which constitute the measured $0_2^+ \rightarrow 2_1^+ \rightarrow 0_1^+$ correlations at 34°. The anisotropy of this correlation, even though it has been attenuated in the perturbation (see fig. 6.20), is obvious from the differences in the intensities of the two field-up peaks and the field-down peaks. Also, the similarity of the peaks with opposite gating *and* field directions illustrates the relationships of eq. 5.3.

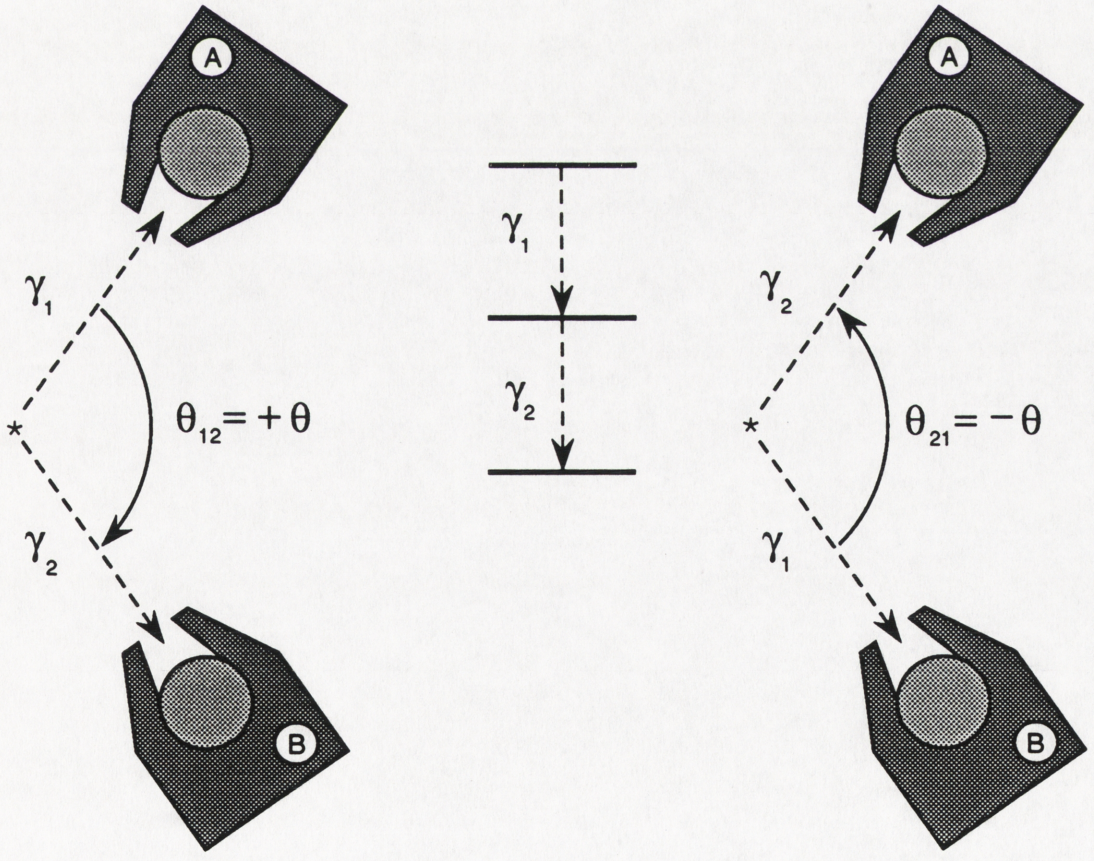

Figure 5.2: The gating directions for a detector pair observing correlated γ-rays.

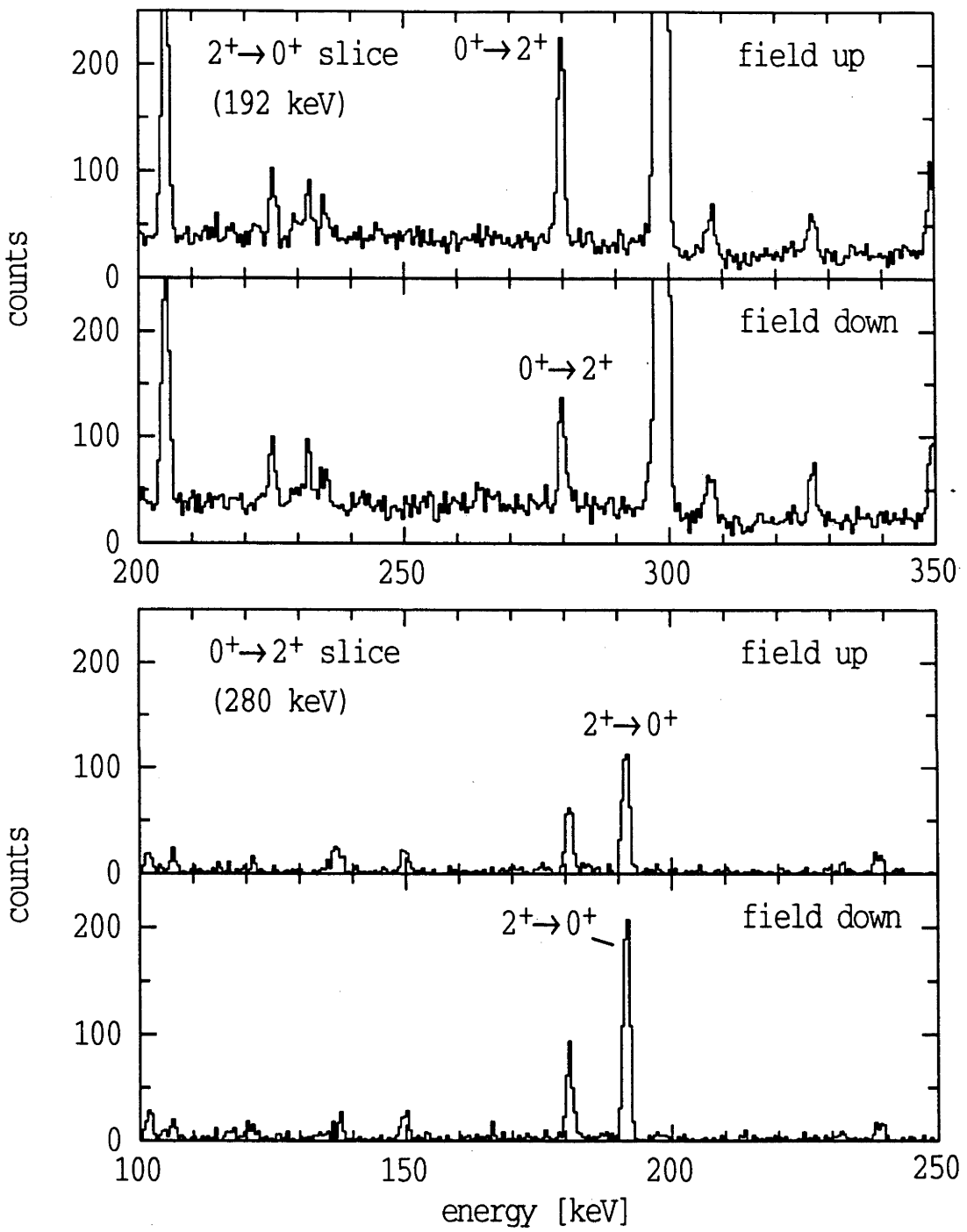

Figure 5.3: Data collected in the ^{186}Pt experiment at an angular separation of 34°. The upper frame shows part of the spectrum obtained by slicing on the $2_1^+ \rightarrow 0_1^+$ transition for both field directions and, similarly, for $0_2^+ \rightarrow 2_1^+$ in the lower frame. Apparent is the anisotropy of the $0_2^+ \rightarrow 2_1^+ \rightarrow 0_1^+$ angular correlation and the equivalence of reversing the gating and field directions, see text.

5.3.1 Detector efficiencies

For coincident transitions with γ-ray energies $E_{\gamma 1}$ and $E_{\gamma 2}$, the number of counts registered in a pair of detectors, labelled A and B, for each of these correlations can be written

$$N(+\theta,+B) = n_0^{up}\,\epsilon_A(E_{\gamma 1})\,\epsilon_B(E_{\gamma 2})\,W(+\theta,+B)$$

$$N(-\theta,+B) = n_0^{up}\,\epsilon_A(E_{\gamma 2})\,\epsilon_B(E_{\gamma 1})\,W(-\theta,+B)$$

$$N(+\theta,-B) = n_0^{down}\,\epsilon_A(E_{\gamma 1})\,\epsilon_B(E_{\gamma 2})\,W(+\theta,-B)$$

$$N(-\theta,-B) = n_0^{down}\,\epsilon_A(E_{\gamma 2})\,\epsilon_B(E_{\gamma 1})\,W(-\theta,-B) \quad , \tag{5.4}$$

where the ϵ values denote detector efficiencies, and n_0^{up} and n_0^{down} are the normalization factors for the amount of data collected in the two field directions. When data from several 'equivalent' pairs of detectors are combined, the product of efficiencies is replaced by the appropriate sum over products of efficiencies.

Efficiency calibrations of the HPGe detectors were made with the γ-ray singles spectra collected in each experiment. The peak areas for each transition of interest, as observed in each detector, were measured as described above. The relative detector efficiencies for these γ-ray energies were then extracted and used as fixed values in eqs. 5.4. These were also checked against efficiencies for each detector taken from ^{152}Eu source data.

5.4 Determining the Precession

An important consideration is the fraction of implanted nuclei that did not experience the full internal field for Pt in Fe, but a magnetic field of reduced strength. As noted above in sect. 4.3.4, this results in the measurement of a superposition of radiation patterns with different perturbations. For recoils implanted in a ferromagnetic medium this is caused by nuclei with final resting sites in non-substitutional sites of the host lattice and structural damage to the ferromagnet from the implantation process. With the implantation-decay technique, another

consideration is the displacement of nuclei by the recoil-energy produced by β^+-decay. Also, a small fraction of the ions stopped in the front, non-ferromagnetic layer of the target where the nuclei were not subject to the hyperfine field.

In sect. 4.3.4 it was determined that these effects are all relatively small. To account for them a 'two-site' model was used: the implanted nuclei were assumed to experience either no hyperfine field at all, so that the γ-radiation was emitted without perturbation, or the full field strength for Pt impurities in Fe. The first group specifically includes those nuclei in the target layer. This approach is generally considered adequate when only a small fraction of nuclei are at damaged areas or non-unique sites of a ferromagnet where they may experience a partial hyperfine field.

The analysis allowed for this by fitting the data to a sum of the perturbed and *un*perturbed integrated correlation functions (eqs. 3.14 and 3.19), weighted by the fraction of implanted nuclei at full-field and field-free sites, respectively. By specifying the fraction of implanted nuclei experiencing the full hyperfine field and the detector efficiencies, the only fit parameters are the precession angle, $\omega_L\tau$, and the normalization constants, n_0^{up} and n_0^{down}. A least-squares fit to the time-integrated function (eq. 3.19) was performed simultaneously for the four data sets of each γ-γ cascade. The twenty-five degrees of freedom originate from the twenty-eight ($= 4 \times 7$) data points and three unknowns. The code used can also include, in a simultaneous fit, data for several cascades through the intermediate state of interest. Alternatively, the weighted average may be taken of the results obtained in the separate examinations of the individual γ-ray cascades.

5.4.1 The ratio function

As an alternative approach to the analysis, the data for the four correlations may be combined in a ratio function ρ, thereby, eliminating the normalization factors and efficiencies:

$$\rho = \sqrt{\frac{N(+\theta,+B)\,N(-\theta,-B)}{N(+\theta,-B)\,N(-\theta,+B)}} = \frac{W(+\theta,+B)}{W(+\theta,-B)} \quad . \tag{5.5}$$

With the present arrangement, for a least-squares fit to a single cascade there are six degrees of freedom from the seven data points and single parameter, $\omega_L\tau$.

This measure of the perturbation is sensitive to the *rotation* of the correlation, but the *attenuation* effect is largely 'cancelled out' when taking the ratio. As a

consequence, for precessions larger than about 100 mrad, where the correlation is attenuated significantly and the rotation is more difficult to measure (see fig. 3.6), a fit to this function is much less precise than examining the whole correlation. As the longer 2_1^+-state lifetimes for the lighter Pt isotopes (see table 6.1 below) cause large perturbations, in the present work the ratio method has been used only as a check of the full angular correlation analyses.

5.5 Solid-angle Corrections

A correction is needed for attenuation of the anisotropy of the measured radiation pattern by the finite solid-angles subtended by the detectors. This is expressed through the solid-angle attenuation coefficients Q_{kk}, where eq. 3.5 becomes

$$W(\theta) = \sum_k Q_{kk}\, A_k(1)\, A_k(2)\, P_k(\cos\theta) \tag{5.6}$$

and, for an angular correlation, $Q_{kk} = Q_k(1)\, Q_k(2)$.

The calculations were made using the method described in ref. [Kr72]. The parameterization [Do88] of the total energy absorption cross-section for photons in germanium, was determined from the tabulated values of Storm and Israel [St70] and is sufficiently accurate for the present work. For the seven, very similar detectors of the CAESAR array (the details of which are given in sect. 4.2.1), the calculated coefficients were found to be equivalent: $Q_{22} = 0.965 \pm 0.010$ and $Q_{44} = 0.885 \pm 0.030$. The quoted errors more than cover the small dependence on γ-ray energy.

5.6 Other Spectroscopic Information

For sufficiently precise measurements of the nuclear precessions, it was necessary to collect considerable amounts of data in each experiment. These provided the opportunity to examine other aspects of the spectroscopy of the Pt nuclei. This was done primarily using the standard method of combining all the coincidence data for a measurement in a single γ-γ matrix. However, as the decay schemes for $^{184-192}$Pt following β^+-decay have been studied extensively [Fi89, Fi88, Si90a, Si90b, Sh91], this served mainly to confirm documented transition and level energies, and some transition multipolarities and state spin

assignments. The exception was identification of the 265.4 keV, $(3)^+ \rightarrow 4_1^+$ transition in ^{188}Pt, which is included in the results reported in sect. 6.3. The statistical precision of the present γ-γ coincidence measurement allowed us to resolve it from the large $2_1^+ \rightarrow 0_1^+$ peak at 265.6 keV.

Chapter 6

Results

6.1 ^{192}Pt Measurement

The first measurement using the implantation-decay technique was made on the naturally-occurring nuclide ^{192}Pt. This provided both a check of the experimental method and a calibration of the effective magnetic field strength, which was needed to extract g-factors from the measurements on the unstable Pt isotopes. The 2_1^+-state lifetime, $\tau(2_1^+)$, and g-factor, $g(2_1^+)$, are known from previous experiments (see table 6.1).

The full projection of the 'total' γ-γ matrix from the ^{192}Pt measurement, which includes the coincidence data collected in every detector pair and both field directions, is shown in fig. 6.1 for energies $E_\gamma \leq 900\,\mathrm{keV}$. The peaks in this spectrum labelled by their γ-ray energies correspond to transitions in the decay of ^{192}Pt, as shown in the simplified decay scheme for this nucleus following population by β^+-decay (fig. 6.2).

Because the nucleus ^{192}Tl was formed in the heavy-ion reaction, the γ-radiation emitted in the decay of the ^{192}Pt parent nuclei, ^{192}Hg and ^{192}Au, was observed. The γ-rays marked as 'contaminant' were from reactions of the heavy-ion beam with the ferromagnet. As expected for the implantation-decay technique this radiation was not overwhelming (sect. 4.1). Another feature of this spectrum, which is also apparent in the spectra recorded in the other experiments, is the peak at 511 keV from β^+-annihilation.

Figure 6.3 shows background-subtracted coincidence spectra (sect. 5.2) for data collected with the internal field *up* and an effective detector separation of $+14°$. The slices correspond to the $2_1^+ \rightarrow 0_1^+$, $2_2^+ \rightarrow 2_1^+$ and $0_2^+ \rightarrow 2_1^+$ transitions

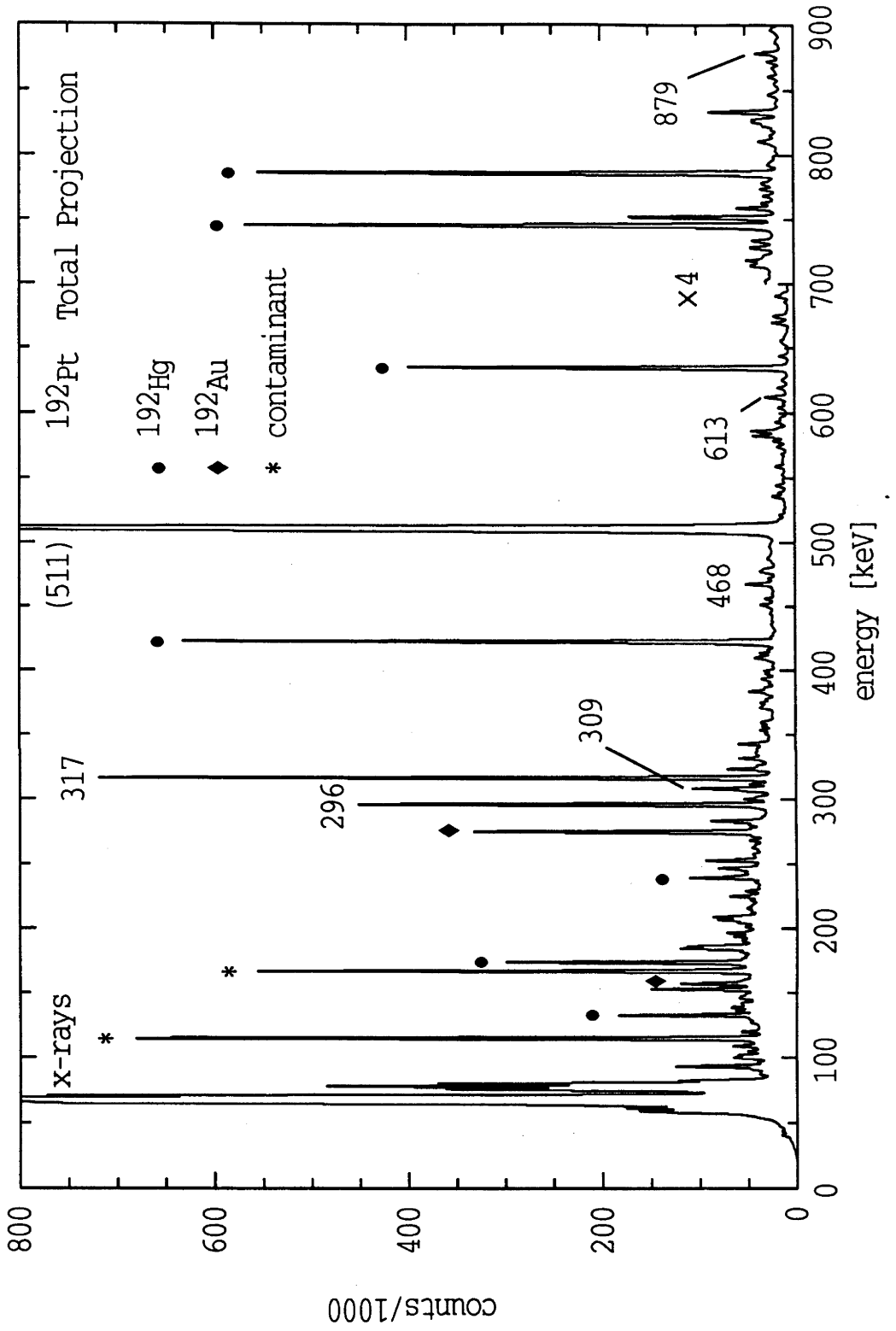

Figure 6.1: The total projection (see text) recorded in the ^{192}Pt measurement. The labelling of the peaks of interest is described in the text.

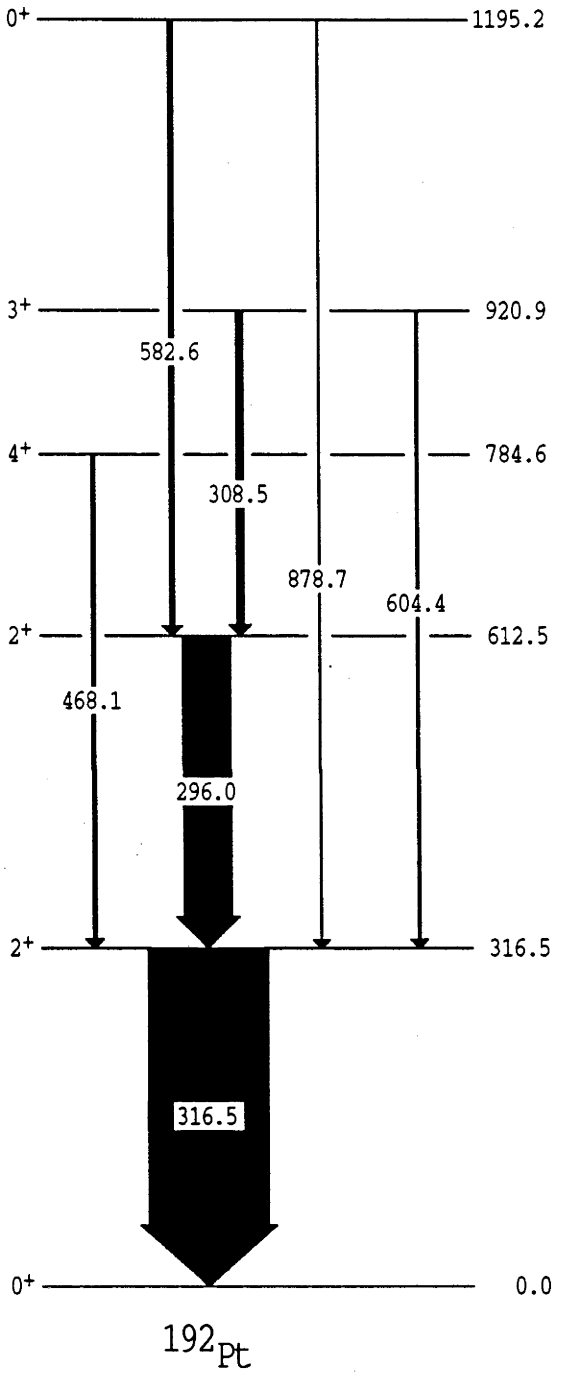

Figure 6.2: Partial level scheme at low excitation energies for ^{192}Pt, following the β^+-decay of ^{192}Au.

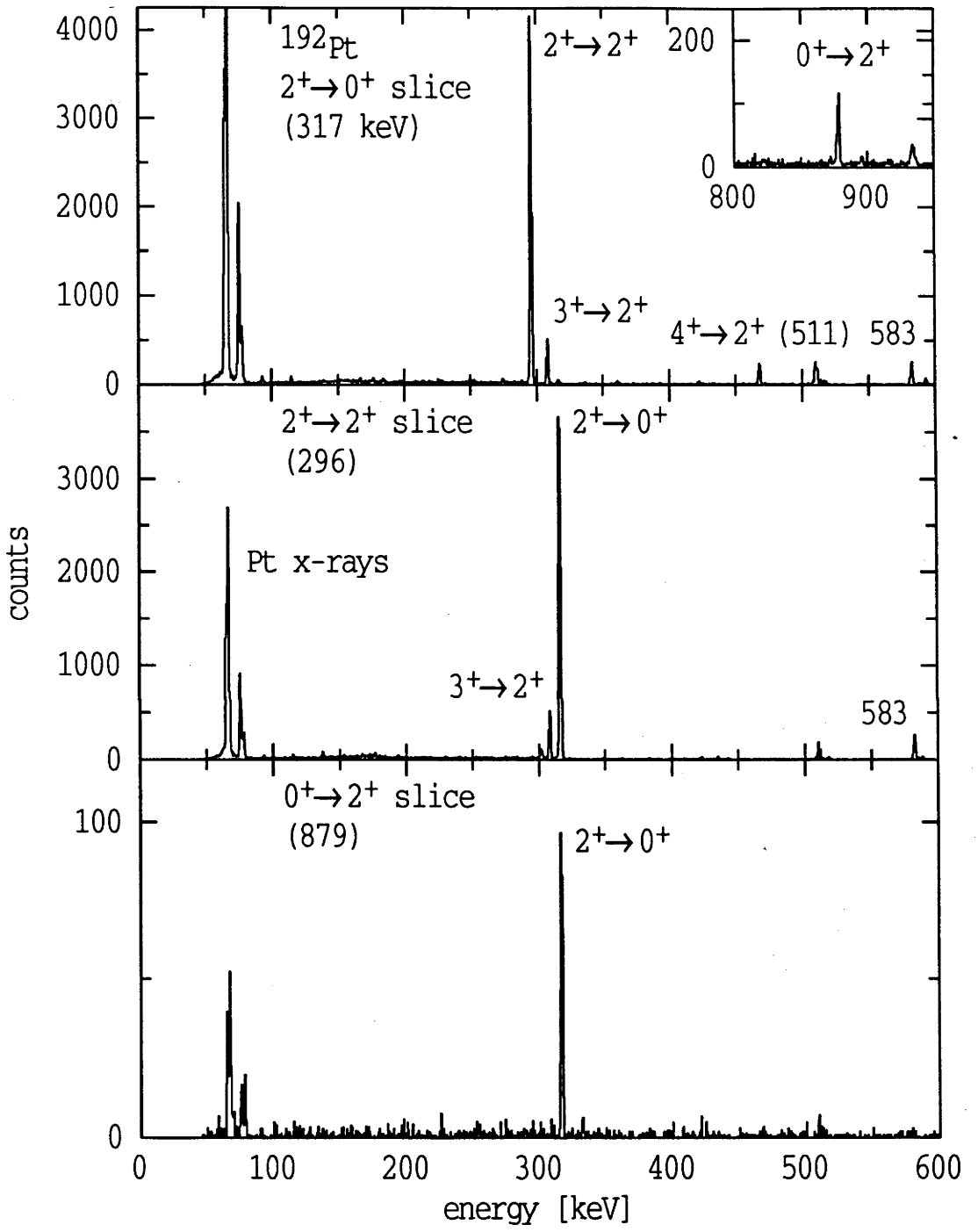

Figure 6.3: The spectra measured in coincidence with the $2_1^+ \rightarrow 0_1^+$, $2_2^+ \rightarrow 2_1^+$ and $0_2^+ \rightarrow 2_1^+$ γ-ray transitions in the decay of ^{192}Pt with the magnetic field up and forward gating. The angular separation of the γ-ray detectors is 14°.

in ^{192}Pt. The major γ-rays in the decay of ^{192}Pt are marked, including the 582.6 keV transition between the 0_2^+ and 2_2^+ states. The low background levels in these spectra are as expected for γ-γ coincidence measurements made out-of-beam (sect. 4.1) and are typical of each experiment in the series (figs. 6.9, 6.12, 6.18 and 6.25).

The four independent measures of the perturbed angular correlation (sect. 5.3) for the $0_2^+ \rightarrow 2_1^+ \rightarrow 0_1^+$ γ-ray cascade in ^{192}Pt are displayed in fig. 6.4. Also shown are the distributions from a simultaneous least-squares fit of the experimental data to a two-site model, as described in sect. 5.4. With 8% of the implanted nuclei at field-free sites, a result to be discussed in detail in sect. 6.1.1, this analysis gave $\omega_L\tau(2_1^+) = +104 \pm 12$ mrad.

The data were also analyzed with the ratio function ρ (of eq. 5.5). This gave a precession angle of $\omega_L\tau(2_1^+) = +98 \pm 16$ mrad, again for 8% of the nuclei not experiencing the hyperfine field. This result is displayed in fig. 6.5 with the experimental data points.

Figure 6.6 shows the chi-squared per degree of freedom, χ^2/ν, as a function of precession angle for the least-squares fits described above. The results obtained from the two analysis methods are clearly in agreement. The more precise measurement of the precession is made with the 'angular correlation' analysis, even though the 'well' at the chi-squared minimum appears shallower than that from the 'ratio function' method. This is because there are twenty-five degrees of freedom in the angular correlation analysis compared with six when taking the ratio (sect. 5.4).

The measured radiation patterns for the $2_2^+ \rightarrow 2_1^+ \rightarrow 0_1^+$ cascade are displayed in fig. 6.7. For concise presentation of the data, in this and all following diagrams, only *two* measures of the perturbed angular correlation are shown. These are labelled as the two field directions: where the weighted averages of the corresponding points in the 'field up/forward gating' and 'field down/reverse gating' directions form field *up*; and the 'down/forward' and 'up/reverse' data sets were combined for field *down*.

The $2_2^+ \rightarrow 2_1^+$ transition has mixed $E2/M1$ multipolarity with a (previously measured) mixing ratio of $\delta(E2/M1) = +10.0 \pm 0.4$ [Sh91]. This value was used in the present analysis, of the four separate data sets, and the best-fit to the integral correlation function with 8% of the recoils at field-free sites, $\omega_L\tau(2_1^+) = +113 \pm 9$ mrad, is also shown in fig. 6.7. The value $\delta(E2/M1) = +9^{+3}_{-2}$ was

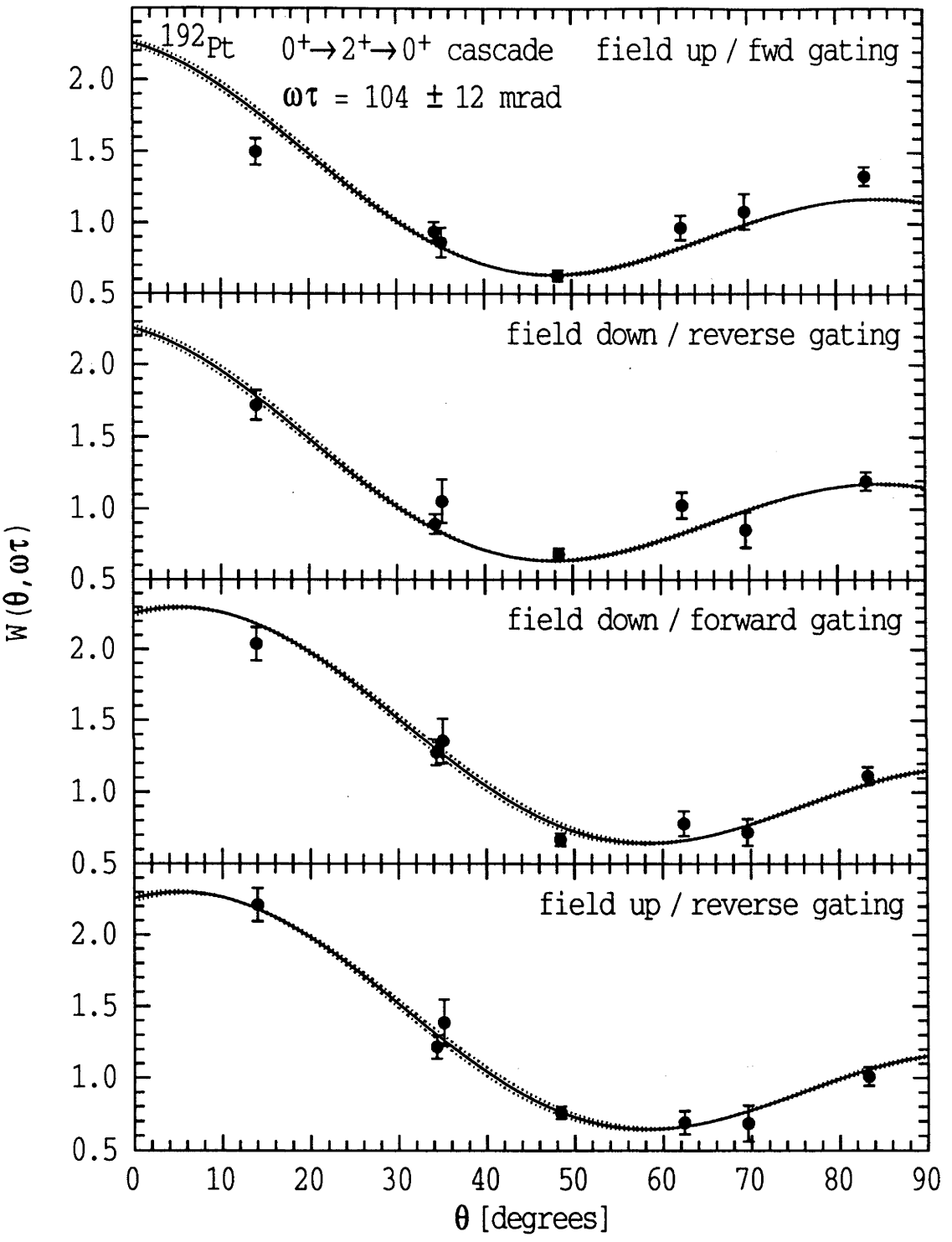

Figure 6.4: The γ-γ perturbed angular correlations for the $0_2^+ \rightarrow 2_1^+ \rightarrow 0_1^+$ cascade in ^{192}Pt. The four measured distributions (from the different combinations of field and gating directions) are shown with calculations for a precession angle of $\omega_L \tau(2_1^+) = +104 \pm 12$ mrad and 8% of the recoils at field-free sites (see text).

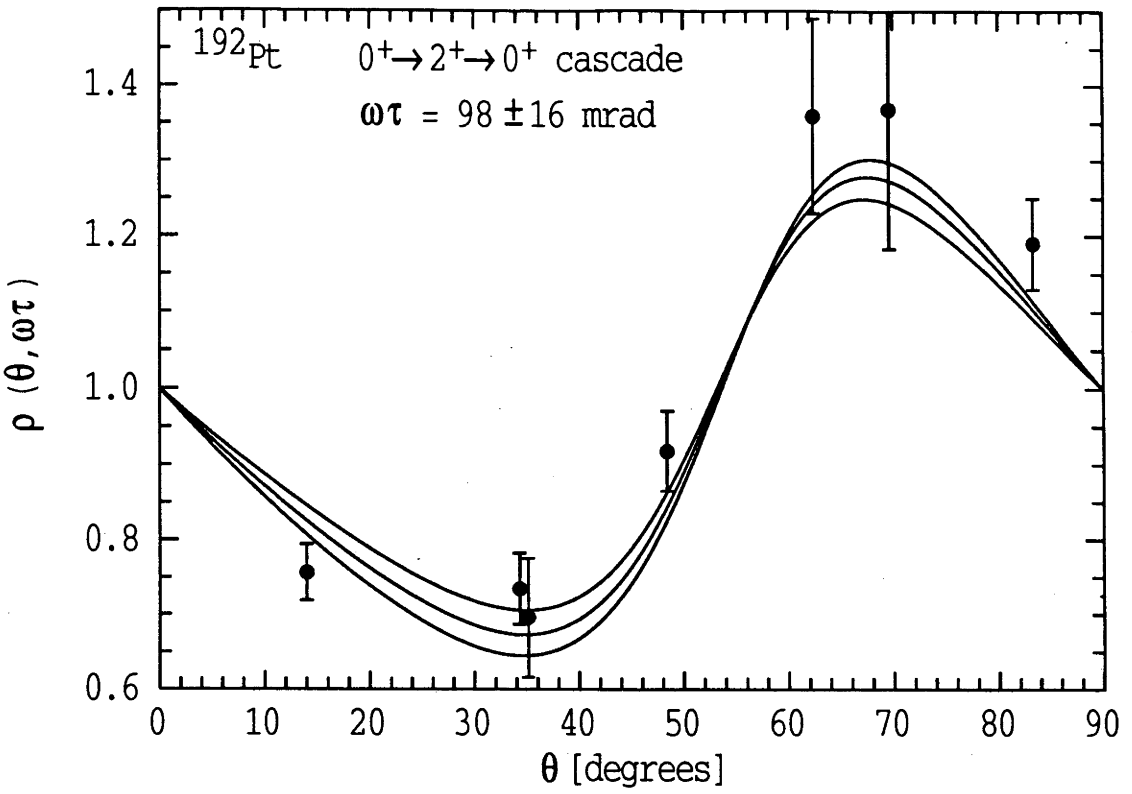

Figure 6.5: The measured (data points) ratio ρ for the ^{192}Pt $0_2^+ \rightarrow 2_1^+ \rightarrow 0_1^+$ γ-ray cascade. Also shown are the calculated values (lines) for the best-fit of $\omega_L\tau(2_1^+) = +98 \pm 16$ mrad (see text).

determined here by fixing the precession to 100 mrad and varying the mixing ratio. This is consistent with, although much less precise than, the value quoted above.

A much larger fraction of the β^+-decay passes through the $2_2^+ \rightarrow 2_1^+$ transition (and the corresponding $2_2^+ \rightarrow 2_1^+ \rightarrow 0_1^+$ γ-γ cascade) than the $0_2^+ \rightarrow 2_1^+$ transition. This is displayed in the decay scheme of fig. 6.2 and is also apparent in the intensities of the corresponding peaks in the spectra of figs. 6.1 and 6.3. The smaller error associated with each data point of the measured radiation pattern results in a more precise measurement of the perturbed $2^+ \rightarrow 2^+ \rightarrow 0^+$ angular correlation. However, as the anisotropy here is much less than that for the $0^+ \rightarrow 2^+ \rightarrow 0^+$ angular correlation (which is apparent from the vertical scales of figs. 6.4 and 6.7), the precessions, $\omega_L\tau(2_1^+)$, measured using the two cascades have similar precision.

Analyses were also performed on other less prominent γ-ray cascades in the nucleus. Although the results are generally very imprecise, for transitions feeding

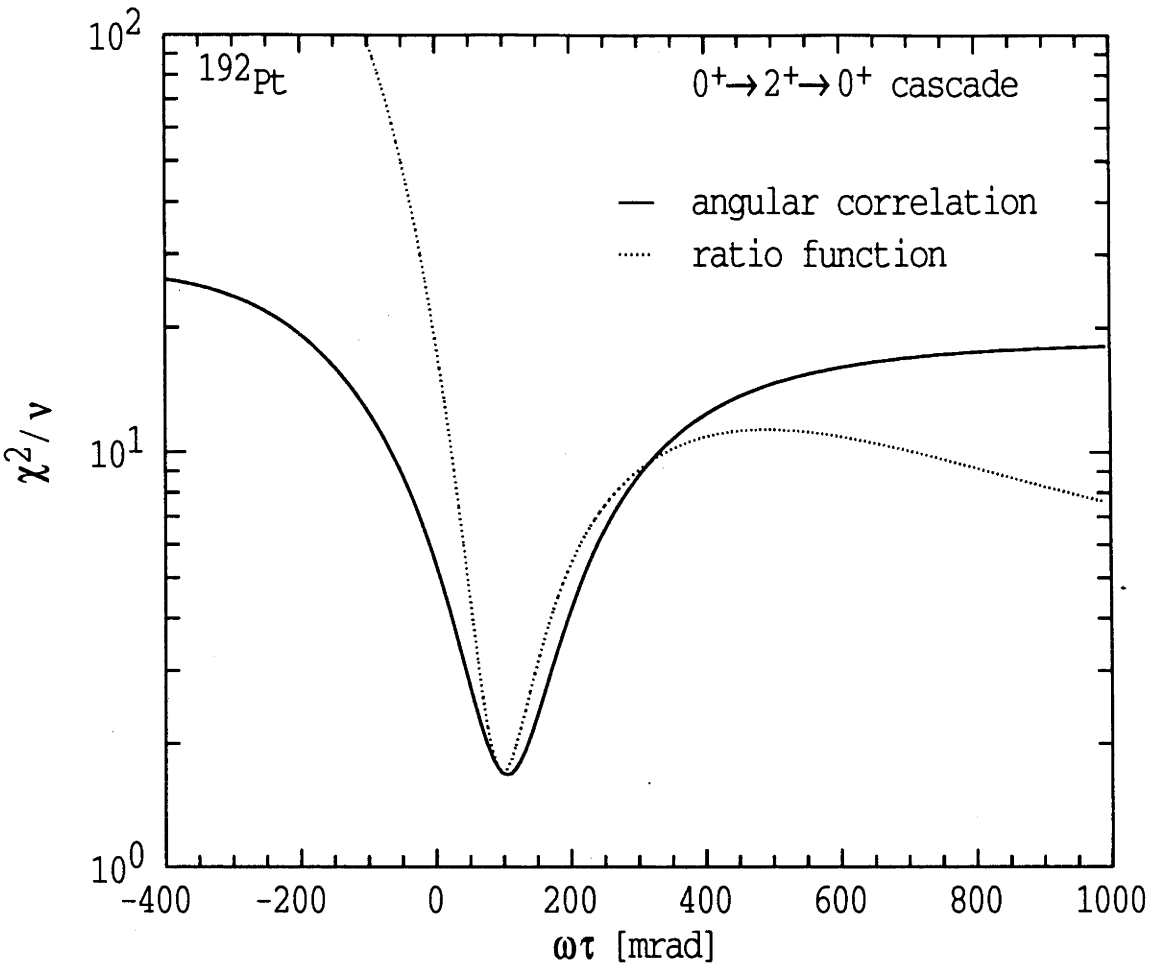

Figure 6.6: Plot of the chi-squared per degree of freedom versus the nuclear precession, for best-fits of the ^{192}Pt $0_2^+ \rightarrow 2_1^+ \rightarrow 0_1^+$ data to the full angular correlation and the ratio function.

the 2_1^+ state they were found to be consistent with those of analyses using the $0_2^+ \rightarrow 2_1^+$ and $2_2^+ \rightarrow 2_1^+$ transitions. The measured data points and the best-fit of $\omega_L\tau(2_1^+) = +120 \pm 30$ mrad for the reasonably well populated $3_1^+ \rightarrow 2_1^+ \rightarrow 0_1^+$ cascade, where the first transition is mixed with $\delta(E2/M1) = -1.48 \pm 0.02$ [Sh91], are displayed in fig. 6.8.

The six-day measurement on ^{192}Pt provided determination of the nuclear precession to $\lesssim 7\%$ precision, from the weighted average of the results obtained with the $0_2^+ \rightarrow 2_1^+ \rightarrow 0_1^+$ and $2_2^+ \rightarrow 2_1^+ \rightarrow 0_1^+$ cascades (see table 6.1). This confirmed the feasibility of the implantation-decay technique.

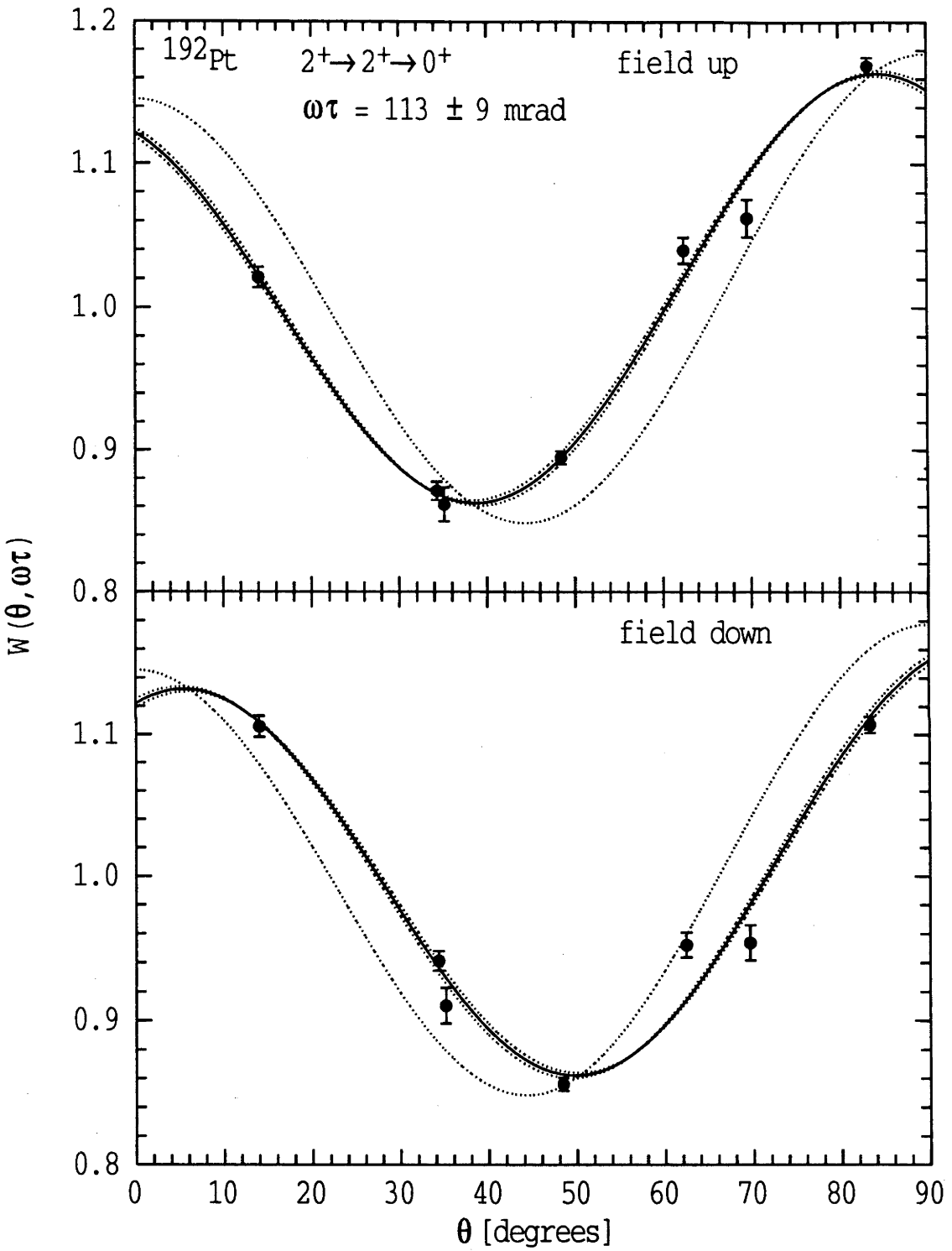

Figure 6.7: The measured and calculated perturbed angular correlations for the $2_2^+ \rightarrow 2_1^+ \rightarrow 0_1^+$ γ-ray cascade in ^{192}Pt. For clarity, the four measures have been combined into two (see text). The unperturbed correlation ($\omega_L \tau = 0$) is also shown.

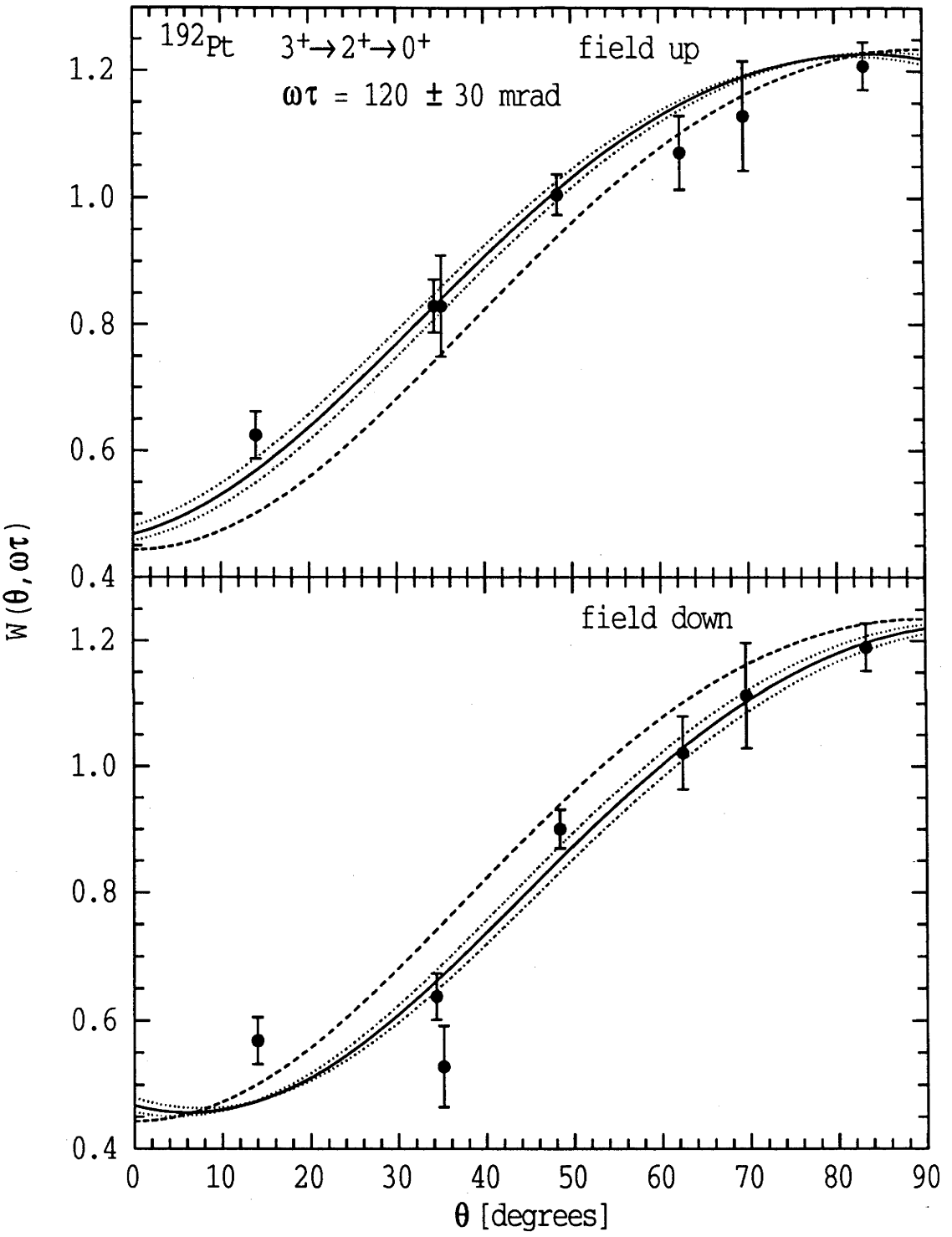

Figure 6.8: The measured (data points) and calculated (lines) perturbed angular correlations for the ^{192}Pt $3_1^+ \rightarrow 2_1^+ \rightarrow 0_1^+$ γ-ray cascade. The dashed line shows the unperturbed correlation.

6.1.1 Determining the fraction of recoils at field-free sites

If all of the implanted ^{192}Pt nuclei were on unique lattice sites and experienced the full hyperfine field strength for Pt in Fe, of $B_{st}^{300K}(\text{Pt}\underline{\text{Fe}}) = -123 \pm 3$ Tesla (sect. A.5.2), the expected precession in the first-excited state would be $\omega_L\tau(2_1^+) = +110 \pm 6$ mrad. This comes from eq. 3.3 with the known 2_1^+-state g-factor and lifetime: $g(2_1^+,^{192}\text{Pt}) = 0.299 \pm 0.010$ (sect. 7.3.2.1) and $\tau(2_1^+,^{192}\text{Pt}) = 62.1 \pm 2.0$ ps [Ra87]. In analyzing the ^{192}Pt data a two-site model (sect. 5.4) was used and the fraction of recoils at field-free sites varied to find agreement with this expected precession angle. It was found that $92 \pm 8\%$ of the nuclei experienced the full field, which corresponds to an effective internal field strength of -113 ± 10 Tesla. This result is consistent with the discussion of sect. 4.3.4. There is agreement with: the implantation studies reported in appendix A, where $\lesssim 10\%$ of the nuclei were implanted into field-free sites; the $\lesssim 3\%$ reduction from β^+-decay induced site changes; and Monte-Carlo calculations of reaction kinematics, which found $\sim 3\%$ of the recoiling ions came to rest in the front, non-ferromagnetic layer of the target.

The heavy ions, beam energies, targets and reactions used in the present implantation-decay experiments on ^{184,186,188,190,192}Pt are listed in table 4.3. The resulting reaction kinematics are similar and, in each experiment, the average kinetic energy of the parent nuclei as they entered the Fe foil was approximately 10 MeV. In view of the likeness of these nuclei and their recoil energies, similar final implantation sites can be expected for each experiment. As the β^+-decays employed in the measurements were alike, one expects essentially equivalent effects from β-induced recoils in each case. Also, the fraction of ions which stopped in the non-ferromagnetic target layer only varied from $\sim 3\%$ to $\lesssim 2\%$ (sect. 4.3.4). This small difference is even less significant when the magnitude of the effect is compared with the much larger $\sim 10\%$ reduction inherent in the implantation process. Due to their similarities with the ^{192}Pt measurement, the data from each experiment were analyzed with the two-site model and assuming 8% of the implants were at field-free sites.

While we are confident of the effective field strength of -113 ± 10 T, there are, in addition, precise *absolute* limits available. The upper limit is the full hyperfine field of -123 ± 3 T, which is consistent with the adopted value, and the lower limit is the in-beam (Coulomb excitation) field strength of -92 ± 5 T (sect. A.6). The

implications of these limits for the inferred g-factors are discussed in sect. 6.6.

6.2 ^{190}Pt Measurement

The total projection recorded in the ^{190}Pt measurement and coincidence spectra for +34° field-up data are given in figs. 6.9 and 6.10, respectively. The marked lines may be compared with the ^{190}Pt decay scheme of fig. 6.11.

It is apparent from the peak heights in the spectra that significantly less data were collected here than in the other measurements. This experiment was abandoned after one and a half days, compared with running times of around five days for the other experiments (table 4.3), as the count rate was too slow for the measurement to be completed in a reasonable time with the ^{25}Mg + ^{170}Er reaction. Unfortunately, this was the only beam/target combination available at the time. Although ^{176}Yb(^{19}F, 5n)^{190}Au ($E \simeq 93$ MeV) may have proven better,

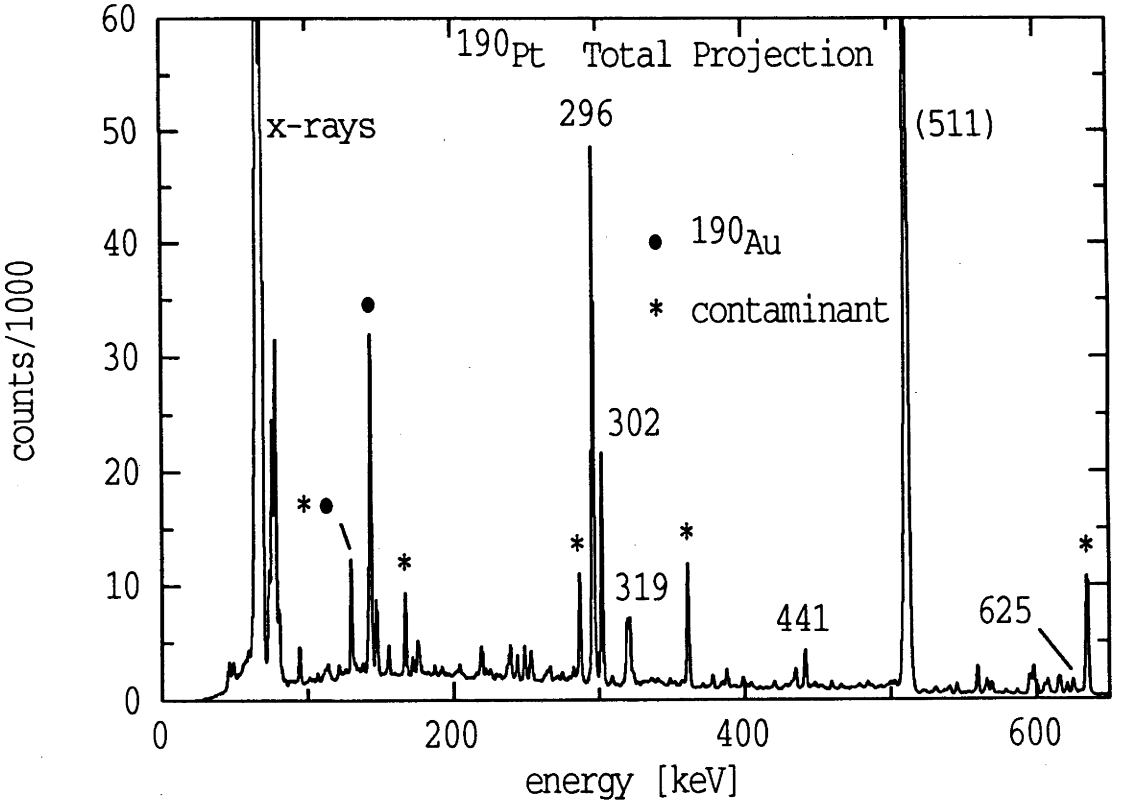

Figure 6.9: The total coincidence spectrum from the ^{190}Pt measurement. The γ-rays emitted in the decay of ^{190}Pt (as shown in the level scheme of fig. 6.11) are marked here with their energies.

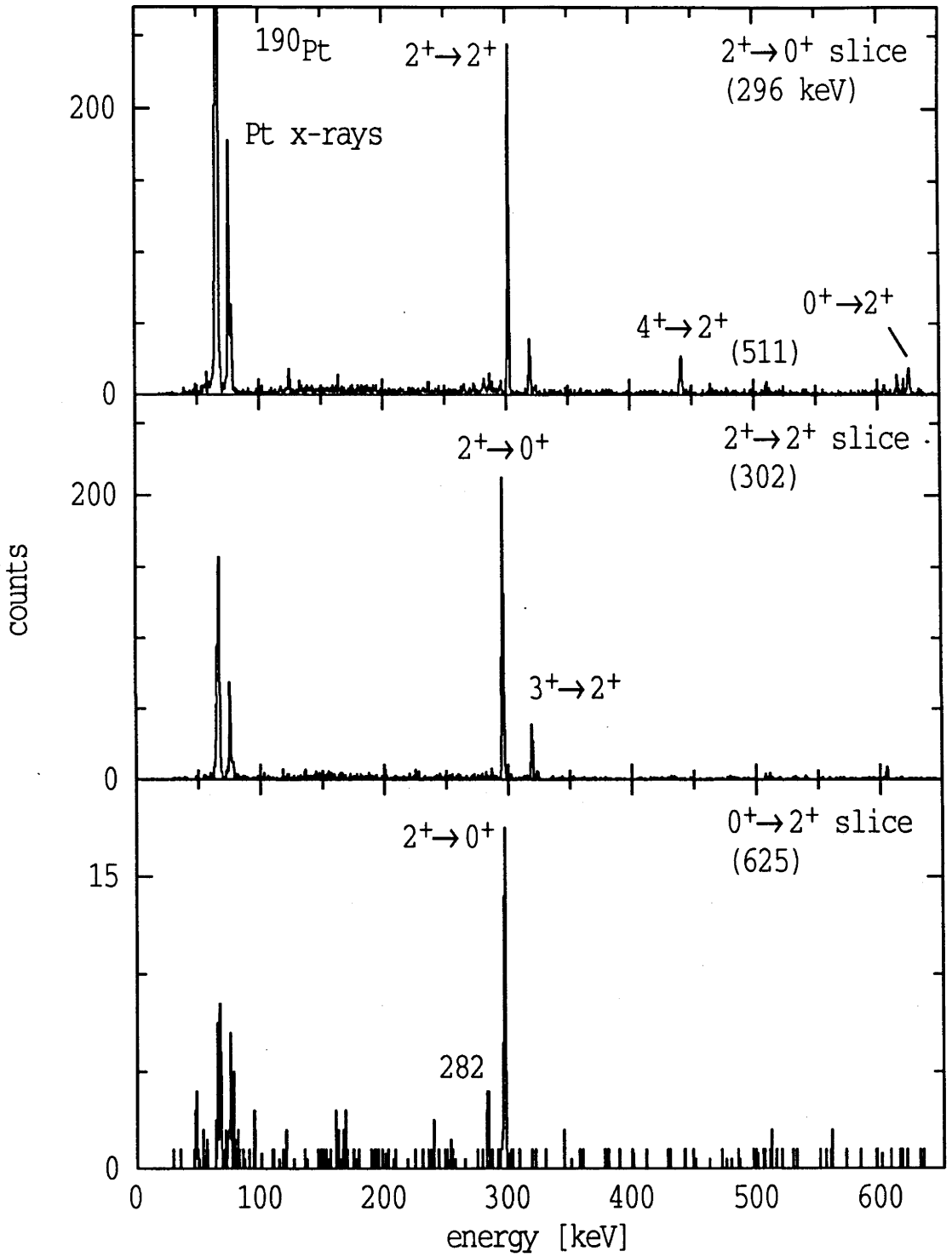

Figure 6.10: The coincidence spectra for the $2_1^+ \rightarrow 0_1^+$, $2_2^+ \rightarrow 2_1^+$ and $0_2^+ \rightarrow 2_1^+$ transitions in ^{190}Pt at $+34°$ with the internal field up.

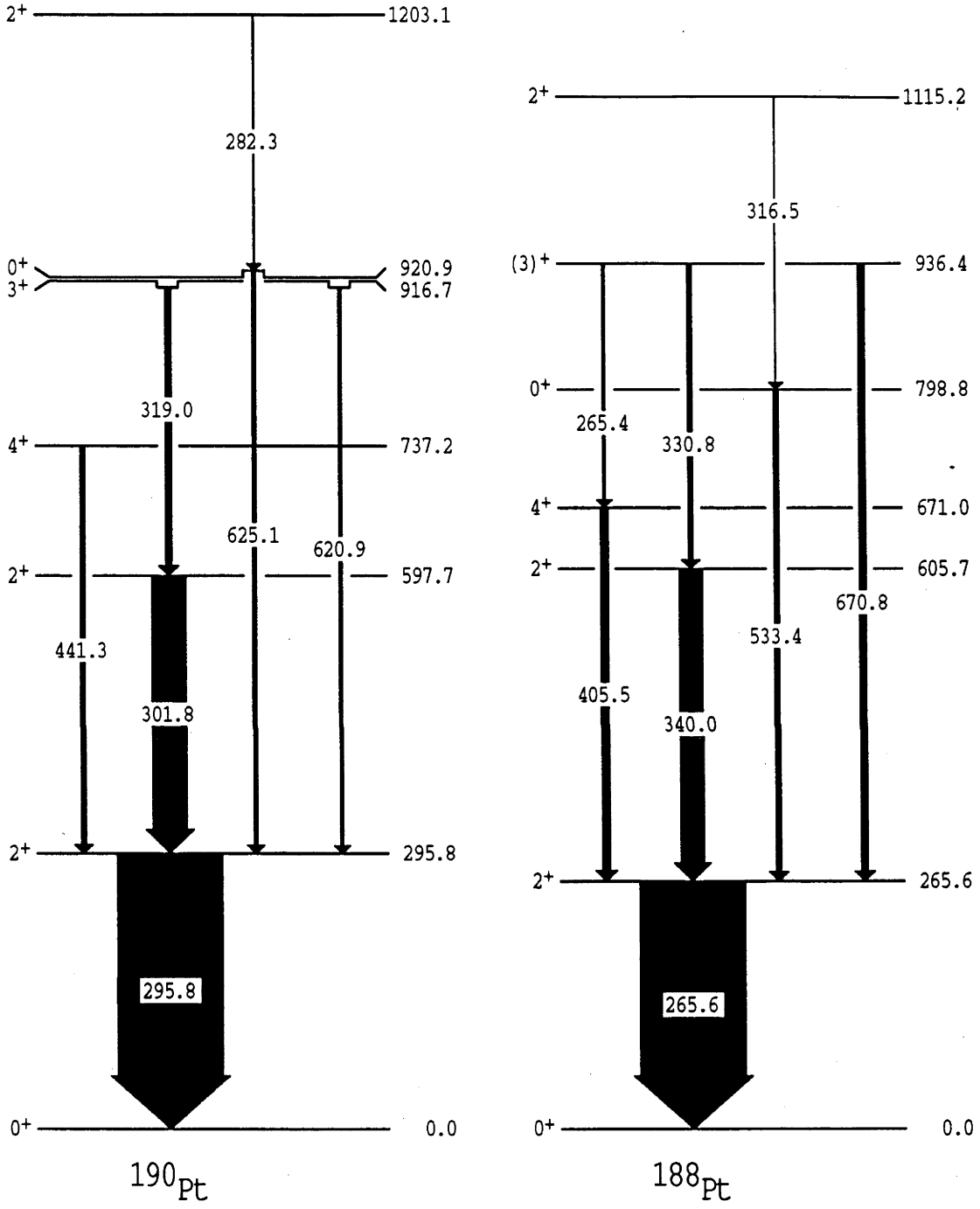

Figure 6.11: Partial decay schemes for ^{190}Pt and ^{188}Pt following the β^+-decay of their respective Au parent nuclei.

when isotopically enriched ^{190}Pt became available, a separate measurement of $g(2_1^+)$ in ^{190}Pt using the transient-field technique (sect. 3.5.2) was performed. This is described in chapter 7.

6.3 ^{188}Pt Measurement

The total projection of all coincidence data collected in the ^{188}Pt measurement is shown in fig. 6.12 for energies $E_\gamma \leq 600\,\text{keV}$. The major transitions in the decay of ^{188}Pt, as shown in the ^{188}Pt decay scheme included in fig. 6.11, are labelled with their γ-ray energies. Also marked in the spectrum is the γ-radiation emitted in the decay of the parent nucleus ^{188}Hg, and that from reactions of the ion beam with the Fe foil. In the bombardment of ^{169}Tm by ^{24}Mg at 128 MeV, ^{186}Au was populated directly in the ^{169}Tm(^{24}Mg, 2p5n) reaction channel with a cross-section approximately an order of magnitude smaller than that for ^{188}Tl. The γ-rays from the subsequent β^+-decay to ^{186}Pt were also observed (with low intensity).

The spectra measured in coincidence with the $2_1^+ \rightarrow 0_1^+$, $2_2^+ \rightarrow 2_1^+$ and $0_2^+ \rightarrow 2_1^+$

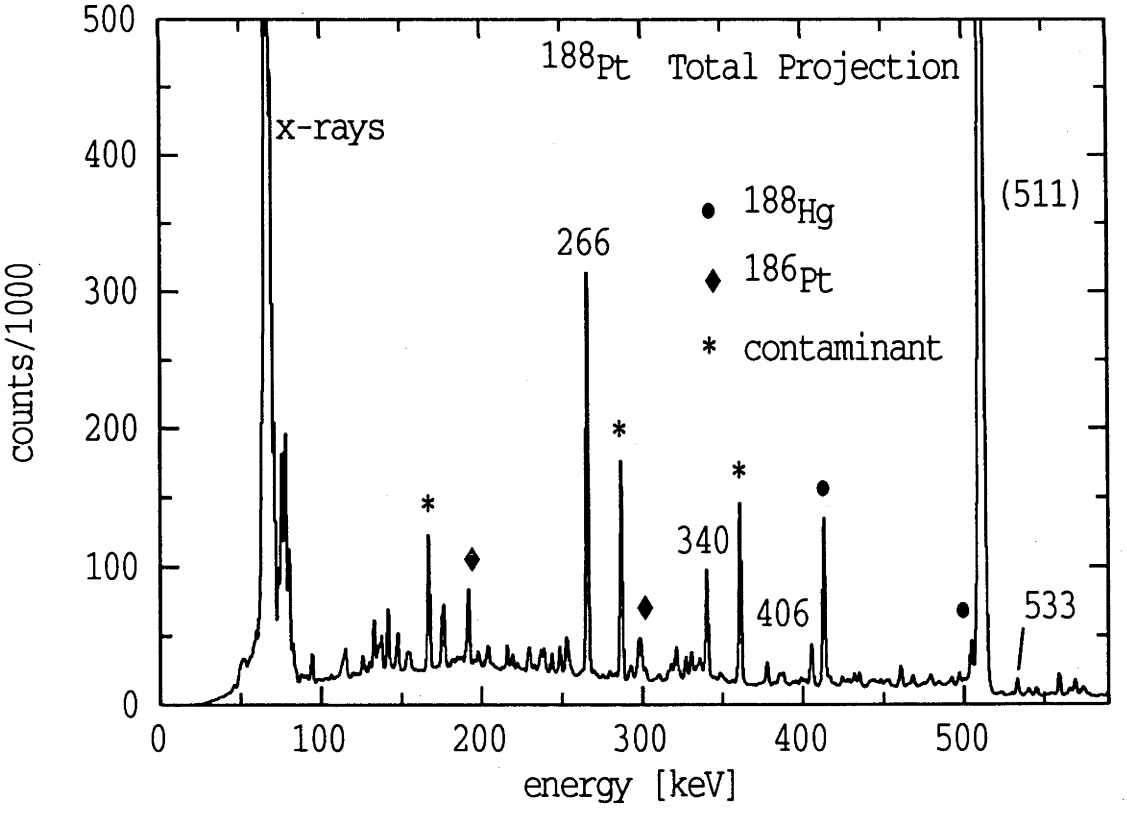

Figure 6.12: The total coincidence spectrum for the ^{188}Pt measurement.

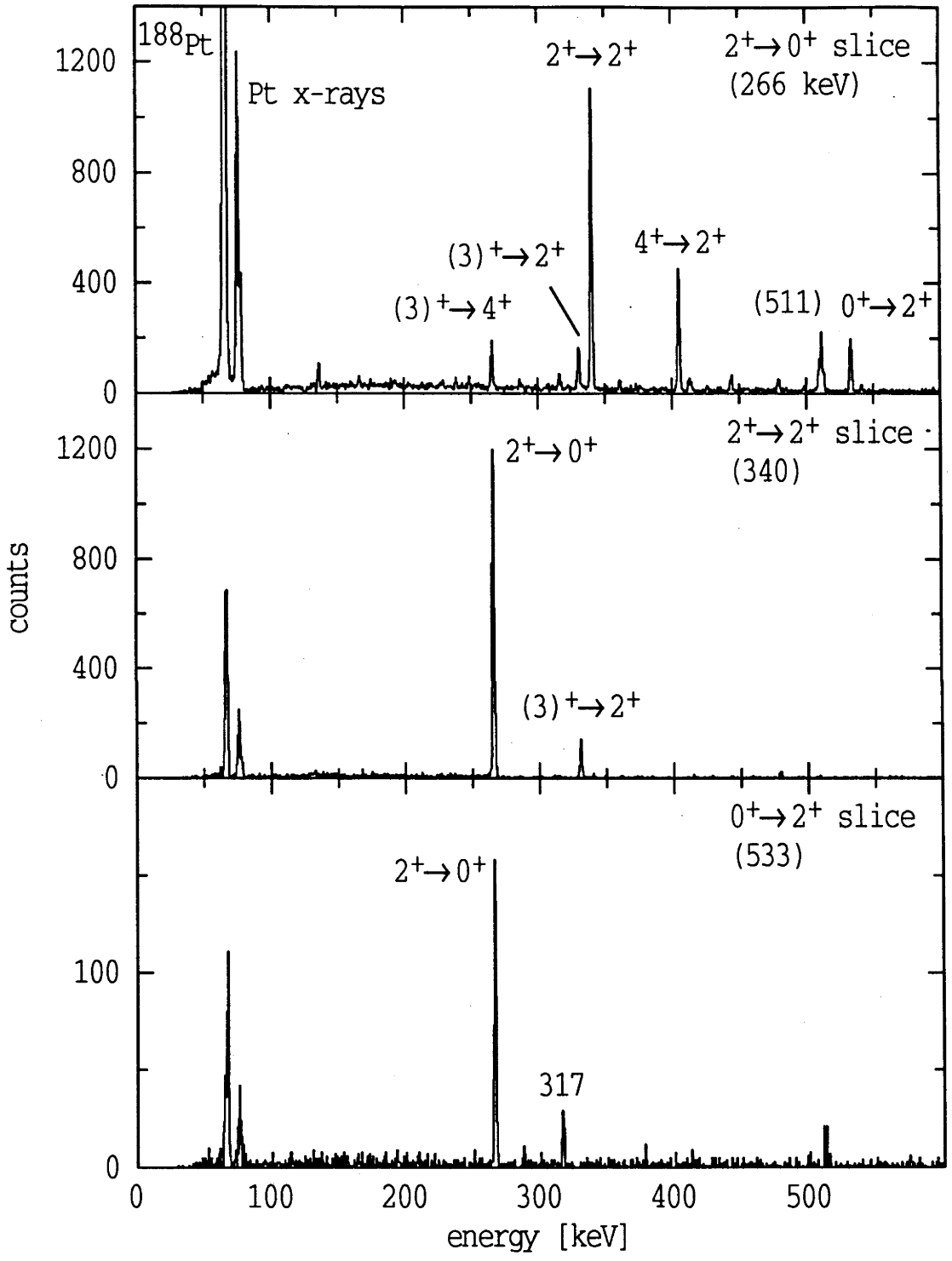

Figure 6.13: Spectra measured in coincidence with the ^{188}Pt $2_1^+ \rightarrow 0_1^+$, $2_2^+ \rightarrow 2_1^+$ and $0_2^+ \rightarrow 2_1^+$ transitions at +48° with the field up.

transitions for field-up data collected at +48° are given in fig. 6.13. Included in the labelling is the 316.5 keV, $2_3^+ \rightarrow 0_2^+$ transition. Clearly visible in the $2_1^+ \rightarrow 0_1^+$ slice is the 265.4 keV γ-ray feeding the 4_1^+ state from the $(3)^+$ level at 936.4 keV, which, as noted in sect. 5.6, was previously unidentified.

The measured perturbed angular correlations for the $0_2^+ \rightarrow 2_1^+ \rightarrow 0_1^+$, $2_2^+ \rightarrow 2_1^+ \rightarrow 0_1^+$ and $3_1^+ \rightarrow 2_1^+ \rightarrow 0_1^+$ γ-ray cascades are shown in figs. 6.14, 6.15 and 6.16, respectively. The calculations included in the diagrams are for precessions of $\omega_L\tau(2_1^+) = +155 \pm 11$ mrad, $+189 \pm 22$ mrad and $+123 \pm 42$ mrad, respectively, as determined using the two-site model with 92% of the nuclei experiencing the full field strength (sect. 6.1.1). The uncertainty in the $2_2^+ \rightarrow 2_1^+ \rightarrow 0_1^+$ result includes a contribution from the error in the mixing ratio for the $2_2^+ \rightarrow 2_1^+$ transition, determined as $\delta(E2/M1) = +6 \pm 2$. The $3_1^+ \rightarrow 2_1^+$ transition is primarily $E2$ and, as the inferred precession angle was found to be insensitive to the inclusion of small $M1$ admixtures, the fit shown in fig. 6.16 assumes a pure $E2$ multipolarity γ-ray.

6.4 ^{186}Pt Measurement

The partial level scheme for ^{186}Pt following population by β^+-decay from ^{186}Au is included in fig. 6.17. The total coincidence spectrum for the precession measurement is displayed in fig. 6.18. As the β^+-decay lifetime of the unstable ^{186}Pt nucleus is only 2 hours, γ-rays from the decay of the daughter ^{186}Os nucleus were also observed.

The coincidence spectra of fig. 6.19, for the $2_1^+ \rightarrow 0_1^+$, $4_1^+ \rightarrow 2_1^+$ and $0_2^+ \rightarrow 2_1^+$ transitions in ^{186}Pt, were measured at an effective detector separation of $-83°$ (where the minus sign refers to the reverse gating direction) with the internal field down. An excited $(4)^-$ level at 1.383 MeV (not shown in fig. 6.17) is relatively strongly populated in the β^+-decay of ^{186}Au, and the 205.0 keV and 430.3 keV, mixed $E2/M1$ multipolarity transitions de-exciting this state are visible in these spectra.

The overlap of the peaks corresponding to the $4_1^+ \rightarrow 2_1^+$ transition and the 297 keV γ-ray in ^{186}Os is apparent in the total projection. This caused the appearance of Os x-rays and γ-radiation from the ^{186}Os nucleus in the 299 keV slice. Also, as there was some contamination around 280 keV in the total projection, the $0_2^+ \rightarrow 2_1^+$ peak was not fully resolved. This resulted in the low-energy (< 200 keV)

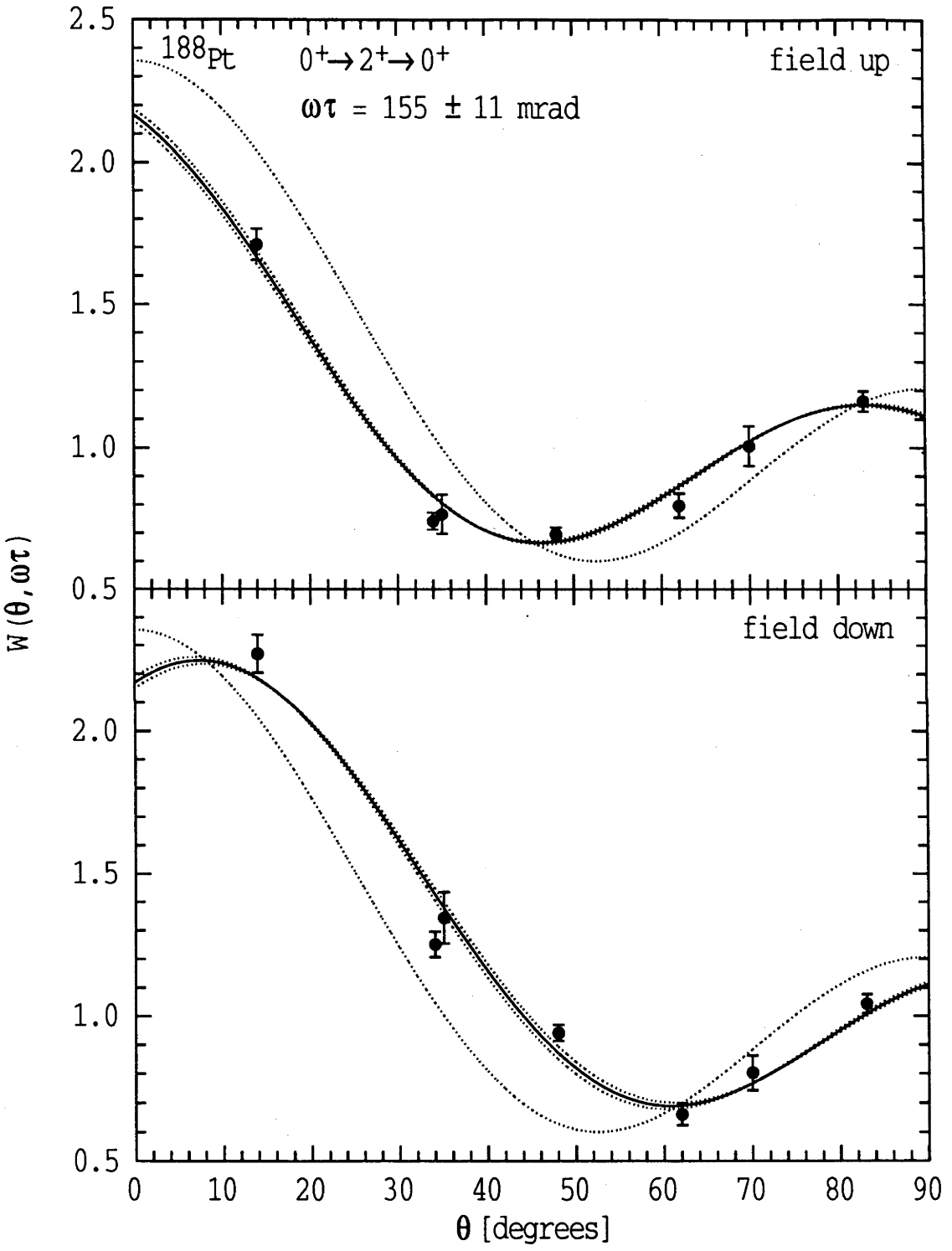

Figure 6.14: The measured radiation distributions for the $0_2^+ \rightarrow 2_1^+ \rightarrow 0_1^+$ γ-ray cascade in ^{188}Pt. The calculated correlations are for the best-fit value of $\omega_L\tau(2_1^+) = +155 \pm 11$ mrad (with 92% of the implants subject to the full field) and $\omega_L\tau = 0$.

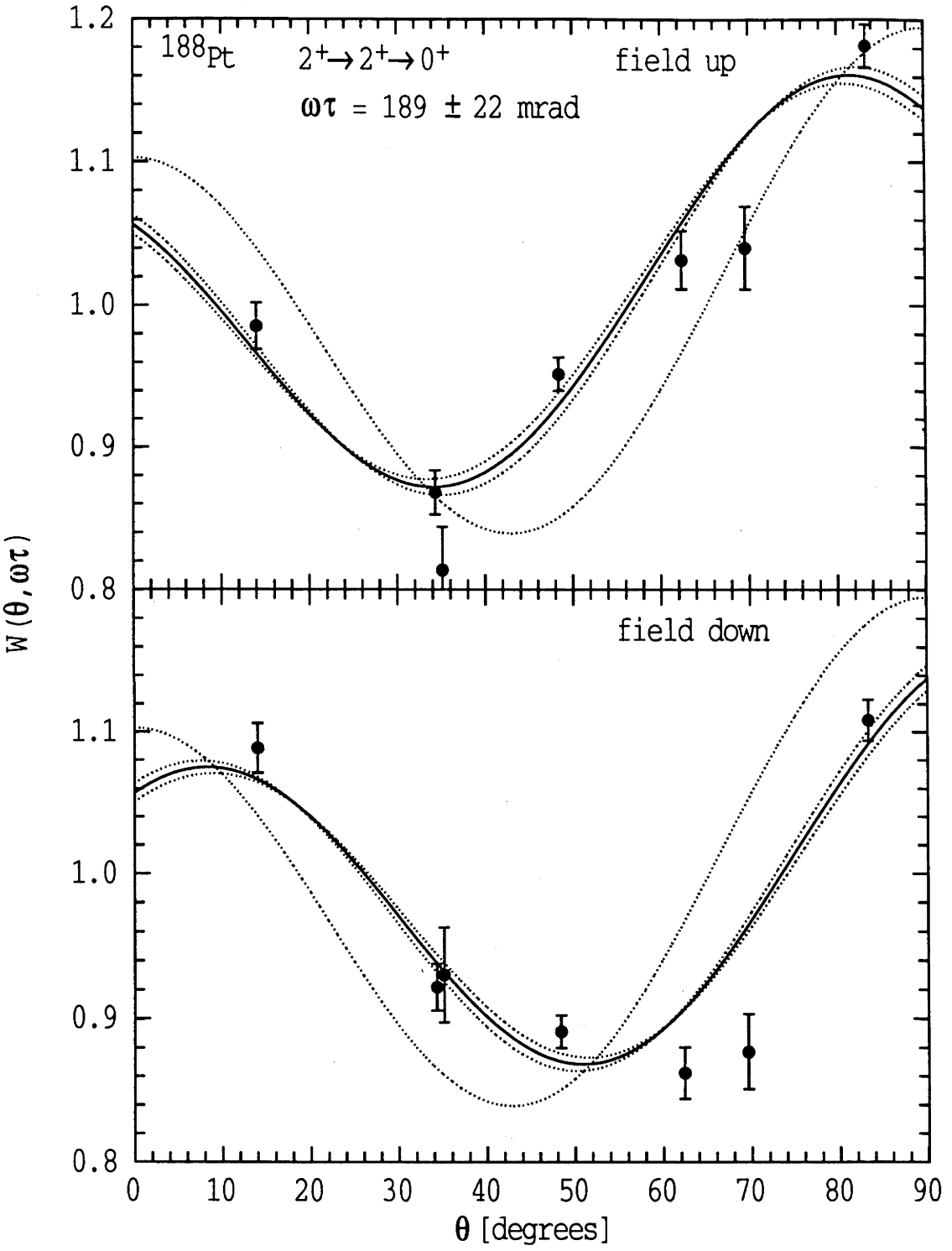

Figure 6.15: The perturbed angular correlations for the ^{188}Pt $2_2^+ \rightarrow 2_1^+ \rightarrow 0_1^+$ cascade, where the first γ-ray has mixing ratio $\delta(E2/M1) = +6 \pm 2$ (see text).

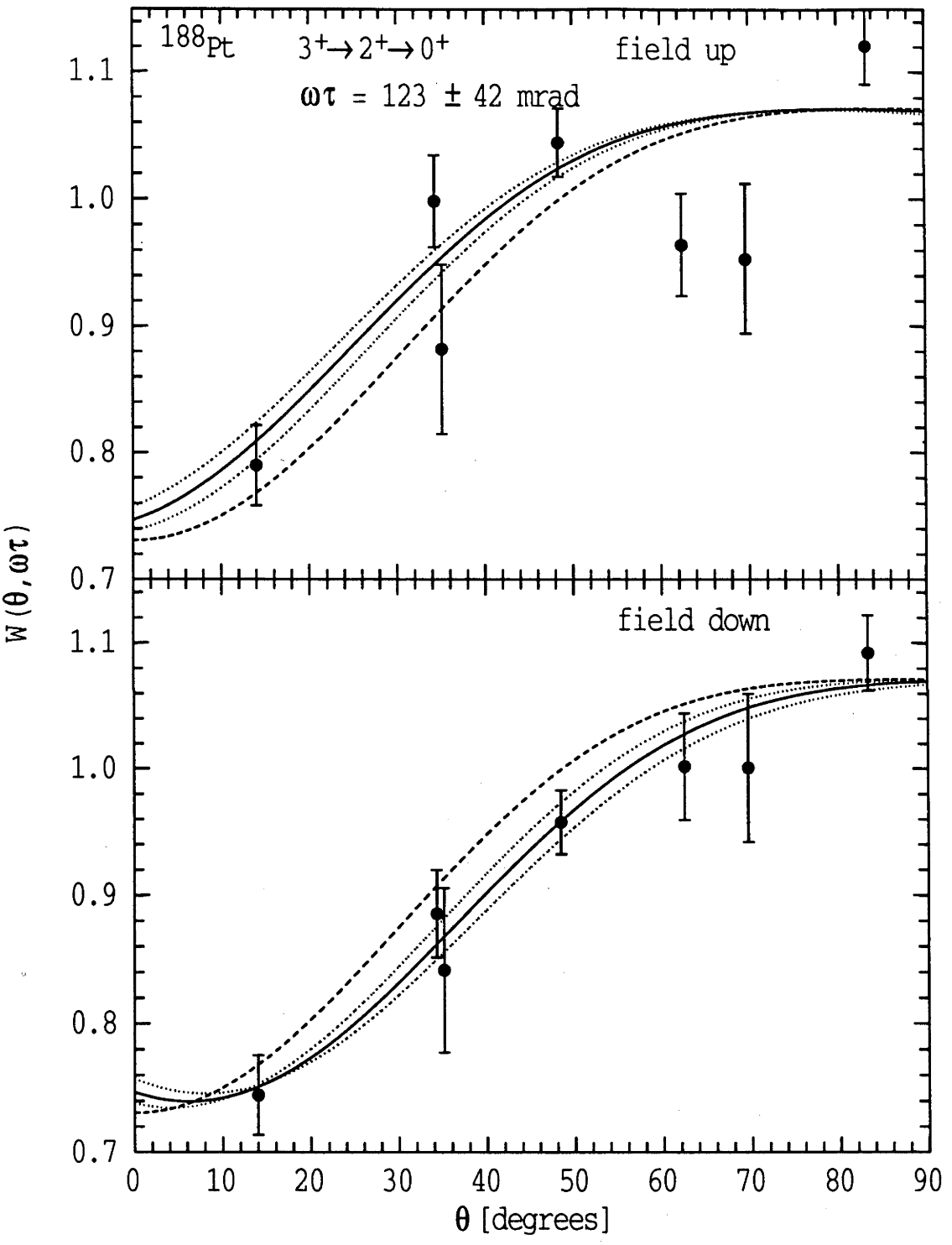

Figure 6.16: The measured and calculated angular correlations for the $3_1^+ \rightarrow 2_1^+ \rightarrow 0_1^+$ γ-ray cascade when the $3_1^+ \rightarrow 2_1^+$ transition has pure $E2$ multipolarity. The unperturbed distribution is shown by the dashed line.

γ-rays in the 280 keV slice. The excited 0^+ state (at 471.6 keV) is fed primarily by the 326.8 keV transition de-populating the 2_3^+ state at 798.5 keV.

The ^{186}Pt and ^{184}Pt nuclei (with $N = 108$ and 106, respectively) are near the middle of the $N = 82-126$ neutron shell and each have a deformed, rotational ground-state band, unlike the heavier Pt isotopes. This can be seen in the partial Pt decay schemes of fig. 6.17 compared with figs. 6.2 and 6.11. The intensity of the β^+-decay is more strongly directed down the ground-state band in the lighter ^{184,186}Pt isotopes; i.e. the intensity of the $6_1^+ \rightarrow 4_1^+$ and $4_1^+ \rightarrow 2_1^+$ transitions is enhanced and the $2_2^+ \rightarrow 2_1^+$ reduced. For these nuclei the $4_1^+ \rightarrow 2_1^+ \rightarrow 0_1^+$ cascade is more intensely populated than the $2_2^+ \rightarrow 2_1^+ \rightarrow 0_1^+$ and, therefore, more useful for extracting the precession angle.

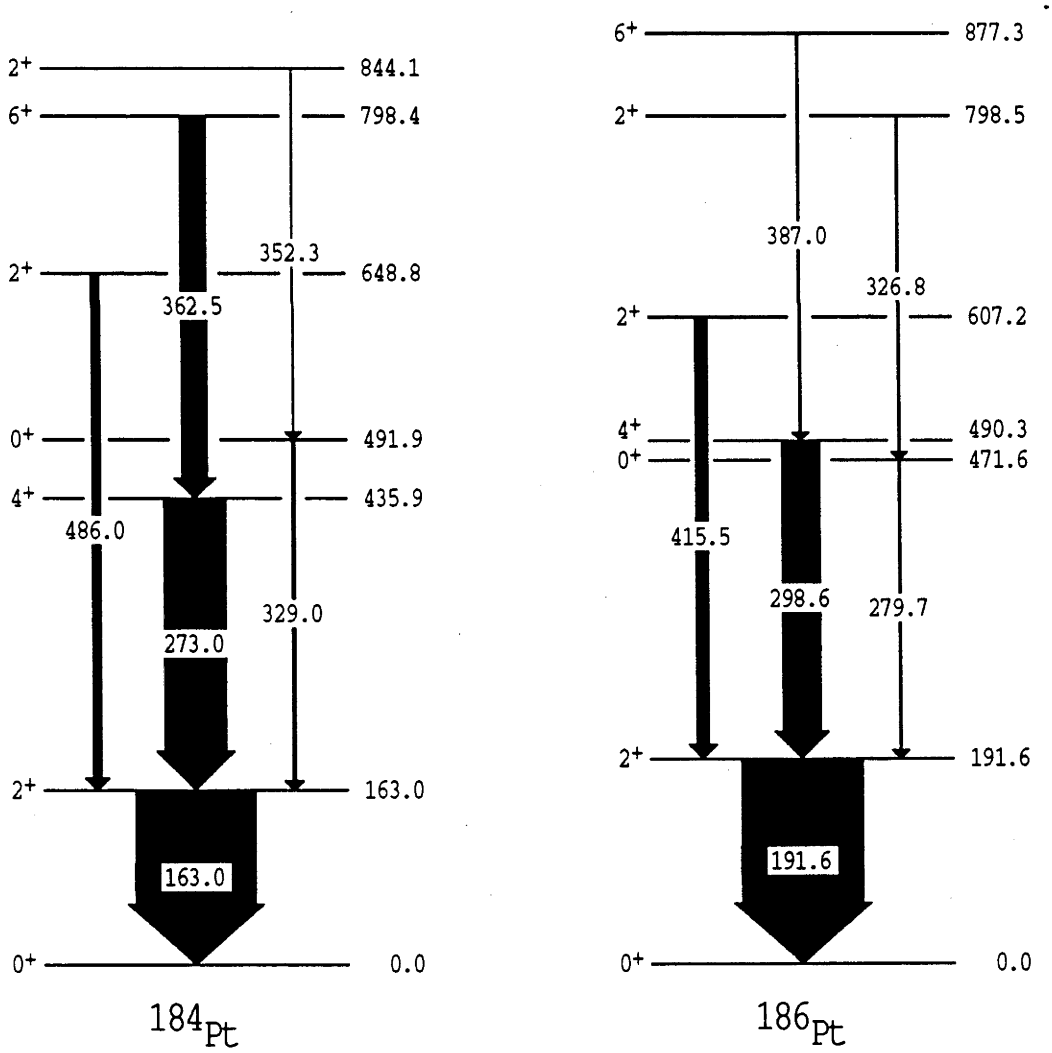

Figure 6.17: Partial decay schemes for ^{186}Pt and ^{184}Pt populated by β^+-decay.

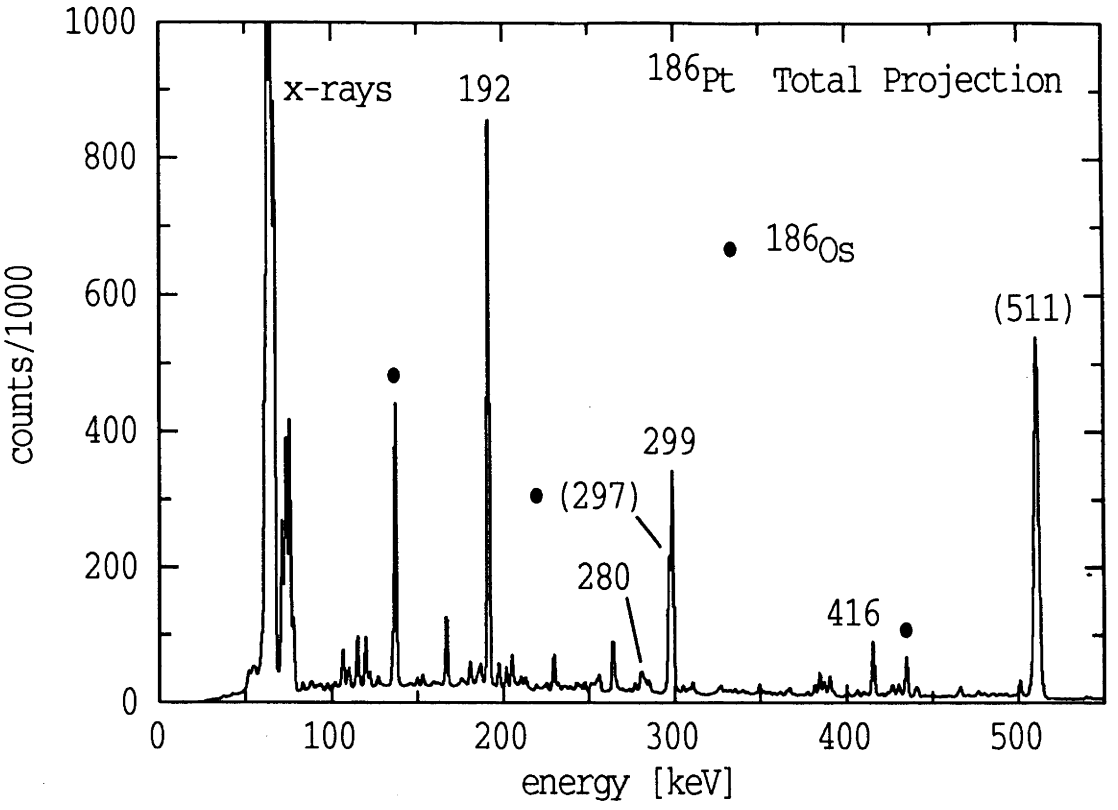

Figure 6.18: The total γ-γ projection from the ^{186}Pt measurement.

Figures 6.20, 6.21, 6.22 and 6.23 display the measured radiation patterns for the $0_2^+ \rightarrow 2_1^+ \rightarrow 0_1^+$, $4_1^+ \rightarrow 2_1^+ \rightarrow 0_1^+$, $2_2^+ \rightarrow 2_1^+ \rightarrow 0_1^+$ and $3_1^+ \rightarrow 2_1^+ \rightarrow 0_1^+$ cascades in ^{186}Pt. The calculated perturbed angular correlations are for the best-fit values of $\omega_L\tau(2_1^+) = +624\pm53$ mrad, $+590\pm64$ mrad, $+522\pm98$ mrad and $+628\pm105$ mrad, respectively, assuming 8% of the nuclei experienced no field. The 2_1^+-state lifetime for this nucleus is much longer than those of the heavier isotopes (see table 6.1). This caused a larger nuclear precession, which resulted in the more pronounced perturbations observed here.

Van Walle *et al.* [Va85] have measured the mixing ratios for the $2_2^+ \rightarrow 2_1^+$ and $3_1^+ \rightarrow 2_1^+$ transitions as $\delta(E2/M1) = 18.7^{+19.5}_{-7.7}$ or -0.382 ± 0.042 and $\delta(E2/M1) = 0.322 \pm 0.016$ or $15.7^{+4.3}_{-2.9}$, respectively. The present measurement allowed determination of a_4 values for the correlations and, therefore, confirmed the values $\delta = +18.7^{+19.5}_{-7.7}$ (see fig. 6.22) and $\delta = +15.5^{+4.3}_{-2.9}$. The first value is in conflict with that chosen in the Nuclear Data Sheets [Fi88]. Unfortunately, these imprecise mixing ratios contribute significantly to the uncertainties in the precession angles determined using these cascades. Although the large mixing

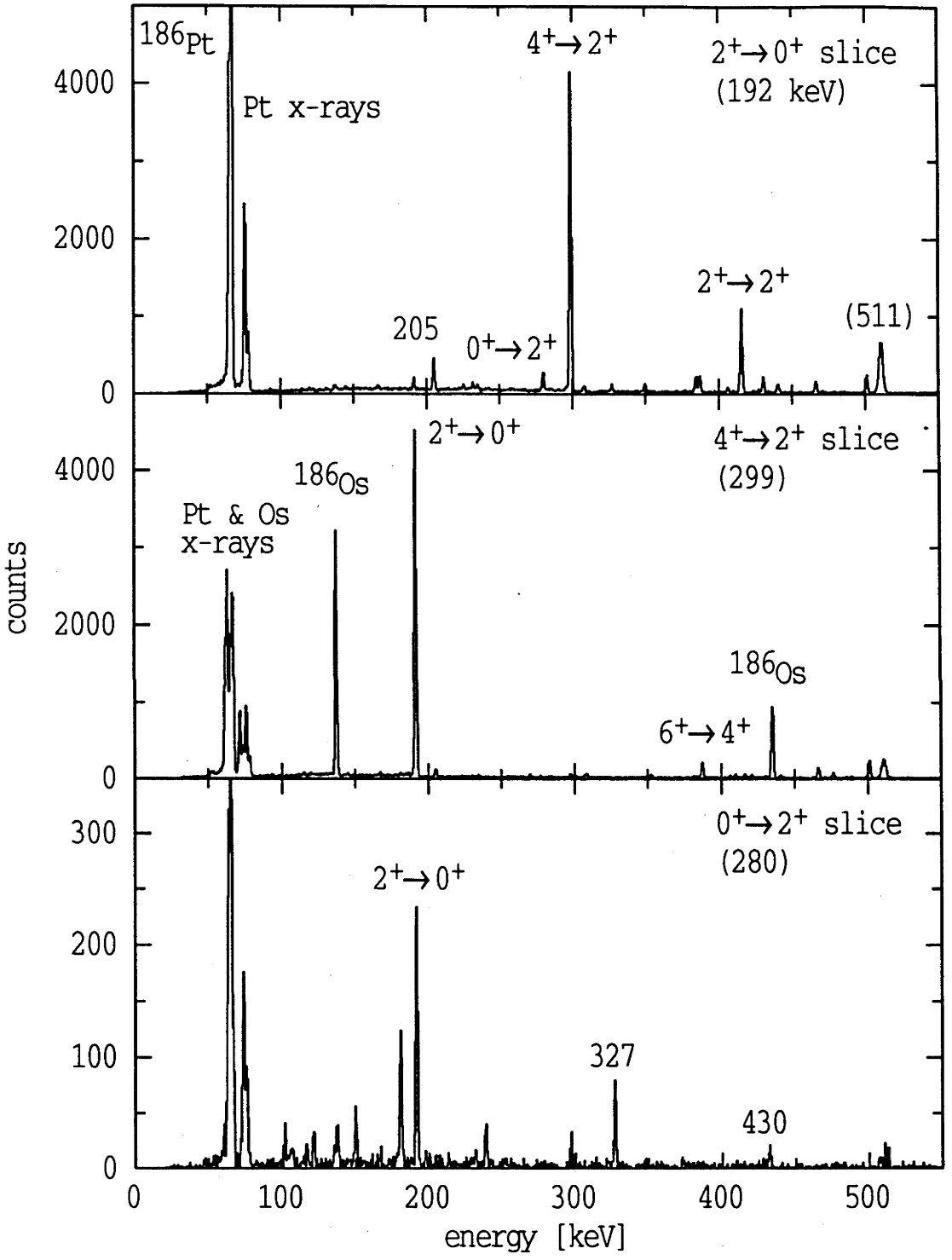

Figure 6.19: The coincidence spectra for the $2_1^+ \rightarrow 0_1^+$, $4_1^+ \rightarrow 2_1^+$ and $0_2^+ \rightarrow 2_1^+$ transitions in ^{186}Pt at an angular separation of 83° with reverse gating and the field down.

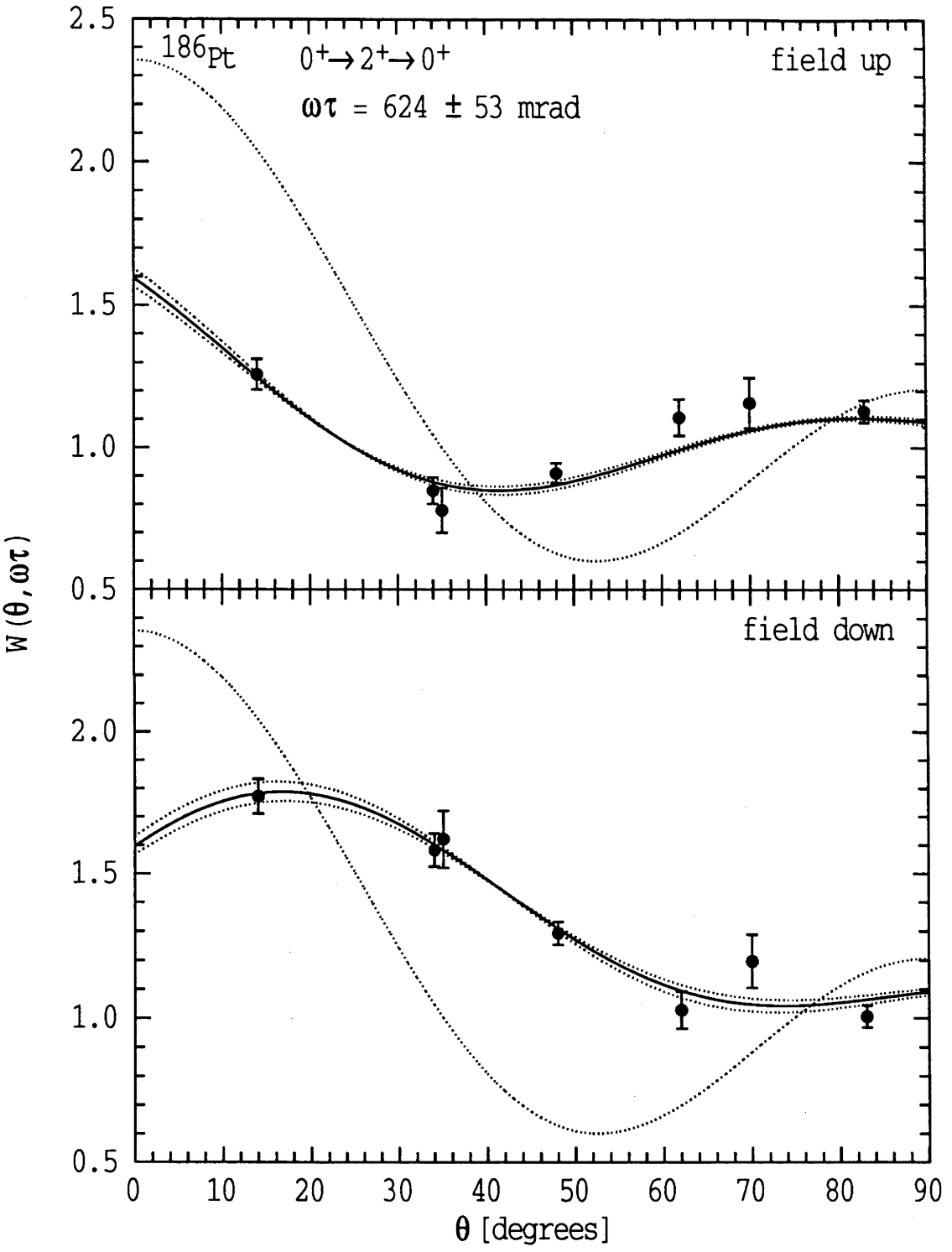

Figure 6.20: The measured and calculated perturbed angular correlations for the $0_2^+ \rightarrow 2_1^+ \rightarrow 0_1^+$ γ-ray cascade in ^{186}Pt. The unperturbed correlation is also given.

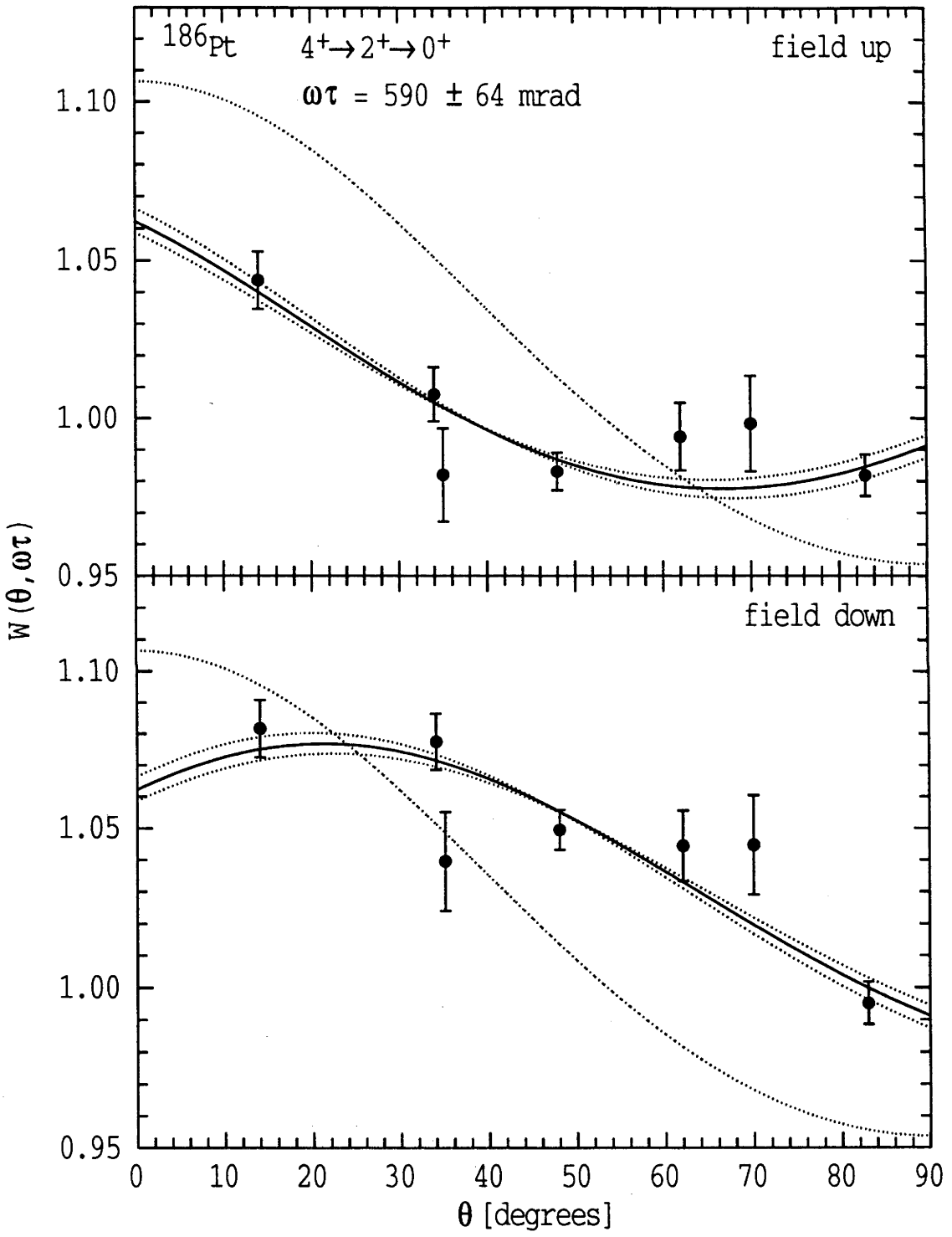

Figure 6.21: The perturbed γ-γ angular correlations for the ^{186}Pt $4_1^+ \rightarrow 2_1^+ \rightarrow 0_1^+$ cascade. The correlation for $\omega_L \tau = 0$ is also shown.

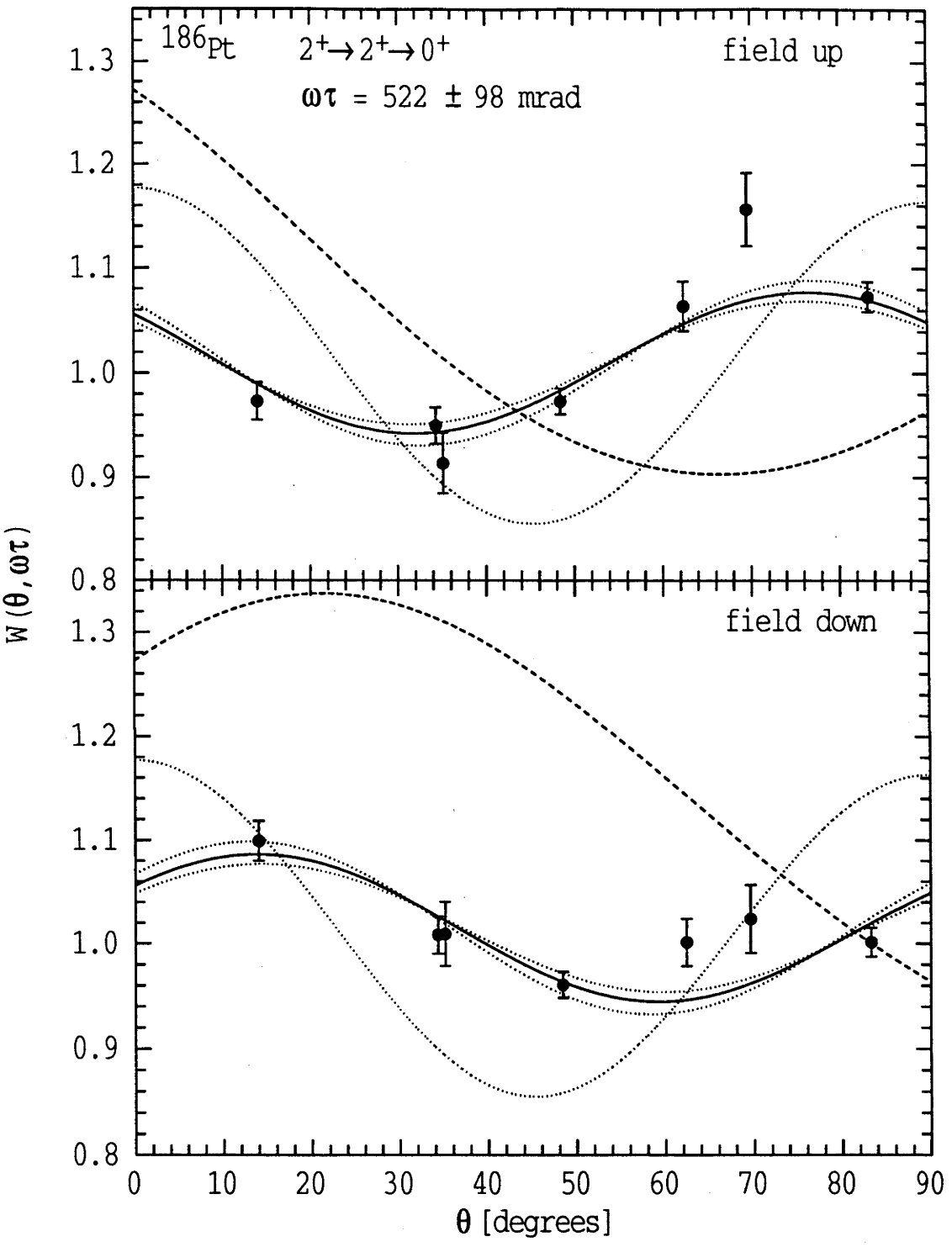

Figure 6.22: The measured radiation patterns for the ^{186}Pt $2_2^+ \rightarrow 2_1^+ \rightarrow 0_1^+$ cascade. The calculated correlations with $\omega_L\tau(2_1^+) = +522 \pm 98$ mrad (and $\omega_L\tau = 0$, dotted line) assume a mixing ratio of $\delta(E2/M1) = +18.7^{+19.5}_{-7.7}$ for the first transition. The calculated distributions for $\delta = -0.382 \pm 0.042$ and $\omega_L\tau = +600$ mrad are shown by the dashed lines, and clearly do not reproduce the data.

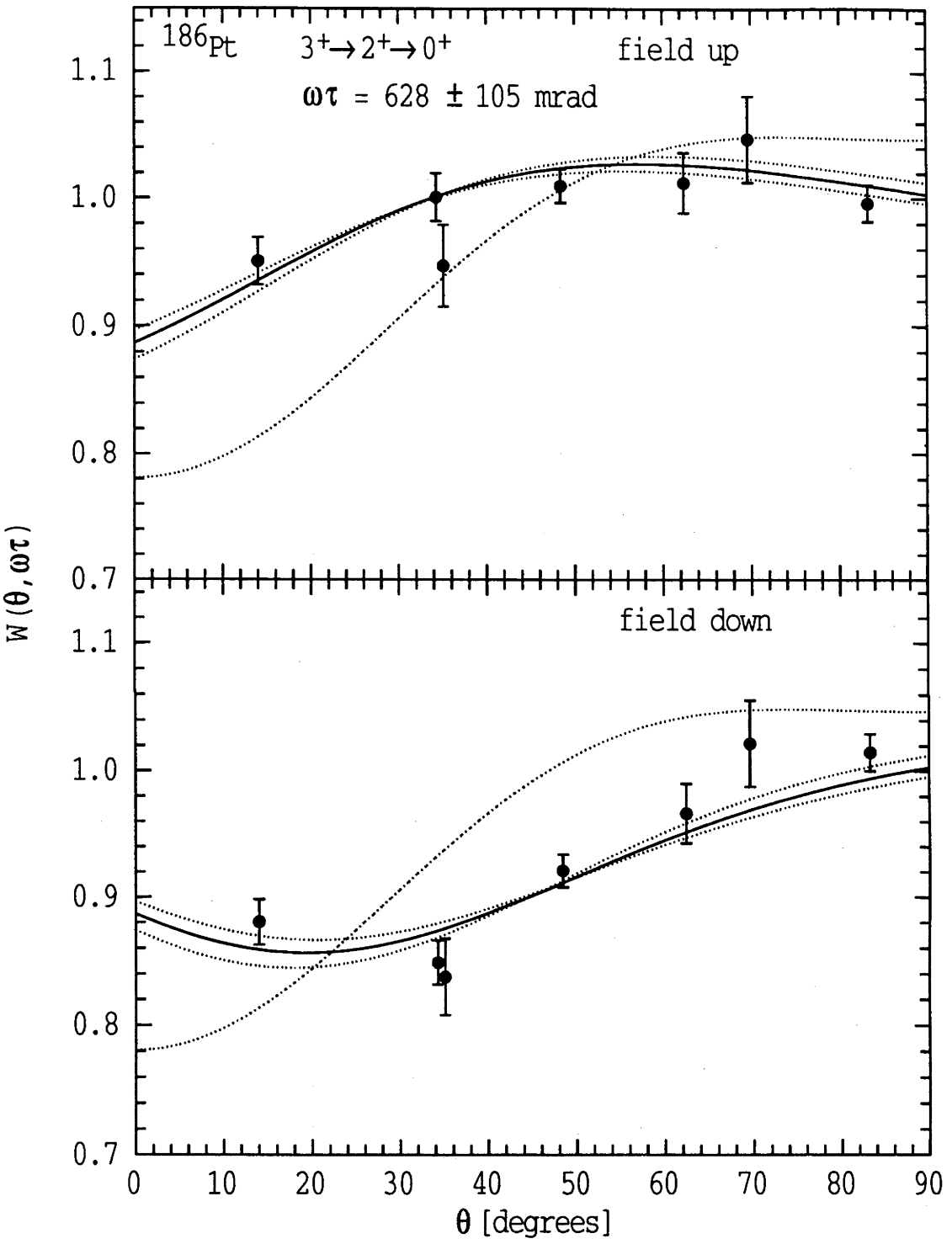

Figure 6.23: The measured and calculated angular correlations for the $3_1^+ \rightarrow 2_1^+ \rightarrow 0_1^+$ γ-ray cascade, where the $3_1^+ \rightarrow 2_1^+$ transition has a mixing ratio of $\delta(E2/M1) = +15.5^{+4.3}_{-2.9}$. The unperturbed correlation is also shown.

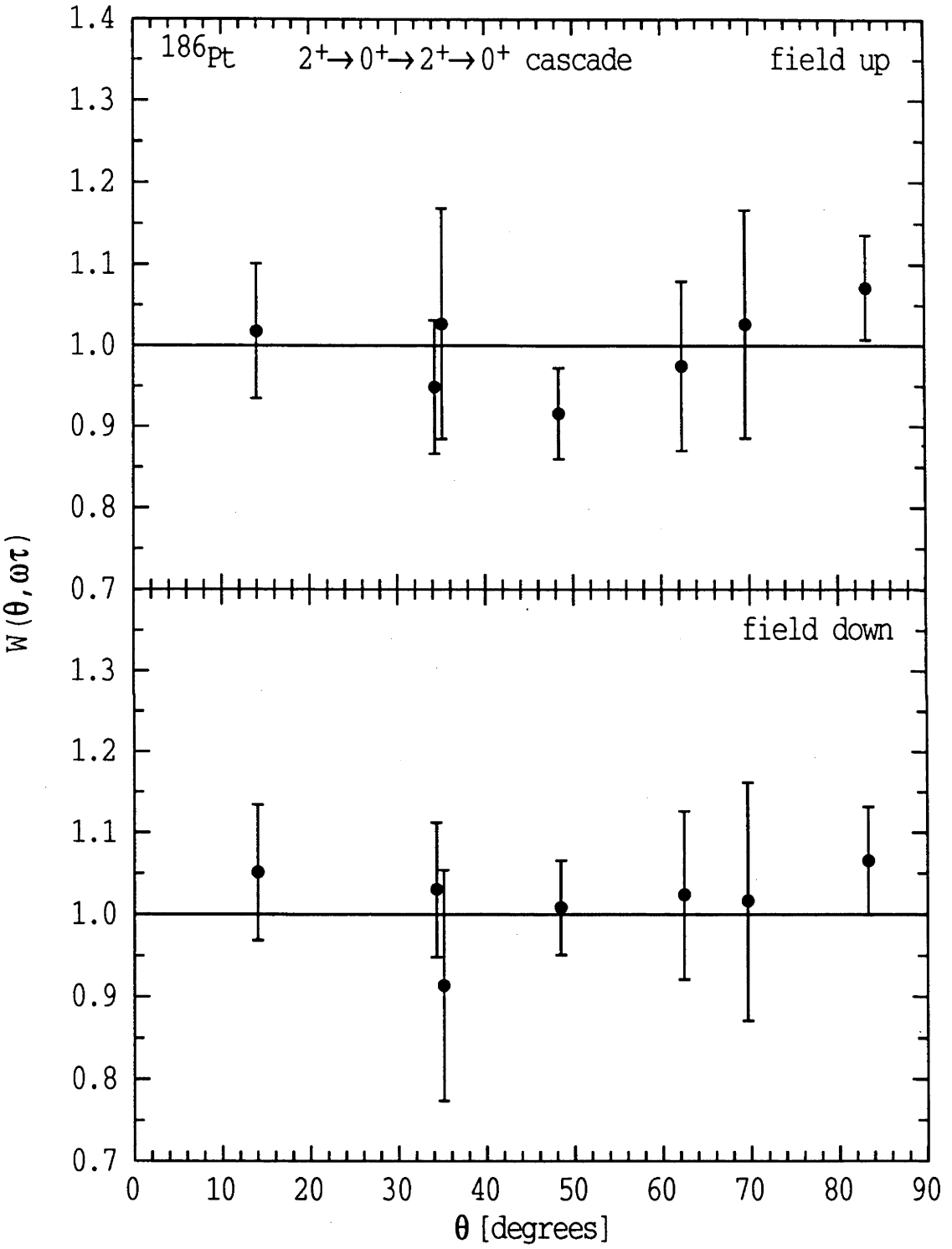

Figure 6.24: The isotropic radiation distributions measured for coincidences between the ^{186}Pt $2_3^+ \rightarrow 0_2^+$ and $2_1^+ \rightarrow 0_1^+$ γ-rays, where the intermediate $0_2^+ \rightarrow 2_1^+$ transition was unobserved.

ratios imply that the transitions have nearly pure $E2$ multipolarity, including the small $M1$ components had a significant effect on the angular correlations.

The intensity of the 326.8 keV γ-ray feeding the excited 0^+ state allowed the measurement of the correlation between this and the $2_1^+ \rightarrow 0_1^+$ transition, where the intermediate $0_2^+ \rightarrow 2_1^+$ decay remained unobserved. As the excited 0^+ state may not be aligned, the radiation was emitted isotropically (see sect. 4.3.3) and the distribution unchanged by the perturbation from the nuclear precession. This null effect was observed experimentally as shown in fig. 6.24.

6.5 ^{184}Pt Measurement

Figures 6.25 and 6.26 display coincidence spectra taken from the total γ-γ matrix for the ^{184}Pt measurement. The full projection of the matrix is in fig. 6.25 and the background-subtracted slices for the 163 keV, 273 keV and 486 keV γ-rays are in fig. 6.26. The corresponding partial decay scheme for the nucleus appeared in

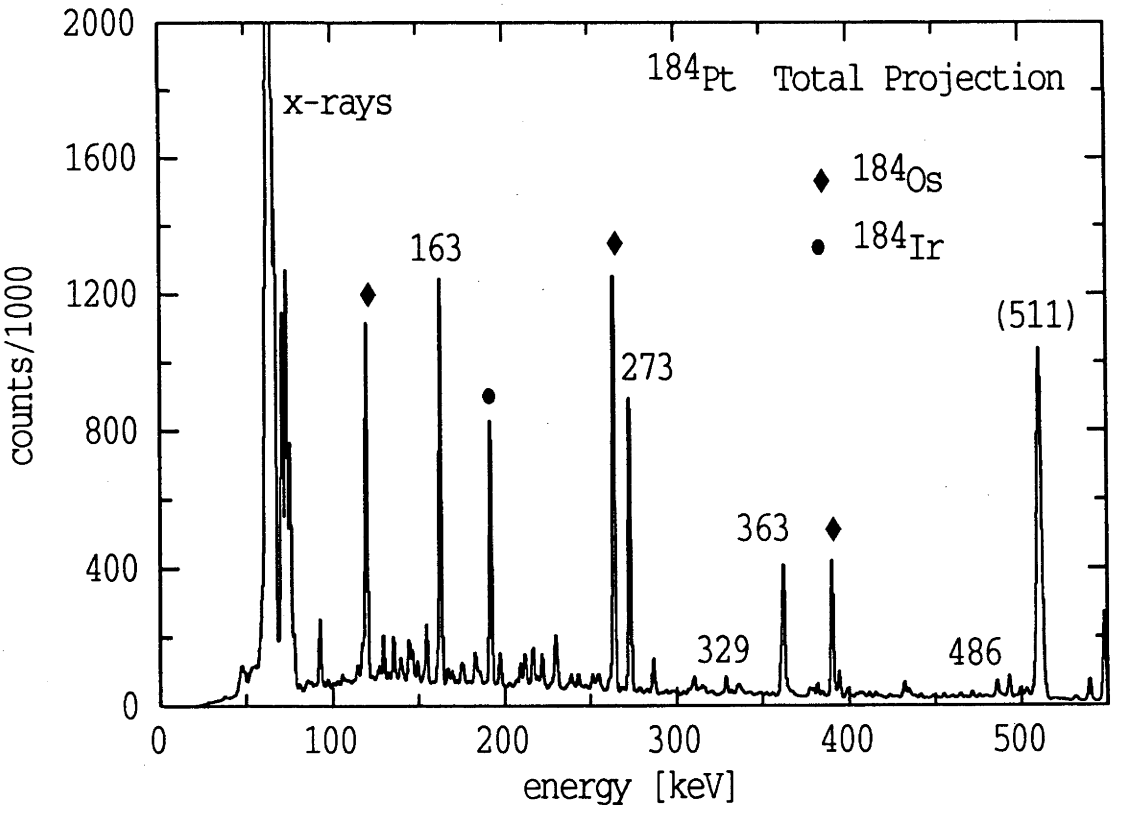

Figure 6.25: The full projection of the total γ-γ matrix recorded in the ^{184}Pt measurement.

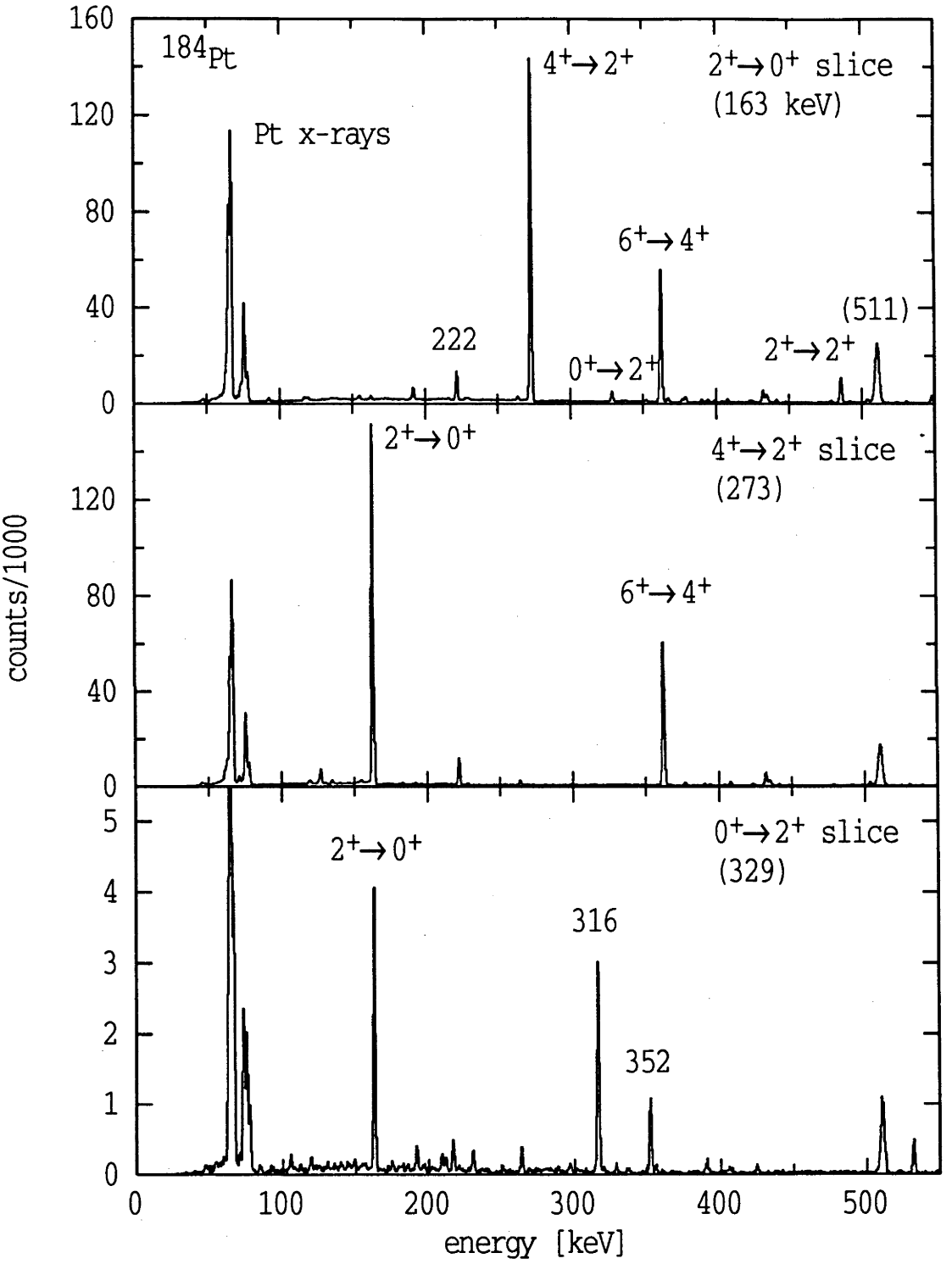

Figure 6.26: The coincidence spectra for the $2_1^+ \rightarrow 0_1^+$, $4_1^+ \rightarrow 2_1^+$ and $0_2^+ \rightarrow 2_1^+$ transitions in ^{184}Pt projected from the total γ-γ matrix.

fig. 6.17. Visible in some of these spectra is the 222.0 keV γ-ray from the 4^+ state at an excitation energy of 2.553 MeV, which feeds the ground-state band. The subsequent β^+-decay of ^{184}Pt results in the observation of γ-radiation de-exciting the ^{184}Ir and ^{184}Os nuclei.

The perturbed angular correlations for the $0_2^+ \rightarrow 2_1^+ \rightarrow 0_1^+$ and $4_1^+ \rightarrow 2_1^+ \rightarrow 0_1^+$ cascades with best-fit precessions of $\omega_L\tau(2_1^+) = +1005 \pm 83$ mrad and $+810 \pm 81$ mrad are shown in figs. 6.27 and 6.28, respectively. The $\gtrsim 500$ ps lifetime for the 2_1^+ state in ^{184}Pt (table 6.1) leads to a significant attenuation of the measured radiation patterns which, in turn, reduces the sensitivity of the measurement to the perturbation (sect. 3.2). To overcome this the statistics were improved by running for longer (see table 4.3) to collect more data. The number of counts in the peaks of the ^{184}Pt total projection are greater than those in the spectra for the other measurements.

The perturbed angular correlation for the $6_1^+ \rightarrow 4_1^+ \rightarrow 2_1^+ \rightarrow 0_1^+$ cascade is displayed in fig. 6.29. The intermediate, stretched $E2$ $4_1^+ \rightarrow 2_1^+$ transition goes undetected. The measured value of $\omega_L\tau(2_1^+) = +917 \pm 138$ mrad was obtained from a least-squares fit to the total precession angle, of $\omega_L\tau = +979 \pm 140$ mrad, after correction for the nuclear precession which occurred in the 4_1^+ state, $\omega_L\tau(4_1^+) = +62 \pm 9$ mrad. The level lifetime $\tau(4_1^+) = 36.5 \pm 1.3$ ps [Ga86] and a g-factor equal to that for the first-excited 2^+ state, $g(2_1^+) = g(4_1^+)$, were assumed.

6.6 Inferred g-factors

The results of the individual analyses for each γ-ray cascade of interest in ^{184,186,188,192}Pt are summarized in the third column of table 6.1. A weighted average of the precessions for each Pt nucleus has been calculated. These were found to agree with the results of analyses which simultaneously fitted data sets for several cascades. Relative g-factors (given in the fifth column) were inferred directly from the measured precession angles and adopted lifetimes (fourth column).

The absolute $g(2_1^+)$ (final column of table 6.1) were extracted from g-factor ratios and the adopted value for ^{192}Pt, $g(2_1^+) = 0.299 \pm 0.010$ (sect. 7.3.2.1). Each quoted error incorporates the uncertainties in the effective field strength, the measured precession and the adopted meanlife for the 2_1^+ state in the given nucleus. The final errors in the measured precessions are around 7%, but lifetime errors of similar magnitude result in an uncertainty for the absolute g-factors of

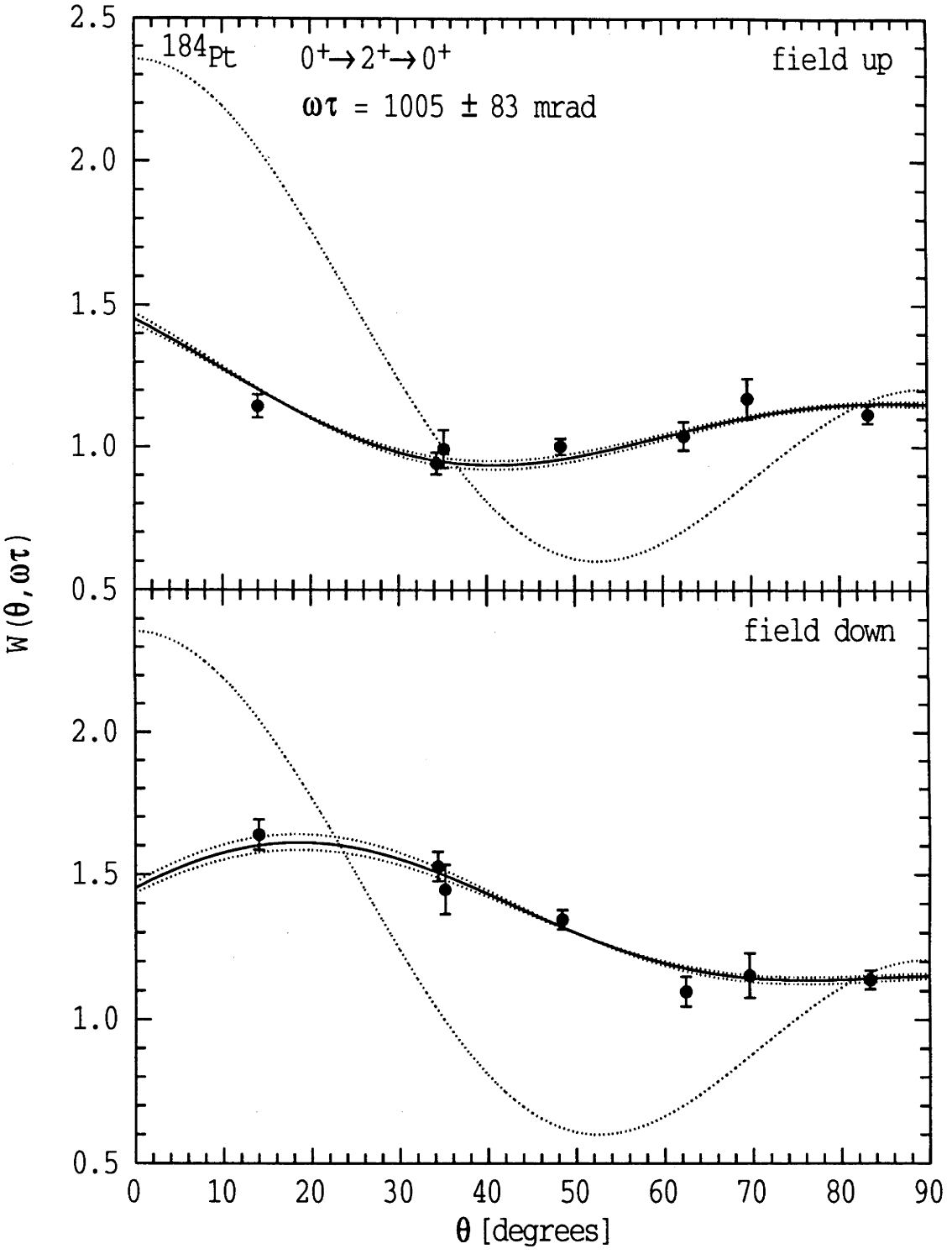

Figure 6.27: The measured (data points) and calculated (lines) angular correlations, including that for $\omega_L \tau = 0$, for the $0_2^+ \rightarrow 2_1^+ \rightarrow 0_1^+$ γ-ray cascade in ^{184}Pt.

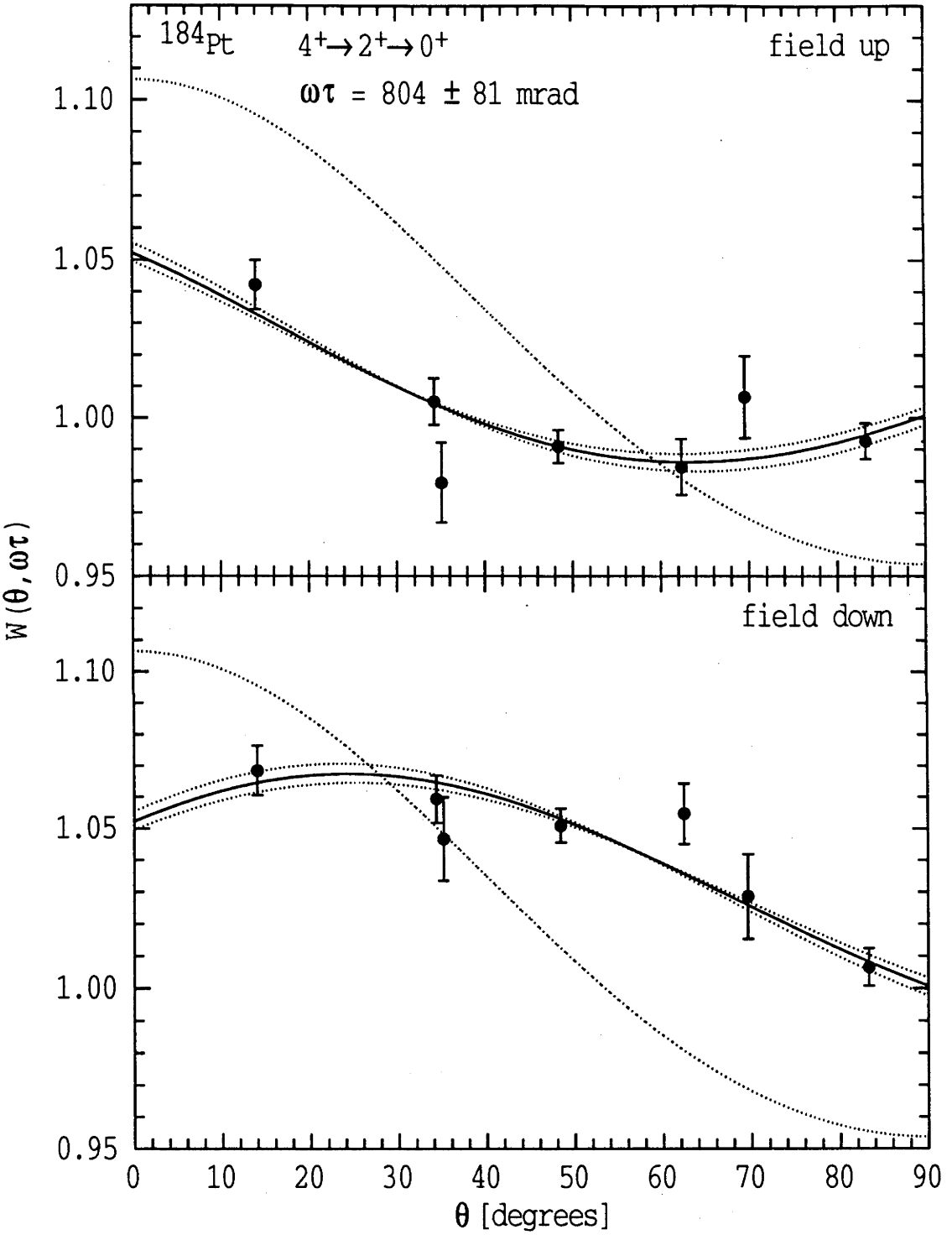

Figure 6.28: The measured perturbed angular correlations for the ^{184}Pt $4_1^+ \rightarrow 2_1^+ \rightarrow 0_1^+$ γ-γ cascade in ^{184}Pt, with calculations for the best-fit of $\omega_L \tau(2_1^+) = +804 \pm 81$ mrad and the unperturbed case.

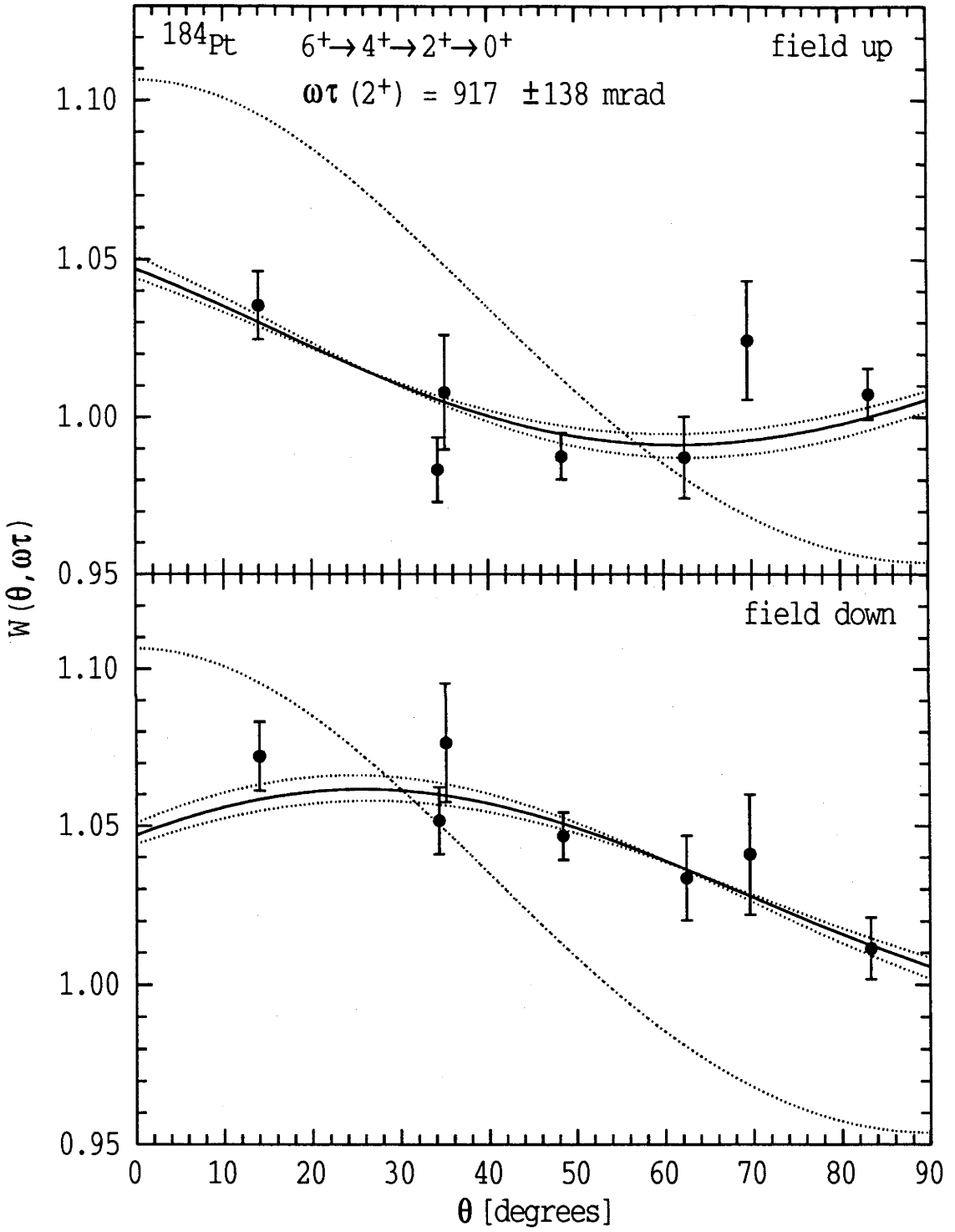

Figure 6.29: The perturbed angular correlations between the $6_1^+ \rightarrow 4_1^+$ and $2_1^+ \rightarrow 0_1^+$ transitions, where the alignment was transferred by the unseen intermediate γ-ray. The calculations are for $\omega_L\tau(2_1^+) = +917 \pm 138$ mrad and $\omega_L\tau = 0$.

Table 6.1: Measured precession angles and inferred 2_1^+-state g-factors.

Nuclide	γ-ray cascade	$\omega_L\tau(2_1^+)$[a] [mrad]	$\tau(2_1^+)$ [ps]	$g/g(^{192}\mathrm{Pt})$[b]	$g(2_1^+)$
^{192}Pt	$0_2^+ \rightarrow 2_1^+ \rightarrow 0_1^+$	104(12)	62(2)[d]	1.00	0.299(10)[e]
	$2_2^+ \rightarrow 2_1^+ \rightarrow 0_1^+$	113(9)			
	$3_1^+ \rightarrow 2_1^+ \rightarrow 0_1^+$	120(30)			
		⟨110(7)⟩[c]			
^{188}Pt	$0_2^+ \rightarrow 2_1^+ \rightarrow 0_1^+$	155(11)	93(7)[f]	0.97(12)	0.29(4)
	$2_2^+ \rightarrow 2_1^+ \rightarrow 0_1^+$	189(22)			
	$3_1^+ \rightarrow 2_1^+ \rightarrow 0_1^+$	123(42)			
		⟨160(10)⟩[c]			
^{186}Pt	$0_2^+ \rightarrow 2_1^+ \rightarrow 0_1^+$	624(53)	375(14)[g]	0.90(9)	0.27(3)
	$4_1^+ \rightarrow 2_1^+ \rightarrow 0_1^+$	590(64)			
	$2_2^+ \rightarrow 2_1^+ \rightarrow 0_1^+$	522(98)			
	$3_1^+ \rightarrow 2_1^+ \rightarrow 0_1^+$	628(105)			
		⟨601(35)⟩[c]			
^{184}Pt	$0_2^+ \rightarrow 2_1^+ \rightarrow 0_1^+$	1005(83)	519(17)[g]	0.98(10)	0.29(3)
	$4_1^+ \rightarrow 2_1^+ \rightarrow 0_1^+$	804(81)	582(22)[h]	0.88(9)	0.26(3)
	$6_1^+ \rightarrow 4_1^+, 2_1^+ \rightarrow 0_1^+$	917(138)			
		⟨904(53)⟩[c]			

[a] Precession angles with 8% of recoils at field-free sites (see text).

[b] Derived from measured precessions and adopted lifetimes.

[c] Weighted average.

[d] From ref. [Ra87].

[e] Adopted g-factor (table 7.2) used as a calibration (see text).

[f] Adopted meanlife, from sect. 8.5.

[g] From ref. [Fi72].

[h] From ref. [Ga86].

$\sim 10\%$.

As discussed in sect. 4.3.4, the final implantation sites in each experiment were considered to be similar, and in each analysis it was assumed that 8% of the implanted nuclei were not subject to a magnetic field, while the rest experienced the 'full' field of 123 T. It was found that the relative g-factors are insensitive to the exact fraction of nuclei on field-free sites, provided this fraction did not vary significantly from case to case. An alternative analysis assuming all the nuclei experienced an 'effective' field of 113 ± 10 T gave very similar results.

The *absolute* limits for the effective field strength are given in sect. 6.1.1. Taking a field of -92 ± 5 T as the lower limit would increase the inferred $g(2_1^+)$ values by, at most, $\sim 20\%$. Even so, as will be seen below (chapter 9), 2_1^+-state g-factors of such magnitude are not expected. With the upper-limit field strength of 123 ± 3 T the g-factors decrease by $\sim 8\%$, but remain consistent with the quoted values which have errors of around 10%.

For ^{184}Pt, the weighted average of the two measurements of the 2_1^+ meanlife (table 6.1) is $\langle \tau \rangle = 542 \pm 13$ ps, which corresponds to a g-factor of $g(2_1^+) = 0.28 \pm 0.03$.

Chapter 7

The 2_1^+-state g-factor in ^{190}Pt

7.1 Introduction

The implantation-decay technique has been used to measure the 2_1^+-state g-factors of the neutron-deficient ^{184,186,188}Pt nuclei. However, as described in sect. 6.2, the ^{190}Pt experiment was abandoned due to a slow count rate from the reaction used. When material enriched in ^{190}Pt became available, we opted to make an independent measurement using the transient-field technique (which is described briefly in sect. 3.5.2). This chapter reports the first measurement of $g(2_1^+)$ in ^{190}Pt, relative to the g-factors for the heavier, stable Pt isotopes. Determination of the 2_1^+-state lifetime was made indirectly, through simultaneous measurement of the relative $B(E2; 0_1^+ \rightarrow 2_1^+)$ excitation strengths in ^{190,194,196}Pt. The measurement was unusual in that the enriched sample used had only a small percentage (4.19%) of ^{190}Pt, which has a natural abundance of only 0.01%, and a half-life of 6×10^{11} years.

7.2 Experimental Procedure

A complete description of the experimental and analysis procedures for the transient-field technique is given elsewhere [St81a, St85, By87] and only the details relevant to the present measurement are given here.

A beam of 160 MeV ^{58}Ni ions, from the ANU 14UD Pelletron Accelerator, was incident upon a multilayered target, Coulomb exciting Pt nuclei to the low-lying 2_1^+ levels of interest. The first layer of the target consisted of a 2.19 mg/cm^2 thick Pt foil, rolled from metal enriched in ^{190}Pt. This was backed by a 3.85 mg/cm^2

thick, previously annealed, Gd foil attached using a thin ($210\,\mu g/cm^2$) flashing of In as an adhesive. A thick ($6.2\,mg/cm^2$) Cu layer was evaporated on the downstream side to provide a magnetic perturbation-free environment in which the recoiling Pt nuclei came to rest. The Pt foil was enriched in ^{190}Pt to $4.19 \pm 0.04\%$, and also contained $2.02 \pm 0.02\%$ ^{192}Pt, $49.86 \pm 0.20\%$ ^{194}Pt, $14.45 \pm 0.10\%$ ^{196}Pt and $3.18 \pm 0.03\%$ ^{198}Pt with the remaining $26.30 \pm 0.10\%$ ^{195}Pt (Oak Ridge National Laboratory isotopic analysis). Foil and layer thicknesses were determined by weight and area measurements made during target preparation.

Precessions of the particle-γ perturbed angular correlations were measured using four, HPGe γ-ray detectors; two were placed at $\pm 65°$ to the beam direction and at a distance so as to subtend an angle of 40°, while the other pair at $\pm 115°$ subtended an angle of 24°. The de-exciting γ-radiation was registered in coincidence with backscattered beam ions, detected in an annular counter at 150°–167° to the beam direction. Events were, therefore, recorded for Pt ions recoiling forward with a mean half-angle of $\sim 8°$. These Pt ions traversed the Gd foil, taking an average of 0.75 ps and with average entrance and exit velocities of $4.1\,v_0$ and $2.1\,v_0$, respectively, before coming to rest in the Cu backing ($v_0 = c/137$, Bohr velocity).

The target was cooled with liquid nitrogen to a temperature of ~ 90 K and polarized perpendicular to the γ-ray detection plane by an external field of $\sim$ 0.05 Tesla. To minimize possible systematic experimental errors the field direction was reversed automatically, approximately every 15 minutes.

Unperturbed particle–γ-ray angular correlations were also measured. The forward detectors were moved so as to sample the γ-radiation at the angles 0°, $\pm 15°$, $\pm 30°$, $\pm 45°$, $\pm 55°$ and $\pm 65°$. Normalization was provided by the backward pair which remained at $\pm 115°$. To facilitate the sampling of the angular correlation at each of these angles, the forward detector in the negative quadrant was moved further from the target during the angular correlation measurement, so that it subtended an angle of 28°.

The particle-γ angular correlations for the $2_1^+ \rightarrow 0_1^+$ transitions in each Pt nucleus were also calculated using a version of the Winther-de Boer Coulomb excitation code [Wi66], which takes into account the effects of a finite particle-detection angle, beam energy loss in the target and feeding from populated higher-excited states.

The angle, $\Delta\theta$, through which the nucleus precesses, due to the interaction

between its magnetic moment with the transient hyperfine field, is given by

$$\Delta\theta = g\,\phi \quad , \tag{7.1}$$

where

$$\phi = -\frac{\mu_N}{\hbar}\int_{T_1}^{T_2} B_{tr}(t)\,e^{-t/\tau}\,dt \quad , \tag{7.2}$$

g is the g-factor and τ the lifetime of the nuclear state, B_{tr} is the strength of the transient field (which varies with time as the ion slows in the ferromagnetic layer) and $T_{1(2)}$ the entrance (exit) time for the Pt ion traversing the Gd foil. As $\tau \gg T_2 \simeq 0.75\,\text{ps}$ for all of the states of present interest, ϕ is essentially a constant factor and the ratios of the g-factors are given, to a very good approximation, by the ratios of the measured precessions.

For small precessions ($\lesssim 100\,\text{mrad}$) the measured precession angle may be determined from

$$\Delta\theta = \frac{\epsilon}{S} \quad , \tag{7.3}$$

where ϵ is the experimental field up/down counting asymmetry (or 'effect') and S is the logarithmic derivative of the angular correlation for a detector pair placed at symmetric angles with respect to the beam direction, $\pm\theta_\gamma$:

$$S = \frac{1}{W}\frac{dW}{d\theta}\Big|_{\theta_\gamma} \quad . \tag{7.4}$$

The effect is defined as

$$\epsilon = \frac{1-\rho}{1+\rho} \quad . \tag{7.5}$$

Possible systematic experimental uncertainties are reduced by taking the double ratio for each detector pair:

$$\rho = \sqrt{\frac{\mathrm{N}(+\theta_\gamma)\uparrow}{\mathrm{N}(+\theta_\gamma)\downarrow}\,\frac{\mathrm{N}(-\theta_\gamma)\downarrow}{\mathrm{N}(-\theta_\gamma)\uparrow}} \quad , \tag{7.6}$$

where $\mathrm{N}(\pm\theta_\gamma)(\uparrow,\downarrow)$ are the counting rates in the detectors at $\pm\theta_\gamma$ for the alternative field directions ($\uparrow$ and $\downarrow$).

7.3 Results

7.3.1 Measured precessions

Figure 7.1 shows a typical γ-ray spectrum measured in coincidence with backscattered beam-ions, following Coulomb excitation of the Pt target nuclei. The lower frame shows the part of the spectrum of current interest in more detail.

It is apparent in fig. 7.1 that for ^{194}Pt, which is the main component of the target material (sect. 7.2), population of the higher-excited states ($I^\pi = 2_2^+, 4_1^+$), while weak compared with the intensity of its $2_1^+ \rightarrow 0_1^+$ transition, is comparable to the population of the 2_1^+ level in ^{190}Pt. Nevertheless, the energy separation of the $2_1^+ \rightarrow 0_1^+$ transition in ^{190}Pt (295.8 keV) and the $2_2^+ \rightarrow 2_1^+$ transition in ^{194}Pt (293.5 keV) is sufficient for accurate determination of both peak areas.

The measured and calculated particle–γ-ray angular correlations for the $2_1^+ \rightarrow 0_1^+$ transitions in each of the even-even $^{190-198}$Pt nuclei are displayed in fig. 7.2. The measured angular correlations were used to confirm the calculations (sect. 7.2) and also to provide a check of the γ-detector angular position, even though this is not so important in a relative simultaneous measurement.

Details of the measured counting asymmetries, calculated logarithmic derivatives of the angular correlations and the derived precession angles are given in table 7.1. The calculated logarithmic derivatives are corrected for the effects of cascade feeding, which reduced the unfed S values by $\sim 5\%$, and detector positioning, which caused a further reduction of $\sim 3.5\%$. When measuring relative precessions, as in the present work, these corrections only have a small effect because each isotope is subject to essentially the same correction factor; consequently, the associated uncertainties are not very important and are neglected in table 7.1. Uncertainties in S are included when the absolute g-factors are evaluated in table 7.2, below.

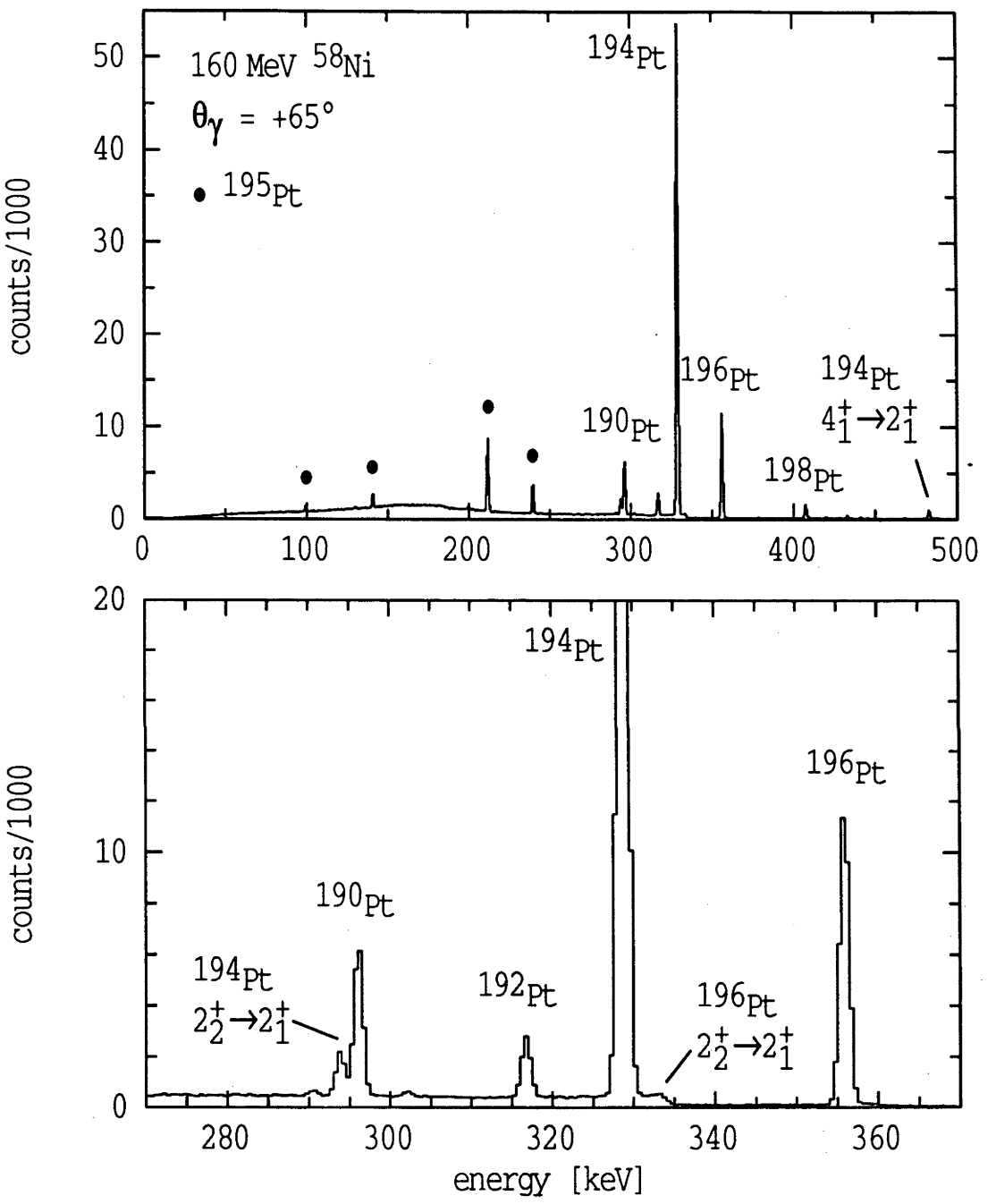

Figure 7.1: A typical coincidence γ-ray spectrum following Coulomb excitation of the Pt target by an incident beam of 160 MeV ^{58}Ni. The lower frame is an enlargement of part of the spectrum above. The $2_1^+ \rightarrow 0_1^+$ transitions in ^{190,192,194,196,198}Pt are indicated. This corresponds to about 35% of the data accumulated during the precession measurements at +65° and with the field direction 'down'.

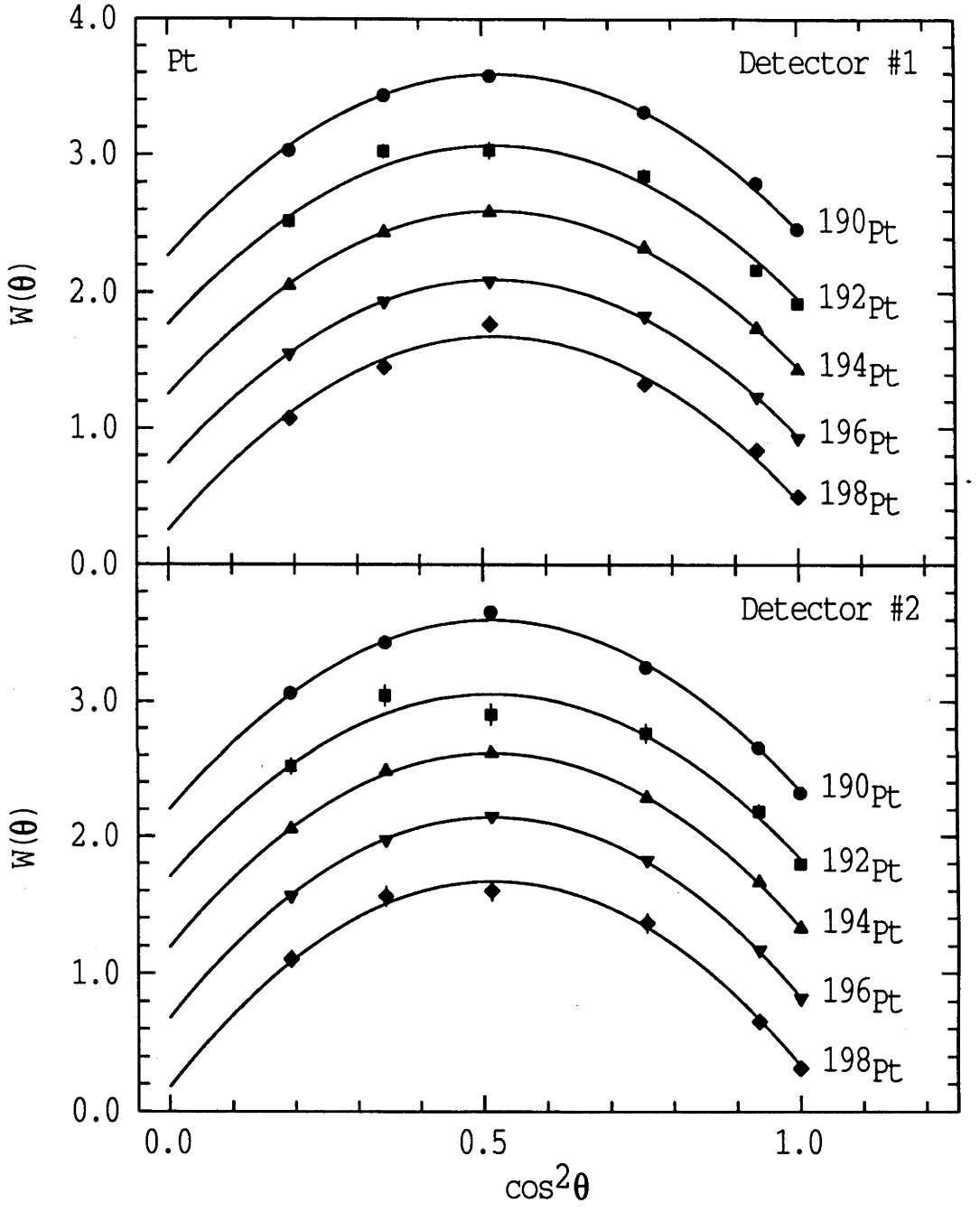

Figure 7.2: Particle–γ-ray angular correlations for the $2_1^+ \rightarrow 0_1^+$ transitions of ^{190,192,194,196,198}Pt in coincidence with backscattered ^{58}Ni beam ions. The measured (data points) and calculated (lines) correlations are shown for the γ-ray detectors in the positive and negative forward quadrants, which are labelled #1 and #2, respectively. For clarity, offsets of +2.0, +1.5, +1.0 and +0.5 have been applied to the correlations for ^{190}Pt, ^{192}Pt, ^{194}Pt and ^{196}Pt, respectively.

Table 7.1: Results of the present precession measurement for the 2_1^+ states in the Pt isotopes.

Nucleus	ϵ_F[a] ($\times 10^3$)	S_F[b]	$-\Delta\theta_F$[c] [mrad]	ϵ_B[a] ($\times 10^3$)	S_B[b]	$-\Delta\theta_B$[c] [mrad]	$-\langle\Delta\theta\rangle$[d] [mrad]
^{190}Pt	96.0(2.8)	−2.42	39.7(1.2)	−120.4(4.2)	2.83	42.5(1.5)	40.8(0.9)
^{192}Pt	102.0(5.5)	−2.40	42.5(2.3)	−119.5(7.6)	2.82	42.4(2.7)	42.5(1.8)
^{194}Pt	104.1(0.9)	−2.45	42.5(0.4)	−122.3(1.2)	2.89	42.3(0.4)	42.4(0.3)
^{196}Pt	108.0(1.8)	−2.49	43.4(0.7)	−122.7(2.4)	2.92	42.0(0.8)	42.8(0.5)
^{198}Pt	117.0(5.0)	−2.50	46.8(2.0)	−128.2(6.6)	2.93	43.8(2.3)	45.5(1.5)

[a] Measured counting asymmetries (eq. 7.5) with errors, for the forward (F) and backward (B) detector pairs.

[b] Calculated logarithmic derivative of the angular correlation (see text) for both detector pairs.

[c] Precession angle (eq. 7.3 text) for each detector pair.

[d] Weighted average of $\Delta\theta_F$ and $\Delta\theta_B$.

7.3.2 Adopted g-factors

Summarized here are the 2_1^+-state g-factors adopted from the literature for the Pt nuclei. As a general rule, lifetime-dependent values have been corrected so as to correspond to the lifetimes adopted in the compilation of Raman *et al.* [Ra87]. Although the absolute values for the g-factors in the even $^{194-198}$Pt isotopes were a subject of controversy for some time, this has been resolved (e.g. ref. [St94a]) and there is now agreement between experimental groups [St91a, Bo92, Br92, Ta93].

7.3.2.1 ^{192}Pt

For ^{192}Pt, the listed value from previous experimental work, $g(2_1^+;^{192}\text{Pt}) = 0.299 \pm 0.010$, is the weighted average of: (*i*) the IPAC results of Katayama *et al.* [Ka75] and Bodenstedt *et al.* [Bo92] and the external-field measurement of Bodenstedt *et al.* [Bo92], all normalized to the adopted meanlife of ref. [Ra87] to give $g = 0.294 \pm 0.011$; and (*ii*) the transient-field measurement of Brandolini *et al.* [Br92], which gives $g = 0.323 \pm 0.023$ relative to the present adopted value for ^{194}Pt (see below).

7.3.2.2 ^{194}Pt

The $g(2_1^+)$ value adopted for ^{194}Pt, namely $g(2_1^+;^{194}\text{Pt}) = 0.300 \pm 0.013$, is the weighted average of the IPAC result of Katayama *et al.* [Ka75], corrected for more recent lifetime data (as in ref. [St91a]), and Gd-host transient-field measurements made relative to ^{184,186}W [St91a].

7.3.2.3 ^{196}Pt

For ^{196}Pt, the adopted 2_1^+ g-factor, $g(2_1^+;^{196}\text{Pt}) = 0.297 \pm 0.010$, is the weighted average of static field data, as compiled by Berkes *et al.* [Be72] (and re-evaluated in ref. [St91a]), and transient-field measurements made relative to the W isotopes [St91a] and ^{194}Pt [Hä79, Le82, Br92, Ta93] (which were averaged and normalized to the value given above, to give $g = 0.305 \pm 0.017$).

7.3.2.4 ^{198}Pt

The results of previous transient-field measurements made on ^{198}Pt [Hä79, St81a, St91a, Ta93] have been averaged following re-evaluation for consistency with the

new adopted values for ^{194}Pt (giving $g = 0.339 \pm 0.026$ for refs. [Hä79, Ta93]) and ^{196}Pt ($g = 0.295 \pm 0.022$ for ref. [St81a]). This gives the adopted previous value of $g(2_1^+;^{198}\text{Pt}) = 0.309 \pm 0.015$.

7.3.3 Transient field calibration and absolute g-factors

Table 7.2 gives the measured transient field precessions, inferred ratios and absolute g-factors. As noted above, for each of the Pt isotopes $\tau \gg T_2$ and, therefore, ϕ (eq. 7.2) has almost the same value for all the states of interest. Evaluation of the integral ϕ gave corrections for the finite lifetimes of the order of 1%, which were insensitive to alternative assumptions for the velocity-dependence of the transient field. The measured precessions corrected for decays-in-flight are in the second column of table 7.2.

The adopted $g(2_1^+)$ for ^{194,196}Pt have been used to calibrate the transient field in the present measurement. The normalization, $\langle\phi\rangle = 144.1 \pm 5.5$, is the weighted average of the values determined from $\phi = \Delta\theta/g$ for ^{194}Pt and ^{196}Pt. The quoted error includes an uncertainty of 2.5% in the S values from corrections for detector positioning and feeding (sect. 7.3.1). The g-factors extracted by this procedure are given in the fifth column of table 7.2.

Table 7.2: Measured transient-field precession angles and inferred g-factors for the 2_1^+ states in ^{190,192,194,196,198}Pt.

Nucleus	$\Delta\theta^a$ [mrad]	$g/g(^{194}\text{Pt})^b$	$g(2_1^+)$ previous^c	present	adopted
^{190}Pt	−41.1(1.0)	0.96(3)	-	0.285(13)	0.285(13)
^{192}Pt	−42.8(1.8)	1.00(4)	0.299(10)	0.297(17)	0.299(10)
^{194}Pt	−42.7(0.4)	1.00	0.300(13)^d	-	0.300(13)
^{196}Pt	−43.2(0.7)	1.01(2)	0.297(10)^d	-	0.297(10)
^{198}Pt	−46.1(1.6)	1.08(4)	0.309(15)	0.320(17)	0.314(11)

[a] Measured precession angles (see table 7.1) with decay-in-flight corrections (see text).

[b] Derived from present results.

[c] Adopted values from previous work (see text).

[d] Previous $g(2_1^+)$ values used as a calibration for the present measurement (see text).

The present results for the isotopes ^{192}Pt and ^{198}Pt are in agreement with earlier measurements. Shown in the final column of table 7.2 are the g-factor values adopted in the discussion of chapter 9: i.e. for ^{190}Pt this is the present result; for ^{194}Pt and ^{196}Pt, the adopted previous values; and for ^{192}Pt and ^{198}Pt, the weighted average of the present and previous values.

7.3.4 Measured $B(E2; 0_1^+ \rightarrow 2_1^+)$ value for ^{190}Pt

The total γ-ray intensities of the $2_1^+ \rightarrow 0_1^+$, $4_1^+ \rightarrow 2_1^+$, $2_2^+ \rightarrow 2_1^+$ and $2_2^+ \rightarrow 0_1^+$ transitions in the decays of the ^{190,192,194,196,198}Pt nuclei were obtained from the present angular correlation data (sect. 7.2 and fig. 7.2), and corrected for γ-ray detection efficiencies and internal conversion. The relative excitation strengths for the 2_1^+ states were determined from these measured transition intensities after correcting for the isotopic abundances in the target material (sect. 7.2). The Coulomb excitation cross-sections for the 2_1^+ states in each Pt nucleus were then calculated using the version of the Winther-de Boer code described in sect. 7.2. Matrix elements for ^{194,196}Pt were taken from refs. [Li90b, Li92, Gy86]. The $B(E2; 0_1^+ \rightarrow 2_1^+)$ values in these works agree with those adopted by Raman *et al.* [Ra87]. To obtain a new experimental value for $B(E2; 0_1^+ \rightarrow 2_1^+)$ in ^{190}Pt, the matrix element $\langle 0_1^+ || M(E2) || 2_1^+ \rangle$ was varied to reproduce the observed ratio of the 2_1^+-state excitation probability in ^{190}Pt to the 2_1^+-state excitation probabilities in ^{194,196}Pt, as shown in fig. 7.3. Matrix elements for higher-excited states in ^{190}Pt were taken from model predictions and extrapolations from the heavier isotopes. Within statistical uncertainties, the chosen values were not critical due to the weak population of these states.

The value $B(E2; 0_1^+ \rightarrow 2_1^+, ^{190}\text{Pt}) = 1.823 \pm 0.088\,\text{e}^2\text{b}^2$ was obtained by averaging the results relative to ^{194}Pt and ^{196}Pt. This corresponds to a meanlife of $\tau(2_1^+, ^{190}\text{Pt}) = 89 \pm 4\,\text{ps}$ (for the γ-ray energy $E_\gamma = 295.93\,\text{keV}$ and total conversion coefficient $\alpha = 0.104$). This result agrees very well with, but is more precise than, the early Coulomb excitation work of Grodzins *et al.* [Gr66b] (using a sample enriched to only 0.85% in ^{190}Pt): $B(E2; 0_1^+ \rightarrow 2_1^+, ^{190}Pt) = 1.75 \pm 0.22\,\text{e}^2\text{b}^2$ or $\tau(2_1^+) = 93 \pm 12\,\text{ps}$ (normalized to the present adopted value for $B(E2; 0_1^+ \rightarrow 2_1^+)$ in ^{194}Pt [Ra87]). The only direct measurement of this lifetime [Fi72] gave the rather imprecise value of $\tau(2_1^+) = 65 \pm 22\,\text{ps}$.

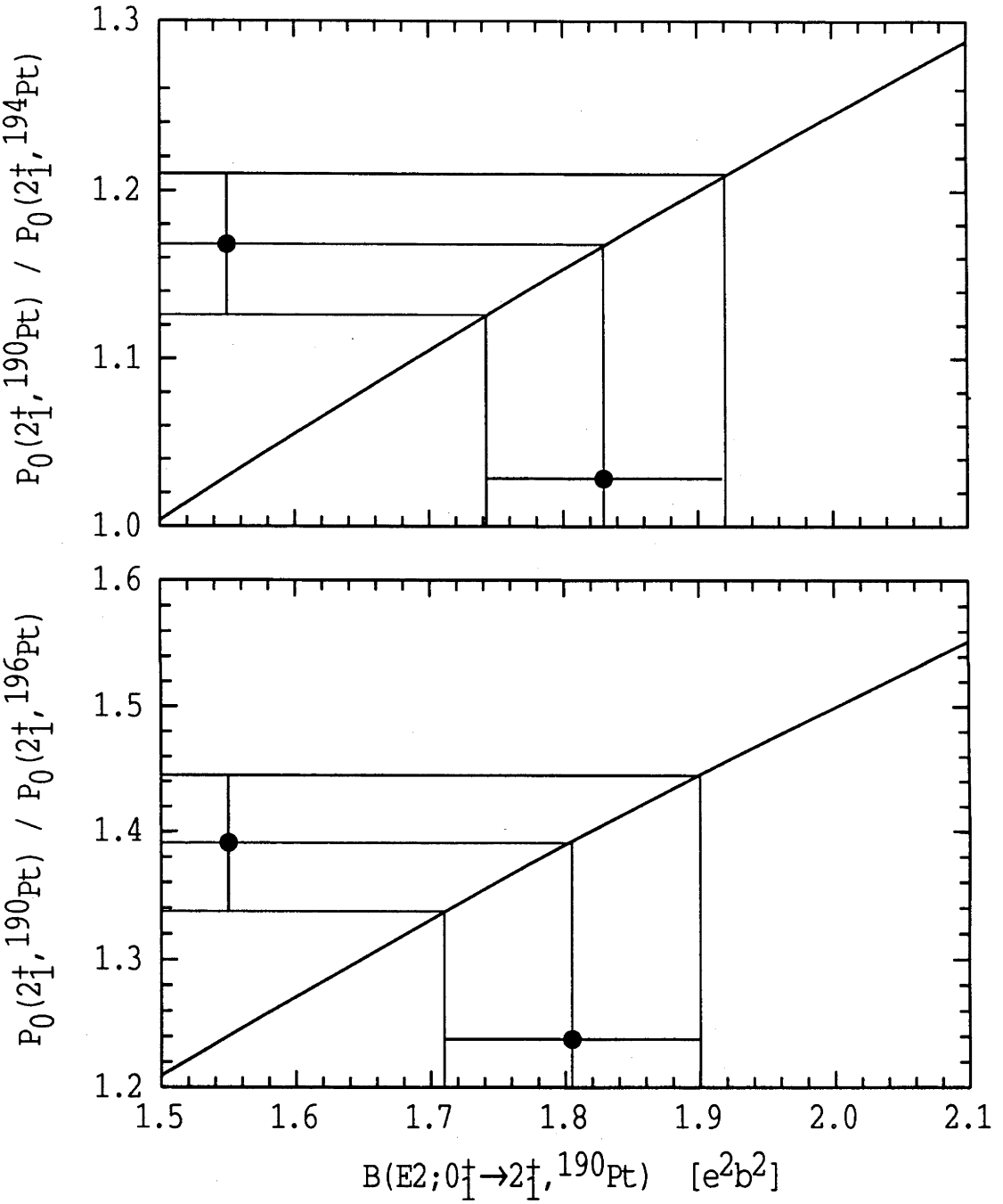

Figure 7.3: Plots of the $B(E2; 0_1^+ \rightarrow 2_1^+)$ value in ^{190}Pt versus the measured ratios of the 2_1^+-state excitation probability in ^{190}Pt to those in ^{194}Pt and ^{196}Pt.

Chapter 8

Lifetime Measurement for ^{188}Pt

8.1 Motivation

In the implantation-decay experiments, the precessions of the first-excited 2^+ states in ^{184,186,188,192}Pt were measured with precisions of 7% or better (table 6.1). To extract $g(2_1^+)$ values from these measured quantities, however, the 2_1^+-state lifetimes for the nuclei are needed. While these meanlives for the ^{184,186,192}Pt isotopes have all been measured precisely with errors of less than 4%; $\tau(2_1^+, ^{192}\,\mathrm{Pt}) = 62.1 \pm 2.0\,\mathrm{ps}$, $\tau(2_1^+, ^{186}\,\mathrm{Pt}) = 375 \pm 14\,\mathrm{ps}$ and $\tau(2_1^+, ^{184}\,\mathrm{Pt}) = 519 \pm 17$ or $581 \pm 22\,\mathrm{ps}$ (see table 6.1), the uncertainty of nearly 20% in the only previous measurement of the meanlife in ^{188}Pt [Fi72], $\tau(2_1^+) = 104 \pm 19\,\mathrm{ps}$, would lead to an imprecise value for the 2_1^+-state g-factor in this nucleus. This prompted the present lifetime measurement.

8.2 The Doppler-shift Recoil-distance Method

The 2_1^+-state lifetime in ^{188}Pt was measured using the Doppler-shift recoil-distance method, following a heavy-ion induced nuclear reaction. This is a well-established technique [St76] and, consequently, only a brief overview is given here. As shown in fig. 8.1, excited nuclei of interest recoil across a vacuum gap of variable distance, D, between a target foil and a metal stopper, at a known and constant velocity, v. For forward (backward) detection angles the Doppler effect causes the γ-radiation from nuclei decaying during flight to be shifted, by ΔE, to a higher (lower) energy than that from recoils in the stopper. The lifetime of the excited nuclear state may be determined from the number of recoils measured as

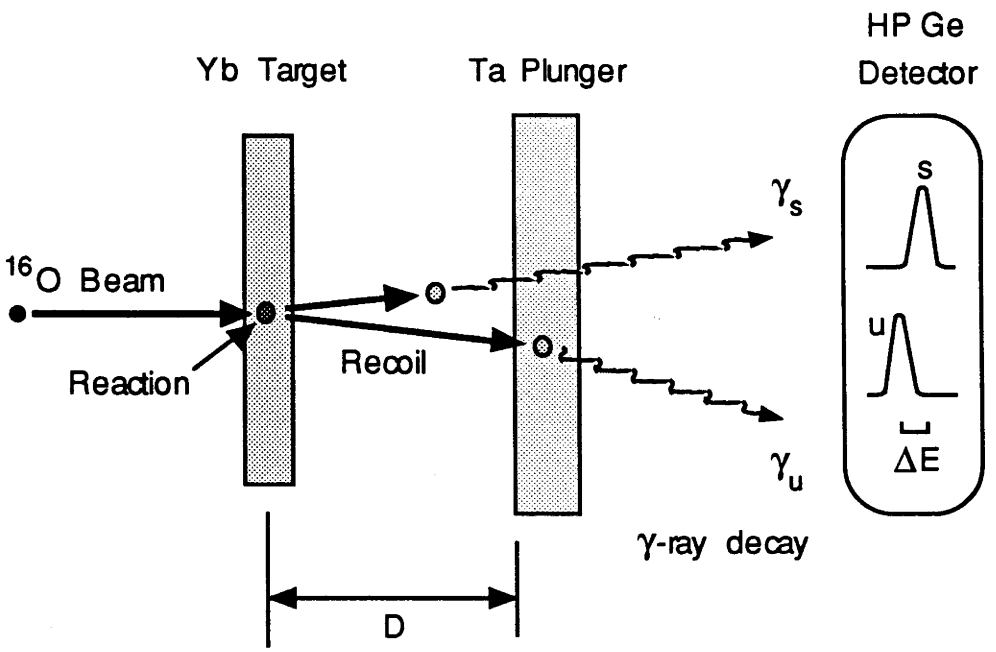

Figure 8.1: Schematic of the basic experimental arrangement for the Doppler-shift recoil-distance technique (adapted from ref. [St76]).

surviving for selected times $t = D/v$.

The ratio R of the intensity of the 'shifted' (from the in-flight decays) and 'unshifted' (stopped nuclei) components, for the corresponding γ-ray transition de-exciting the level, is formed as

$$R = \frac{I_{st}}{I_{st} + I_{sh}} = e^{-D/v\tau} \quad . \tag{8.1}$$

Thus, in principle, the slope of a plot of $\ln R$ versus D yields the state lifetime, τ. In practice, however, there are a number of corrections which must be made. When populating the nuclei in a heavy-ion induced reaction it is necessary to consider the effects of cascade feeding. Along with feeding corrections, the effects of a finite target thickness and attenuation of the γ-ray angular distribution, due to vacuum deorientation of the nuclear alignment produced in the reaction, must be accounted for. There are also corrections for the position- and velocity-dependence of the detector solid-angle, and a small change in detector efficiency for the shifted and unshifted γ-ray energies. A thorough treatment of these is given in ref. [St76].

8.3 Experimental Details

The measurement was made with a 'plunger' device [Si77, Li90a], similar to that described in ref. [Al70]. Four days of beam time at the ANU 14UD Pelletron accelerator laboratory were used. The nuclei were formed in the $^{176}Yb(^{16}O, 4n)^{188}Pt$ reaction at a beam energy of 78 MeV. The γ-rays were measured in two HPGe detectors, with 1 mm thick Cd and Cu absorbers to reduce the low-energy γ-ray flux, placed at angles of 0° and 150° to the beam direction and 12 cm from the target. A thin ($220\,\mu g/cm^2$) layer of enriched ^{176}Yb was evaporated on the 'downstream' side of a stretched, $1.40\,mg/cm^2$ thick Ta foil.

The energy produced in the ion-beam bombardment gave the recoiling nuclei a velocity of $0.7\%\,c$ ($\simeq 2\,\mu m/ps$). For the $2_1^+ \rightarrow 0_1^+$ transition in ^{188}Pt with $E_\gamma =$ 266 keV, this resulted in a Doppler shift of $\sim$ 2 keV. The recoils were stopped in a $\sim 10\,mg/cm^2$ thick stretched Ta foil. Data were taken in measurements of approximately 2 hours duration for 33 target-to-stopper distances ranging from 10 μm to 2.2 mm, corresponding to times-of-flight of $\sim$ 5 ps to 1 ns.

8.4 Experimental Results

The relevant part of the ^{188}Pt decay scheme [Si90a] is shown in fig. 8.2. The rather complex feeding patterns for the low-lying levels of the ground-state band are in accord with the transition strengths measured in the present experiment.

The γ-ray spectrum collected in the detector at 0° with the small target-to-stopper separation of 10 μm, where all of the γ-decay is effectively from stopped recoils, is displayed in fig. 8.3. Immediately obvious is the level of background radiation from heavy-ion induced reactions with Ta. Although the cross-sections for ^{16}O on ^{181}Ta are much lower than for ^{16}O on ^{176}Yb, there was much more material in the Ta target support and stopper than the Yb target. Along with the significant γ-radiation from Coulomb excitation of ^{181}Ta, there are decays of compound-nucleus reaction products, primarily ^{193}Tl (which are marked in fig. 8.3), ^{194}Tl and ^{193}Hg. There is also radiation from the Coulomb excitation of the ^{176}Yb target material.

Apparent in the lower frame of fig. 8.3, the peak corresponding to the $4_1^+ \rightarrow 2_1^+$ transition in ^{188}Pt is unresolved from contaminant radiation near 405 keV, of which a γ-ray in the decay of ^{193}Tl is a large component. Also, the 514 keV

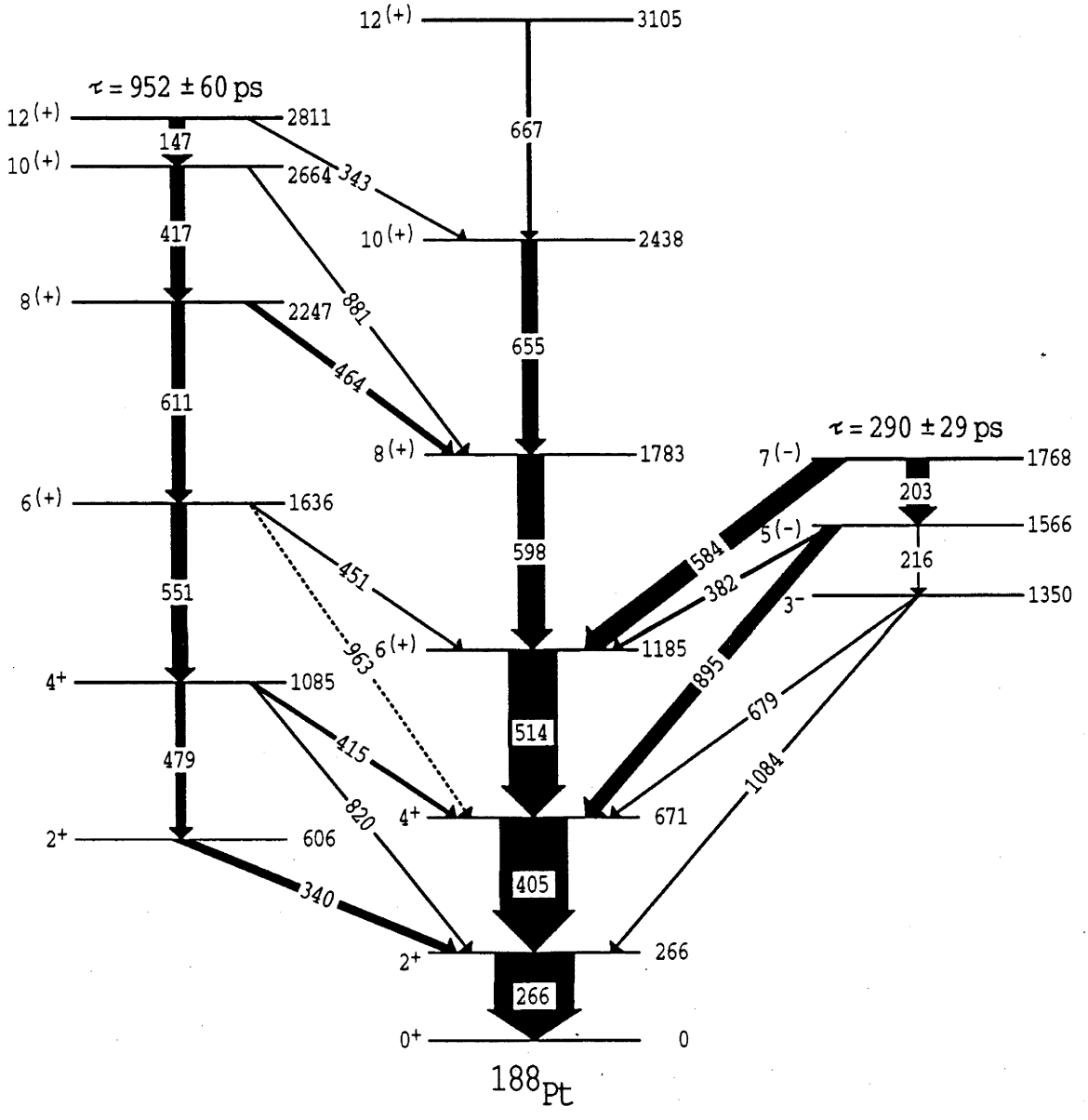

Figure 8.2: Partial decay scheme for ^{188}Pt, populated directly in a (HI, x n) reaction [Si90a].

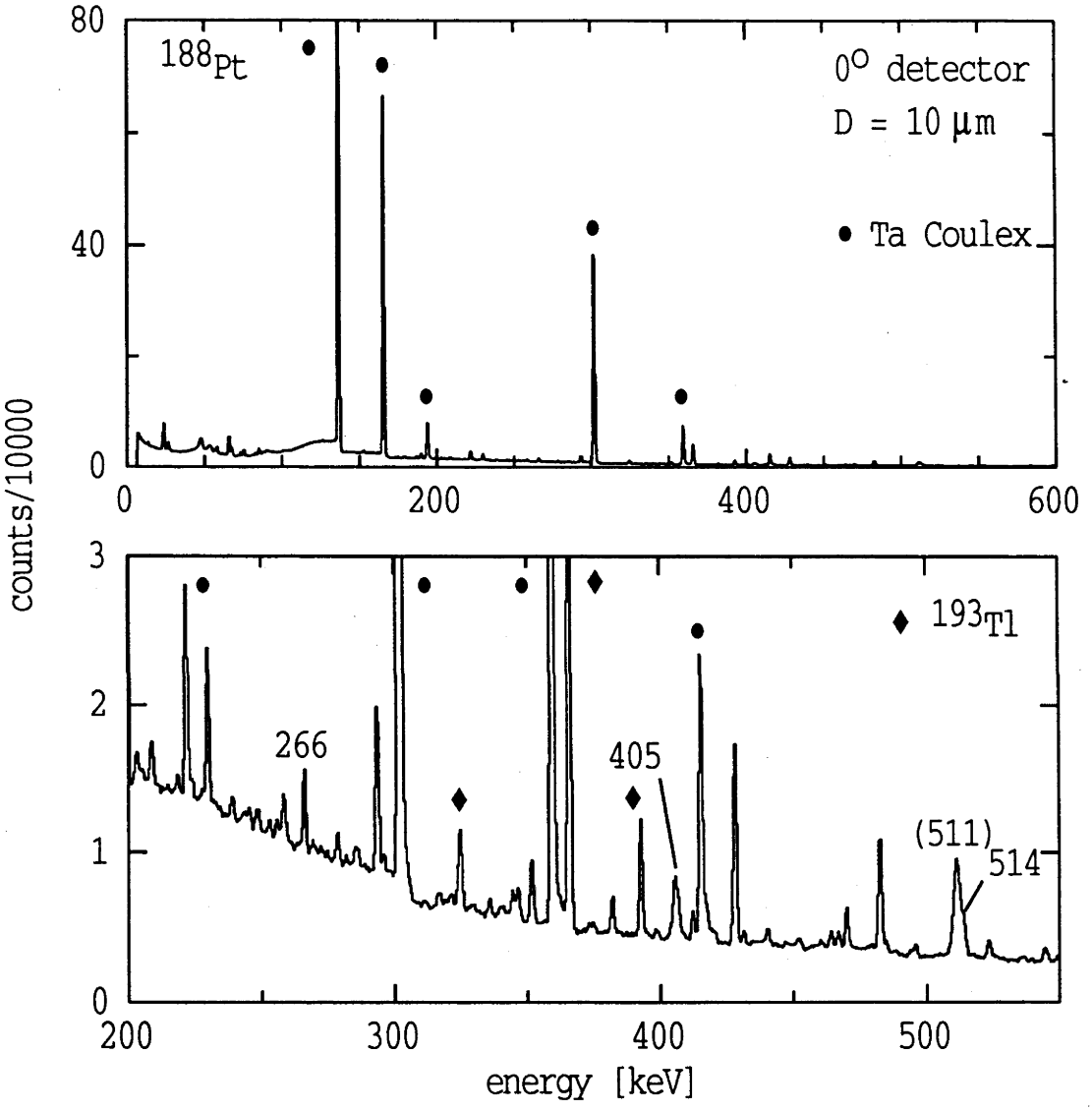

Figure 8.3: The spectrum recorded in the 0° γ-ray detector for a target-to-stopper distance of 10 μm. The peaks labelled by their γ-ray energy are in the decay of ^{188}Pt (as shown in the decay scheme of fig. 8.2), except for the 511 keV line. Contaminant radiation (see text) is also marked.

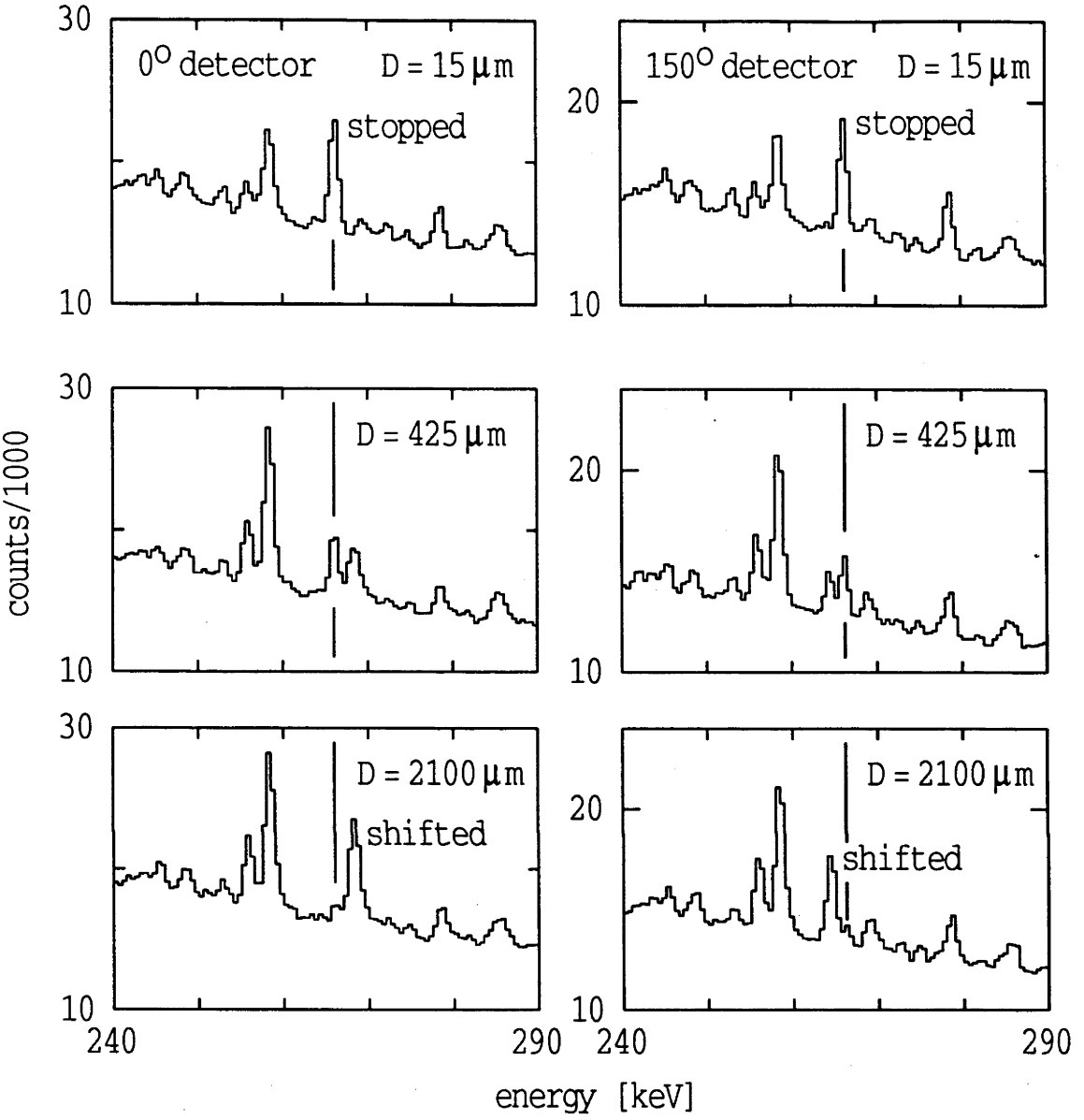

Figure 8.4: The spectra (for 240 keV $\lesssim E_\gamma \lesssim$ 290 keV) observed in both detectors (at forward and backward angles of 0° and 150°, respectively) for target-to-stopper separations of 15, 425 and 2100 μm.

$6_1^+ \rightarrow 4_1^+$ transition is on the high-energy side of the broad peak at 511 keV from positron annihilation.

Figure 8.4 shows typical spectra for peaks from the 266 keV $2_1^+ \rightarrow 0_1^+$ γ-ray, as measured in both detectors and with different target-to-stopper distances. For the forward angle of 0° the Doppler effect increases the γ-ray energy, whereas in the backward angle (150°) detector the radiation from the nuclei decaying in-flight is lowered from that for the stopped recoils. For the 266 keV line, the shifted and

stopped peaks are clearly resolved from one another in both detectors.

The contaminant γ-radiation emitted following the radioactive decay of the initial reaction products is recognizable in this diagram. The peaks at 255 keV and 258 keV became progressively larger as the activity increased; the chronological order of the runs was from smaller to larger distances. Another peak of approximately half the intensity of the 255 keV line is situated at 268.5 keV, underneath the forward-shifted component of the $2_1^+ \rightarrow 0_1^+$ transition. This made a difficult correction necessary when measuring this peak area in the 0° detector.

In both detectors the shifted components of the $4_1^+ \rightarrow 2_1^+$ transition were somewhat removed from the contaminant radiation near 405 keV, allowing measurement of their intensities. The stopped peaks, however, were not clearly resolved and in the backward detector, where less data were collected, the extraction of an area was not possible. For the $6_1^+ \rightarrow 4_1^+$ transition, a reliable measurement was possible only for the forward-angle shifted peak at 518 keV.

8.5 Data Analysis and the Extracted Lifetime

For each transition, as seen in both detectors, stopped and shifted decay curves were extracted from the corresponding peak areas that were able to be measured: for the $2_1^+ \rightarrow 0_1^+$ transition, all the decay curves were obtained; for the $4_1^+ \rightarrow 2_1^+$ transition, all except the stopped curve in the 150° detector; and for the $6_1^+ \rightarrow 4_1^+$ γ-ray, only the forward-shifted curve. Consequently, only the ratio sets for the $2_1^+ \rightarrow 0_1^+$ γ-ray from both detectors and the $4_1^+ \rightarrow 2_1^+$ in the forward detector were determined. These are shown in fig. 8.5 and have the features expected for cascade decays in the ground-state band of a nucleus populated following a (HI, x n) reaction, where there is significant feeding from higher-excited levels with longer lifetimes.

The analysis of the decay curves was performed with the computer code LIFETIME [We85]. This code was specifically designed for measurements following (HI, x n) reactions, in that it allows for side-feeding to the levels and accounts for the effects described in sect. 8.2. Further, it allows the stopped and shifted peaks to be fitted separately, which is imperative in situations, like the present, where one or the other may be contaminated.

In least-squares fits to the decay curves, the meanlives of the states in the ground-state band were varied. The lifetimes and relative populations of relevant

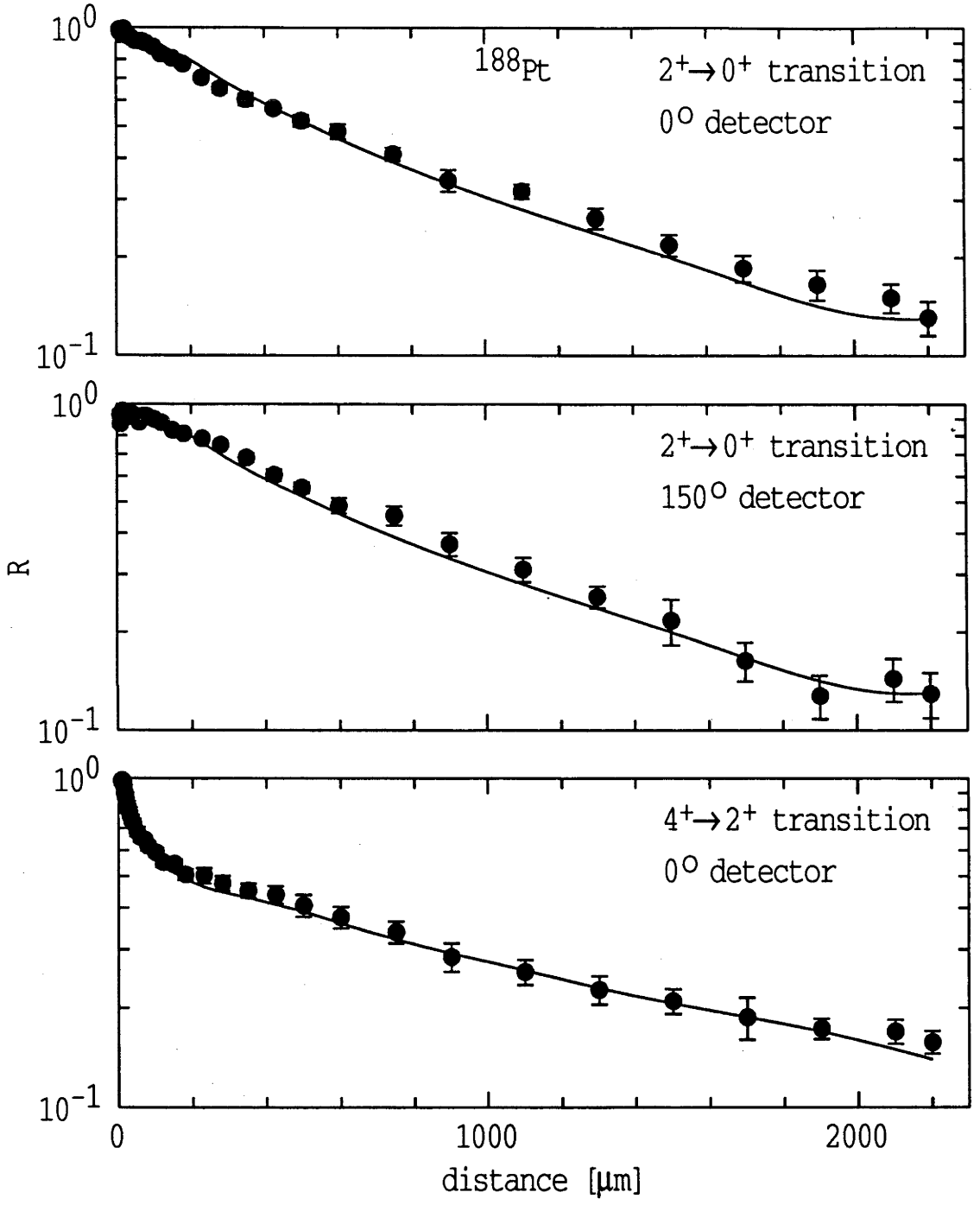

Figure 8.5: The ratio decay curves (see text) for the $2_1^+ \rightarrow 0_1^+$ transition measured in both detectors and $4_1^+ \rightarrow 2_1^+$ transition in the forward detector. The best-fit calculations (lines) are also shown.

feeding states and the branching ratios for the transitions depopulating these levels were fixed where possible, with values as specified in the decay scheme of fig. 8.2, or varied with restrictions, in accord with the specifications of the code. The best-fit to the decay curves, illustrated partially in fig. 8.5 which shows the ratios R, gave the meanlife for the 2_1^+ state as 91 ± 7 ps.

The precision of this measurement was severly limited by our inability to extract many peak areas, as noted in sect. 8.4, due to contaminant radiation. The most important consequence of this was the loss of data for the higher-lying 4_1^+ and 6_1^+ states, which carries information on the amount and path of cascade feeding. There were long-lived components to the side-feeding, originating from the states at 1768 and 2811 keV with meanlives of 290 ± 29 and 952 ± 60 ps, respectively [Si90a] (see fig. 8.2), which significantly reduced the sensitivity of the $2_1^+ \rightarrow 0_1^+$ decay curve to the lifetime of the first-excited state.

Nevertheless, the present result is a marked improvement on the $\sim 20\%$ precision of the only previous measurement [Fi72] which gave $\tau(2_1^+) = 104 \pm 19$ ps. The weighted average of these values yields $\tau(2_1^+, {}^{188}\mathrm{Pt}) = 93 \pm 7$ ps. To improve upon this, and measure the lifetimes of higher-excited states in ^{188}Pt, would require repetition of the present experiment with some form of discrimination to eliminate the contaminant γ-rays from nuclear reactions on the stopper material. (There is no alternative reaction available.)

8.6 The 2_1^+ Lifetime Data for Even Pt Nuclei

In fig. 8.6, the $B(E2; 0_1^+ \rightarrow 2_1^+)$ values for the even $^{182-198}$Pt nuclei are presented. They show a general increase for decreasing mass, consistent with greater collectivity approaching midshell, and possibly hint at a change in structure at $A \simeq 190$. These changing $B(E2)$ values contrast with the constancy of the Pt 2_1^+-state g-factors. In the attempts to describe the g-factor systematics which follow (sects. 9.3.1.2 and 9.3.2.1), we will also try to reproduce the $B(E2)$ data.

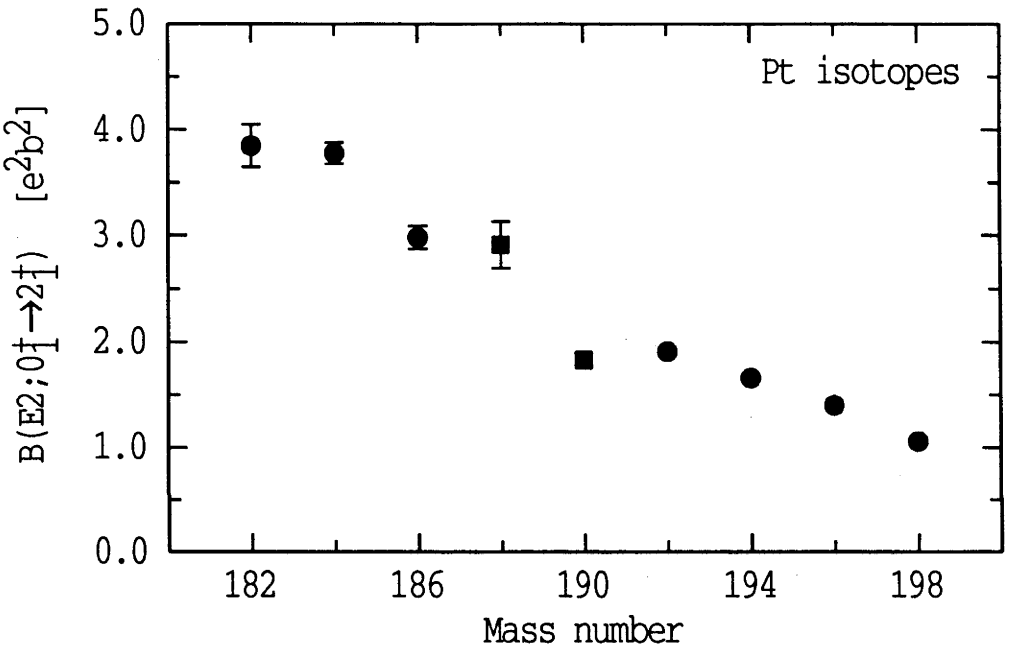

Figure 8.6: Plot of measured $B(E2; 0_1^+ \rightarrow 2_1^+)$ for the Pt isotopes. The values were taken from a number of sources: for ^{182}Pt, from ref. [Wa93]; for ^{184}Pt, determined from the meanlife given in sect. 6.6 (which is the weighted average of the measured lifetimes in refs. [Fi72] and [Ga86]); for ^{188}Pt, determined from the lifetime quoted above; for ^{190}Pt, as reported in chapter 7; and for $^{186,192-198}$Pt, from the compilation of Raman *et al.* [Ra87]. Not shown is $B(E2; 0_1^+ \rightarrow 2_1^+, ^{180}\text{Pt}) = 6.8 \pm 0.4$ e^{2}b^2 [Vo90].

Chapter 9

Discussion

9.1 Introduction

The experimental work reported in chapters 6 and 7 has significantly extended the mass-dependent systematics for the g-factors of the first-excited states in the even Pt nuclei. Infact, there is now magnetic moment data for the even isotopes from ^{184}Pt to ^{198}Pt, which almost span the upper half of the valence neutron shell. These 2_1^+-state g-factors (taken from tables 6.1 and 7.2) are presented in fig. 9.1.

The measured 2_1^+ g-factors for the Pt isotopes remain almost constant, with only a slight decrease with decreasing mass. The present transient-field measurement (chapter 7) confirmed the constancy, within experimental uncertainties, of the $g(2_1^+)$ values in the heavier $^{192-198}$Pt nuclei [St91a]. This trend is continued to lighter mass with the new results of the present work, namely: the value for ^{190}Pt also from the transient-field experiment, and the implantation-decay results for ^{184,186,188}Pt, which constitute the first g-factor measurements made on the unstable even Pt nuclei.

This behaviour of the Pt g-factors is in contrast with the marked inter-nucleus variations of the $g(2_1^+)$ for the isotopes of the neighbouring W and Os nuclei, as displayed in fig. 9.2 and to be considered in detail in sect. 9.3. Also shown in fig. 9.2 and as noted in sect. 2.2.3, the simple, geometrical-model estimate of $g = Z/A$ (sect. 1.2.1) fails to reproduce the mass-dependent systematics observed for $g(2_1^+)$ in the W and Os nuclei. In contrast, the constancy of the neighbouring Pt g-factors is approximated, although the magnitude is overestimated by $25-30\%$.

The proton-neutron interacting boson model (IBM-2, sect. 2.2), in the limit

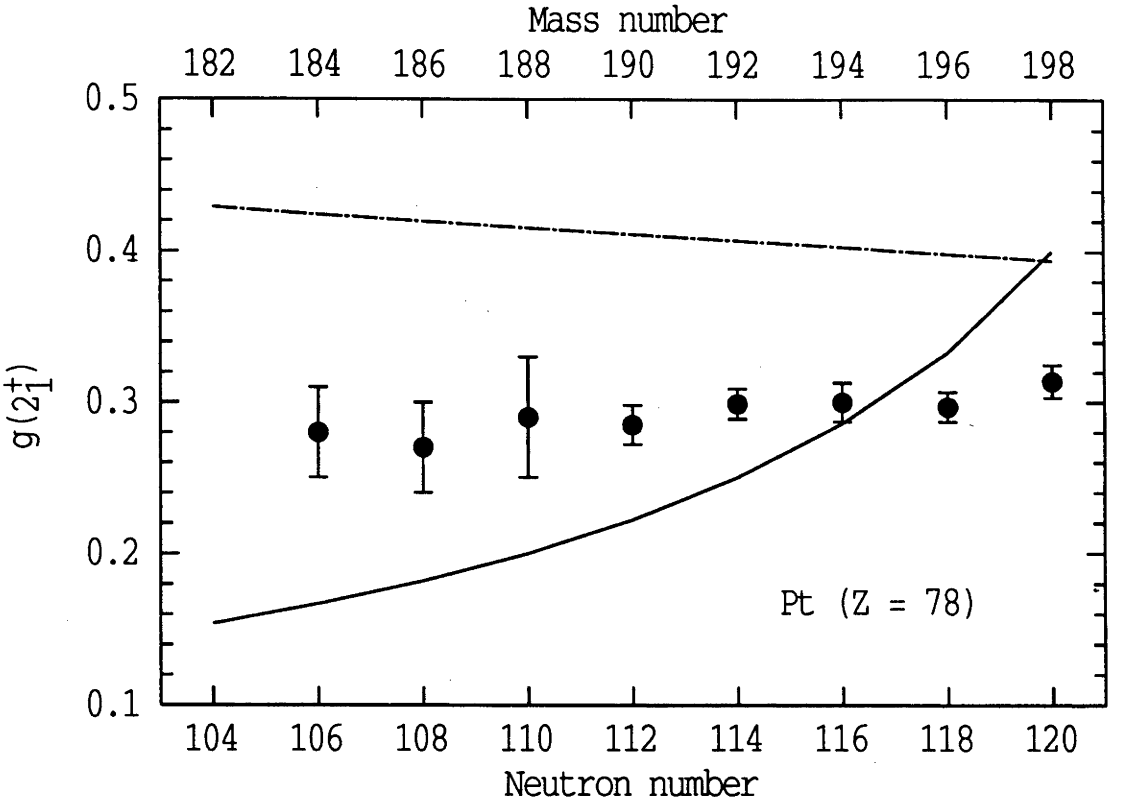

Figure 9.1: The experimental $g(2_1^+)$ values for the even $^{184-198}$Pt isotopes. Also shown are the simple IBM-2 estimate of eq. 2.13 (solid line) and $g = Z/A$ (sect. 1.2.1, dot-dashed line).

of F-spin symmetry, predicts a g-factor mass variation (described by eq. 2.13) in clear disagreement with the constant Pt $g(2_1^+)$ values (fig. 9.1), even though it does reproduce the W and Os data quite well (fig. 9.2). After a brief survey of other theoretical calculations, the IBM-2 description of the magnetic dipole moments for the Pt nuclei will be the focus of the following discussion. Firstly, in sect. 9.2, the phenomenon of shape coexistence is incorporated approximately into IBM-2 calculations for the lighter isotopes with $A \leq 188$. Then in sect. 9.3, recent developments in the IBM-2 description [Ba92, Wo93, Da94b, Ku95, St94b] are considered for the heavier $^{190-198}$Pt isotopes, particularly, the effects of F-spin mixing on the g-factors and $2_2^+ \rightarrow 2_1^+$ $M1$ transition rates.

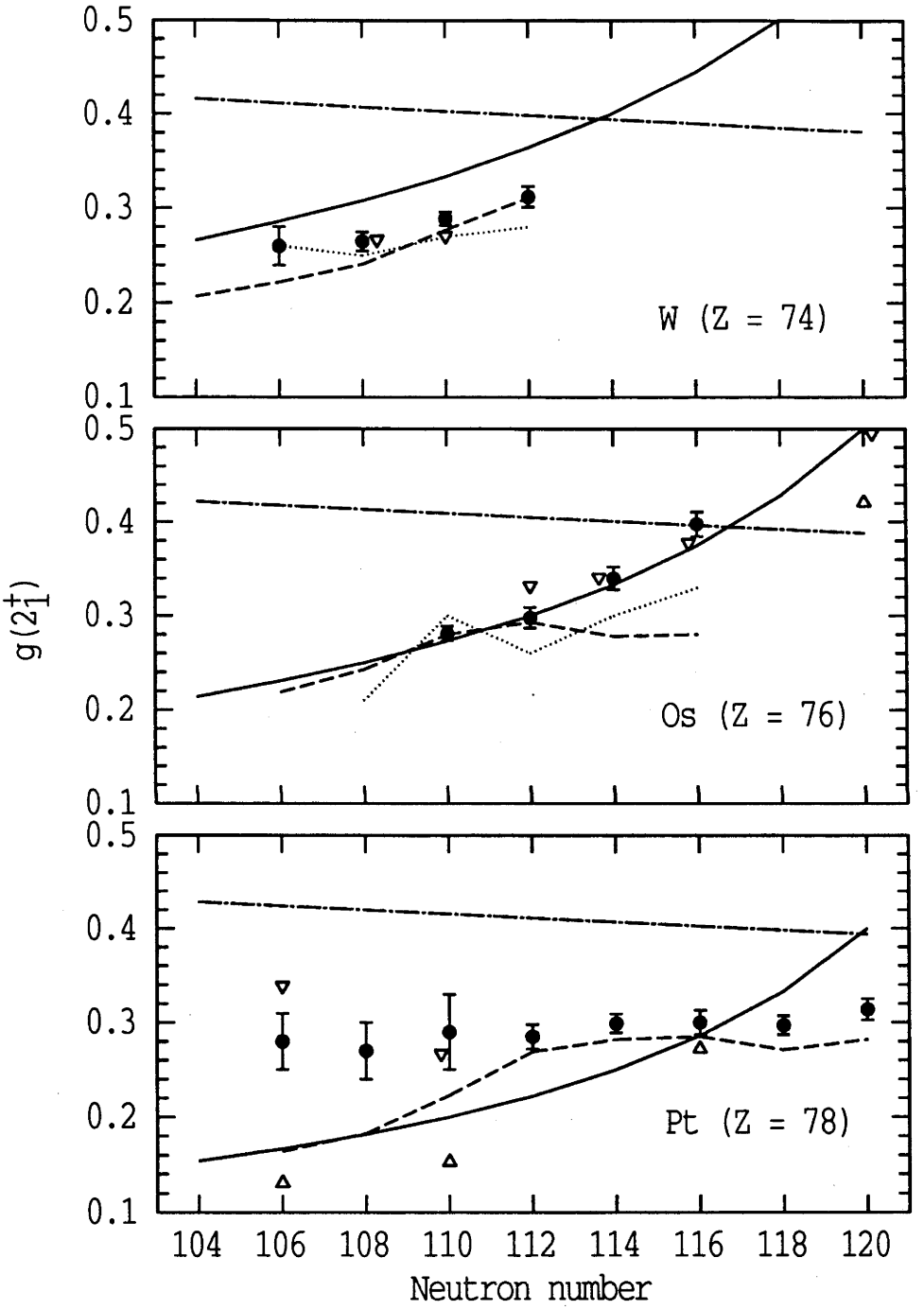

Figure 9.2: Comparison of experimental $g(2_1^+)$ (filled points) for the even $^{180-186}$W [Zi73, Pe68, Al84, St91a], $^{186-192}$Os [Wa70, St92] and $^{184-198}$Pt nuclei with the IBM estimate and the calculations of Prior *et al.* [Pr68], Kumar and Baranger [Ku68] (dotted and dashed lines, respectively) and Sprung *et al.* [Sp79] for oblate (open triangles) and prolate (upside down triangles) deformations.

9.1.1 Comparison with models other than the IBM

This section includes a brief review of the magnetic dipole properties of the transitional nuclei as described by several distinct theoretical models other than the IBM. The calculated 2_1^+ magnetic moments from boson expansion theory (BET) [We80] (not shown in fig. 9.2) mimic the trend of the IBM-2 estimate but are somewhat larger in magnitude. Figure 9.2 compares the experimental $g(2_1^+)$ for the even $^{180-186}$W, $^{186-192}$Os and $^{184-198}$Pt isotopes with several calculations based on the cranking model. The early works of Nilsson and Prior [Ni61, Pr68], where odd-even mass differences were used to determine pairing strength parameters, and Kumar and Baranger [Ku68], with the pairing-plus-quadrupole model, both used pair-correlated, deformed Nilsson single-particle wavefunctions. Sprung *et al.* [Sp79] calculated the g-factors for certain nuclei with the cranking formalism and wavefunctions determined in density-dependent Hartree-Fock calculations.

In transitional nuclei that are soft towards γ-deformation, the single-particle orbitals can be rearranged or aligned with small driving forces and a thorough microscopic treatment becomes very involved. An unfortunate consequence is that only Kumar and Baranger [Ku68] have fully examined the 2_1^+ g-factor systematics for the Pt isotopes. Their prediction is in reasonable agreement with the experimental $g(2_1^+)$ values for the heavier $^{190-198}$Pt nuclei but fails for the lighter isotopes. These pairing-plus-quadrupole model calculations also adequately describe the 2_1^+ g-factors for the W and Os isotopes, with the obvious exceptions of ^{190,192}Os (fig. 9.2). Ansari [An88] has made extensive calculations of the Os isotopes and found it necessary to adjust either the strength of the pairing force in the pairing-plus-quadrupole hamiltonian or the single-particle energies for the $\pi h_{11/2}$ (see fig. 9.5) and $\nu i_{13/2}$ orbitals to reproduce the observed marked increase in $g(2_1^+)$ with mass. The extension of semi-microscopic calculations to include the Pt isotopes has been promised by Saha and Sen [Sa93].

The phenomenon of shape coexistence is believed to exist in the lighter Pt nuclei, see e.g. ref. [Wo92]. Indeed, Sprung *et al.* [Sp79] have made separate calculations of g-factors in ^{184,188}Pt assuming prolate- and oblate-static deformations. In sect. 9.2.2, a band-mixing interpretation of the low-lying levels in ^{184,186,188}Pt is introduced to account for the 2_1^+-state g-factors.

9.2 Interpretation of the ^{184,186,188}Pt g-factors

9.2.1 Shape coexistence

The level schemes and spectroscopies of the very neutron-deficient Pt isotopes ($A \leq 186$) are indicative of nuclear structures with different deformations coexisting at low-excitation energies and interacting at low spin. Spectroscopic studies provided the first experimental evidence of a larger than expected $2_1^+ \rightarrow 0_1^+$ transition energy in each nucleus, compared with transitions between levels in the ground-state band at higher spin, which implies increasing deformation in the yrast band with increasing spin [Ha78]. The level energy systematics for the even Pt isotopes are displayed in fig. 9.3. From the observation of low-lying ($\sim 500\,\mathrm{keV}$) excited 0^+ states and 2^+ and 4^+ levels [Fi72], it was proposed that the mutual repulsion of the 0^+ states in a nucleus, caused by their mixing, lowers the ground-state energy [Wo81]. The large $2_1^+ \rightarrow 0_1^+$ transition energies show that this effect is much smaller for the 2^+ states (of the rotational bands built on the structures) because they have a much larger initial separation than the 0^+ states. The level schemes may then be interpreted in terms of two rotational bands having different moments of inertia (i.e. distinct deformations), which interact to produce the observed states.

In qualitative accord with this experimental situation, several microscopic calculations using different techniques have found two coexisting minima in the potential energy surfaces for the ^{182,184,186}Pt nuclei [Ku68, We80, He81, Be87b]. These correspond to nuclear shapes with large prolate ($\gamma = 0°$) and weakly oblate ($\gamma = 60°$), or near-spherical, deformations. Figure 9.4 displays the potential wells for certain even Pt nuclei calculated by Bengtsson *et al.* [Be87b]. Apparent for ^{184}Pt is a prolate ground-state and an excited oblate secondary-minimum. In ^{180}Pt, the oblate minimum was found to have a somewhat higher excitation-energy relative to the ground-state than in ^{184}Pt. Also shown are calculations for ^{188}Pt, which has similar energies for prolate and oblate shapes and is very soft towards γ-deformation, and ^{192}Pt with a single oblate-minimum, which is typical for the heavier Pt isotopes.

The more-deformed structure has been ascribed to an intruder configuration formed by the promotion of a proton pair across the $Z = 82$ shell gap into the $h_{9/2}$ orbital. Wood [Wo82] suggested that this configuration is deformed, noting

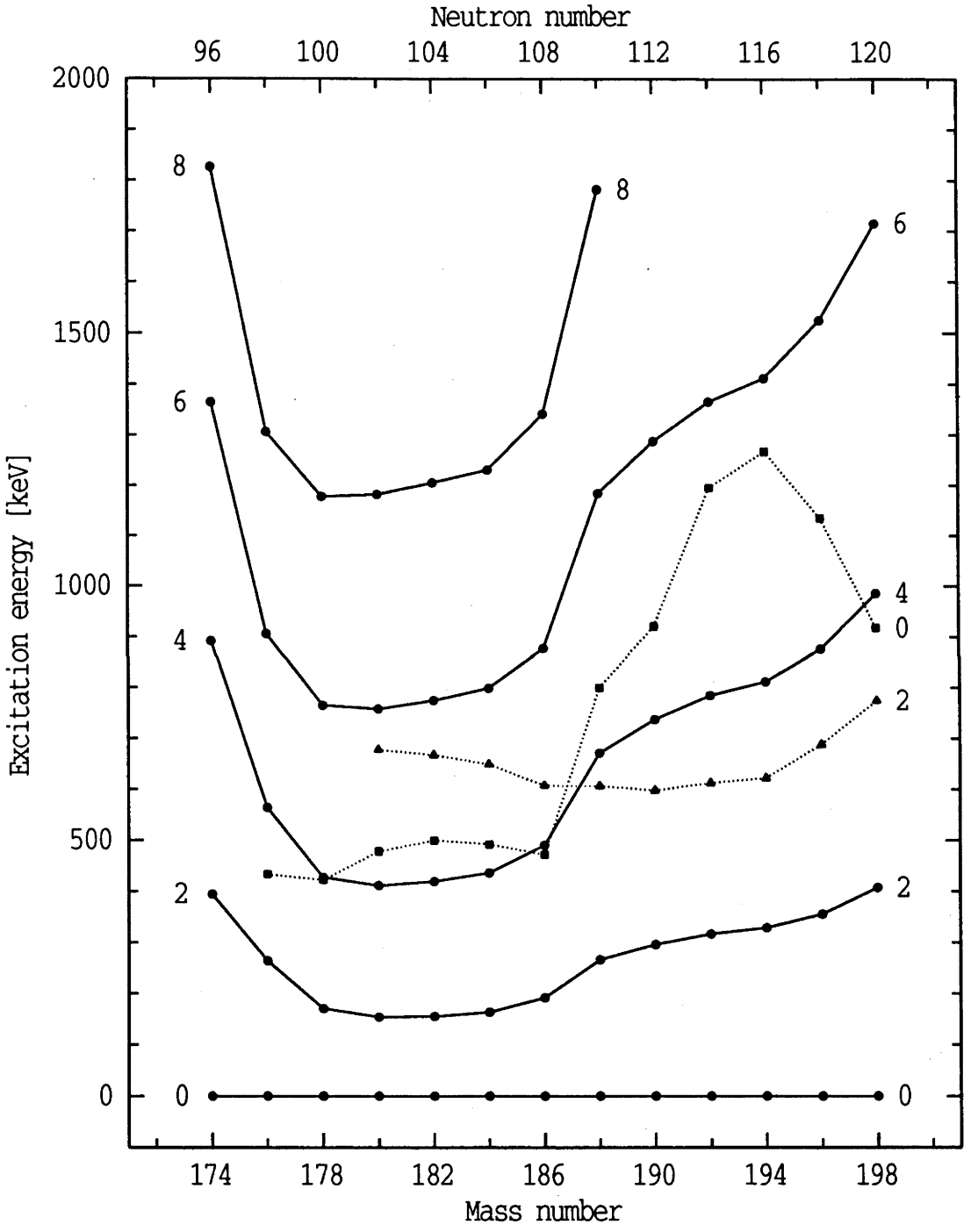

Figure 9.3: The energy level systematics for the even Pt isotopes.

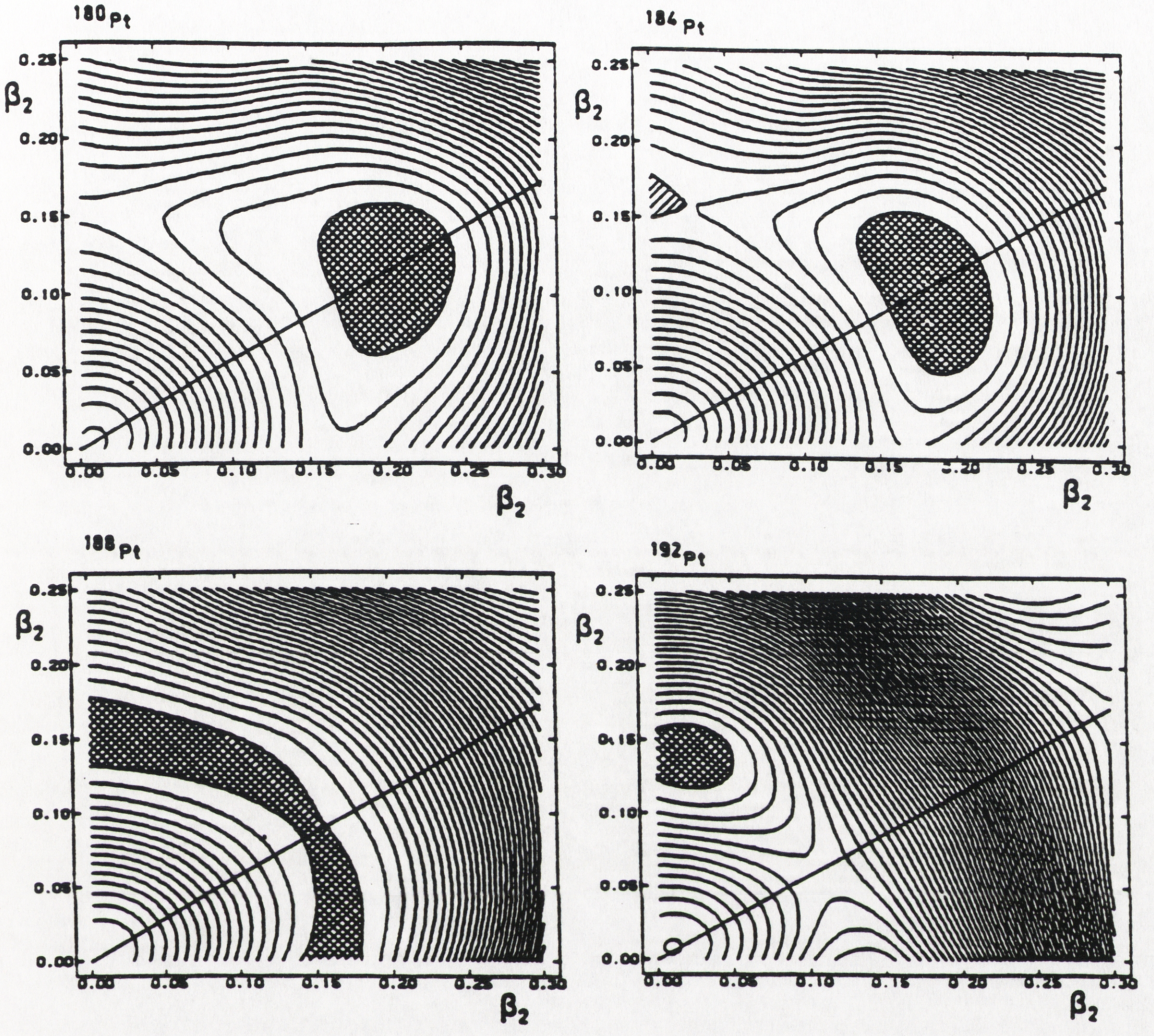

Figure 9.4: Calculated potential energy surfaces in the (β_2, γ)-plane for ^{180,184,188,192}Pt, from ref. [Be87b]. Contour lines represent an energy difference of 0.1 MeV.

that the proton excitations optimise the attractive proton-neutron interaction between valence nucleons by increasing the effective number of valence protons, through both the occupation of the $h_{9/2}$ orbital above the $Z = 82$ shell and by the creation of holes in the $h_{11/2}$ and $d_{3/2}$ valence orbitals. As can be seen in the Nilsson diagram of fig. 9.5, the downward sloping lines with increasing deformation, ϵ_2 ($\propto \beta_2$), for the low Ω orbitals with $h_{9/2}$ parentage, indicate that these proton orbitals favour (larger) prolate deformations.

A representation of the relevant proton configurations in the even Pt nuclei is shown in fig. 9.6. The energy of the deformed, intruder (proton 6 hole – 2 particle) configuration is reduced in energy with respect to the normal (proton 4 hole) one by the residual proton-neutron force. This attractive interaction increases with

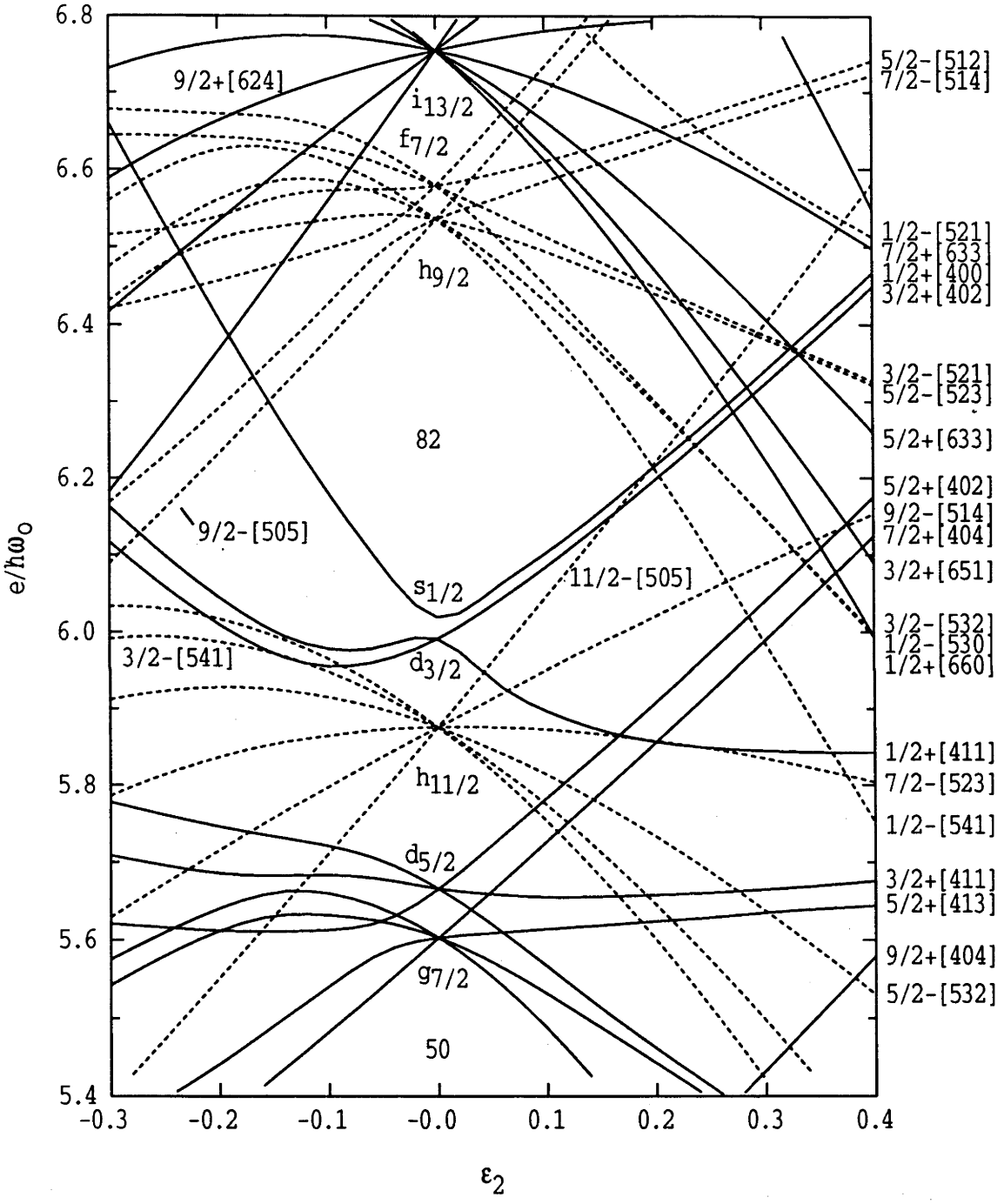

Figure 9.5: Nilsson diagram for protons near the $Z = 82$ shell gap (with $\epsilon_4 = \epsilon_2^2/6$), where $\beta_2 \simeq 1.06\epsilon_2 + 0.35\epsilon_2^2$.

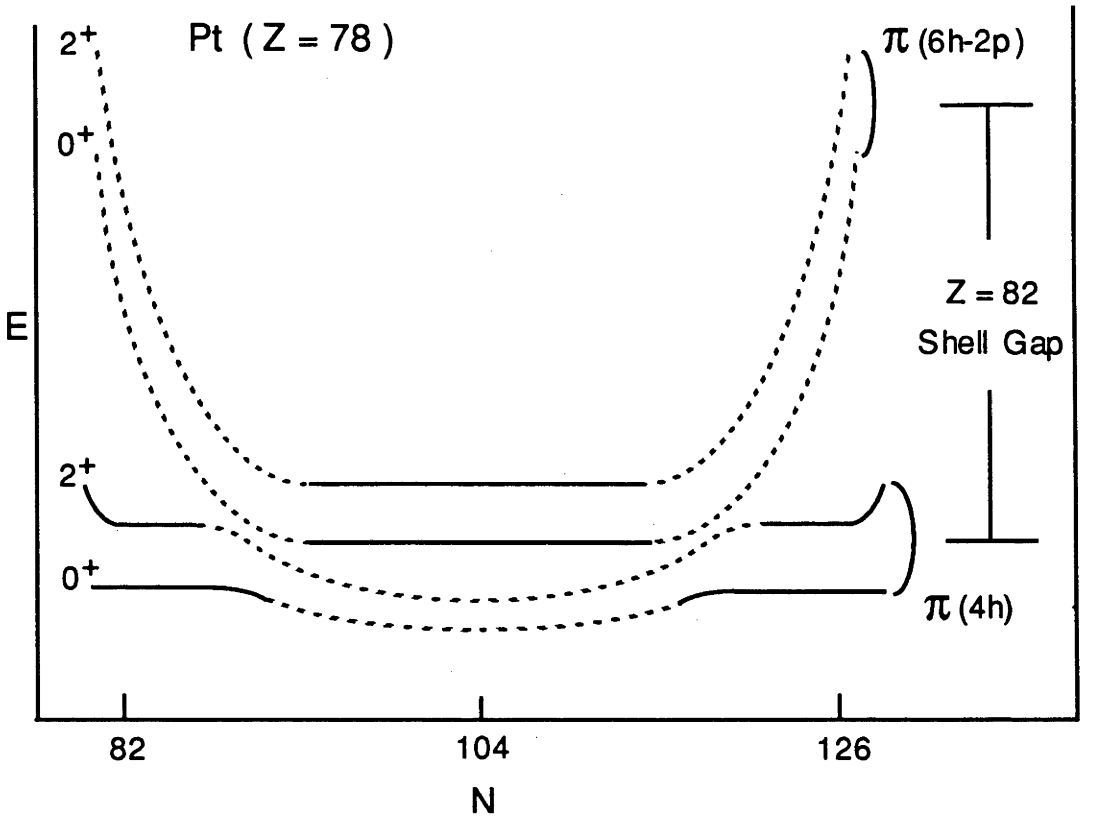

Figure 9.6: Illustration of the excitation energies for the 0^+ and 2^+ states of the configurations that cause shape coexistence in the even Pt isotopes (from ref. [Wo81]). The intruder (π 6h–2p) lies lowest in energy around the middle of the shell, and the mixing of states with the same spin and parity is included.

the number of *active* nucleons so that the intruder lies lowest in energy near the middle of the neutron shell ($N = 104$, ^{182}Pt), where the number of valence neutrons is largest.

A similar situation is found in the light $^{182-188}$Hg nuclei, where spectroscopic studies [Co84] have revealed complete coexisting bands with 0^+-state band-heads and different deformations. One difference between the Pt and Hg isotopes is that the deformed configuration comes below the 'normal', less-deformed or oblate one for ^{178,180,182,184}Pt (fig. 9.6), whereas in the Hg isotopes the intruder does *not* become the ground state. This difference may be attributed to an increase in the number of valence nucleons for Pt ($Z = 78$), as it has two protons less (i.e. two more valence holes) than Hg ($Z = 80$), which increases the residual proton-neutron interaction and lowers the energy of the intruder configuration [Wo81].

The mixing of two states with the same spin and parity (I^π), and similar

excitation energies, causes the mutual repulsion of the levels, as shown approximately in fig. 9.6. This occurs mainly in the regions where the energies of the configurations 'cross', near ^{176,178}Pt and ^{184,186}Pt. The observed level energies for the Pt nuclei, shown in fig. 9.3, display the characteristics expected for two coexisting shapes with some 'distortions' from the effects of mixing between the two unperturbed structures.

More recent and detailed spectroscopic studies of the light Pt nuclei [Dr86, Ga86, Da94a] have also been interpreted in terms of the shape-coexistence phenomenon. Dracoulis *et al.* [Dr86] have measured the yrast states in ^{176,178}Pt and analyzed the low-lying levels of $^{176-188}$Pt with a band-mixing interpretation. They determined band-head energies and moments of inertia for the original (*un*perturbed) structures which support the shape-coexistence model.

Garg *et al.* [Ga86] measured the lifetimes of yrast states, up to spin 18^+, in ^{184}Pt using the recoil distance method. $B(E2)$ values for the transitions depopulating these states were extracted from the lifetimes. They found a marked increase in the $B(E2)$'s between spins 2^+ and 4^+, which corresponds to an increasing deformation and is consistent with the shape-coexistence picture. The observed $B(E2)$ ratio for the $4_1^+ \rightarrow 2_1^+$ and $2_1^+ \rightarrow 0_1^+$ transitions agrees with the value calculated in their two-band analysis for ^{184}Pt, which is similar to the one by Dracoulis *et al.* [Dr86].

9.2.2 Band-mixing interpretation

In this section, the measured $g(2_1^+)$ values for ^{184,186,188}Pt are described in terms of a semi-empirical approach based on the shape-coexistence phenomenon. The first consideration is determining the structure of the 2_1^+ states for these nuclei, from the interplay of two competing structures. This is accomplished here with band-mixing calculations, similar to those of Dracoulis *et al.* [Dr86], by analyzing the observed excitation energies in terms of two interacting rotational bands built on coexisting shapes with different deformations.

9.2.2.1 Two-state mixing

Firstly, the definitions for simple 'two-state mixing' [Br77c] are reviewed briefly. Consider the situation in fig. 9.7, where there are two states in a nucleus with the same spin and parity, initial energies of $E_{\rm I}$ and $E_{\rm II}$ and wavefunctions $\phi_{\rm I}$ and $\phi_{\rm II}$.

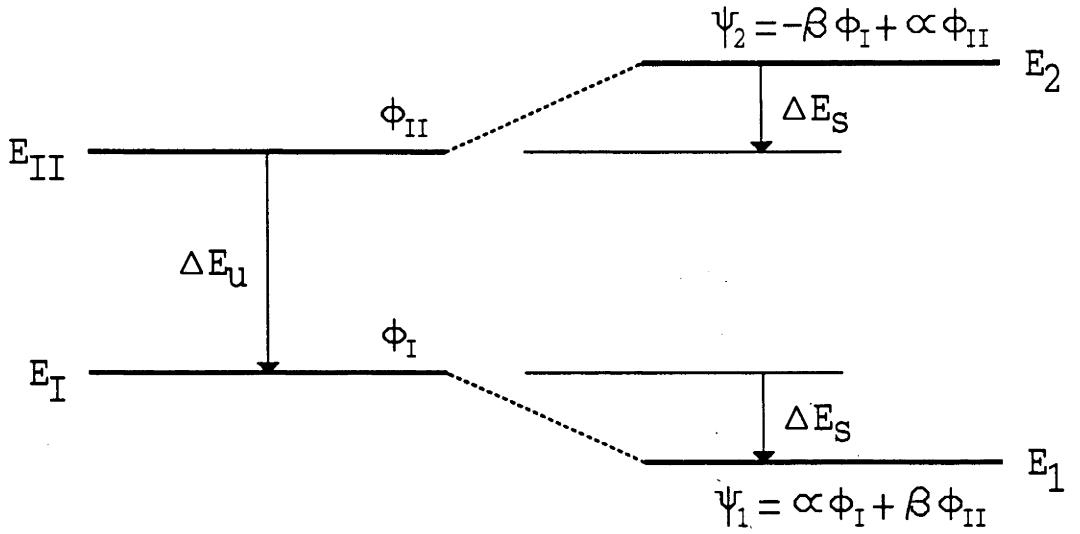

Figure 9.7: Illustration of the energy separation caused by two-state mixing (adapted from ref. [Ca90b]), with the notation as described in the text.

Mixing between them, which is dependent on their original separation ΔE_u and the strength of the interaction V, will cause their mutual repulsion by $2 \times \Delta E_s$ for final energies E_1 and E_2 and wavefunctions ψ_1 and ψ_2, respectively. These perturbed energies are given by

$$E_{2,1} = \frac{1}{2}\{ E_I + E_{II} \pm \sqrt{(E_{II} - E_I)^2 + (2V)^2} \} \tag{9.1}$$

and, equivalently, the interaction is

$$V^2 = (E_I - E_p) \times (E_{II} - E_p) \ , \quad p = 1, 2 \ . \tag{9.2}$$

This yields

$$E_I - E_1 = -(E_{II} - E_2) = \Delta E_s \tag{9.3}$$

and the energy separation of the mixed states,

$$E_2 - E_1 = \sqrt{(\Delta E_u)^2 + (2V)^2} \ . \tag{9.4}$$

9.2.2.2 Band-mixing calculations

From the shape-coexistence picture, it is assumed that the original, *un*perturbed bands have similar band-head energies but different moments of inertia and, therefore, interact only at low spin. If there is no mixing at higher spin, yrast states

with $I > 6\hbar$ can be assumed to be identical to the levels in the original band with larger deformation. Consequently, from the excitation energies of the known yrast states with $I^\pi = 8^+, ..., 14^+$, we estimate the energies for low-lying levels ($I^\pi = 0^+, 2^+, 4^+, 6^+$) in the unperturbed band of the more deformed structure (labelled band I, giving $E_u^{\rm I}(I^\pi)$), via a fit to the formula

$$E_x(I^\pi = 8_1^+, ..., 14_1^+) = E_0 + A\,I(I+1) + B\,[I(I+1)]^2 = E_u^{\rm I}(I^\pi) \quad . \qquad (9.5)$$

The interaction, V, between the *un*perturbed 0^+ states can then be determined with two-state mixing considerations (described above). Using eq. 9.2 with the extrapolated band-head energy for band I, $E_u^{\rm I}(0^+) = E_0$, the (observed) zero energy of the ground state, $E_x(0_1^+) = 0\,{\rm keV}$, and the observed excitation energy of the excited 0_2^+ state, $E_x(0_2^+)$:

$$\begin{aligned} V^2 &= \{\,E_u^{\rm I}(0^+) - E_x(0_1^+)\,\} \times \{\,E_x(0_2^+) - E_u^{\rm I}(0^+)\,\} \\ &= E_0\,\{\,E_x(0_2^+) - E_0\,\} \quad . \end{aligned} \qquad (9.6)$$

The unperturbed band built on the less-deformed structure, band II, has band-head energy $E_u^{\rm II}(0^+)$, given by eq. 9.3,

$$\begin{aligned} E_x(0_1^+) - E_u^{\rm I}(0^+) &= E_u^{\rm II}(0^+) - E_x(0_2^+) \\ \Rightarrow\ E_u^{\rm II}(0^+) &= E_x(0_2^+) - E_u^{\rm I}(0^+) \quad . \end{aligned} \qquad (9.7)$$

The level energies for other states in band II, $E_u^{\rm II}(I^\pi)$, in particular $E_u^{\rm II}(2^+)$, were then extracted individually. We assumed a spin-independent interaction between the unperturbed bands V, which was taken from the analysis of the 0^+ states described above, and used the energies of the states with the same spin in both the unperturbed (deformed) band I, $E_u^{\rm I}(I^\pi)$, and the observed yrast sequence, $E_x(I_1^\pi)$;

$$E_u^{\rm II}(I^\pi) = \frac{E_x(I_1^\pi)\,\{E_u^{\rm I}(I^\pi) - E_x(I_1^\pi)\} + V^2}{E_u^{\rm I}(I^\pi) - E_x(I_1^\pi)} \quad . \qquad (9.8)$$

The structures of the perturbed levels, both yrast and yrare, may be expressed in terms of the wavefunctions for the states with the same angular momentum in the original bands I and II, $\phi_{\rm I}$ and $\phi_{\rm II}$ (see fig. 9.7). For the 2_1^+ state the mixed wavefunction is

Table 9.1: Results of the band-mixing analyses, including: 0_2^+- and 2_1^+-state excitation energies; fit parameters; energies for the *un*perturbed levels[a]; and the interaction strength, V.

Nuclide	Level energies[b]		Fit parameters					Band II[a]	
	$E_x(2_1^+)$ [keV]	$E_x(0_2^+)$ [keV]	A [keV]	B [eV]	E_0[a] [keV]	$E_u^{\rm I}(2^+)$ [keV]	V [keV]	$E_u^{\rm II}(0^+)$ [keV]	$E_u^{\rm II}(2^+)$ [keV]
^{188}Pt	265.9	798.8	21.92	-22.5	308.5	439.2	389	491	1141
^{186}Pt	191.5	471.6	17.13	-22.9	233.4	335.3	236	239	579
^{184}Pt	163.2	493.0	15.04	-15.0	228.4	318.1	246	265	554
^{182}Pt	154.9	499.4	14.81	-10.8	196.3	284.7	244	303	614

[a] The unperturbed level energies are $E_0 = E_u^{\rm I}(0^+)$; $E_u^{\rm I}(2^+)$, $E_u^{\rm II}(0^+)$ and $E_u^{\rm II}(2^+)$.
[b] $E_x(0_1^+) = 0$ keV.

$$\psi(2_1^+) = \alpha\,\phi_{\rm I}(2^+) + \beta\,\phi_{\rm II}(2^+) \quad , \tag{9.9}$$

where the mixing amplitudes, α and β, are the eigenvectors of the two-state mixing matrix, so that $\alpha^2 + \beta^2 = 1$. They may be determined using the analytical expression [Ca90b]

$$\beta = \frac{1}{\sqrt{1 + \{\frac{R}{2} + \sqrt{1 + \frac{R^2}{4}}\}^2}} \quad , \tag{9.10}$$

where

$$R = \frac{E_u^{\rm II}(2^+) - E_u^{\rm I}(2^+)}{V} \quad . \tag{9.11}$$

Given in table 9.1 are the results of the band-mixing analyses performed for each Pt nucleus of interest. Included are the observed excitation energies for the 0_2^+ and 2_1^+ states, the fit parameters and level energies for the *un*perturbed 2^+ states, and the extracted interaction strengths. Finally, the mixing amplitudes (squared) for the 2_1^+ states are in table 9.2. The original and perturbed rotational

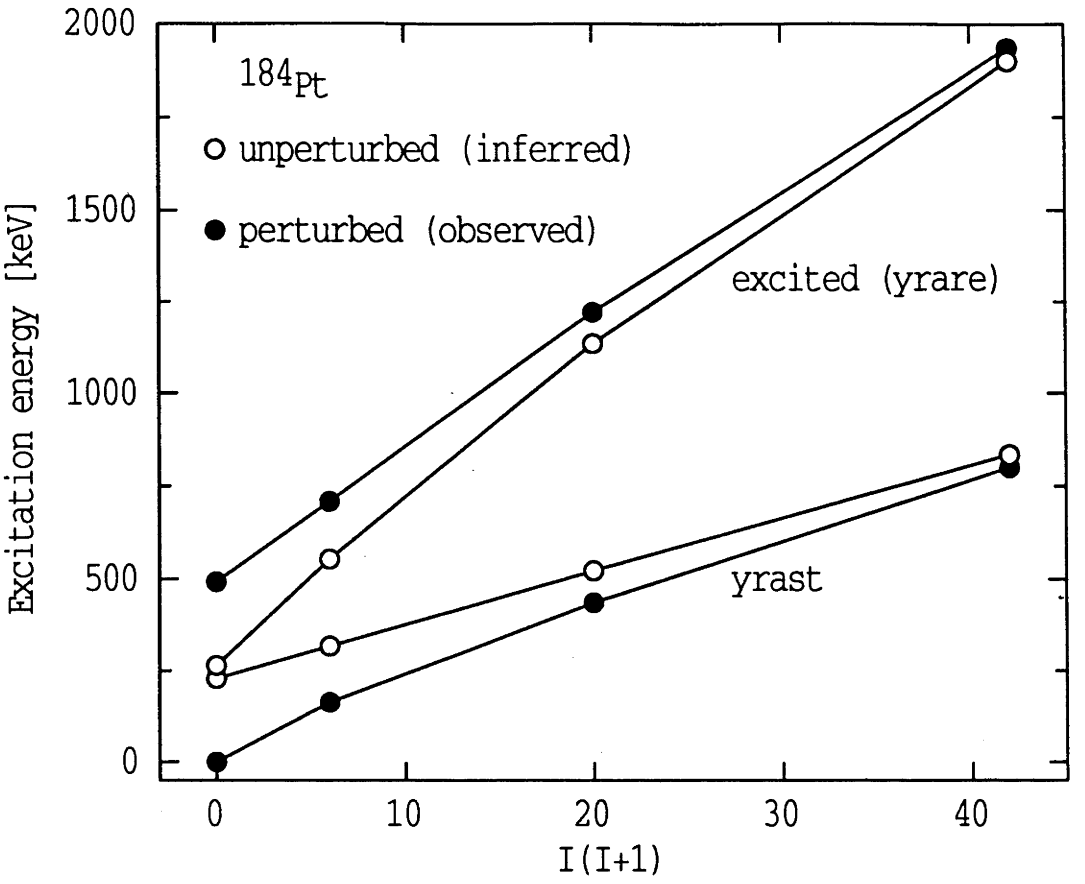

Figure 9.8: Results of the band-mixing analysis performed on ^{184}Pt (see table 9.1).

bands, where the latter are the observed level energies determined in the analysis of ^{184}Pt, are plotted in fig. 9.8.

9.2.2.3 Derived g-factors

The 2_1^+-state g-factor in each of these Pt nuclei may now be calculated using theoretical $g(2^+)$ values for the *unperturbed* structures and the empirical estimate of the mixing between them;

$$g(2_1^+) = \alpha^2\, g_I(2^+) + \beta^2\, g_{II}(2^+) \quad , \tag{9.12}$$

where band I (II) is based on the more (less) deformed structure and the weighting is provided by the mixing amplitudes, α and β.

From the interpretation of the Pt nuclei given in sect. 9.2.1, the intruder (π 6h–2p) states possess two more proton bosons than those with the normal (π 4h) configuration. Then for these deformed states, N_π must be replaced by $N_\pi + 2$

(where $N_\pi = 2$ for Pt) and the IBM expression of eq. 2.14 for the 'normal' levels,

$$g_{normal} = g_{II} \simeq \frac{N_\pi}{N_\pi + N_\nu} \quad , \tag{9.13}$$

becomes

$$g_{deformed} = g_I \simeq \frac{N_\pi + 2}{N_\pi + N_\nu + 2} \quad . \tag{9.14}$$

These estimates of the g-factors for the configurations in the Pt nuclei are compared with experiment in fig. 9.9. Also shown, and given in table 9.2, are the 'mixed' g-factors for ^{184,186,188}Pt obtained by inserting the amplitudes derived above.

As an alternative, not relying on the IBM, the density-dependent Hartree-Fock calculations of Sprung *et al.* [Sp79] for the unperturbed 2^+-state g-factors in ^{184}Pt and ^{188}Pt may be used. The g-factors calculated for both prolate and oblate static deformations are given in table 9.3, with the 'mixed' $g(2_1^+)$ determined from these values. Figure 9.10 compares these and the microscopic calculation for an oblate

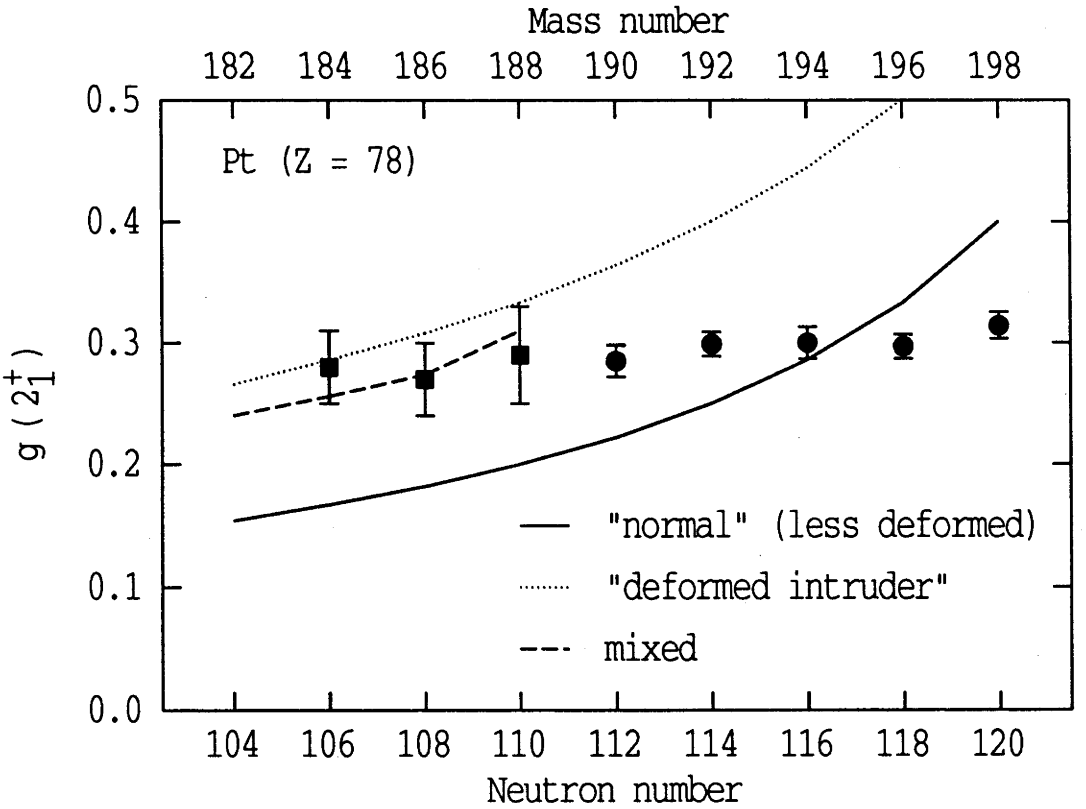

Figure 9.9: Comparison of experimental $g(2_1^+)$ values with IBM-2 predictions for 'normal' and 'intruder' configurations and the 'mixed' values of table 9.2.

Table 9.2: Comparison of experimental g-factors with simple IBM-2 estimates for the normal, intruder and 'mixed' configurations.

Nuclide	Mixing amplitudes		IBM-2			
	α^2	β^2	$g_{intruder}$	g_{normal}	g_{mixed}[a]	$g_{exp}(2_1^+)$
^{188}Pt	0.835	0.165	0.333	0.200	0.311	0.29(4)
^{186}Pt	0.729	0.270	0.308	0.182	0.274	0.27(3)
^{184}Pt	0.716	0.284	0.286	0.167	0.256	0.28(3)
^{182}Pt	0.780	0.221	0.266	0.154	0.240	-

[a] From eq. 9.12

^{194}Pt nucleus [Sp79] with the measured $g(2_1^+)$ values.

The agreement between the measured g-factors and both sets of calculations is reasonable, especially given the simplicity of this approach. In conclusion, the experimental $g(2_1^+)$ for the lighter Pt isotopes are consistent with the band-mixing interpretation (of shape coexistence) for these nuclei, which has also been successful in describing the measured energy levels [Dr86] and lifetimes [Ga86]. Note that a description of the ^{184,186,188}Pt g-factors is possible with eq. 9.14 (for the intruder configuration), if $g_\pi \lesssim 1$ (and $g_\nu \simeq 0$). Even so, the measured g-factors support the proton 6 hole$-$2 particle configurations proposed for the deformed bands in $^{184-198}$Pt.

Although the g-factors have been interpreted using band-mixing, with the present level of experimental precision it is not possible to determine mixing amplitudes from the $g(2_1^+)$ values themselves. To fully elucidate the dependence of experimental properties, including these 2_1^+-state g-factors, on the shape-coexistence phenomenon requires more rigorous theoretical treatment of the neutron-deficient Pt nuclei. A calculation using the configuration mixing formalism for the IBM [Du81], along the lines of those made for the Hg isotopes by

Table 9.3: Comparison of $g(2_1^+)$ values from experiment with a microscopic calculation for prolate and oblate shapes.

Nuclide	Mixing amplitudes		$g_{calc}(2_1^+)$[a]			
	α^2	β^2	$g_{prolate}$	g_{oblate}	g_{mixed}[b]	$g_{exp}(2_1^+)$
^{194}Pt	-	-	-	0.272	-	0.300(13)
^{188}Pt	0.835	0.165	0.267	0.153	0.25	0.29(4)
^{186}Pt	0.729	0.270	-	-	-	0.27(3)
^{184}Pt	0.716	0.284	0.339	0.131	0.28	0.28(3)

[a] Microscopic calculations of Sprung *et al.* [Sp79]

[b] From eq. 9.12

Barfield *et al.* [Ba83], would be instructive, but is beyond the scope of the present work.

The ^{188,190}Pt nuclei are at the transition between the neutron-deficient Pt isotopes, which exhibit shape coexistence, and the heavier nuclei with stable, oblate ground states. This is apparent in the potential energy surfaces of fig. 9.4, where ^{188}Pt is found to be very γ-soft and does not exhibit a stable minimum. In a somewhat arbitrary choice, ^{188}Pt was considered here with the lighter isotopes and ^{190}Pt in sect. 9.3 with the other naturally-occurring nuclides.

The structure of the unstable Pt nuclei, and in particular ^{188}Pt, is obviously more complicated than that given by the simple 'configuration-crossing' picture. Although it may then be somewhat inappropriate to determine the g-factors using band-mixing of two distinct and separate structures, more sophisticated theoretical calculations are beyond the scope of the present work.

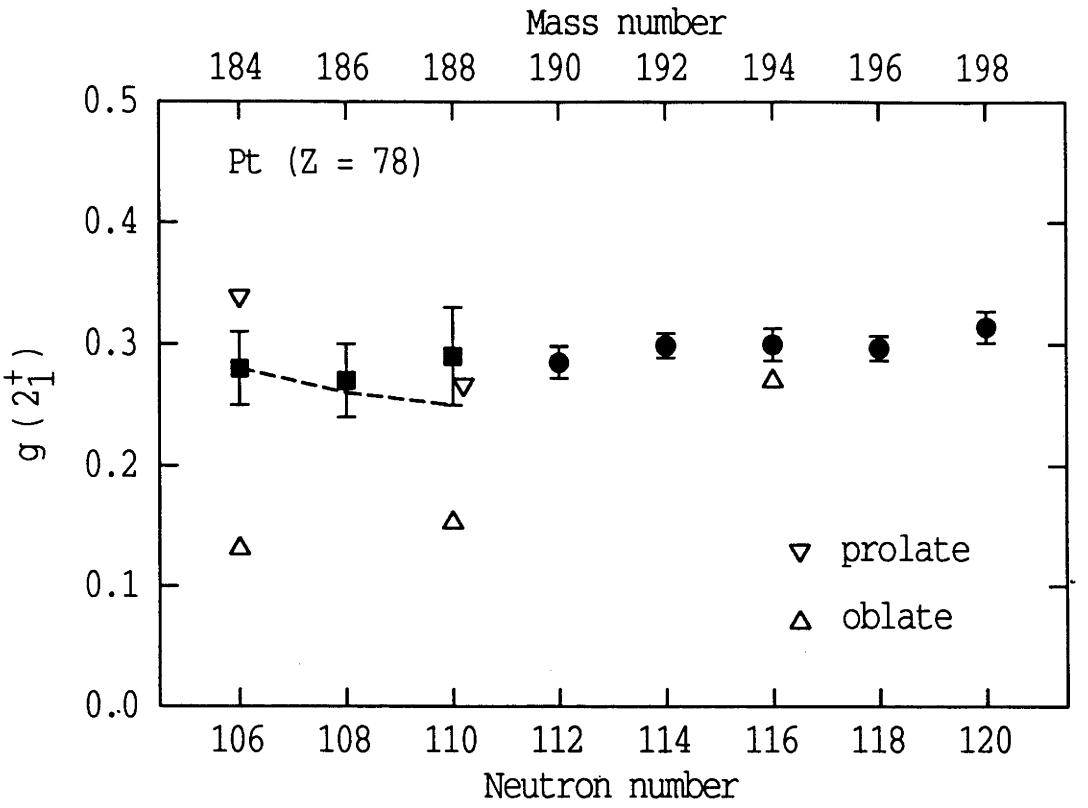

Figure 9.10: Comparison of experimental $g(2_1^+)$ with the calculations of Sprung *et al.* [Sp79] for prolate and oblate deformations and the 'mixed' values of table 9.3.

9.3 The Heavier Isotopes and the IBM-2

9.3.1 Review

As discussed in sect. 2.2.3, the g-factors of states with low-excitation energy in the even-even rare-earth nuclei have been studied several times using the proton-neutron interacting boson model (IBM-2). In general the assumption has been made that low-lying levels have maximum F-spin, that is the nuclei are symmetric in the proton and neutron degrees of freedom, and the g-factors are given by the expression (eq. 2.13)

$$g(I) = \frac{1}{N_\pi + N_\nu} \left(g_\pi N_\pi + g_\nu N_\nu \right) \quad , \tag{9.15}$$

where g_π (g_ν) is the proton (neutron) boson g-factor and N_π (N_ν) is the proton (neutron) boson number. With values for the boson g-factors similar to the microscopic estimate of $g_\pi = 1$ and $g_\nu = 0$, which assumes only the orbital angular momentum of the fermions contributes, this gives a qualitative description of the

mass dependence for 2_1^+-state g-factors over a large region (fig. 2.1).

There are, however, differences between many of the measured g-factors and this global estimate. Also, in some cases (e.g. $g(2_1^+)$ in $_{60}$Nd, $_{62}$Sm and $_{78}$Pt), there are large discrepancies for a number of the isotopes of the given nucleus, resulting in an observed mass variation for the g-factors of the isotopic series which is in striking contrast with that predicted. The failures of this approach may be attributed to two effects: (i) differences in the boson g-factors or boson numbers from their nominal values, possibly caused by changes in the underlying fermion structure of the nuclei; and (ii) shortcomings of eq. 9.15, due to non-maximal F-spin admixtures in the low-lying states or the need to include either the g-boson degrees of freedom or higher-order terms in the $M1$ operator.

Changes in the single-particle structure of the bosons may be analysed with eq. 9.15 and the g-factor systematics through (i) deviations of the boson g-factors from their nominal values and/or (ii) the effective proton and neutron boson numbers compared with the numbers obtained by conventional counting from closed shells. In sect. 9.3.1.1, we describe fitting the boson g-factors to the $g(2_1^+)$ systematics for the W, Os and Pt isotopic series, and in sect. 9.3.1.2, the Pt 2_1^+-state g-factors are examined by varying the boson numbers. It will be shown that these approaches are not satisfactory.

In the second category, inclusion of the g-bosons is considered in sect. 9.3.1.3. Then, in sects. 9.3.1.4, 9.3.1.5 and 9.3.2.1, the effects of F-spin mixing in the *sd*-IBM-2 are discussed.

9.3.1.1 Fitting the boson g-factors

The g-factors for a given state in a series of nuclei, usually an isotopic sequence, may be analysed in terms of eq. 9.15 by fitting the boson g-factors, see e.g. refs. [Wo87a, St91a]. The $g(2_1^+)$ systematics in the $^{180-186}$W and $^{186-192}$Os isotopic series are described adequately by eq. 9.15 with the simple estimate of $g_\pi \simeq 1$ and $g_\nu \simeq 0$. Least-squares fits to eq. 9.15, similar to those in ref. [St91a], give values of $g_\pi = 1.09$ and $g_\nu = -0.03$ for the Os isotopes, and $g_\pi = 0.80$, $g_\nu = 0.03$ for W. A calculation using $g_\pi = 0.94$ and $g_\nu = 0.0$ is shown in fig. 9.11 for the isotopic sequences of the W, Os and Pt nuclei and, in each case, this predicts a significant increase in $g(2_1^+)$ with increasing mass. Clearly, this is in disagreement with the constancy of the measured Pt g-factors. A similar fit of the $g(2_1^+)$ for the $^{190-198}$Pt isotopes finds effective values of $g_\pi = 0.38 \pm 0.03$ and $g_\nu = 0.26 \pm 0.01$,

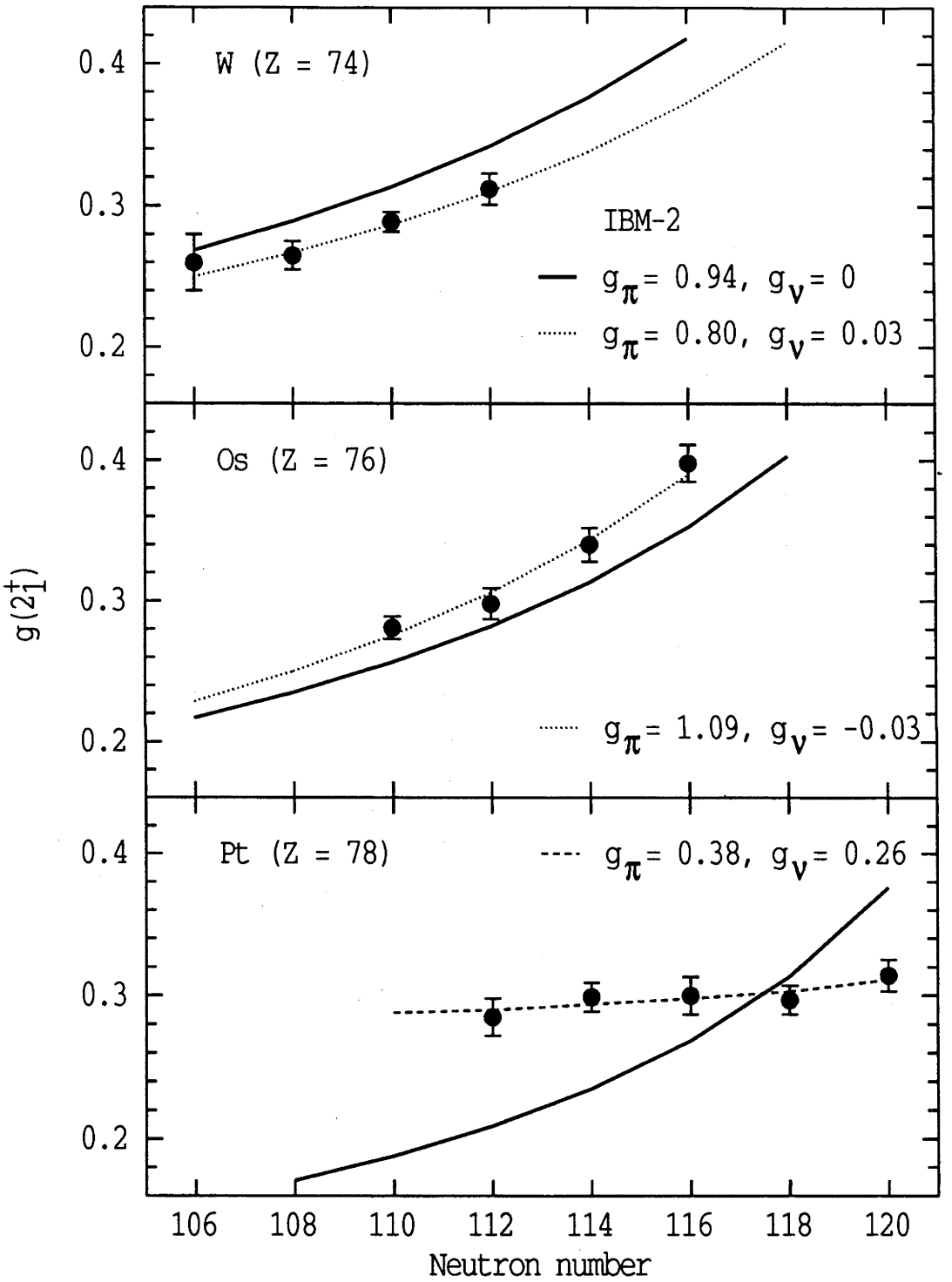

Figure 9.11: Comparison of the $g(2_1^+)$ systematics for the W, Os and Pt isotopic series with IBM-2 calculations using eq. 9.15 and various values for the boson g-factors (see text).

in agreement with a similar analysis in ref. [St91a] for $^{192-198}$Pt, and the findings in ref. [Zi85b].

At first sight, the pronounced discrepancy between the values of the boson g-factors found empirically for Pt and those expected theoretically, and which are appropriate for the neighbouring W and Os nuclei, could signify an underlying structural difference in the Pt nuclei, possibly related to the observed nuclear shape change from prolate to oblate deformation between ^{192}Os and $^{(190)}$Pt [Gy86, Li88]. However, it is currently believed (see the next section) that the boson g-factors do not deviate much from their 'bare' values. If eq. 9.15 is to retain validity for the $^{190-198}$Pt isotopes, it should do so with $g_\pi \simeq 1$ and $g_\nu \simeq 0$.

9.3.1.2 Effective boson numbers

Another approach is to interpret the mass dependence of the g-factors in terms of effective proton and neutron boson numbers, N_π^{eff} and N_ν^{eff}. Wolf and Casten [Wo87b] highlighted the subshell closure at $Z = 64$ for nuclei with $A \leq 152$, by analyzing simultaneously $g(2_1^+)$ and $B(E2; 2_1^+ \rightarrow 0_1^+)$ data in terms of changes in the number of active bosons, with boson g-factors and charges fixed, using eq. 9.15 and an approximate $B(E2)$ expression.

With this method Stuchbery *et al.* [St91a] examined the $^{192-198}$Pt data for a proposed subshell closure at $N = 114$ (for $Z \geq 78$) [Ca85]. The effective neutron boson numbers extracted were consistent with counting from the closed shell at $N = 126$ and not sensitive to any neutron subshell closure. However, an unexpected mass dependence in the deduced N_π^{eff} prompted further study where the boson g-factors were also varied. They simultaneously analysed the $g(2_1^+)$ and $B(E2; 2_1^+ \rightarrow 0_1^+)$ data for $^{192-198}$Pt assuming the reasonable values of $g_\pi = 0.90$, $N_\pi \simeq 2$ and boson charges $e_\pi = 0.22$ and $e_\nu \simeq 0.1$, to infer the neutron parameters, g_ν and N_ν. This again found the N_ν^{eff} supported conventional boson counting, but also that the constancy of the measured g-factors can be related phenomenologically to a pronounced decrease in the neutron-boson g-factor, g_ν, with increasing mass.

This analysis has been repeated here with the Pt g-factors adopted in the present work (table 7.2), lifetime information from ref. [Ra87] and the present ^{190}Pt $B(E2; 2_1^+ \rightarrow 0_1^+)$ value (sect. 7.3.4). As shown in fig. 9.12, this yields very similar results with g_ν levelling off for the lighter isotopes.

Phenomenological analysis does not provide a physical description of the re-

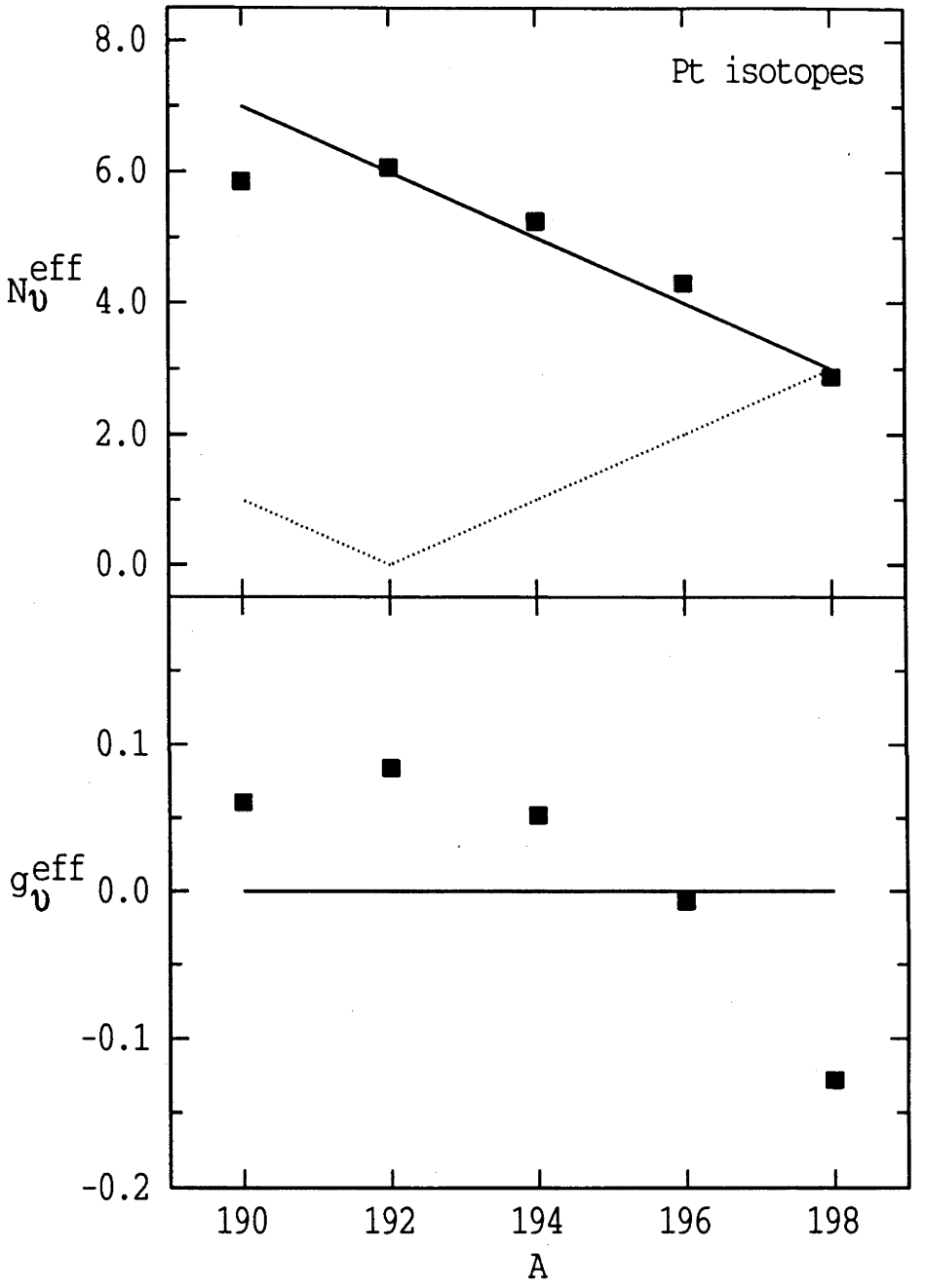

Figure 9.12: Results of our simultaneous analysis of Pt $g(2_1^+)$ and $B(E2;2_1^+ \rightarrow 0_1^+)$ data, as described in the text. Here $g_\pi = 0.95$, $N_\pi = 2$, $e_\pi = 0.22$ and $e_\nu = 0.10$. The N_ν expected from normal counting are shown by the solid line and from the proposed subshell closure with the dotted line.

sults, however, Stuchbery *et al.* [St91a] considered that in the weakly oblate (near spherical) Pt nuclei there may be small non-collective components in the wave-functions of the low-lying levels. A contribution from the $\nu 3p_{3/2}$ single-particle orbital (with $g = -0.82$ [Ba73] compared to $g = -0.18$ for the $\nu 1i_{13/2}$ orbital) that increases with mass would produce the g_ν mass-dependence, and reduce the g-factor values obtained from eq. 9.15 (shown in fig. 9.1) for the heavier ^{196,198}Pt nuclei, as observed. With the present result for ^{190}Pt, however, the enhancement of the $g(2_1^+)$ from the IBM predictions (and g_ν values) in the lighter Pt isotopes ($A = 190, 192$) must now be addressed. This is more difficult to reconcile with non-collective effects.

There is a need for comprehensive calculations of the boson model parameters for the Pt nuclei, in particular g_ν. Sambataro *et al.* [Sa84] and, recently, Davis and Navrátil [Da94b] have made microscopic estimates of the d-boson g-factors for the rare-earth nuclei with $50 \leq Z \leq 82$ and $82 \leq N \leq 126$. Both works support the values $g_\pi \simeq 1$ and $g_\nu \simeq 0$ with significant discrepancies only near the ends of the shells. From ref. [Da94b], $g_\pi \simeq 1.1$ and $g_\nu \simeq -0.01 \rightarrow -0.07$ for $^{190-198}$Pt. This is clearly inconsistent with the values $g_\pi \simeq g_\nu \simeq 0.3$ and is insufficient to account for the empirical variation of g_ν across the Pt isotopes. This suggests that the observed discrepancies between the experimental g-factors and those given by eq. 9.15 have physical causes beyond those included in its derivation.

9.3.1.3 Including the g-boson – sdg-IBM-2

A criticism of the commonly used sd-IBM-2 is that high-spin states are not generally well described, as the s- and d-bosons have spins of only 0^+ and 2^+, respectively. This may be improved by the inclusion of a g-boson with spin 4^+, which is also required to properly account for hexadecapole properties. With respect to magnetic nuclear properties, the sdg-version of the IBM-2 has been applied to the Sm isotopes [Mi91] to explain $M1$ excitation strengths from the 0^+ ground states to 1^+ 'scissors mode' levels. This also allowed description of the magnetic moments of Sm nuclei with d-boson g-factors, $g_{d\pi}$ and $g_{d\nu}$ (which are the same as g_π and g_ν but with the d-subscripts included), that are compatible with microscopic expectations.

Of present interest is whether the introduction of the g-boson degree of freedom can generally account for the discrepancies between the values of d-boson

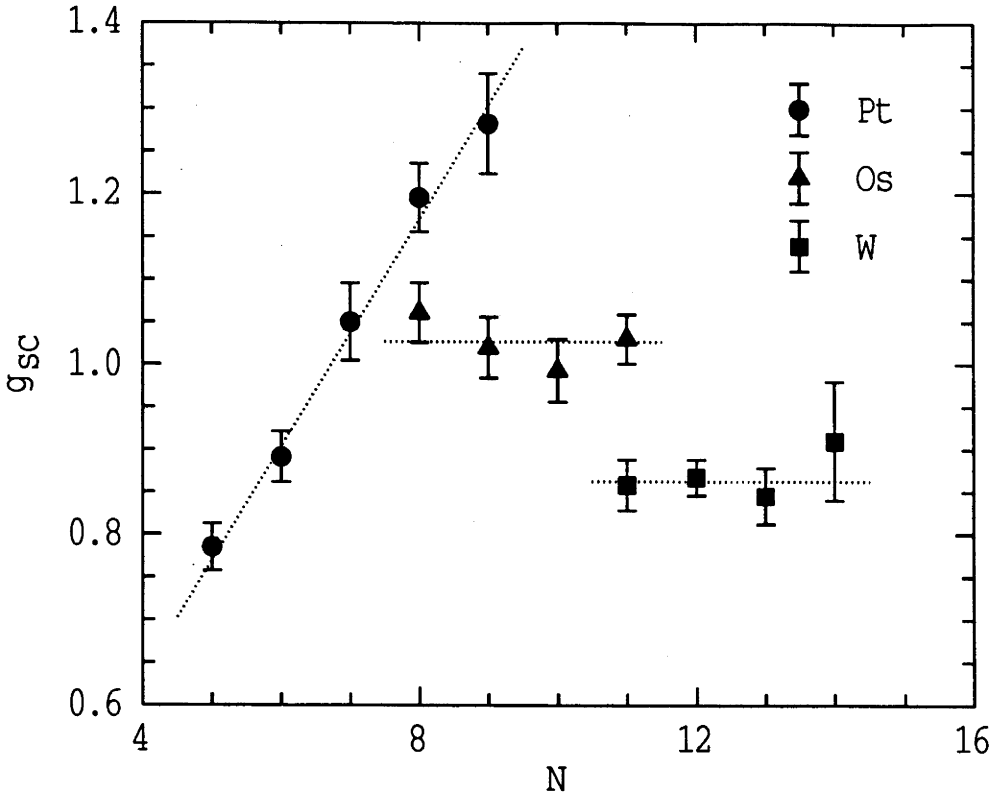

Figure 9.13: Plot of g_{sc} (see text) versus N for the isotopes of Pt, Os and W.

g-factors found phenomenologically and those expected microscopically. Barrett *et al.* [Ba92] have considered the ground-state band magnetic moments of even-even rare-earth nuclei with the *sdg*-IBM-2. Their calculations for Os and Pt nuclei imply that for the g-boson degree of freedom to resolve the discrepancy the scaled g-factors, $g_{sc} = g(2_1^+)\, N/N_\pi$, should be only very weakly N dependent. Figure 9.13 shows a plot of g_{sc} versus N for the W and Os isotopes, similar to that in ref. [Ba92]. Although the approximate constancy of g_{sc} for W and Os is encouraging, Barrett *et al.* could not unequivocally state that the introduction of the g-boson alone would solve the g-factor problem. They concluded that more detailed microscopic study is required to clarify this situation. However, they also state that improved experimental data for the Pt nuclei would be valuable, as their results imply that the *sdg*-model used would not be able to accomodate a variation in g_{sc} across the Pt isotopic chain of more than around 10%.

The present measurements (and those in ref. [St91a]) provide us with data for the Pt isotopes (from sect. 7.3.2 and presented in fig. 9.13), which are considerably better than those considered by Barrett *et al.* [Ba92]. Clearly, g_{sc} is strongly N

dependent, as it increases by more than 60% from ^{198}Pt ($N = 5$) to ^{190}Pt ($N = 9$). The results of Barrett *et al.* then imply that the inclusion of the g-boson degree of freedom cannot account for the differences between $g_{d\pi,\nu}$ values from experimental data and theoretical considerations.

This conclusion was also reached in the recent work of Davis and Navrátil [Da94b]. From their detailed microscopic calculations of both d- and g-boson g-factors, they found that the difference between them is typically too small for the inclusion of the g-boson to have an effect of larger than a few percent on $g(2_1^+)$ values. Also, Lac and Kuyucak [La92] have studied the $E2$ and $E4$ properties of the transitional Os and Pt nuclei with the *sdg*-IBM-1. They found that they required large g-boson energies for the Pt nuclei, as the excitation energy of the 4^+ (g-boson) state is relatively high, and, therefore, that the g-boson does not play an important role in the spectroscopy of low-lying levels. (Some of their results for $E2$ properties in the $^{192-198}$Pt nuclei will be shown later, in tables 9.6 and 9.7.)

Barrett *et al.* [Ba92] also suggested that including a two-body term in the $M1$ operator, instead of the g-boson, may be required. Nuclear magnetic properties have been studied with the IBM-1 in this manner with limited success, see ref. [Li90c]. As its microscopic origins are not clear, this is a less preferable choice, and as such, it has not been used recently and will not be considered further here.

9.3.1.4 F-spin symmetry breaking with $\epsilon_\pi \neq \epsilon_\nu$

As noted in sect. 2.1, $M1$ transitions vanish in the IBM unless higher-order terms are included in the $M1$ operator or F-spin symmetry is broken. Consequently, as one would expect, there have been several studies of the $M1$ transition rates for low-lying nuclear states with respect to the symmetry of the valence proton and neutron degrees of freedom (see ref. [Li90c]). Some of these have suggested departures from F-spin purity, e.g. refs. [Wa86, Di87, Ge87, Ha87].

However, the effects of F-spin symmetry breaking on g-factors have been largely overlooked until recently. Initially, this was due to the availability of a simple analytic expression for g-factors in the limit of F-spin symmetry (eq. 9.15), and to the assumption that non-maximal F-spin admixtures are small in low-lying states (sect. 2.2.2) and thus have a small effect on the g-factors. In an early study, Stuchbery *et al.* [St85] attempted to account for the 'crossing' of $g(2_1^+)$ and $g(2_2^+)$ in the Os isotopes (where $g(2_1^+)$ increases with N_ν, as expected, but

$g(2_2^+)$ decreases) using F-spin mixing. However, the use of the very non F-spin symmetric hamiltonian obtained from level energies and $B(E2)$ rates by Bijker *et al.* [Bi80], proved inappropriate to reproduce the g-factor systematics. The 'F-spin mixing approach' was then abandoned for some time.

More recently, Ginnochio *et al.* [Gi92] have proposed the examination of, in particular, the ratio of g-factors for γ- and ground-state bands to determine F-spin mixing. Also, Kuyucak [Ku94] investigated the effects of various F-spin symmetry-breaking mechanisms on the g-factors of low-lying excited states, within the $1/N$ expansion formalism.

In a phenomenological procedure, Wolf *et al.* [Wo93] have estimated the magnitudes of F-spin impurities in the 2_1^+ states of 17 even-even rare-earth nuclei, with $46 \leq Z \leq 78$, from experimental $g(2_1^+)$ data. They tuned the difference in the proton and neutron d-boson energies, $\Delta\epsilon = \epsilon_{d\nu} - \epsilon_{d\pi}$, to generate non-maximal F-spin admixtures (with $\epsilon_{d\pi} \neq \epsilon_{d\nu}$, see sect. 2.2.2) in low-lying, excited states. For each nucleus of interest, the $g(2_1^+)$ values were fitted by varying $\Delta\epsilon$ in numerical diagonalizations of the IBM-2 hamiltonian with an established set of values for the other parameters. The calculated level energies were not greatly affected by $\Delta\epsilon$, and agreement with experiment was obtained by adjusting κ (sect. 2.2) and the magnitudes of ϵ_ν and ϵ_π.

Wolf *et al.* found F-spin admixtures in the 2_1^+ states of up to around 10% and that, in general, negative values of $\Delta\epsilon$ were needed. This is in accord with microscopic estimates that imply the boson energies are usually different, with $\epsilon_{d\pi} > \epsilon_{d\nu}$, as proton 2^+ excitations are often at higher energies than neutron 2^+ excitations. They also concluded that discrepancies between $g_\pi \simeq 1, g_\nu \simeq 0$ and the empirical boson g-factors extracted from experimental 2_1^+-state g-factors may be accounted for, at least partially, by the effects of F-spin breaking.

Davis and Navrátil [Da94b] have since derived simple analytical expressions that indicate an explicit dependence of 2_1^+ g-factors on the difference between d-boson energies. They explain that this dependence comes from the effect of $\Delta\epsilon$ on d-boson occupation numbers for the 2_1^+ state. A large (negative) value for $\Delta\epsilon$ generally corresponds to more active proton bosons, which have a substantial g-factor, relative to neutron bosons, with a negligible g-factor, and vice versa.

Expanding on this, and the work of Wolf *et al.* [Wo93], Davis and Navrátil have argued, both qualitatively and semi-quantitatively, that F-spin impurities generated by $\Delta\epsilon$ can account for the systematics of measured $g(2_1^+)$ in the $Z =$

50−82, $N = 82-126$ shell. This is based upon correlations between the global microscopic estimates for $\Delta\epsilon$ [Na91] and the observed values of Δg, where Δg is the difference between experimental $g(2_1^+)$ and the maximal F-spin prediction.

9.3.1.5 F-spin symmetry breaking with $\Delta\epsilon$ and $\chi_\pi \neq \chi_\nu$

A more complete approach should use F-spin symmetry breaking to describe all of the low-excitation $M1$ properties, including the g-factors for the 2_1^+ and 2_2^+ states and the mixing ratio of the $2_2^+ \rightarrow 2_1^+$ transition. This has been attempted in the intrinsic state and 1/N expansion formalisms [Gi92, Ku89, Ku94] using algebraic expressions for selected magnetic moments, which include F-spin mixing explicitly. These theoretical works showed an explicit dependence for various $M1$ properties on the quadrupole operators χ_π and χ_ν, which may be used to break F-spin symmetry (independently of $\epsilon_{\pi,\nu}$) by choosing $\chi_\pi \neq \chi_\nu$ (sect. 2.2.2).

With the 1/N expansion method, Kuyucak [Ku94] derived analytic expressions for $g(2_1^+)$ and $g(2_2^+)$ in the Os-Pt isotopes, and pointed out that these g-factors behave similarly to one another for F-spin breaking of the one-body energies (i.e. $\epsilon_\pi \neq \epsilon_\nu$) but have distinct reactions to breaking in the quadrupole interaction ($\chi_\pi \neq \chi_\nu$). From this, he suggested that with appropriate F-spin mixing using both symmetry-breaking mechanisms, it would be possible to reproduce both the constant Pt 2_1^+, 2_2^+ g-factors and the 'crossing' of $g(2_1^+)$ and $g(2_2^+)$ in the Os isotopes (sect. 9.3.1.4). While these analytic expressions provided this insight they have limitations for transitional nuclei, which have γ-soft energy surfaces and few active bosons.

Following up on this work, Kuyucak and Stuchbery [Ku95, St94b] examined the $M1$ properties for Os and Pt nuclei, through exact diagonalizations of the IBM-2 hamiltonian. They studied the effects of $\epsilon_\pi \neq \epsilon_\nu$ and $\chi_\pi \neq \chi_\nu$ breaking on both g-factors and $M1$ transition rates in ^{190}Os and, from their observations, found that by invoking principally $\chi_\pi \neq \chi_\nu$ breaking they could explain the crossing of the Os 2^+-state g-factors. The parameter set obtained by Kuyucak and Stuchbery in a global fit of the $M1$ properties for $^{186-192}$Os and $^{190-198}$Pt includes both symmetry-breaking mechanisms.

In the following section, more complete results and comparisons, including both $M1$ and $E2$ data, are presented for the Pt isotopes than appeared in the short account published by Kuyucak and Stuchbery [Ku95, St94b].

9.3.2 Present calculations

9.3.2.1 *F*-spin mixing for the Pt nuclei

As discussed in sect. 2.2.1, γ-soft nuclei are usually described with $\chi_\pi \simeq -\chi_\nu$. Accordingly, Bijker *et al.* [Bi80] interpreted the O(6)-like spectra of the Os and Pt nuclei with values for χ_π and χ_ν that are very different, i.e. $\chi_\pi \simeq -\chi_\nu$ and $|\chi|$ large. However, this parameter set was found to be incompatible with the F-spin symmetry breaking needed to account for the Os g-factors [St85]. Subsequently, Kuyucak and Stuchbery [Ku95, St94b] have sought more appropriate values of $\chi_{\pi,\nu}$ to describe the $M1$ properties. Alternatively, Davis and Navrátil [Da94b] concluded that the $\chi_\pi \neq \chi_\nu$ mechanism is unimportant for Pt, as the g-factors are dependent on $\epsilon_\pi \neq \epsilon_\nu$ breaking. Their microscopic estimates suggest that $\chi_\pi \simeq \chi_\nu$, and they found, in a semi-quantitative analysis, that their $\Delta\epsilon$ estimates are compatible with the observed behaviour: $\Delta\epsilon$ is positive for $N < 108$ (with $Z = 78$) and Δg (sect. 9.3.1.4) changes sign to positive (i.e. the measured Pt

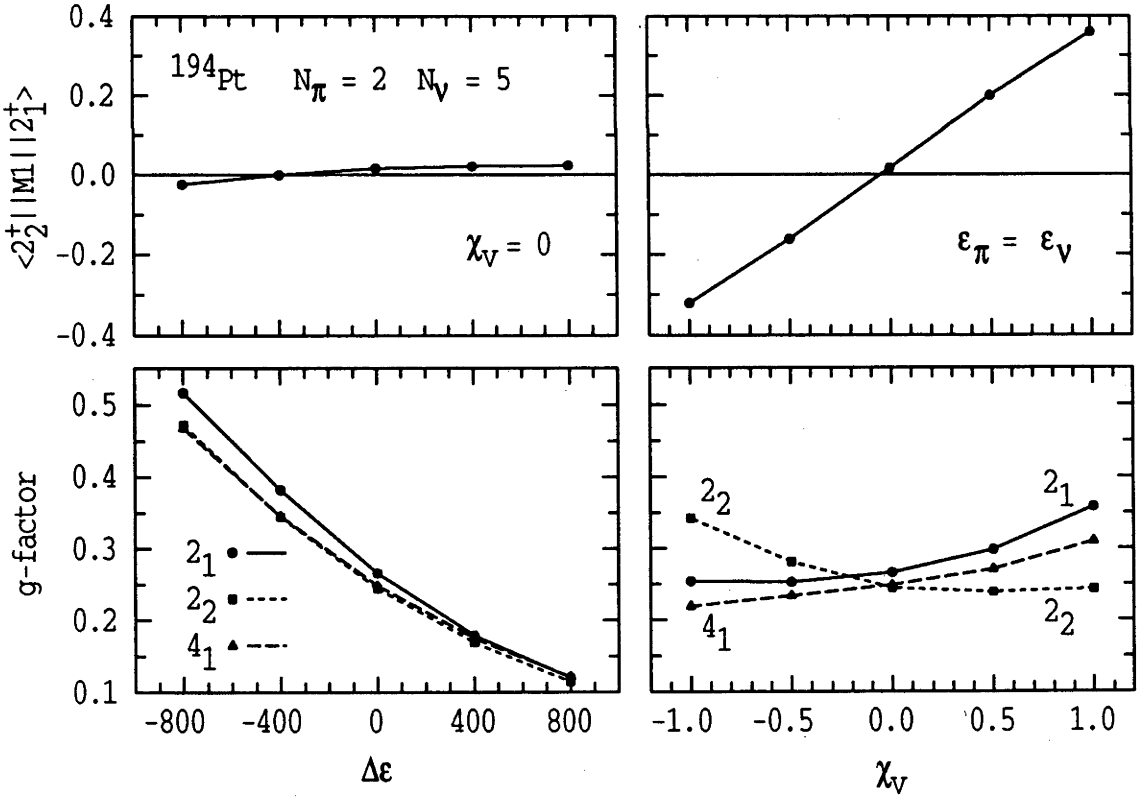

Figure 9.14: Dependence of selected magnetic dipole properties in ^{194}Pt on the symmetry-breaking parameters $\Delta\epsilon$ and χ_ν. Here $\epsilon = \frac{1}{2}(\epsilon_\pi + \epsilon_\nu) = 550\,\text{keV}$, $\chi_S = 0.18\,\text{MeV}$, $\kappa = -0.18\,\text{MeV}$ and $\xi = 0.17\,\text{MeV}$.

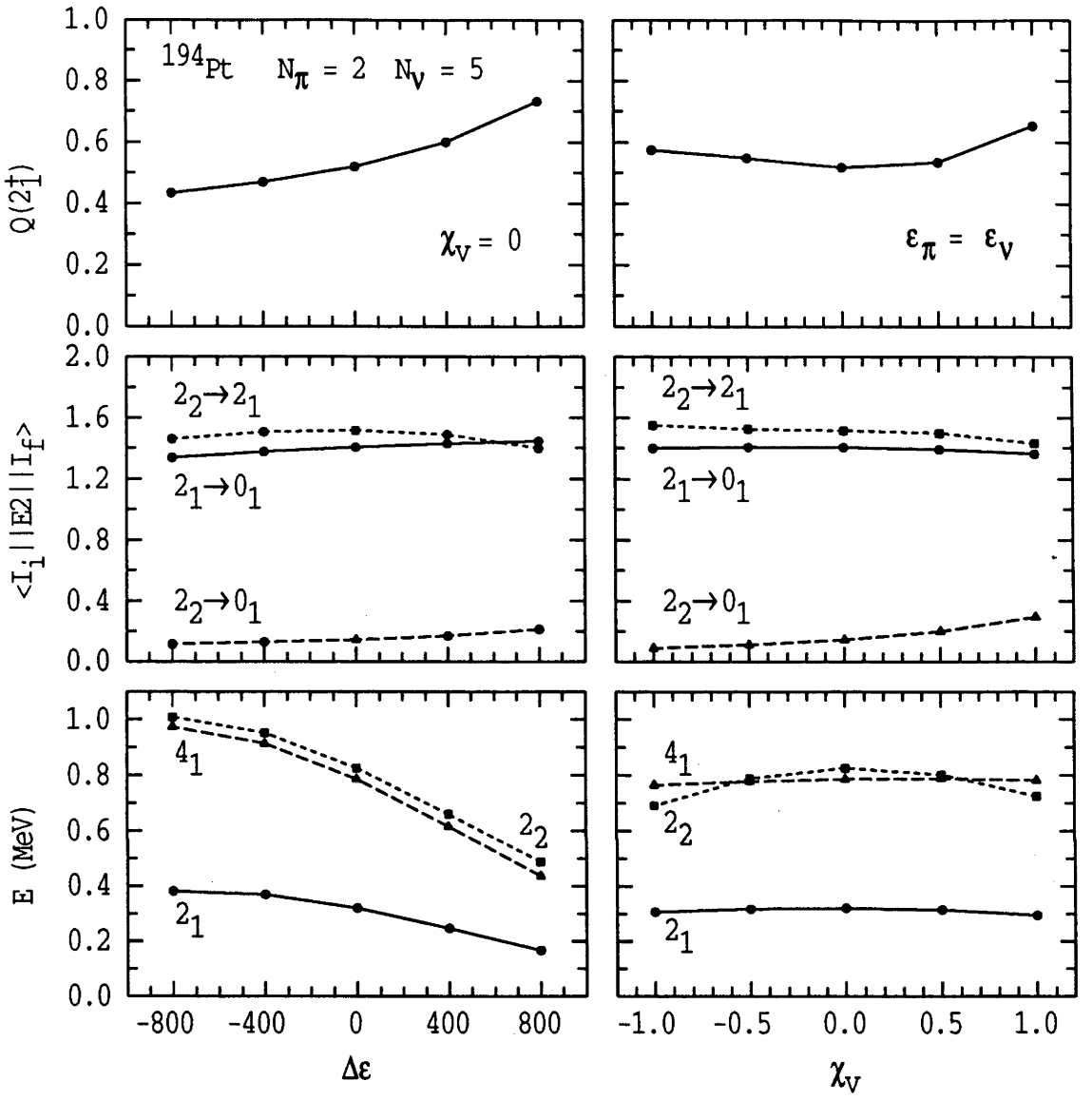

Figure 9.15: Dependence of selected level energies and $E2$ properties in ^{194}Pt on the symmetry-breaking parameters $\Delta\epsilon$ and χ_V.

$g(2_1^+)$ become larger than the F-spin symmetric predictions) for $N \lesssim 114$.

Separate and systematic studies have been made of the effects of $\epsilon_\pi \neq \epsilon_\nu$ (or $\Delta\epsilon$) and $\chi_\pi \neq \chi_\nu$ breaking on the nuclear properties for the oblate ^{190}Pt, ^{194}Pt and ^{198}Pt nuclei. These calculations are similar to those performed for ^{190}Os in refs. [St94b, Ku95], and involved diagonalizing the hamiltonian of eq. 2.6 using the code NPBOS [Ot85]. For convenience, we define the usual scalar and vector χ parameters, $\chi_S = \frac{1}{2}(\chi_\pi + \chi_\nu)$ and $\chi_V = \frac{1}{2}(\chi_\pi - \chi_\nu)$. The results for the g-factors and $2_2^+ \rightarrow 2_1^+$ $M1$ transition in ^{194}Pt are displayed in fig. 9.14. The dependence

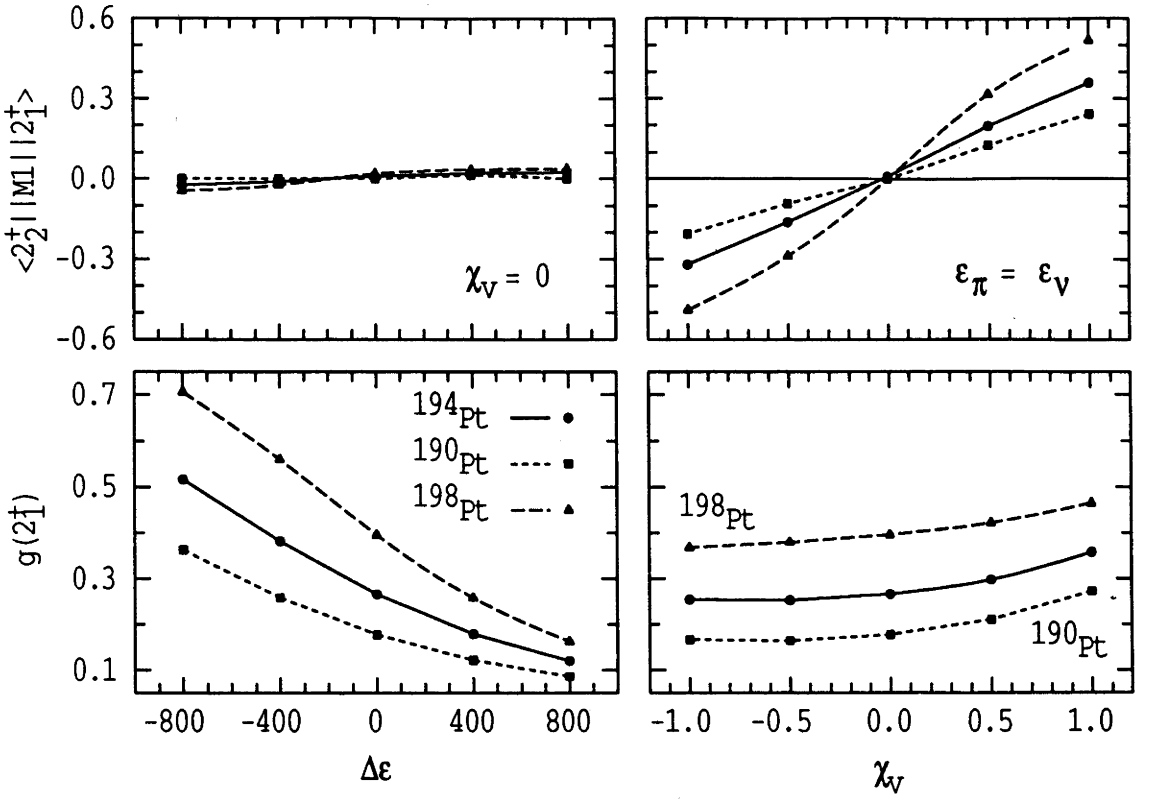

Figure 9.16: Dependence of the $g(2_1^+)$ and $2_2^+ \rightarrow 2_1^+$ matrix element in the ^{190,194,198}Pt isotopes on the symmetry-breaking parameters $\Delta\epsilon$ and χ_V. Here $\epsilon = 450, 550$ and 580 keV, respectively, $\chi_S = 0.18$ MeV, $\kappa = -0.18$ MeV and $\xi = 0.17$ MeV.

of ^{194}Pt level energies and $E2$ properties are shown in fig. 9.15. A comparison of the 2_1^+ g-factors and $2_2^+ \rightarrow 2_1^+$ $M1$ matrix elements for the ^{190,194,198}Pt isotopes is given in fig. 9.16.

The general trends observed in the Pt nuclei (fig. 9.14) are somewhat different to those noted (by Kuyucak and Stuchbery) for ^{190}Os, mainly due to the change in shape from prolate (Os) to oblate (Pt). In both cases, increasing $\Delta\epsilon$ (with $\epsilon = \frac{1}{2}(\epsilon_\pi + \epsilon_\nu)$ fixed and $\chi_V = 0$) produces very weak $2_2^+ \rightarrow 2_1^+$ $M1$ transitions and nearly equivalent monotonic decreases in $g(2_1^+)$ and $g(2_2^+)$. In contrast with this, varying χ_V (with χ_S constant) creates large $M1$ rates and a discrepancy between $g(2_1^+)$ and $g(2_2^+)$, where $g(2_1^+)$ increases with χ_V for the Pt nuclei but decreases for Os. As expected, $E2$ transitions and, for the most part, energy levels and quadrupole moments are *not* strongly dependent on either of these symmetry-breaking mechanisms (see fig. 9.15).

In the schematic calculations for the Pt nuclei there is a (slightly) greater non-linearity in the dependence of the magnetic properties on $\Delta\epsilon$ and, in particular,

Table 9.4: Fit values for the F-spin symmetry-breaking parameters ϵ_ρ [keV] and χ_ρ [MeV] in the Pt ($N_\pi = 2$) nuclei[a]. Other parameters were set to zero, except for $\kappa = -0.18\,\mathrm{MeV}$ and $\xi = 0.17\,\mathrm{MeV}$.

Nucleus	N_ν	ϵ_π	ϵ_ν	ϵ[b]	$\Delta\epsilon$	χ_π	χ_ν	χ_S[c]	χ_V[c]
^{190}Pt	7	200	700	450	-250	0.28	0.08	0.18	0.10
^{192}Pt	6	330	670	500	-170	0.28	0.08	0.18	0.10
^{194}Pt	5	480	620	550	-70	0.23	0.13	0.18	0.05
^{196}Pt	4	600	560	580	20	-0.02	0.38	0.18	-0.20
^{198}Pt	3	680	480	580	100	-0.12	0.48	0.18	-0.30

[a] Taken from ref. [Ku95]

[b] $\epsilon = \frac{1}{2}(\epsilon_\pi + \epsilon_\nu)$

[c] The scalar and vector parameters are defined in the text.

χ_V than in ^{190}Os. This is probably related to the proximity of the $Z = 82$ (and $N = 126$) closed shell(s), i.e. the smaller number of active bosons. The mass-dependence of the g-factors and $M1$ transition rates is displayed for the $A = 190, 194, 198$ isotopes in fig. 9.16.

To determine a parameter set for the even $^{186-192}$Os and $^{190-198}$Pt nuclei, a global fit of the available $E2$ and $M1$ nuclear data was performed [St94b, Ku95]. The values for ϵ and χ_S (which were varied with N_ν) and κ and ξ (held constant) were determined by fitting the level energies and $E2$ transition rates; $\Delta\epsilon$ and χ_V were then extracted from the $M1$ data. The parameters for the Pt isotopes are given in table 9.4. The results of the fit for some magnetic dipole properties are compared with experiment in figs. 9.17 and 9.18. The satisfactory agreement with measured $E2$ properties is evident in tables 9.5, 9.6 and 9.7, where values from selected, previous theoretical studies are also given.

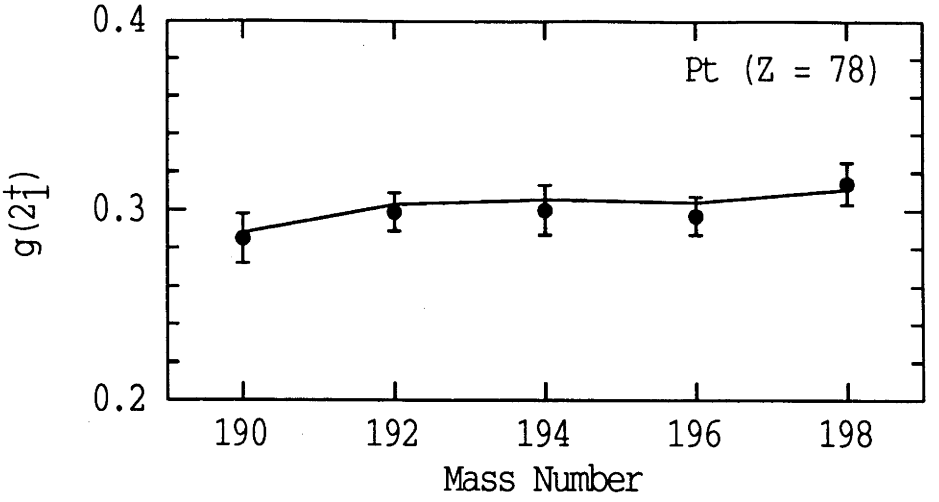

Figure 9.17: Comparison of measured $g(2_1^+)$ for $^{190-198}$Pt with the results of the fit [Ku95] described in the text and table 9.4 (fig. 9.19).

The $\epsilon_{\pi,\nu}$ and $\chi_{\pi,\nu}$ parameters are smoothly varying functions of mass (N_ν) in fig. 9.19. Clearly, there is substantial χ_V breaking. The values used for parameters other than $\chi_{\pi,\nu}$, i.e. $\epsilon_{\pi,\nu}$, $\kappa = -0.18\,\mathrm{MeV}$ and $\xi = 0.17\,\mathrm{MeV}$, are typical of those found in IBM-2 studies (see refs. [Wo93, Da94b] and sect. 2.2.1). The maximum F-spin component in the low-lying states was calculated as ranging from 96% to 98%.

The constant Pt g-factors have been reproduced in the standard *sd*-IBM-2 without including anomalous boson g-factors, effective boson numbers or shape coexistence effects, none of which are supported by other experimental data for these nuclei. It may also be concluded that it is necessary to include both $\Delta\epsilon$ and χ_V variations for a proper description of the $M1$ properties of the Pt nuclei. However, the interpretation of the boson model parameters is still, at least partially, an open question.

It has been shown [Le90] that the degree of F-spin mixing is largely determined by differences in the deformations of the proton- and neutron-boson condensates. In light of this, the present IBM-2 description of the Pt $M1$ properties has been related qualitatively to the deformations of the proton and neutron 'fluids' in the nuclei [Ku95]. It appears that the ratio of the proton-to-neutron deformation may increase with neutron number. Although the proton and neutron deformations in a nucleus are usually thought to be similar, if they were to differ the most plausible picture would have the neutrons becoming less deformed as the $N = 126$ closed shell is approached. Interestingly, a similar analysis of the neighbouring

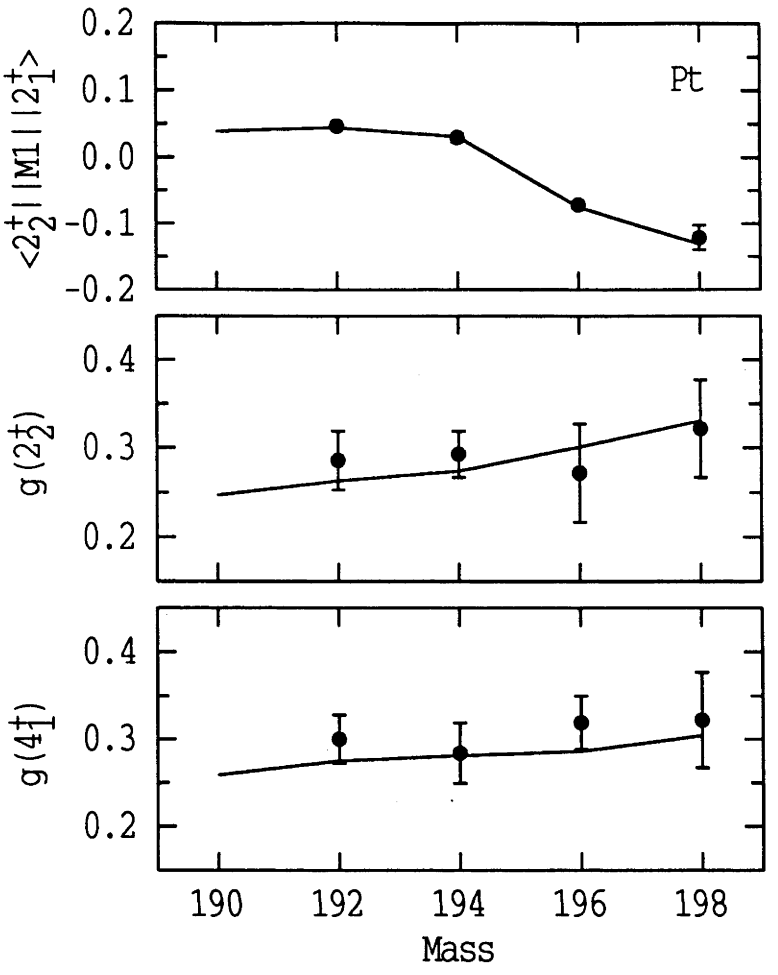

Figure 9.18: Comparison of experimental values (refs. [Kr80, St81b] and references therein) with fit [Ku95] results (see text and table 9.4) for selected magnetic dipole properties in the Pt isotopes.

Os isotopes based on the geometrical model [St95b] is consistent with the same qualitative mass-dependent systematics for the proton-to-neutron deformation. This matter clearly requires further investigation.

It has been demonstrated here that a consistent phenomenological description of the $E2$ and $M1$ properties for the heavy transitional nuclei is possible. Future work should include clarification of the interpretation of phenomenological parameters in terms of the geometrical model and then, eventually, their interpretation with microscopic considerations.

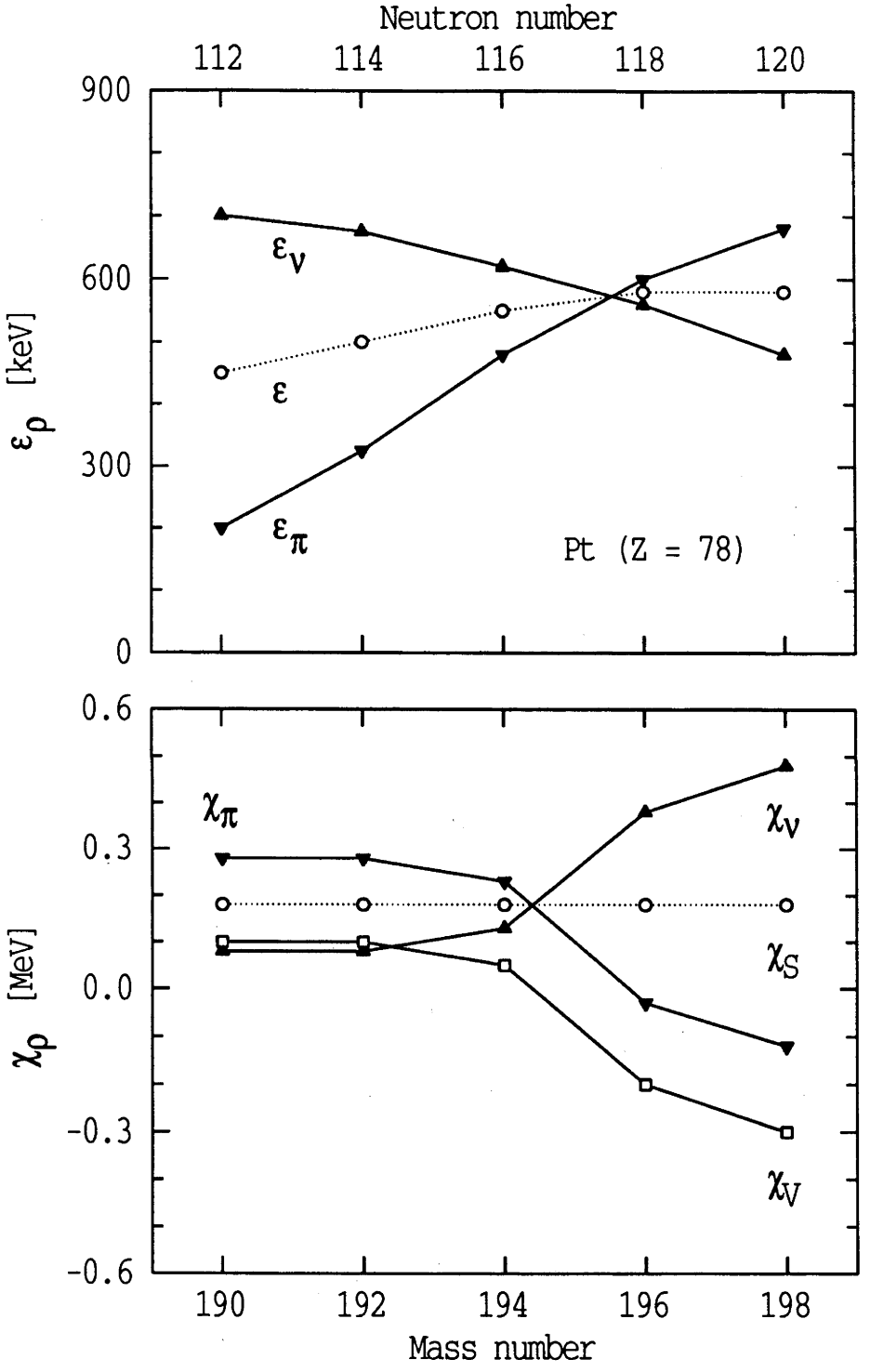

Figure 9.19: Values for the F-spin symmetry-breaking parameters ϵ_ρ and χ_ρ in the Pt ($N_\pi = 2$) nuclei, from a fit to the $M1$ properties [Ku95] (see text and table 9.4).

Table 9.5: Comparison of measured $E2$ matrix elements for ^{190}Pt with calculated values by Bijker *et al.* [Bi80] and from fitting the level energies and $E2$ transitions as in ref. [Ku95], which is discussed in the text.

	$\mid < J_f \mid\mid$ T(E2) $\mid\mid J_i > \mid_{calc.}$		$\mid < J_f \mid\mid$ T(E2) $\mid\mid J_i > \mid_{exp.}$	
$J_i \rightarrow J_f$	Bijker	present[a]	Value	Reference
$2_1^+ \rightarrow 0_1^+$	1.645	1.471	1.350 ± 0.033	present
$4_1^+ \rightarrow 2_1^+$	2.632	2.356		
$6_1^+ \rightarrow 4_1^+$	3.360	3.005		
$2_2^+ \rightarrow 2_1^+$	1.668	1.530		
$2_2^+ \rightarrow 0_1^+$	0.310	0.218		
$2_1^+ \rightarrow 2_1^+$	1.085	0.891		

[a] From ref. [Ku95]

Table 9.6: Comparison of measured $E2$ matrix elements for ^{192}Pt and ^{194}Pt with calculations from the *sdg*-IBM [La92] (see sect. 9.3.1.3) and refs. [Bi80, Ku95].

Nucleus	$J_i \rightarrow J_f$	$\lvert < J_f \rVert$ T(E2) $\lVert J_i > \rvert_{calc.}$			$\lvert < J_f \rVert$ T(E2) $\lVert J_i > \rvert_{exp.}$	
		sdg	Bijker	present[a]	Value	Ref.
^{192}Pt	$2_1^+ \rightarrow 0_1^+$	1.449	1.469	1.353	1.449 ± 0.035	[Ei85, Ya88]
	$4_1^+ \rightarrow 2_1^+$	2.294	2.334	2.154	2.343 ± 0.038	[Ya88]
					2.362 ± 0.057	[Ei85]
	$6_1^+ \rightarrow 4_1^+$	2.908	2.980	2.725	2.472 ± 0.473	[Jo77]
	$2_2^+ \rightarrow 2_1^+$	1.760	1.438	1.518	2.179 ± 0.080	[Ya88]
					1.517 ± 0.082	[Ei85]
	$2_2^+ \rightarrow 0_1^+$	0.183	0.079	0.176	0.152 ± 0.008	[Ya88]
					0.148 ± 0.008	[Ei85]
	$2_1^+ \rightarrow 2_1^+$	0.797	0.191	0.739	0.818 ± 0.079	[Ra89]
					0.726 ± 0.277	[Ra89]
^{194}Pt	$2_1^+ \rightarrow 0_1^+$	1.284	1.337	1.232	1.284 ± 0.006	[Si89]
	$4_1^+ \rightarrow 2_1^+$	2.025	2.114	1.947	1.987 ± 0.038	[Si89]
	$6_1^+ \rightarrow 4_1^+$	2.550	2.660	2.434	2.893 ± 0.140	[Si89]
	$8_1^+ \rightarrow 6_1^+$	2.933	2.959	2.731	3.205 ± 0.304	[Si89]
	$2_2^+ \rightarrow 2_1^+$	1.335	1.609	1.336	1.478 ± 0.027	[Si89]
	$2_2^+ \rightarrow 0_1^+$	0.160	0.013	0.129	0.089 ± 0.002	[Si89]
	$2_1^+ \rightarrow 2_1^+$	0.707	0.171	0.586	0.633 ± 0.185	[Ra89]
					0.831 ± 0.079	[Ra89]
					$0.540\ (^{+0.081}_{-0.059})$	[Wu83]
	$4_1^+ \rightarrow 4_1^+$	0.593	0.624	0.645	$1.000\ (^{+0.120}_{-0.140})$	[Wu83]
	$6_1^+ \rightarrow 6_1^+$	0.405	1.213	0.657	$0.280\ (^{+0.120}_{-0.269})$	[Wu83]
	$2_2^+ \rightarrow 2_2^+$	0.670	0.034	0.526	0.66 ± 0.66	[Ra89]
					$0.400\ (^{+0.120}_{-0.052})$	[Wu83]

[a] From ref. [Ku95]

Table 9.7: Comparison of measured and calculated $E2$ matrix elements for ^{196}Pt and ^{198}Pt.

Nucleus	$J_i \rightarrow J_f$	$\lvert < J_f \rVert$ T(E2) $\lVert J_i > \rvert_{calc.}$			$\lvert < J_f \rVert$ T(E2) $\lVert J_i > \rvert_{exp.}$	
		sdg[a]	Bijker[b]	present[c]	Value	Ref.
^{196}Pt	$2_1^+ \rightarrow 0_1^+$	1.200	1.202	1.103	1.200 ± 0.029	[Bo81]
	$4_1^+ \rightarrow 2_1^+$	1.881	1.885	1.727	1.904 ± 0.076	[Bo81]
					$1.997\ (^{+0.070}_{-0.047})$	[Ma90]
	$6_1^+ \rightarrow 4_1^+$	2.345	2.305	2.119	2.339 ± 0.322	[Bo81]
					$2.534\ (^{+0.056}_{-0.133})$	[Ma90]
	$8_1^+ \rightarrow 6_1^+$	2.660	2.349	2.298	$3.132(^{+0.149}_{-0.166})$	[Ma90]
	$2_2^+ \rightarrow 2_1^+$	1.230	1.414	1.208	1.323 ± 0.059	[Bo81]
					$1.145\ (^{+0.122}_{-0.118})$	[Ma90]
	$2_2^+ \rightarrow 0_1^+$	0.148	0.002	0.085	< 0.003	[Ca78, Ca87]
	$2_1^+ \rightarrow 2_1^+$	0.671	0.364	0.470	0.871 ± 0.158	[Ra87]
					0.810 ± 0.230	[Ma90]
	$4_1^+ \rightarrow 4_1^+$	0.577	0.816	0.581	$0.389\ (^{+0.302}_{-0.322})$	[Ma90]
	$6_1^+ \rightarrow 6_1^+$	0.412	1.412	0.659	$0.176\ (^{+0.749}_{-0.794})$	[Ma90]
	$8_1^+ \rightarrow 8_1^+$	0.203	2.187	0.703	$0.227\ (^{+0.903}_{-1.344})$	[Ma90]
	$2_2^+ \rightarrow 2_2^+$	0.627	0.223	0.383	$0.303\ (^{+0.258}_{-0.455})$	[Ma90]
^{198}Pt	$2_1^+ \rightarrow 0_1^+$	1.010	1.062	0.964	1.010 ± 0.050	[Bo81]
	$4_1^+ \rightarrow 2_1^+$	1.565	1.639	1.483	1.559 ± 0.066	[Bo81]
	$6_1^+ \rightarrow 4_1^+$	1.919	1.905	1.759	≥ 2.266	[Bo81]
	$2_2^+ \rightarrow 2_1^+$	1.041	1.220	1.036	1.145 ± 0.083	[Bo81]
					0.962 ± 0.062	[Bo81]
	$2_2^+ \rightarrow 0_1^+$	0.108	0.085	0.081	0.039 ± 0.006	[Bo81]
	$2_1^+ \rightarrow 2_1^+$	0.514	0.390	0.423	0.554 ± 0.158	[Ra87]
					0.712 ± 0.158	[Ra87]

[a] Ref. [La92]

[b] Ref. [Bi80]

[c] From ref. [Ku95]

Chapter 10

Conclusions

The main aim of this work was to develop and implement an experimental method for measuring the g-factors of short-lived excited states in unstable nuclei. This was achieved using a novel implantation-decay technique. In a series of measurements on the neutron-deficient ^{184,186,188,190,192}Pt isotopes, nuclear precessions were determined to better than 7% precision and the g-factors of the 2_1^+ states inferred. The usefulness of this technique is well illustrated by the results of these experiments, which have extended the measured $g(2_1^+)$ values to include those for the unstable Pt nuclei near mid-shell.

Future experimental work could include similar magnetic moment measurements on the neutron-deficient Os isotopes and experiments using third-generation γ-ray detector arrays. Our collaboration in an experiment to measure $g(2_1^+)$ in ^{180}Pt on the GaSp array at INFN, Legnaro [Br94], highlighted some of the advantages and difficulties in such measurements. The present generation of arrays are not optimised for measuring perturbed angular correlations due to small detector solid-angles, which reduce the count-rate, and the positioning of detectors at unhelpful angles.

The IBM-2 has had considerable success in describing the level energies and $E2$ properties of the transitional nuclei, where traditional models have struggled. In its simplest F-spin symmetric form, the IBM-2 predicts a marked increase with neutron number for the Pt 2_1^+-state g-factors, as observed for the neighbouring W and Os nuclei. Kumar and Baranger predicted similar systematics for the lighter Pt isotopes with $A \leq 188$. In this context, the near constancy of the measured g-factors for the even isotopes from ^{184}Pt to ^{198}Pt was unexpected, highlighting the difficulties encountered by theoretical descriptions of the $M1$ properties in

transitional nuclei.

In the lighter Pt nuclei, the implications of shape coexistence for the 2_1^+ g-factors were considered through simple band-mixing calculations. The deformed intruder configuration, with a greater number of effective proton bosons, gives rise to larger g-factors in agreement with experiment. As discussed in sect. 9.2, a more rigorous treatment of configuration mixing in the calculations using the IBM, and other microscopic models, would be valuable.

For the heavier isotopes, the measured g-factors and $M1$ transition rates have been reproduced in the IBM-2 through appropriate F-spin mixing, without significantly compromising the descriptions of energy levels and $E2$ properties. For the transitional Os-Pt nuclei, the inclusion of χ_V symmetry-breaking was found to be necessary. While this phenomenological description can be related qualitatively to a decreasing deformation of the neutron fluid in the heavier isotopes, a quantitative interpretation in terms of conventional nuclear model parameters is yet to be found.

This work has contributed to a consistent phenomenological description of both the $E2$ and $M1$ properties of heavy-mass transitional nuclei in the IBM-2. The constant $g(2_1^+)$ values for the Pt isotopes appear to result from a combination of F-spin mixing effects, in the heavier, oblate nuclei, and changes in the number of active proton bosons for the lighter, predominantly prolate isotopes. A fully microscopic interpretation will probably remain elusive for some time. In the interim, it would be valuable to model these processes through the shape transition, with a view to better understanding the evolution of each and the interaction between them.

Appendix A

Implantation Study

A.1 Introduction

The static hyperfine magnetic field present at the nuclei of Pt impurities in magnetized iron (Fe) has been measured several times using the first-excited states in the ^{192}Pt, ^{194}Pt and ^{196}Pt nuclei as probes. The radioactivity technique, which measures integral perturbed γ-γ angular correlations (IPAC) following the β-decay of a parent nucleus present as a dilute radioactive impurity in an alloy with Fe (sect. 3.5.3.2), has often yielded conflicting results [Ca64, Bu64, Ke65, Ag66, Mu67, Bé68, Mu68, Ke69, Ke70, Le70, Gr70, Bé70, Ka75, Ka81, Bo92]. Recently, possible systematic errors in the preparation and subsequent measurement of dilute radioactive alloys have been examined by workers [Ka75, Ka81, Bo92] whose measured fields are significantly larger than those most often obtained in earlier experiments. Katayama *et al.* [Ka75] suggested discrepancies may result from incomplete magnetization of the ferromagnetic alloy in several earlier works, while Bodenstedt *et al.* [Bo92] discussed the possibility of incomplete dissolution of the Ir parent nuclei in the Fe medium during source preparation.

The internal field for Pt<u>Fe</u> has also been measured using in-beam experiments [Ka67, Ku69, Ga74], following the implantation of Coulomb-excited Pt nuclei into an Fe medium, as described in sect. 3.5.3.1. An inherent feature of this method is that the implantation site is not well controlled and the possibility that some implanted Pt nuclei will not experience the full internal field cannot be excluded. An added complication is that the excited nuclei experience the transient hyperfine field as they slow to rest in the ferromagnetic host, and earlier implantation studies were performed at a time when the transient field of Pt

in Fe was not well known. Infact, it will be seen below that the transient field contribution in the early work was overestimated by almost a factor of six.

With a recent measurement [Bo92] confirming the full hyperfine field available with a well prepared radioactive source [Ka75, Ka81], and new data on the transient field for Pt in Fe [St94a] it is now appropriate to re-examine the relation between the static hyperfine field for Pt in Fe obtained in implantation measurements compared with radioactivity and other studies. Although this examination of the in-beam implantation field for Pt may not be exactly applicable to our study of the magnetic moments of short-lived excited states in unstable Pt nuclei, which uses internal fields obtained following the implantation of β^+-decay parent nuclei (e.g. Au isotopes), it does provide a bound for the effective hyperfine field strength.

In the present work, we consider the differences that appear in the measured static hyperfine field strength under different conditions of implantation or source preparation, and the question of why a reduced field is sometimes, but not universally, found following implantation. In sect. A.5, the static fields measured for $_{78}$Pt in Fe using various techniques are surveyed. Comparisons of static field data for the neighbouring impurities $_{76}$Os, $_{77}$Ir, $_{78}$Pt, and $_{79}$Au are made in sect. A.6. It is shown that the observation of reduced static fields in IMPAC measurements can be correlated with the lifetimes of the nuclear states used to sample the static field strength, and that the data currently available for the Pt region are consistent with there being a period of the order of 10 ps following ion-implantation during which the static field is quenched.

A.2 Experimental Design

The static hyperfine field strength present at Pt nuclei implanted into Fe may be determined by measuring the perturbations of particle-γ angular correlations following Coulomb excitation of the first-excited 2^+ states in ^{194,196,198}Pt, as the magnetic moments and lifetimes of these nuclear levels are known. As noted above, the probe nuclei interact with both the static field, of present interest, and the transient hyperfine field which is effective as the ions slow to rest within the ferromagnet. The total measured precession angle may be written

$$\Delta\theta_{total} = \Delta\theta_{tr} + \omega_L \tau \, \mathrm{e}^{-T_s/\tau} \quad , \tag{A.1}$$

where $\Delta\theta_{tr}$ is the precession angle caused by the interaction with the transient field and $\omega_L\tau$ is that due to the static field, with a small correction factor for the finite stopping time (T_s) during which the static field is inactive.

As described in sect. 3.3.2.2, the static hyperfine field behaves like a large, externally-applied magnetic field acting on the impurities at rest within a ferromagnetic medium. The precession angle caused by the interaction of the field with the dipole moment of the excited Pt nuclear state over its lifetime can be written

$$\omega_L\tau = -g\frac{\mu_N}{\hbar}B_{st}\tau \quad , \tag{A.2}$$

where τ is the meanlife of the excited nuclear level and the Larmor precession frequency, ω_L, is determined by the g-factor of the state and the field strength, B_{st}.

As the stopping time for the Pt ions is much shorter than the nuclear lifetime ($T_s \ll \tau$), the transient field may be treated as an intense, time-dependent magnetic impulse. Consequently, the transient field precession is

$$\Delta\theta_{tr} = -g\frac{\mu_N}{\hbar}\int_0^{T_s} B_{tr}(t)\,dt \quad . \tag{A.3}$$

In the present work the transient precession angles are virtually identical for the different isotopes, because the g-factors of the 2_1^+ states in ^{194,196,198}Pt are the same within experimental uncertainties (see table A.2).

The internal static field for Pt<u>Fe</u> is negative (its direction is opposite that of the externally applied magnetic field) while the transient field is positive. Therefore, the precessions caused by the static and transient fields cancel somewhat, although the static field contribution dominates because $\tau \gg T_s$. In the present experiments, the transient field precession was varied by changing the initial recoil energy, through use of incident heavy-ion beams of differing mass and energy.

A.3 Experimental Procedure

The experimental arrangement has been described elsewhere, chapter 7 and refs. [St81a, St85, By87]. A target at room temperature ($\sim$ 300 K), consisting of a 0.44 mg/cm^2 natural Pt layer backed by a thick ($\sim$ 4 mg/cm^2), previously-annealed ferromagnetic Fe foil, was bombarded by beams of 36 MeV ^{16}O, 60 MeV ^{28}Si and 80 MeV ^{34}S from the ANU 14UD Pelletron Accelerator. Target nuclei (of principal interest here, ^{194,196,198}Pt) were Coulomb excited and recoil-implanted into the Fe backing. Forward recoil was assured by requiring the de-exciting γ-radiation be recorded in coincidence with the backscattered beam ions detected in an annular counter at 150°–167° to the beam direction. The ferromagnetic Fe backing foil was polarized perpendicular to the γ-ray detection plane by an external field of $\sim$ 0.05 Tesla, which was reversed in direction approximately every 15 minutes.

The γ-radiation was detected in four HPGe detectors. Precession data were collected with two detectors placed at $\pm$65° to the beam direction and at a distance so as to subtend an angle of 40°; another pair at $\pm$115° subtended an angle of 28°. During each beam bombardment, the particle–γ-ray angular correlation was measured using the forward detectors at a number of angles (0°, $\pm$10°, $\pm$20°, $\pm$30°, $\pm$40°, $\pm$45°, $\pm$55° and $\pm$65°), while the backward pair were kept fixed to serve as monitors. Some precession data with an incident ^{16}O beam were also acquired with the backward detector pair at $\pm$120° and subtending an angle of 24°.

The precession angles were determined in the usual manner, described in sect. 7.2, from the measured, field up/down counting asymmetry, ϵ, and the calculated logarithmic derivative of the angular correlation, S, for each detector pair placed at symmetric angles to the beam direction:

$$\Delta\theta = \frac{\epsilon}{S} \quad . \tag{A.4}$$

A.4 Results

A.4.1 Measured precessions

Figure A.1 shows a coincidence γ-ray spectrum of the de-exciting transitions measured at +65° to the beam direction, following Coulomb excitation of the Pt nuclei by the incident beam 80 MeV ^{34}S. Measured counting asymmetries and derived precession angles are given in table A.1. The particle–γ-ray angular correlations of the $2_1^+ \rightarrow 0_1^+$ transitions in ^{194,196,198}Pt for each incident beam are displayed in figs. A.2, A.3 and A.4. The angular correlation measurements confirm the calculations (sect. A.3) and provide a means of checking the angular positioning of the γ-ray detectors. Uncertainties in the γ-ray detector angles were allowed for in subsequent analysis.

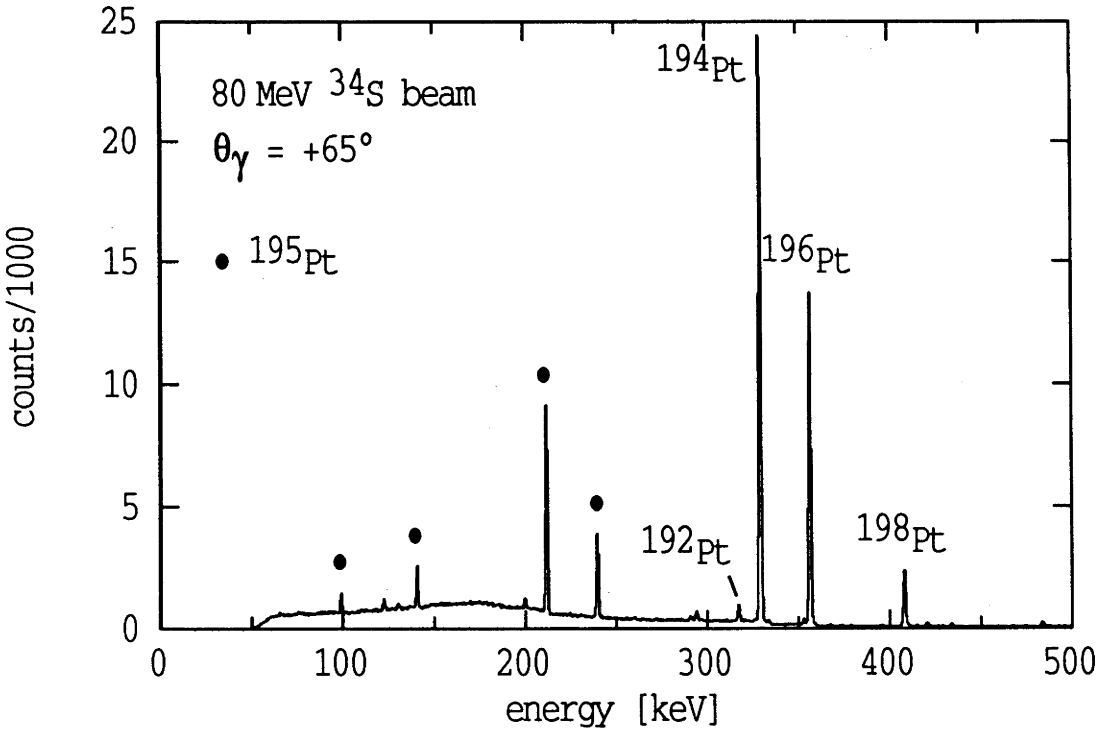

Figure A.1: The γ-ray spectrum measured in coincidence with backscattered ^{34}S beam ions. The $2_1^+ \rightarrow 0_1^+$ transitions in ^{192,194,196,198}Pt are indicated.

Table A.1: Results of the measurements for the 2_1^+ states in ^{194,196,198}Pt.

Nucleus; Expt.[a]	ϵ_F[b] ($\times 10^3$)	S_F[c]	ϵ_B[b] ($\times 10^3$)	S_B[c]	$\Delta\theta_F$[d] [mrad]	$\Delta\theta_B$[d] [mrad]
36 MeV ^{16}O beam						
^{194}Pt ; I	−165.6(7.7)	−2.28	211.8(9.9)	2.76	72.6(3.4)	76.7(3.6)
; II	−171.6(5.9)	−2.28	162.9(6.9)	2.05	75.3(2.6)	79.5(3.4)
^{196}Pt ; I	−133.2(10.4)	−2.28	155.6(13.2)	2.76	58.4(4.6)	56.4(4.8)
; II	−145.6(8.0)	−2.28	120.9(9.4)	2.05	63.9(3.5)	59.0(4.6)
^{198}Pt ; I	−88(29)	−2.28	105(40)	2.76	38.6(12.7)	38.0(14.5)
; II	−92(22)	−2.28	120(26)	2.05	40.4(9.6)	58.5(12.7)
60 MeV ^{28}Si beam						
^{194}Pt	−155.1(3.7)	−2.445	175.5(4.2)	2.765	63.4(1.5)	63.5(1.6)
^{196}Pt	−124.3(4.9)	−2.445	129.4(5.6)	2.765	50.8(2.0)	46.8(2.0)
^{198}Pt	−47(13)	−2.445	71(15)	2.76	19.1(5.5)	25.8(5.5)
80 MeV ^{34}S beam						
^{194}Pt	−141.0(3.1)	−2.48	150.5(3.3)	2.76	56.9(1.3)	54.5(1.2)
^{196}Pt	−106.2(4.0)	−2.485	112.8(4.3)	2.77	42.7(1.6)	40.7(1.6)
^{198}Pt	−53(11)	−2.49	47(11)	2.775	21.2(4.3)	16.8(4.1)

[a] Two separate experiments were performed with a 36 MeV ^{16}O beam, see text.

[b] Measured counting asymmetries with errors (see text) for the forward (F) and backward (B) detector pairs.

[c] Logarithmic derivative of the angular correlation (see text) for both detector pairs.

[d] Precession angle (see text) for each detector pair, errors due only to uncertainty in measured ϵ values.

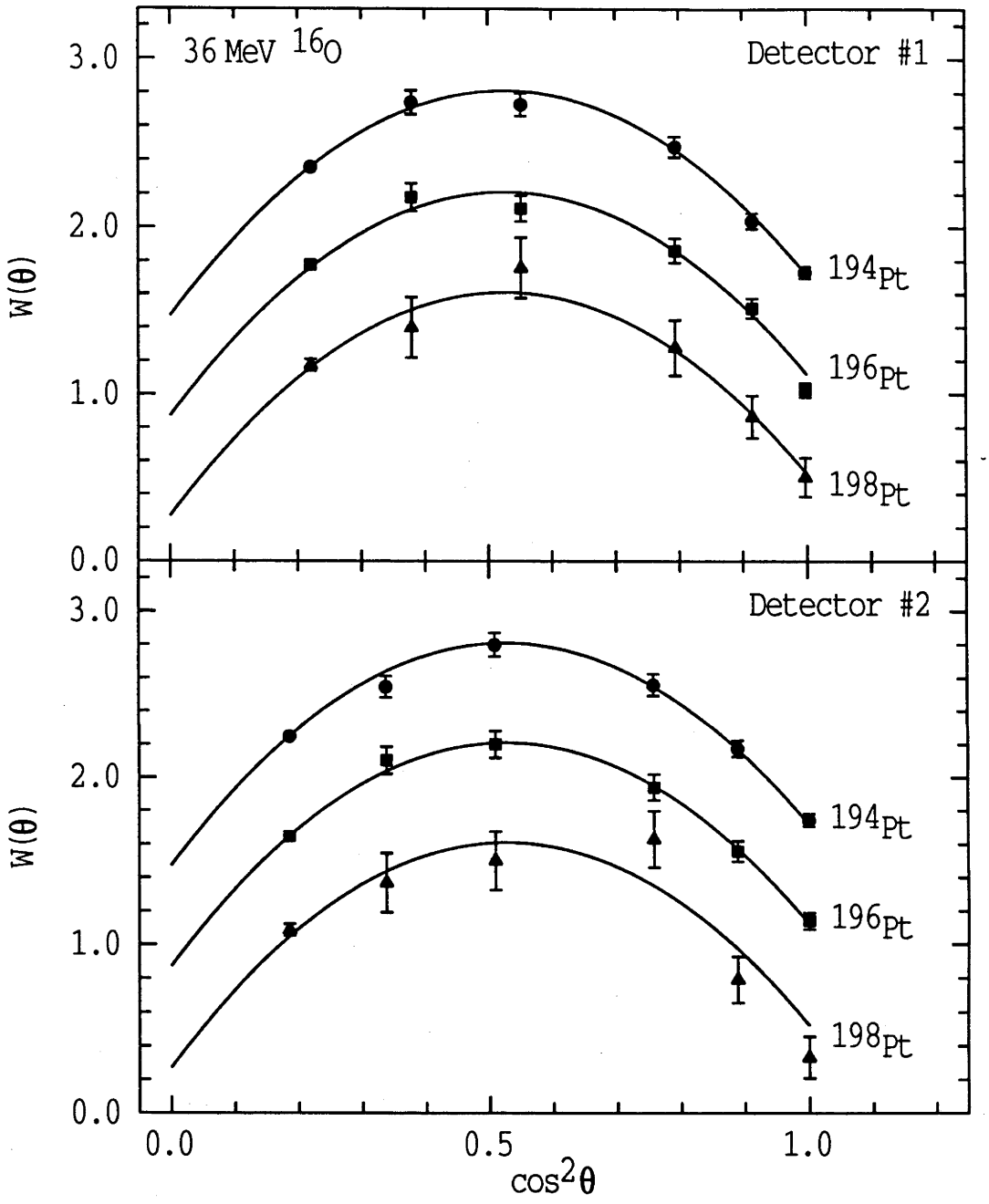

Figure A.2: Particle–γ-ray angular correlations for the $2_1^+ \rightarrow 0_1^+$ transitions in ^{194,196,198}Pt following Coulomb excitation by 36 MeV ^{16}O ions. The forward angle γ-ray detectors in the positive and negative quadrants are labelled #1 and #2, respectively. Measured (data points) and calculated (lines) correlations are shown for both detectors. For clarity, those for ^{194}Pt and ^{196}Pt have been offset by +1.2 and +0.6, respectively.

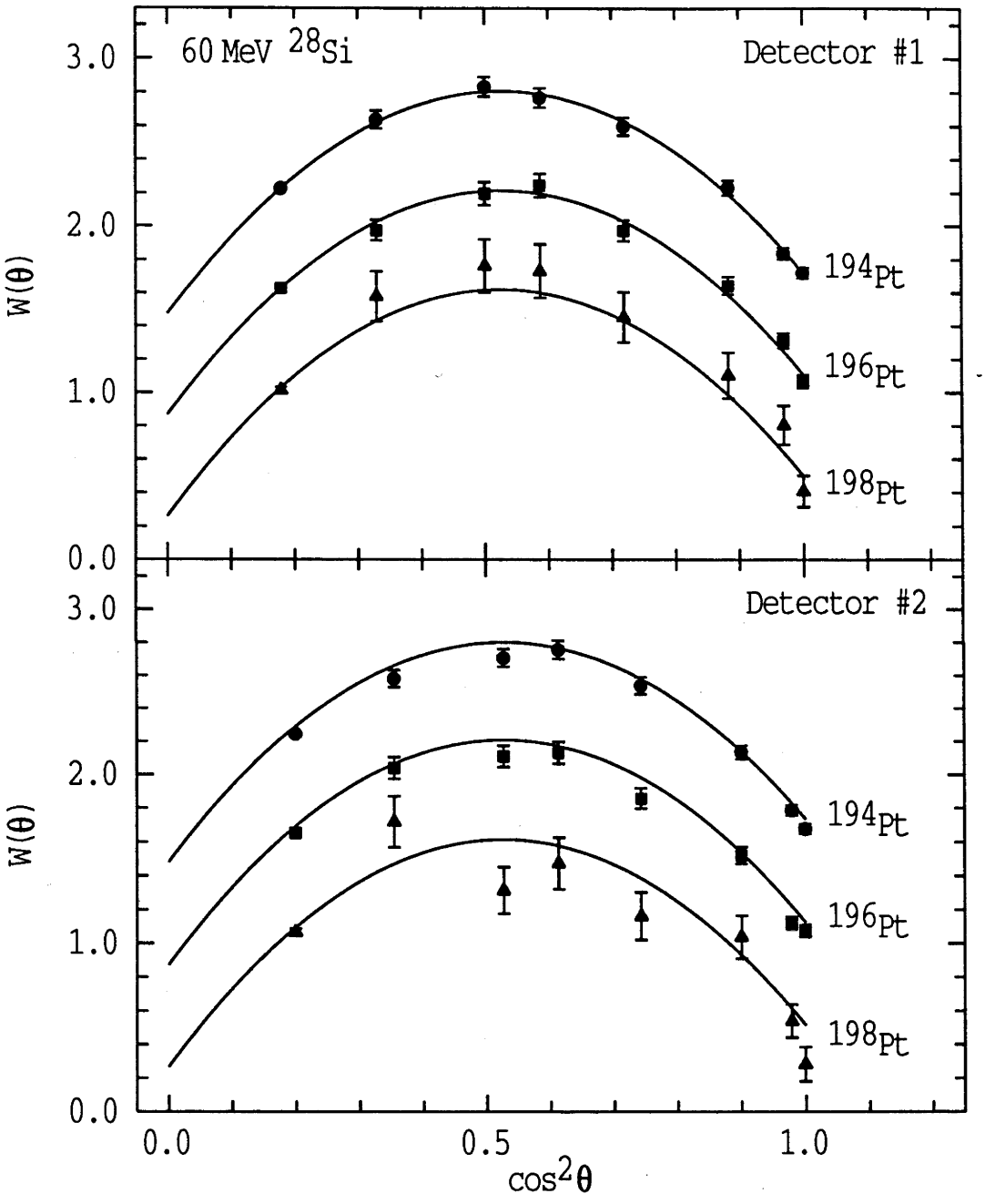

Figure A.3: Same as fig. A.2, for 60 MeV ^{28}Si ion bombardment.

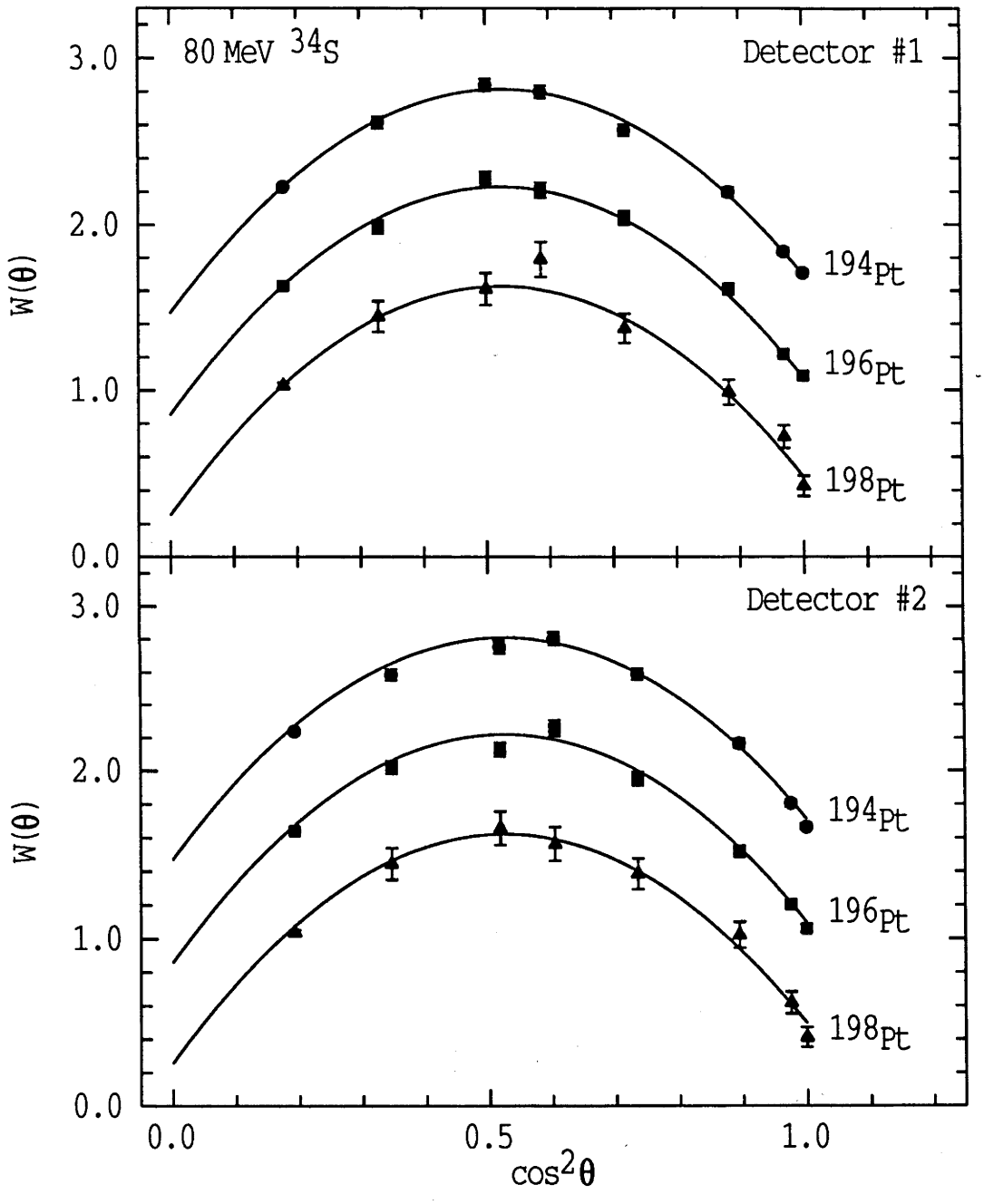

Figure A.4: Same as fig. A.2, for 80 MeV ^{34}S ion bombardment.

A.4.2 Correction for transient field contribution

The transient field strength apparent as the Pt ions recoiled through the polarized Fe was calculated using the parameterization found recently by Stuchbery *et al.* [St94a], for Pt ion velocities in the range $1v_0 < v < 5v_0$. This expresses the transient field strength in terms of the velocity, v, and atomic number, Z, of the ion ($v_0 = \frac{c}{137}$ is the Bohr velocity):

$$B_{tr} = a\,Z\left(\frac{v}{v_0}\right)\exp[-\beta(v/v_0)] \qquad (a = 14.9 \pm 0.2\,\mathrm{T},\ \beta = 0.085 \pm 0.010) \quad . \tag{A.5}$$

The recoil energy imparted to the Pt nuclei varied with the beam species, resulting in different velocity ranges for the Pt recoils in the ferromagnet and varying interaction times with the transient field ($\sim$ 500 fs for the 36 MeV ^{16}O beam bombardment and $\sim$ 1 ps with the ^{34}S beam). The average ion entrance velocities into the Fe foil and calculated transient field precession angles with the different beams are given in table A.2. Unfortunately, the behaviour of the transient field is not well known at ion velocities below the Bohr velocity, v_0. The large uncertainties in the quoted precessions (see table A.2) cover uncertainties in ion stopping times, and the possibility that at velocities below $v \sim \frac{1}{2}v_0$ the transient field may either cut-off or remain constant at a field strength determined by eq. A.5.

The Lindhard-Winther theory [Li71] predicts a transient field which remains constant below about $1v_0$ with a strength of approximately 1 kT. This is significantly larger than the field calculated using the above parameterization (eq. A.5) and would increase the calculated transient field precession angles, presented in table A.2, by $\sim$ 10 mrad. However, experiments on ^{28}Si and ^{134}Ba ions recoiling at low ion velocities in Fe [De80, Eb80] are consistent with the transient field being proportional to ion velocity down to zero. Speidel *et al.* [Sp81a, Sp81b, Sp81c] have shown that data for Mg, O and Si ions in Fe suggest the transient field is constant with a cut-off at $v \sim \frac{1}{2}v_0$. Although the inferred velocity-dependence of the transient field differs in these works, in no case do they support the presence of a Lindhard-Winther contribution. Predictions of the transient field strength from K-vacancy measurements by Dybdal *et al.* [Dy79, Ru86, Dy87] are not sufficiently accurate to draw definite conclusions about the Lindhard-Winther field. The applicability of linear response theory used by Lindhard and Winther has

Table A.2: Experimental particulars, measured precession angles and inferred static field strengths.

Nucleus	$\Delta\theta_{total}$[a] [mrad]	$\frac{v_{in}}{v_o}$[b]	$\Delta\theta_{tr}$[c] [mrad]	$\omega_L\tau$[d] [mrad]	$\tau(2_1^+)$[e] [ps]	$g(2_1^+)$[e]	B_{st}[f] [Tesla]
36 MeV ^{16}O beam							
^{194}Pt	75.9(2.5)	1.32	5(3)	82.8(3.9)	59.2(2.2)	0.300(13)	97(7)
^{196}Pt	60.2(2.6)	1.31	5(3)	66.7(4.0)	48.3(1.4)	0.297(12)	97(8)
^{198}Pt	43.6(6.1)	1.30	5(3)	50.1(6.8)	33.0(1.6)	0.314(11)	101(15)
60 MeV ^{28}Si beam							
^{194}Pt	63.5(1.9)	2.23	14(3)	78.7(3.6)	59.2(2.2)	0.300(13)	93(7)
^{196}Pt	48.8(1.9)	2.21	14(3)	63.7(3.5)	48.3(1.4)	0.297(12)	93(7)
^{198}Pt	22.5(3.9)	2.19	14(3)	37.0(5.0)	33.0(1.6)	0.314(11)	75(11)
80 MeV ^{34}S beam							
^{194}Pt	55.6(1.7)	2.71	19(3)	76.5(3.4)	59.2(2.2)	0.300(13)	90(7)
^{196}Pt	41.7(1.5)	2.69	19(3)	62.3(3.4)	48.3(1.4)	0.297(12)	91(7)
^{198}Pt	18.9(3.0)	2.67	19(3)	39.3(4.2)	33.0(1.6)	0.314(11)	79(10)

[a] Measured precession angle from weighted average of values given in table A.1; a 2.5% error in S is included.

[b] Entrance velocity of Pt ion in Fe host calculated from known reaction kinematics, target layer thicknesses and the stopping powers of ref. [Zi85a].

[c] Calculated transient field precession, see eqs. A.3 and A.5 and text.

[d] Static field precession angle, including correction for stopping time (see eq. A.5).

[e] Adopted meanlives from ref. [Ra87] and g-factors as in sect. 7.3.2.

[f] Static field strength, eq. A.2.

also been questioned [Pa70, Br77a]. Thus, the weight of evidence is that the Lindhard-Winther field is considerably smaller than predicted, if present at all; consequently, such a contribution has not been included in the calculated transient field corrections of table A.2. It will be seen in the discussion below (sect. A.5.1) that there is experimental evidence which justifies this decision.

A.4.3 Inferred static field precessions

A summary of the experimental particulars, measured precession angles and derived static field strengths is presented in table A.2. The multiple scattering of Pt ions recoiling in the Pt target layer following bombardment by a 36 MeV ^{16}O beam was calculated using the Monte-Carlo code TRIM [Zi85a]. This led to the estimate that $\leq$ 1% of the ions come to rest in the Pt layer for each incident beam, where they are *not* subject to hyperfine magnetic fields and do not precess. This correction was included, as was the stopping time effect ($\sim$ 2%, eq. A.1), in evaluation of the inferred static precession angles, $\omega_L\tau$, given in table A.2.

The weighted average of the static field strengths obtained for the three isotopes and the different beams is -92 ± 5 Tesla. Note that the uncertainty in the transient field corrections, which contributes the same absolute uncertainty to all of our measurements, is a significant portion of the quoted error.

A.5 Comparison of Results

The details of present and previous Pt<u>Fe</u> implantation measurements are summarized in table A.3. The inferred static field strengths from IPAC and IMPAC measurements made on the 2_1^+ states in ^{192,194,196}Pt are compared with the result of a spin-echo experiment [Ko67] in fig. A.5. The results of experiments made on dilute radioactive alloys (i.e. using the radioactivity technique) are presented in the upper frame, while the results of implantation measurements are shown in the lower. Table A.4 provides a summary of the experiments and a key to the references.

A.5.1 Previous in-beam measurements

All previous implantation experiments [Ka67, Ku69, Ga74], except that of Varga *et al.* [Va69], utilized ^{16}O incident ion-beams with energies similar to those in

Table A.3: Comparison of static fields for PtFe from in-beam measurements.

Nucleus	Incident beam	Pt[a] [μg/cm^2]	$\frac{v_{in}}{v_o}$	$\Delta\theta_{total}$[b] [mrad]	$\omega_L\tau$ [mrad]	Ref.
^{194}Pt	33MeV ^{16}O	~150	1.33	72(4)		[Ka67]
	35MeV ^{16}O	300	1.33	73(5)		[Ku69]
	36MeV ^{16}O	150-200	1.39	75(6)		[Ga74]
	36MeV ^{16}O	440	1.32	75.9(2.5)		Present
				$\langle$74.6(1.9)$\rangle$[c]	82(4)	
	60MeV ^{28}Si	440	2.23	63.5(1.1)	79(4)	Present
	80MeV ^{34}S	440	2.71	55.6(0.9)	77(4)	Present
	2.5MeV ^{1}H	-	-	83(5)	83(5)	[Va69]
					$\langle$80(3)$\rangle$[c]	
^{196}Pt	33MeV ^{16}O	~150	1.32	57(3)		[Ka67]
	35MeV ^{16}O	300	1.32	66(13)		[Ku69]
	36MeV ^{16}O	150-200	1.38	56(10)		[Ga74]
	36MeV ^{16}O	440	1.31	60.2(2.6)		Present
				$\langle$58.9(1.9)$\rangle$[c]	66(4)	
	60MeV ^{28}Si	440	2.21	48.8(1.9)	64(4)	Present
	80MeV ^{34}S	440	2.69	41.7(1.5)	62(3)	Present
					$\langle$64(3)$\rangle$[c]	
^{198}Pt	33MeV ^{16}O	~150	1.31	30.5(2.0)		[Ka67]
	36MeV ^{16}O	440	1.30	43.6(6.1)		Present
				$\langle$31.8(1.9)$\rangle$[c]	38(4)	
	60MeV ^{28}Si	440	2.19	22.5(3.9)	37(5)	Present
	80MeV ^{34}S	440	2.67	18.9(3.0)	39(4)	Present
					$\langle$38(3)$\rangle$[c]	

[a] Pt target layer thickness.

[b] Measured precession angle with no transient field correction.

[c] Weighted average.

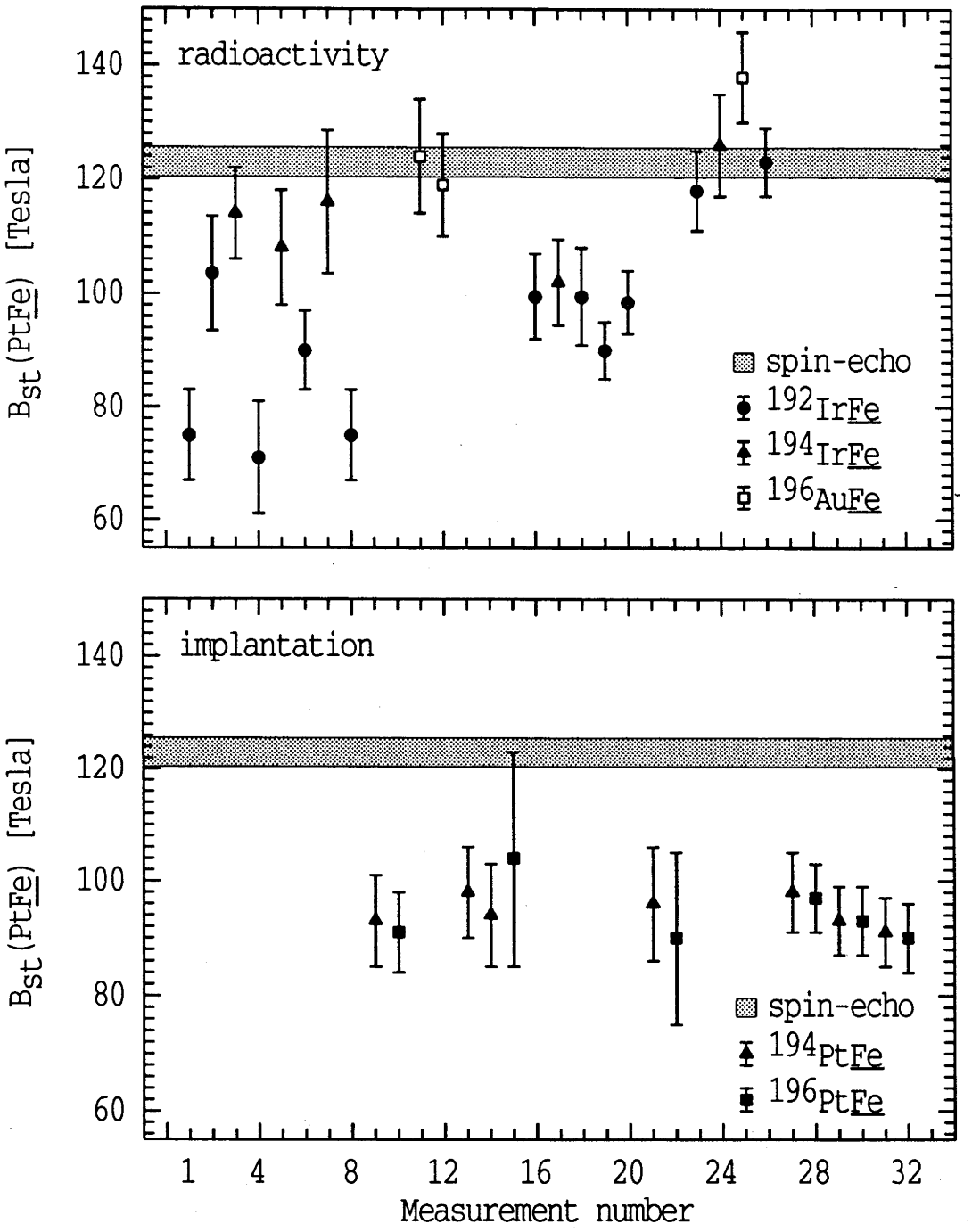

Figure A.5: PtFe static fields from IPAC and IMPAC experiments on ^{192,194,196}Pt, in order of publication date (see table A.4), are compared with a spin-echo result [Ko67]. The field strengths were inferred from measured precessions with adopted 2_1^+-state g-factors (sect. 7.3.2) and lifetimes [Ra87]. Earlier IMPAC data have been re-evaluated using the present transient-field correction, and low-temperature results [Bo92, Ko67] adjusted to room temperature.

Table A.4: Summary of IPAC and IMPAC measurements of the PtFe static hyperfine magnetic field strength.

Measurement number	Year of publication	Technique	Reference
1	1964	R (Ir)[a]	[Ca64]
2,3	1964	R (Ir)	[Bu64]
4,5	1965	R (Ir)	[Ke65]
6,7	1966	R (Ir)	[Ag66]
8	1967	R (Ir)	[Mu67]
9,10	1967	I[b]	[Ka67]
11	1968	R (Au)[c]	[Bé68]
12	1968	R (Au)	[Mu68]
13	1969	in-beam[d]	[Va69]
14,15	1969	I	[Ku69]
16	1969	R (Ir)	[Ke69]
17	1970	R (Ir)	[Ke70]
18	1970	R (Ir)	[Le70]
19	1970	R (Ir)	[Gr70]
20	1970	R (Ir)	[Bé70]
21,22	1974	I	[Ga74]
23,24	1975	R (Ir)	[Ka75]
25	1981	R (Au)	[Ka81]
26	1991	R (Ir)	[Bo92]
27-32[e]	-	I	Present

[a] Radioactivity technique using an IrFe source.

[b] Implantation method following Coulomb excitation with a heavy-ion beam.

[c] Radioactivity technique using a AuFe source.

[d] In-beam experiment using (p, p′) on a PtFe alloy.

[e] In order of increasing incident beam mass (see text).

our ^{16}O beam measurements (see table A.3 for experimental details); the present and previous results for the combined static and transient field effect show good agreement (table A.3). Also, as the kinematics are similar, the transient field precessions in the previous measurements are effectively the same as in our work and may be adequately covered by the present calculated value of 5 ± 3 mrad. This value differs considerably from that assumed earlier [Ku69, Ga74], before the transient field had been sufficiently well studied, namely 28 ± 5 mrad (17.7 ± 3.4 MOe-psec).

Varga *et al.* [Va69] conducted an in-beam measurement by bombarding a Fe-Pt alloy with 2.5 MeV protons. Nuclear states were excited via the (p, p') reaction which caused minimal Pt recoil and resulted in a negligible transient field contribution. The summary of inferred static field precessions, presented in table A.3, shows adequate agreement for the different incident beams; specifically, the present and previous ^{16}O beam experiments, the present ^{28}Si and ^{34}S beam measurements and the proton excitation of Varga *et al.*. This agreement supports the adopted transient field corrections and justifies the decision to discount the Lindhard-Winther field (sect. A.4.2).

In fig. A.5, the results of the present measurements (numbers 27–32) are displayed in order of increasing incident beam mass (see table A.4), i.e. ^{16}O, ^{28}Si and then ^{34}S. These field strengths for $^{194,196}Pt$ may show a decreasing trend with increasing beam mass. However, this is not significant within uncertainties and, as the runs were performed in this beam sequence, there could be be accumulated radiation damage of the Fe foil. Therefore, any beam-related effect that may be present is small and will be ignored in the following discussion.

A.5.2 Radioactivity measurements

A summary of the Pt<u>Fe</u> static field strengths obtained in measurements made on dilute radioactive alloys is presented in the upper frame of fig. A.5. These values, determined from measured precession angles and the present adopted lifetimes and g-factors of the 2_1^+ states in $^{192,194,196}Pt$, are compared with the spin-echo result of Kontani and Itoh [Ko67]: $B_{st}^{300\,K}(Pt\underline{Fe}) = -123 \pm 3$ T (extrapolated to room temperature and corrected for a new value for the ground-state magnetic moment of ^{195}Pt [Sc86]).

Radioactivity measurements using Ir<u>Fe</u> sources found a range of weaker field

strengths [Ca64, Bu64, Ke65, Ag66, Mu67, Ke69, Ke70, Le70, Gr70, Bé70], until the more recent experiments of Katayama *et al.* [Ka75] and Bodenstedt *et al.* [Bo92] measured fields in agreement with the the spin-echo result (see fig. A.5). Katayama *et al.* [Ka75] attributed the discrepancies in earlier works to incomplete magnetization of the sample. As an alternative explanation, Bodenstedt *et al.* [Bo92] suggested that the melting procedure may not have fully dissolved the activated Ir in some Fe samples, thus reducing the number of impurity atoms in substitutional sites within the ferromagnetic host lattice and, therefore, the fraction of Pt nuclei subject to the full hyperfine field. Bodenstedt *et al.* [Bo92] also performed a nuclear-orientation experiment and concluded that their measured field is consistent with that of a perfect alloy.

Interestingly, all measurements made using radioactive ^{196}Au<u>Fe</u> sources [Bé68, Mu68, Ka81] showed fields for Pt in Fe consistent with that of the spin-echo experiment (fig. A.5). The 'full' hyperfine field strength obtained in radioactivity measurements is significantly larger than the average of the present implantation results, -92 ± 5 T (at 300 K).

A.6 Discussion

There is a clear reduction in the Pt<u>Fe</u> static field strength obtained following in-beam implantation compared with the most recent radioactive source experiments [Ka75, Ka81, Bo92]. As incomplete magnetization of the ferromagnetic host is unlikely to be significant in the implantation experiments which use thin Fe foils [Ka75], and given the consistency of the implantation results (see lower frame of fig. A.5), the reduction appears to be an inherent feature of the in-beam implantation method. In the past such reductions have generally been ascribed to radiation damage without considering the damage mechanism, and implicitly assumed that the process is static throughout the lifetime of the probe state.

The implantation-decay measurement on ^{192}Pt, which was performed as a calibration for this technique and is described in sect. 6.1, yielded a field strength of -113 ± 10 T which is somewhat less than the 'full' hyperfine field strength of -123 ± 3 T, but is not consistent with the field found in the present Coulomb excitation measurements (average value -92 ± 5 T). As both implantation techniques employ heavy-ion induced reactions, we can expect, as an initial approximation, that the final sites of the implanted nuclei are similar.

As described in sect. 4.3.4, it has been found from recent nuclear orientation measurements [Hi92] that β-decay may, in some cases, induce lattice site changes. For reasons which will be discussed more fully below, this is considered unlikely to be an important factor here. Rather, we wish to draw attention to the differences in time between implantation and sampling of the static hyperfine field for the two types of experiment. In contrast with the conventional in-beam implantation using Coulomb excitation, where the hyperfine field measurement is typically within 100 ps (10^{-10} s) of the nuclei being implanted, the implantation-decay technique involves measuring the precession following β^+-decay, usually at least several seconds after implantation.

It should be mentioned that the inclusion of a Lindhard-Winther contribution to the transient field might largely account for the difference between the conventional implantation and implantation-decay results. However, this is discounted for the reasons outlined in sects. A.4.2 and A.5.1, and the discrepancy interpreted in terms of time-dependent, pre-equilibrium energy-spike effects, as described in the following.

Near the end of its range, an ion implanted in a solid loses energy through elastic 'nuclear' collisions with lattice atoms. The energy imparted may be sufficient to cause atomic displacements from regular lattice sites, as shown schematically in fig. A.6. As the cross-section for nuclear collisions increases strongly with decreasing projectile energy, the high-density collision-cascade regime is entered near the end of the ion's range. The atomic displacement processes are then most realistically described by an energy spike [Th81], which is believed to temporarily produce damaged zones about the resting position of the ion. This is followed by a dynamic annealing process as the energy disperses. The timescale of these processes is calculated to be of the order of several picoseconds ($\sim 10^{-12}$ to 10^{-11} s), see e.g. ref. [Da84].

If there is no lattice structure surrounding the implanted ion, or it is not in a substitutional site, the nucleus will not experience the full hyperfine field. In the present measurements, the hyperfine field is sampled in the time range up to the lifetime of the states, about 6×10^{-11} s. This means the static hyperfine field may not have reached its equilibrium value, after the disruption caused by the energy spike, until a non-negligible fraction of the nuclear precession has taken place. Therefore, the reduction in the hyperfine field can be due both to pre-equilibrium effects, associated with the dynamics of the ion stopping in the host, and, once

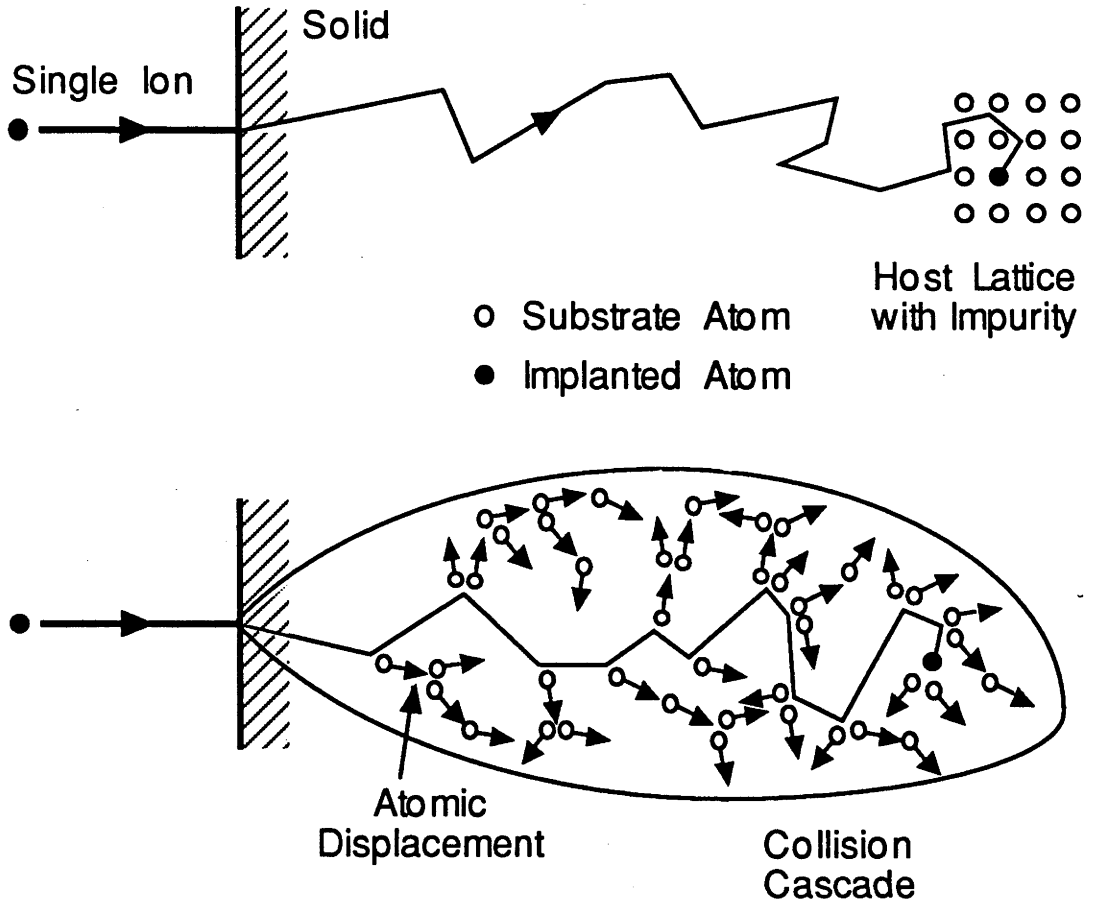

Figure A.6: Illustration of the damage to the host caused by ion-implantation into a solid (adapted from ref. [Wi84]).

equilibrium is reached, a fraction of implanted nuclei sitting at non-lattice sites or sites with residual damage.

The precession in our implantation-decay measurement (sect. 6.1) is unaffected by pre-equilibrium effects because the time taken to reach equilibrium is much shorter than the β^+-decay lifetime. As annealing (or diffusion) of the dilute alloy at room temperature is negligible, and as we have assumed that implantation with the in-beam (Coulomb excitation) and out-of-beam (decay following heavy-ion reaction) techniques are similar, the field of $-113 \pm 10\,\mathrm{T}$ is taken as the *equilibrated* implantation field strength. With the full hyperfine field strength of $-123 \pm 3\,\mathrm{T}$, and assuming a two site model where nuclei lying on interstitial sites experience no magnetic field, this is consistent with $92 \pm 8\%$ of the recoil-implanted ions having final positions in substitutional sites. Béraud *et al.* [Bé68]

compared the hyperfine fields for Pt in Fe using dilute radioactive ^{196}AuFe alloys prepared by either metallurgical techniques (measurement number 11 in table A.4 and fig. A.5) or implantation. Their results imply $95 \pm 12\%$ of the implanted ions are on full-field sites. These conclusions are supported by channelling experiments [Al71] that found $\sim 85\%$ of implanted Au atoms reside on substitutional sites in Fe.

We now return briefly to the question of β-decay induced site changes, as described in sect. 4.3.4. Although the possibility of changes in the nuclear site during the chain of β^+-decay from ^{192}Tl to ^{192}Pt cannot be excluded, there are, however, several reasons why such changes, if present, are of peripheral importance for the present discussion. The results of Hinfurter *et al.* [Hi92] imply a reduction of the net hyperfine field due to β^+-induced recoils of only 2 or 3%. This is both smaller than the precision of the present experiment, and less than the reduction expected due to imperfections in the implantation process (up to $\sim 15\%$, see above) with which the observed hyperfine field following implantation and decay is fully in accord. There is no need to invoke β^+-decay induced site changes to explain the data. Moreover, if present, correction for the presence of β^+-decay induced site changes would move the observed field following implantation and decay closer to the 'full' field value, increasing the disparity between it and the conventional IMPAC result. This could then be interpreted as strengthening the evidence for the dynamic pre-equilibrium effects being considering here.

The observed static field precession would be reduced by in-beam, pre-equilibrium effects and imperfect lattice structure according to

$$(\omega_L \tau)_{obs} = (1 - f_0) \times \omega_L \tau \times e^{-t_e/\tau} \quad , \tag{A.6}$$

where t_e is the time taken for the static hyperfine field to reach its equilibrium value and f_0 is the fraction of implanted ions that, after equilibration, are on interstitial or field-free sites. Alternatively, the ratio of the static hyperfine field observed following an IMPAC measurement, B_{IMPAC}, to the maximum field that would be obtained in the absence of pre-equilibrium effects and with all implanted ions on substitutional sites, B_{max}, can be written

$$B_{IMPAC} \,/\, B_{max} = (1 - f_0) \times e^{-t_e/\tau} \quad . \tag{A.7}$$

Plotting B_{IMPAC}/B_{max} versus the inverse of the lifetime of the probe state,

$(1/\tau)$, provides a convenient means of exposing any pre-equilibrium effects manifested by the IMPAC data. For the present purposes B_{max} is identified with the field strengths measured by NMR or other techniques that employ long-lived probes states [Kr83], as these will not be sensitive to pre-equilibrium effects associated with ion-implantation. The available data for ions with $76 \leq Z \leq 79$ [St87, St92, Kö86, St88], including the present results for Pt, are summarized in table A.5. In fig. A.7 the ratio B_{IMPAC}/B_{max} is plotted versus $(1/\tau)$. The calibration measurement of the implantation-decay technique, described in sect. 6.1, is included. It is associated with $\tau \rightarrow \infty$, since the hyperfine field was sampled several hours after implantation. The upper panel of fig. A.7 shows the results for Pt. In the absence of pre-equilibrium effects these data would be expected to fall on a horizontal line. Instead, they show a trend which is strongly suggestive of a pre-equilibrium quenching of the static field immediately following implantation. The solid line is the best-fit, corresponding to $f_0 = (9 \pm 3)\%$ and $t_e = 10 \pm 2\,\mathrm{ps}$. The combined data for Os, Ir, Pt and Au, shown in the lower panel of fig. A.7, are also consistent with the idea that the static field does not appear until about 10 ps after implantation. The best-fit to the combined data shown in the lower panel of fig. A.7 gave $f_0 = (3 \pm 2)\%$ and $t_e = 13 \pm 2\,\mathrm{ps}$ ($\chi^2_\nu = 0.7$). Acceptable fits are possible with other parameters, e.g. fixing $f_0 = 10\%$ yields $t_e = 9 \pm 2\,\mathrm{ps}$ with $\chi^2_\nu = 1.5$.

The data shown in fig. A.7 are consistent with (i) the presence of pre-equilibrium effects on the anticipated time-scale, and (ii) channelling measurements which imply a large fraction of the implanted ions end up on substitutional sites [Al71]. The proposed scenario provides a natural explanation for the observation that virtually the full field is observed following implantation of Os and Ir ions, where the probe-states live several hundred picoseconds or longer; it also explains the reduced fields observed for states in Ir, Pt and Au which have lifetimes in the range from 25 to 60 ps.

The evidence would be less equivocal, however, if more accurate IMPAC data, preferably for a range of probe-state lifetimes and a single ion-host combination, were available. Improved measurements are required particularly for the shorter-lived states in ^{191,193}Ir and ^{197}Au. New IMPAC data, of sufficient precision, for shorter lifetime states in Os nuclei would also be valuable. Unfortunately, states with lifetimes in both the picosecond and nanosecond range, with precisely known meanlives and g-factors and which are prolifically populated by Coulomb excita-

Table A.5: Comparison of static fields for Os, Ir, Pt and Au impurities in Fe.

Probe	J^π	$\tau(J^\pi)^a$ [ps]	$g(J^\pi)^b$	$B_{IMPAC}{}^c$ [T]	$B_{max}{}^d$ [T]	B_{IMPAC}/B_{max}
^{188}Os	2_1^+	990(27)	0.298(11)	−102(7)	−109	0.94(6)
^{190}Os	2_1^+	551(27)	0.340(12)	−101(4)	−109	0.92(4)
^{192}Os	2_1^+	414(27)	0.398(13)	−109(4)	−109	1.00(4)
^{191}Ir	$5/2_1^+$	178(6)	0.180(9)	−134(12)	−144	0.93(8)
	$7/2_1^+$	33.6(30)	0.59(13)	−105(31)	−144	0.73(22)
^{193}Ir	$5/2_1^+$	127(5)	0.211(12)	−143(12)	−144	0.99(8)
	$7/2_1^+$	29.2(26)	0.62(13)	−92(26)	−144	0.64(18)
^{194}Pt	2_1^+	59.2(2.2)	0.300(13)	−94(6)	−123	0.76(5)
^{196}Pt	2_1^+	48.3(1.4)	0.297(12)	−93(6)	−123	0.76(5)
^{198}Pt	2_1^+	33.0(1.6)	0.314(11)	−77(8)	−123	0.63(7)
^{197}Au	$5/2_1^+$	27(2)	0.296(23)	−58(19)	−112	0.52(17)

[a] Meanlives from refs. [Ra87, Kö86, St88].

[b] g-factors from sect. 7.3.2 and refs. [St94a, St92, Kö86, St88].

[c] IMPAC results for Pt from average precessions in table A.3;
others from refs. [St87, Kö86].

[d] B_{max} from the compilation of Krane [Kr83] and ref. [Ko67], where necessary corrected for room temperature. The relatively small errors are ignored.

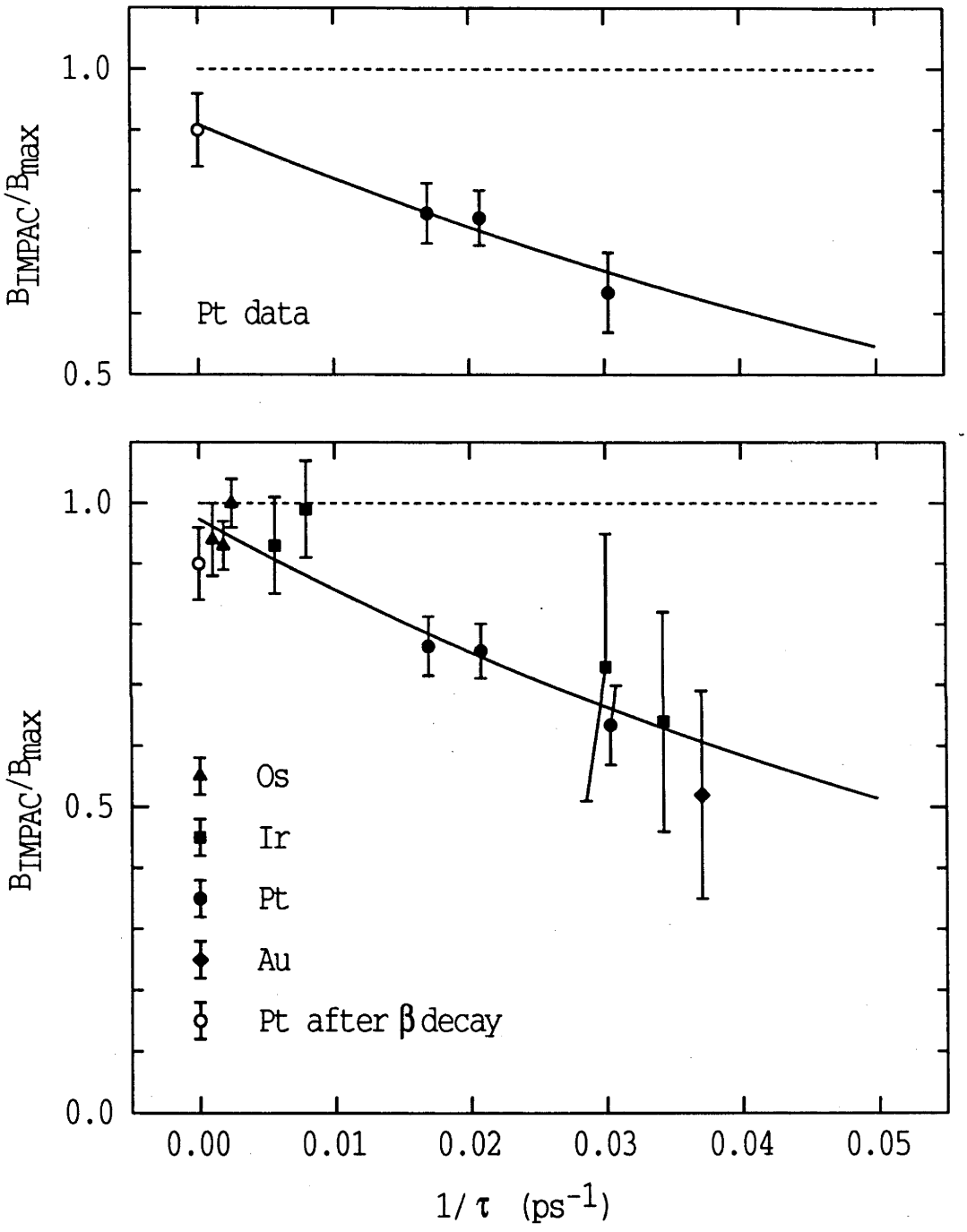

Figure A.7: Ratio of the static fields measured by the IMPAC technique to the 'maximum' static field (as reported in ref. [Kr83]) plotted versus the inverse lifetime of the nuclear probe-state used in the IMPAC measurement.

tion, are not often available in the same probe species. Moreover, as the transient field correction must also be precisely determined, it appears that obtaining incontrovertible evidence for pre-equilibrium effects is not a trivial task.

A.7 Summary and Conclusions

The static hyperfine field acting on ^{194,196,198}Pt in Fe was measured following Coulomb excitation and implantation. The present measured precessions agree with earlier data, but more recent information on the transient field correction leads to an inferred static field strength for the present measurements of -92 ± 5 T, that is $\sim$ 25% smaller than obtained previously [Ka67, Ku69, Ga74]. The static field measured following Coulomb excitation and implantation is markedly smaller than the hyperfine field recently measured using the radioactivity technique [Bo92], which agrees with the spin-echo [Ko67] value of -123 ± 3 T. Furthermore, our out-of-beam implantation-decay experiment on ^{192}Pt obtained a field strength of -113 ± 10 T, which is larger than the in-beam result but on the small side of the 'full' field.

Comparisons have been made between the static fields measured by various techniques for Pt and neighbouring ions in Fe. It is suggested that the discrepancy between the hyperfine fields from NMR or radioactive source experiments and the results of the present in-beam measurements can be attributed to two inherent features of the implantation process: (i) initial structural damage to the Fe host near the resting position of the implanted ion which heals on a timescale of the order of 10 ps, and (ii) the eventual location, after equilibration, of about 10% of the implanted Pt atoms in non-substitutional lattice sites or regions with residual damage. The available IMPAC data for impurities with $76 \leq Z \leq 79$ are consistent with this scenario, as are channelling studies [Al71] which show approximately 85% of Au ions implanted into Fe end up on substitutional locations.

Bibliography

[Ag66] Y.K. Agarval, C.V.K. Baba and S. K. Bhattacherjee, Nucl. Phys. **79** (1966) 437

[Al70] T.K. Alexander and A. Bell, Nucl. Instr. Meth. **81** (1970) 22

[Al71] R.B. Alexander, N.J. Stone, D.V. Morgan and J.M. Poate, in: *Hyperfine Interactions in Excited Nuclei*, ed. G. Goldring and R. Kalish (Gordon and Breach, New York, 1971) p.229

[Al75] K. Alder and R.M. Steffen, in: *The Electromagnetic Interaction in Nuclear Spectroscopy*, ed. W.D. Hamilton (North-Holland, Amsterdam, 1975) p.1

[Al84] A. Alzner, D. Best, E. Bodenstedt, B. Gemünden, T. Merzhäusser, H. Reif, R. Trzcinski, R. Vianden and U. Wrede, Z. Phys. **A316** (1984) 87

[Al88] A. Alzner, E. Bodenstedt, B. Gemünden, J. van den Hoff, S. Piel, R. Sajok, H. Koch, Th. Schäfer and R. Vianden, Z. Phys. **A331** (1988) 277

[An82] H.R. Andrews, O. Häusser, D. Ward, P. Taras, R. Nicole, J. Kienonen, P. Skensved and B. Haas, Nucl. Phys. **A383** (1982) 509

[An88] A. Ansari, Phys. Rev. **C38** (1988) 323

[An95] S.S. Anderssen, A.E. Stuchbery and S. Kuyucak, to be published.

[Ar87] A. Arima and F. Iachello, *The Interacting Boson Model*, (Cambridge University, Cambridge, 1987).

[Ba73] R. Bauer, J. Speth, V. Klemt, P. Ring, E. Werner and T. Yamazaki, Nucl. Phys. **A209** (1973) 535

[Ba83] A.R. Barfield, B.R. Barrett, K.A. Sage and P.D. Duval, Z. Phys. **A311** (1983) 205

[Ba90] D. Bazzacco, F. Brandolini, K. Löwenich, P. Pavan, C. Rossi Alvarez, M. De Poli and A.M.I. Haque, Hyp. Int. **59** (1990) 133

[Ba92] B.R. Barrett, E.D. Davis and A.F. Diallo, Phys. Lett. **B295** (1992) 5

[Bé68] R. Béraud, I. Berkes, J. Danière, M. Lévy, G. Mares R. Rougny, H. Bearnas and D. Spanjaard, in: *Hyperfine Structure and Nuclear Radiations*, ed. E. Matthias and D.A. Shirley (North-Holland, Amsterdam, 1968) p.199

[Bé70] R. Béraud, I. Berkes, R. Chery, R. Haroutunian, M. Lévy, M. Marguier, G. Marest and R. Rougny, Phys. Rev. **C1** (1970) 303

[Be72] I. Berkes, R. Roughny, M. Mayer-Lévy, R. Chéry, J. Danière, G. Lhersonneau and A. Troncy, Phys. Rev. **C6** (1972) 1098; and references therein.

[Be87a] N. Benczer-Koller, D.J. Ballon and A. Pakou, Hyp. Int. **33** (1987) 37

[Be87b] R. Bengtsson, T. Bengtsson, J. Dudek, G. Leander, W. Nazarewicz Phys. Lett. **B183** (1987) 1

[Bi80] R. Bijker, A.E.L. Diéperink, O. Scholten and R. Spanhoff, Nucl. Phys. **A344** (1980) 207

[Bo81] H.H. Bolotin, A.E. Stuchbery, I. Morrison, D.L. Kennedy, C.G. Ryan and S.H. Sie, Nucl. Phys. **A370** (1981) 146

[Bo92] E. Bodenstedt, B. Hamer, P. Herzog, J. Van der Hoff, H. Münning, S. Piel, J. Pronz, R. Sajok, Z. Phys. **A342** (1992) 249

[Br77a] W. Brandt: *Atomic Physics in Nuclear Experiments*, ed. B. Rosner and R. Kalish (Adam Hilger, Bristol, 1977) p.441

[Br77b] R. Brenn, H. Spehl, A. Weckherlin, H.A. Doubt, G. van Middelkoop, Z. Phys. **A 281** (1977) 219

[Br77c] P.J. Brussaard and P.W.M. Glaudemans, *Shell-Model Applications in Nuclear Spectroscopy*, (North-Holland, Amsterdam, 1977) p.56

[Br81] C. Broude, E. Dafni, A. Gelberg, M.B. Goldberg, G. Goldring, M. Hass, O.C. Kistner and A. Zemel, Phys. Lett. **B105** (1981) 119

[Br92] F. Brandolini, M. Ionescu-Bujor, P. Pavan, D. Bazzacco, C. Rossi-Alvarez, M. De Poli, A.M.I. Haque and R.V. Ribas, Nucl. Phys. **A536** (1992) 366

[Br94] F. Brandolini, N.H. Medina, A.E. Stuchbery, S.S. Anderssen, B. Bazzacco, H.H. Bolotin, D. De Acuña, M. De Poli, R. Menegazzo, P. Pavan, C. Rossi-Alvarez and G. Vedovato, in: *1993 Annual Report, INFN-Legnaro*, report **LNL-INFN(Rep)-081/94**, p.58;

A.E. Stuchbery, S.S. Anderssen, F. Brandolini, N.H. Medina, P. Pavan, Bazzacco, H.H. Bolotin and the GaSp Collaboration, in: *1993 Annual Report, Department of Nuclear Physics, Australian National University*, report **ANU-P/1145**, p.43.

[Bu64] A. Buyrn, L. Grodzins, M.I.T. Prog. Rep. **2098** (1964) 251

[By87] A.P. Byrne, A.E. Stuchbery, H.H. Bolotin, C.E. Doran and G.J. Lampard, Nucl. Phys. **A466** (1987) 419

[By91] A.P. Byrne, P.M. Davidson and G.D. Dracoulis, in: *1991 Annual Report, Department of Nuclear Physics, Australian National University*, report **ANU-P/1101**, p.158

[Ca64] J.A. Cameron, Can. J. Phys. **42** (1964) 1680

[Ca85] R.F. Casten, Nucl. Phys. **A443** (1985) 1

[Ca78] R.F. Casten and J.A. Cizewski, Nucl.Phys. **A309** (1978) 477

[Ca87] R.F. Casten and J.A. Cizewski, Phys. Lett. **B185** (1987) 293

[Ca90a] B. Castel and I.S. Towner, *Modern Theories of Nuclear Moments*, (Clarendon, Oxford, 1990) Ch.5

[Ca90b] R.F. Casten, (Oxford University, New York, 1990) p.17

[Ci78] J.A. Cizewski, R.F. Casten, G.J. Smith, M.L. Stelts, W.R. Krane, H.G. Börner and W.F. Davidson, Phys. Rev. Lett. **40** (1978) 167

[Co84] J.D. Cole, J.H. Hamilton, A.V. Ramayya, W. Lourens, B. van Nooijen, H. Kawakami, L.A. Mink, E.H. Spejewski, H.K. Carter, R.L. Mlekodaj, G.A. Leander, L.L. Riedinger, C.R. Bingham, E.F. Zganjar, J.L. Wood, R.W. Fink, K.S. Toth, B.D. Kern and K.S.R. Sastry, Phys. Rev. **C30** (1984) 1267

[Da84] J.A. Davis, in: *Ion Implantation and Beam Processing*, ed. J.S. Williams and J.M. Poate (Academic, New York, 1984) Ch.4 p.81; and references therein.

[Da94a] P.M. Davidson, *Ph.D. Thesis*, Australian National University, Canberra, 1994, unpublished.

[Da94b] E.D. Davis and P. Navrátil, Phys. Rev. **C50** (1994) 2362

[De80] J.A.G. De Raedt, A. Holthuizen, A.J. Rutten, W.A. Sterrenburg and G. Van Middelkoop, Hyp. Int. **7** (1980) 455

[Di87] A.E.L. Dieperink, O. Scholten and D.D. Warner, Nucl. Phys. **A469** (1987) 173

[Do88] C.E. Doran, *Ph.D. Thesis*, University of Melbourne, 1988, unpublished.

[Dr86] G.D. Dracoulis, A.E. Stuchbery, A.P. Byrne, A.R. Poletti, S.J. Poletti, J. Gerl and R.A. Bark, J. Phys, G **12** (1986) L97

[Dr89] G.D. Dracoulis and A.P. Byrne, in: *1989 Annual Report, Department of Nuclear Physics, Australian National University*, report **ANU-P/1052**, p.115

[Du81] P.D. Duval and B.R. Barrett, Phys. Lett. **B100** (1981) 223

[Dy79] K. Dybdal, J.L. Eberhardt and N. Rud, Phys. Rev. Lett. **42** (1979) 592; K. Dybdal, J.S. Forster and N. Rud, Phys. Rev. Lett. **43** (1979) 1711; K. Dybdal, J.S. Forster and N. Rud, Nucl. Instr. Meth. **170** (1980) 233

[Dy87] K. Dybdal and N. Rud, Physica Scripta **35** (1987) 441

[Eb80] J.L. Eberhardt and K. Dybdal, Hyp. Int. **7** (1980) 387

[Ei85] E. Eid and N.M. Stewart, Z. Phys. **A320** (1985) 495

[Ev55] R.D. Evans, *The Atomic Nucleus*, (Mc Graw-Hill, New York, 1955) Ch.15

[Fi72] M. Finger, R. Foucher, J.P. Husson, J. Jastrzebski, A. Johnson, G. Astner, B.R. Erdal, A. Kjelberg, P. Patzelt, A. Hoglund, S.G. Malmskog and R. Henck, Nucl. Phys. **A188** (1972) 369

[Fi88] R.B. Firestone, Nucl. Data Sheets **55** (1988) 583

[Fi89] R.B. Firestone, Nucl. Data Sheets **58** (1989) 243

[Fr65] H. Frauenfelder and R.M. Steffen, in: *Alpha-, Beta- and Gamma-Ray Spectroscopy, Vol. 2*, ed. K. Siegbahn (North-Holland, Amsterdam, 1965) Ch.XIX(A) p.997

[Ga74] D.A. Garber, M. Behar, Z.W. Grabowski, Wm.C. King, Z. Phys. **270** (1974) 163

[Ga74] A. Gavron, Phys. Rev. **C21** (1980) 230

[Ga86] U. Garg, A. Chaudhury, M.W. Drigert, E.G. Funk, J.W. Mihelich, D.C. Radford, H. Helppi, R. Holzmann, R.V.F. Janssens, T.L. Khoo, A.M. Van Den Berg and J.L. Wood, Phys. Lett. **180B** (1986) 319

[Ge87] W. Gelletly, P. van Isacker, D.D. Warner, G. Colvin and K. Schreckenbach, Phys. Lett. **B191** (1987) 240

[Gi92] J.N. Ginocchio, W. Frank and P. von Brentano, Nucl. Phys. **A541** (1992) 211

[Go77] G. Goldring, Y. Niv, Y. Wolfson and A. Zemel, Phys. Rev. Lett. **38** (1977) 221

[Gr66a] W. Greiner, Nucl. Phys. **80** (1966) 417

[Gr66b] L. Grodzins, R.R. Borchers, G.B. Hagemann, Nucl. Phys. **88** (1966) 474

[Gr70] Z.W. Grabowski, Phys. Rev. **C2** (1970) 1093

[Gy86] G.J. Gyapong, R.H. Spear, M.T. Esat, M.P. Fewell, A.M. Baxter and S.M. Burnett, Nucl. Phys. **A458** (1986) 165.

[Ha78] E. Hagberg, P.G. Hansen, P. Hornshoj, B. Johnson, S. Mattsson and P. Tidemand-Peterson, Phys. Lett. **B78** (1978) 29; Nucl. Phys. **A318** (1979) 29

[Hä79] O. Häusser, B. Haas, D. Ward and H.R. Andrews, Nucl. Phys. **A314** (1979) 161

[Hä84] O. Häusser, H.R. Andrews, D. Horn, M.A. Lone, P. Taras, P. Skensved, R.M. Diamond, M.A. Deleplanque, E.L. Dines, A.O. Machiavelli and F.S. Stephens, Nucl. Phys. **A412** (1984) 141

[Ha87] H. Harter, P. von Brentano, A. Gelberg and T. Otsuka, Phys. Lett. **B188** (1987) 295

[Hi92] B. Hinfurter *et al.*, to be published, cited in: E. Hagn, Hyp. Int. **75** (1992) 229

[He81] P.O. Hess, J. Maruhn and W. Greiner, J. Phys. G **7** (1981) 737

[Is86] P. van Isacker, K. Heyde, J. Jolie and A. Sevrin, Ann. Phys. **171** (1986) 253

[Jo77] N.R. Johnson, Phys. Rev. **C15** (1977) 1325

[Ka67] R. Kalish, L. Grodzins, R.R. Borchers, J.D. Bronson and B. Herskind, Phys. Rev. **161** (1967) 160

[Ka75] I. Katayama, S. Morinobu and H. Ikegami, Hyp. Int. **1** (1975) 113

[Ka81] M. Kawamura, T. Tomiyama and H. Kato, J. Phys. Soc. Jpn **50** (1981) 1832

[Ke65] L. Keszthelyi, I. Berkes, I. Deszi and L. Pocs, Nucl. Phys. **71** (1965) 662

[Ke69] D.B. Kenyon, L. Keszthelyi and J.A. Cameron, Can. J. Phys. **47** (1969) 2395

[Ke70] D.B. Kenyon, L. Keszthelyi and J.A. Cameron, Can. J. Phys. **48** (1970) 2730

[Ki71] C. Kittel, *Introduction to Solid State Physics, Fourth Edition*, (Wiley, New York, 1971).

[Ko67] M. Kontani and J. Itoh, J. Phys. Soc. Jpn **22** (1967) 345

[Kö86] W.R. Kölbl, J. Billowes, J. Burde, J.A.G. de Raedt, M.A. Grace, A. Pakou, Nucl. Phys. **A456** (1986) 349

[Kr72] K.S. Krane, Nucl. Instr. Meth. **98** (1972) 205

[Kr80] K.S. Krane, Atomic and Nucl. Data Tables **25** (1980) 29

[Kr83] K.S. Krane, Hyp. Int. **15/16** (1983) 1069

[Ku68] K. Kumar and M. Baranger, Nucl. Phys. **A110** (1968) 529

[Ku69] H.W. Kugel, R.R. Borchers and R. Kalish, Phys. Rev. **A137** (1969) 500

[Ku89] S. Kuyucak and I. Morrison, Ann. Phys. (N.Y.) **195** (1989) 125

[Ku94] S. Kuyucak, in: *Proc. 8th Int. Symp. on Capture γ-ray Spectroscopy*, ed. J. Kern (World Scientific, Singapore, 1994).

[Ku95] S. Kuyucak and A.E. Stuchbery, in press.

[La92] V.-S. Lac and S. Kuyucak, Nucl. Phys. **A539** (1992) 418

[Le70] M. Levanoni, F.C. Zawislac, D.D. Cook, Nucl. Phys. **A144** (1970) 369

[Le78] C.M. Lederer and V.S. Shirley (ed.), *Table of Isotopes, Seventh Edition*, (Wiley, New York, 1978) appendix VII

[Le82] R. Levy, N. Tsoupas, N.K.B. Shu, A. Lopez-Garcia, W. Andrejtscheff and N. Benczer-Koller, Phys. Rev. **C25** (1982) 293

[Le90] A. Leviatan, J.N. Ginocchio and M. Kirson, Phys. Rev. Lett. **65** (1990) 2853

[Li71] J. Lindhard and A. Winther, Nucl. Phys. **A166** (1971) 413

[Li88] C.S. Lim, R.H. Spear, W.J. Vermeer, M.P. Fewell and G.J. Gyapong, Nucl. Phys.**A485** (1988) 399

[Li90a] K.P. Lieb, A.P. Byrne and G.D. Dracoulis, in: *1990 Annual Report, Department of Nuclear Physics, Australian National University*, report **ANU-P/1081**, p.134

[Li90b] C.S. Lim, *Ph.D. Thesis*, Australian National University, Canberra, 1990, unpublished.

[Li90c] P.O. Lipas, P. von Brentano and A. Gelberg, Rep. Prog. Phys. **53** (1990) 1355

[Li92] C.S. Lim, R.H. Spear, M.P. Fewell and G.J. Gyapong, Nucl. Phys. **A548** (1992) 308

[Ma90] A. Mauthofer, K. Stelzer, J. Idzko, Th.W. Elze, H.J. Wollersheim, H. Emling, P. Fuchs, E. Grosse and D. Schwalm, Z. Phys. **A336** (1990) 263

[Mi91] T. Mizusaki, T. Otsuka and M. Sugita, Phys. Rev. **C44** (1991) 1277

[Mo76] H. Morinaga and T. Yamazaki, *In-Beam Gamma-Ray Spectroscopy*, (North-Holland, Amsterdam, 1976) p.40

[Mu67] J. Murray, *Ph.D. Thesis*, Mac Master University, Hamilton, Ontario, 1967.

[Mu68] J. Murray, T.A. McMath and J.A. Cameron, Can. J. Phys. **46** (1968) 75

[Na91] P. Navrátil and J. Dobeš, Nucl. Phys. **A533** (1991) 223

[Ne74] J.O. Newton, in: *Nuclear Spectroscopy and Reactions, Part C*, ed. J. Cerny (Academic, New York, 1974) p.185

[Ni61] S.G. Nilsson and O. Prior, Mat. Fys. Medd. Dan. Vid. Selsk. **32** (1961) No.16

[Ot85] T. Otsuka and N. Yoshida, *Program NPBOS*, report **JAERI-M85-094.**

[Pa70] H. Payne, Phys. Rev. **B1** (1970) 3645

[Pe68] B. Persson, H. Blumberg and D. Agresti, Phys. Rev. **170** (1968) 1066

[Pr68] O. Prior, F. Boehm and S.G. Nilsson, Nucl. Phys. **A110** (1968) 257

[Ra87] S. Raman, C.H. Malarkey, W.J. Milner, C.W. Nestor, Jr. and P.H. Stelson, At. Data Nucl. Data Tables **36** (1987) 1

[Ra89] P. Raghavan, Atomic Data and Nuclear Data Tables **42** (1989) 189

[Re74] E. Recknagel, in: *Nuclear Spectroscopy and Reactions, Part C*, ed. J. Cerny (Academic, New York, 1974) p.93

[Ru86] N. Rud and K. Dybdal, Physica Scripta **34** (1986) 561

[Sa81] M. Sambataro and A.E.L. Diéperink, Phys. Lett. **107B** (1981) 249

[Sa84] M. Sambataro, O. Scholten, A.E.L. Diéperink and G. Piccitto, Nucl. Phys. **A423** (1984) 333

[Sa93] M. Saha and S. Sen, Nucl. Phys **A552** (1993) 37

[Sc86] G. Schutz, E. Hagn, P. Kienle, E. Zech, Phys. Rev. Lett. **56** (1986) 1051

[Sh65] D.A. Shirley and G.A. Westenbarger, Phys. Rev. **138** (1965) A170

[Sh80] N.K.B. Shu, D. Melnik, J.M. Brennan, W. Semmler and N. Benczer-Koller, Phys. Rev. **C21** (1980) 1828

[Sh91] V.S. Shirley, Nucl. Data Sheets **64** (1991) 205

[Si77] S.H. Sie and D.W. Gebbie, Nucl. Phys. **A289** (1977) 217

[Si89] B. Singh, Nuclear Data Sheets **56** (1989) 124.

[Si90a] B. Singh, Nucl. Data Sheets **59** (1990) 133

[Si90b] B. Singh, Nucl. Data Sheets **61** (1990) 243

[Sp79] D.W.L. Sprung, S.G. Lie, M. Vallières and P. Quentin, Nucl. Phys. **A326** (1979) 37

[Sp81a] K.H. Spiedel, G.J. Kumbartzki, W. Knauer, M. Knopp, V. Mertens, P.N. Tandon, J. Gerber and R.M. Freeman, Phys. Lett. **B102** (1981) 6

[Sp81b] K.H. Spiedel, G.J. Kumbartzki, W. Knauer, M. Knopp, V. Mertens, W. Trölenberg, P.N. Tandon, J. Gerber and R.M. Freeman, Ann. Israel Phys. Soc. **4** (1981) 90

[Sp81c] K.H. Spiedel, P.N. Tandon and V. Mertens, Z. Physik. **A302** (1981) 107

[St64] R.M. Steffen and H. Frauenfelder, in: *Perturbed Angular Correlations*, ed. E. Karlsson, E. Matthias and K. Siegbahn (North-Holland, Amsterdam, 1964) p.1

[St70] E. Storm and H.I. Israel, Nucl. Data **A7** (1970) 565

[St75] R.M. Steffen and K. Alder, in: *The Electromagnetic Interaction in Nuclear Spectroscopy*, ed. W.D. Hamilton (North-Holland, Amsterdam, 1975) Chs.12,13

[St76] R.J. Sturm and M. W. Guidry, Nucl. Instr. Meth. **138** (1976) 345

[St81a] A.E. Stuchbery, C.G. Ryan, H.H. Bolotin, I. Morrison and S.H. Sie, Nucl. Phys. **A365** (1981) 317

[St81b] A.E. Stuchbery, C.G. Ryan, I. Morrson and H.H. Bolotin, Phys. Rev. **C24** (1981) 2106

[St85] A.E. Stuchbery, I.Morrison, L.D. Wood, R.A. Bark, H. Yamada and H.H. Bolotin, Nucl. Phys. **A435** (1985) 635

[St87] A.E. Stuchbery, C.E. Doran, A.P. Byrne, H.H. Bolotin and G.D. Dracoulis, Hyp. Int. **36** (1987) 75

[St88] A.E. Stuchbery, L.D. Wood, H.H. Bolotin, C.E. Doran, I. Morrison, A.P. Byrne and G.J. Lampard, Nucl. Phys. **A486** (1988) 374

[St91a] A.E. Stuchbery, G.J. Lampard and H.H. Bolotin, Nucl. Phys. **A528** (1991) 447

[St91b] A.E. Stuchbery, A.G. White, G.D. Dracoulis, K.J. Schiffer and B. Fabricius, Z. Phys. **A338** (1991) 135

[St92] A.E. Stuchbery, S.S. Anderssen, H.H. Bolotin, A.P. Byrne, G.D. Dracoulis, B. Fabricius and T. Kibédi, Z. Phys. **A342** (1992) 373

[St93] A.E. Stuchbery, H.H. Bolotin, F. Brandolini, P. Pavan, S.S. Anderssen, A.P. Byrne, P.M. Davidson, B. Fabricius, G.J. Lane and T. Kibédi, Phys. Lett. **B312** (1993) 40

[St94a] A.E. Stuchbery, T.H. Heseltine, S.S. Anderssen, H.H. Bolotin, A.P. Byrne, B. Fabricius and T. Kibèdi, Hyp. Int. **88** (1994) 97

[St94b] A.E. Stuchbery, in: *Proc. Int. Conf. on Perspectives for the Interacting Boson Model on the Occasion of its 20th Anniversary*, ed. R.F. Casten,

A. Vitturi, A.B. Balantekin, B.R. Barrett, J.N. Ginocchio, G. Maino and T. Otsuka, (World Scientific, Singapore, 1994) p.639

[St95a] A.E. Stuchbery and S.S. Anderssen, Phys. Rev. **C51** (1995) 1017

[St95b] A.E. Stuchbery, in press.

[Ta93] R. Tanczyn, G. Kumbartzki, A. Piqué, T. Vass, A. Pakou and N. Benczer-Koller, Phys. Rev. **C48** (1993) 140

[Th81] D.A. Thompson, Radiation Effects **56** (1981) 105

[Va69] L. Varga, I. Demeter, L. Keszthelyi, Z. Szökofolvi-Nagy and Z. Zamori, Phys. Rev. **177** (1969) 1783

[Va85] E. Van Walle, J. Wouters, D. Vandeplassche, N. Severijns and L. Vanneste, Hyp. Int. **22** (1985) 507

[Vo90] M.J.A. de Voigt, R. Kaczarowski, H.J. Riezebos, R.F. Noorman, J.C. Bacelar, M.A. Deleplanque, R.M. Diamond, F.S. Stephens, J. Sauvage and B. Roussière, Nucl. Phys. **A507** (1990) 472

[Wa70] F. Wagner, D. Kucheida, G. Kaindl and P. Kienle, Z. Phys. **230** (1970) 80

[Wa74] D. Ward, H.R. Andrews, R.L. Graham, J.S. Geiger and N. Rud, Nucl. Phys. **A234** (1974) 94

[Wa86] D.D. Warner, Phys. Rev. **C34** (1986) 1131

[Wa93] J.C. Walpe, U. Garg, S. Naguleswaran, W. Reviol, J. Wei, D. Ye, I. Ahmed, I. Bearden, M.P. Carpenter, R.V.F. Janssens, T.L. Khoo and T. Lauritsen, in: *1990-1993 Tri-Annual Report, Notre Dame*, p.62

[We80] K.J. Weeks and T. Tamura, Phys. Rev. **C22** (1980) 1323

[We85] J.C. Wells, M.P. Fewell and N.R. Johnson, *LIFETIME: A Computer Program for Analyzing Doppler-Shift Recoil-Distance Nuclear Lifetime Data*, report **ORNL/TM-9105**.

[Wi66] A. Winther and J. de Boer, *Coulomb Excitation*, ed. K. Alder and A. Winther (Academic, New York, 1966) p.303

[Wi84] J.S. Williams and J.M. Poate, in: *Ion Implantation and Beam Processing*, ed. J.S. Williams and J.M. Poate (Academic Press, Sydney, 1984) Ch.1

[Wo81] J.L. Wood, in: *Proc. 4th Int. Conf. on Nuclei Far From Stability*, ed. P.J. Hansen and O.B. Nielsen (Helsingor, Denmark, 1981), report **CERN 81-09**, p.612

[Wo82] J.L. Wood, in: *Lasers in Nuclear Physics*, ed. C.E. Bemis Jr and H.K. Carter (*Nuclear Science Res. Conf. Ser. Vol.3*) (Harwood, New York, 1982) p.481

[Wo85] A. Wolf, D.D. Warner and N. Benczer-Koller, Phys. Lett. **B158** (1985) 7

[Wo87a] A. Wolf, R.F. Casten and D.D. Warner, Phys. Lett. **B190** (1987) 19

[Wo87b] A. Wolf and R.F. Casten, Phys. Rev. **C36** (1987) 851

[Wo92] J.L. Wood, K. Heyde, W. Nazarewicz, M. Huyse, P. van Duppen, Phys. Reps. **215** (1992) 101

[Wo93] A. Wolf, O. Scholten and R.F. Casten, Phys. Lett. **B312** (1993) 372

[Wu83] C.Y. Wu, *Ph.D. Thesis*, University of Rochester, 1983.

[Ya67] T. Yamazaki, Nucl. Data **A3** (1967) 1

[Ya88] L. Yabo, H. Dailing, S. Hueibin and D. Zhaozhong, Z. Phys. **A329** (1988) 307

[Zi73] K. Zioutas, B. Wolbeck and B. Persheid, Z. Phys. **262** (1973) 413

[Zi85a] J.F. Ziegler, J.P. Biersack and U. Littmark, *The Stopping and Ranges of Ions in Solids*: Volume 1 of *The Stopping and Ranges of Ions in Matter*, ed. J.F. Ziegler (Pergamon, New York, 1985).

[Zi85b] M. Zimmerman and J. Dobeš, Phys. Lett. **B156** (1985) 7